

https://dspace.org/

Fluxon pinning and geometrical effects in a type 2 superconductor

Doyle, Terence Brian

2015-03-05
http://hdl.handle.net/10539/17192

Downloaded from a DSpace repository. https://dspace.org/

which on substitution, together with A (see above), into equation 5.14 gives:

$$p_m^{\ell}(b,t) \simeq 2\left[(1-f)C_T/\rho\kappa\right](B_{c2}^2(t)/\kappa_1^2(t))\left[\frac{d}{dr}(|\psi|^2 - |\psi|^4)\right]_{max} \qquad 5.18$$

Substituting for p_m^{ℓ} from this expression into equation 5.13 gives finally for the bulk pinning force density in class II ($b > 0.6$):

$$P_v(b,t) \approx k\omega\Gamma\left[(1-f)C_T/\phi_o^{\frac{1}{2}}\kappa\right].b^{-1}.(B_{c2}^{5/2}(t)/\kappa_1^2(t))\left[\frac{d}{dr}(|\psi|^2 - |\psi|^4)\right]_{max} \qquad 5.19$$

To obtain the dependence of P_v on the reduced temperature t and, approximately, on the reduced induction b the approximate form for the term in ψ (from equation 3.12b) is substituted into the above equation giving

$$P_v(b,t) \propto \left[B_{c2}^3(t)/\kappa_1^2(t)\right]b^{-\frac{1}{2}}(1-b) \qquad 5.19b$$

Comparison of the above equations with the experimental results for $P_v(b > 0.6)$ (equation 5.9 and following) shows that the model is in good agreement of $\beta = 1$, and if the predicted temperature dependence behaves like $B_{c2}^{5/2}(t)$ for t not close to unity. For an exact assessment of the predicted t dependence $\left[P_v(b = 0.6)\kappa_1^2(t)/B_{c2}^3(t)\right]$ as obtained experimentally for the $[1\bar{1}0]$ 1 per cent, 2 per cent and 4 per cent deformed specimens (as-quenched - class (ii)) have been plotted against t^2 in figure 5.33. According to the model this plot should show no dependence on t, i.e. the slope should be zero. This is confirmed in the figure for the regime $t < 0.9$. The figure also demonstrates that $P_v(b = 0.6)$ is independent of the extent of deformation for $t < 0.9$. The breakdown of the theory for $t > 0.9$ will be discussed in section 5.5.4.

In figure 5.34 the exact dependence of P_v on b as predicted by equation 5.19a (solid curve) using the results of figure 3.5 (for

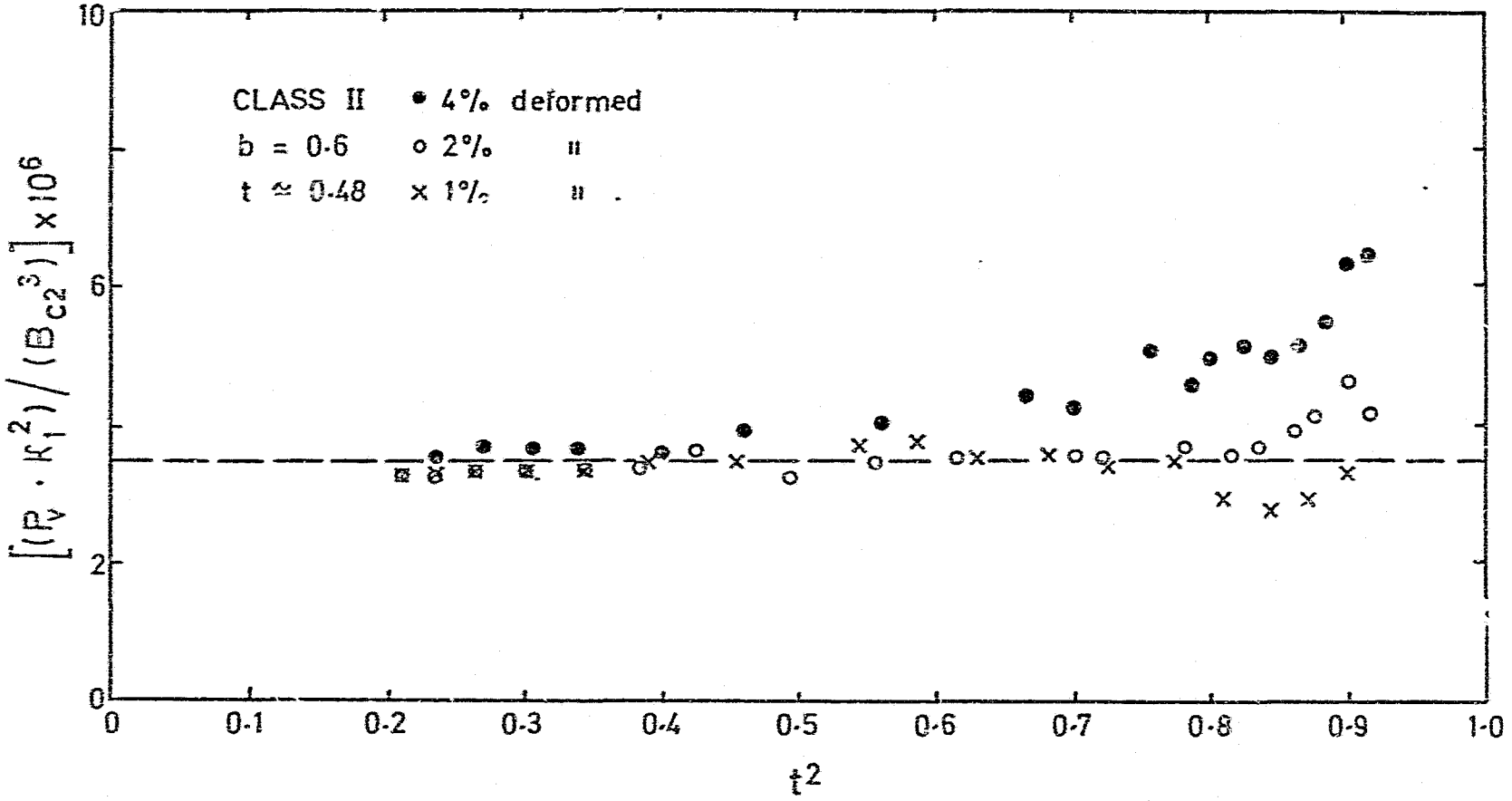


Figure 5.33. A plot of the temperature invariant component of the bulk pinning force density, in accordance with the model for class II, against t^2 for the 4%, 2% and 1% deformed $[1\bar{1}0]$ specimens. The relative deviation from the prediction of the model is small except at $t \rightarrow 1$.

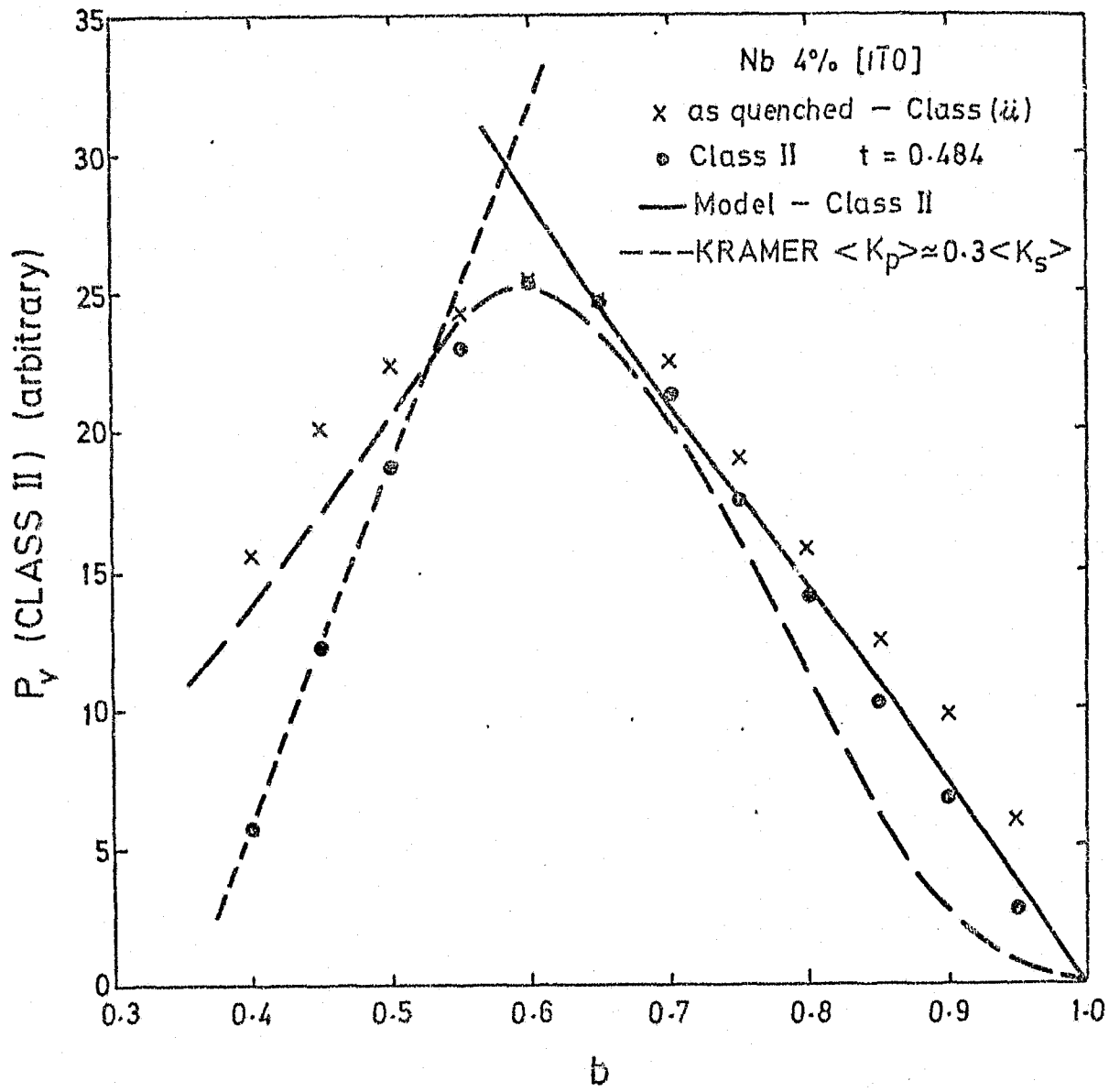


Figure 5.34. Comparison of the predicted b dependence of the bulk pinning force density, from the model for class II (solid curve - $b > 0.6$), with experiment on the as-quenched and aged $[1\bar{1}0]$ 4% deformed specimen (class (ii) and class II respectively). Also shown is the prediction of Kramer's (1972) model with appropriate choice of parameters.

$b > 0.6$) is compared with experiment in class (ii) and Class II (i.e. for the $[1\bar{1}0]$ 4 per cent deformed specimens (as-quenched and aged for 10 minutes at 70K and ditto after subtracting off class I behaviour - see figure 5.28). (A suitable scaling factor on the P_v axis has been chosen for each of the curves to facilitate quantitative comparison.) The model appears to be good qualitative agreement with the class II results for $b > 0.6$. [It is apparent in figure 5.34 that there is evidence of a peak effect anomaly at $b \simeq 0.8$ in the class (ii) curve which is absent in the class II curve. This will be discussed in section 5.5.4.] An approximate quantitative assessment will now be made for p_m^{ℓ} and P_v at $b = 0.6$ and $T = 4.2K$.

Thus for p_m, substituting the following values into equation 5.18, viz: $B_{c2}(4.2K) = 2720$ gauss, $\kappa_1(4.2) = 1.57$, $\kappa = 0.785$ $\rho = 1.5 \times 10^9$ cm^{-2}, $(1-f) = 1$, $C_T = 5 \times 10^{-5}$, $\phi_o = 2.07 \times 10^{-7}$ gauss cm^2 and $\left[\partial/\partial_r(|\psi|^2 - |\psi|^4)\right] = 0.8(B_{c2}/\phi_o)^{\frac{1}{2}}$ (from figure 3.5 with $b = 0.6$) gives $p_m^{\ell} \simeq 2.3 \times 10^{-2}$ dynes cm^{-1}. This is larger than the prediction for a clean edge dislocation (equation 3.2.5) by a factor of approximately 23, but still smaller than the critical pinning force required by Labusch's threshold criterion (equation 3.49 and following) by a factor of 2. Equation 3.49 however applies strictly only for point pinning sites ($d << a_o$) in the dilute-limit and will predict a value for p_c which is too large for line forces as in the present case.

Substituting the above value for p_m^{ℓ} into equation 5.13 for P_v gives $P_v \simeq (6.5 \times 10^{12})\omega k\Gamma$ dynes cm^{-3} at 4.2 and $b = 0.6$. The measured value for $P_v(b = 0.6, T = 4.2K)$ in class II (from figure 5.28) is 2.5×10^5 dynes cm^{-3} so that the required value for $\omega k\Gamma$ is approximately 5×10^{-8} which is quite reasonable since for $k \sim 0.1a_o \sim 10^{-6}$ cm $\omega\Gamma \sim 5.10^{-2}$.

5.5.4 Anomalous behaviour

There are two principal types of anomaly which require attention, viz: (i) the peak effect which occurs at $b \simeq 0.8$ (see for example figures 5.24a and 5.24b) and (ii) departures from the predicted temperature dependence in class I and class II as $t \to 1$ (see figures 5.30 and 5.33). Any discussion of these latter departures can only be speculative however. This is because of the manifold variety of possible physical effects which can be important as $t \to 1$ and the relative paucity of experimental results in this regime. Neglecting possible surface effects there are three bulk effects which should be considered, viz:

(i) as $t \to 1$ the scale of the fluxon lattice (a_o, ξ and λ) increases rapidly with respect to the scale of the defects responsible for pinning. According to appendix A1(h) this could lead to either a positive of negative deviation, in the plot of figure 5.30 (for the multiple dislocation sites), depending on the distribution function for the size of these sites. The Cottrell atmosphere sites should be unaffected by this consideration.

(ii) Taking $B_{c2}(t) \propto (1-t)$ the threshold pinning force (equation 3.49b) has a temperature dependence given approximately by $p_{mc}(t) \propto (1-t)^{3/2}$. For the $\delta\kappa$ mechanism (which obtains in class I and class II) the basic pinning force varies as $(1-t)^{5/2}$ approximately and therefore if p_{mc} falls within the range of variation of the magnitude of $p_m[\delta\kappa]$ for the defects a negative deviation is expected as $t \to 1$.

(iii) The elastic pinning mechanisms also vary with temperature as $(1-t)^{3/2}$ approximately so that if their contribution is finite a positive deviation is expected as $t \to 1$.

(iv) A second-order elastic interaction contribution which depends on C_B will be especially enhanced as $t \to 1$ since, in contrast to $\delta\kappa$, $\delta\varepsilon_v$ and the other δC, δC_B does not go to zero as $t \to 1$ (see chapter 3).

Another effect which will cause an anomaly at any $0 < t < 1$ and which would be sensitively manifest in the plots such as those of figures 5.30 and 5.33 is the so-called matching effect (see chapter 3 and discussion in section 5.5.2(b). This would give rise to a peak in $P_v(b,t)$ at a particular value of B, i.e. at a particular combination of both t and b.

Without a knowledge of the relative importance of the above mentioned effects and considering the approximate nature of the models for class I and class II and the scatter and small size of the deviations from zero slope in the plots of figures 5.30 and 5.33 it is not possible to make definite predictions. In class I (figure 5.30) the plot shows an overall positive deviation for $t > 0.5$, which may be consistent with effects (i), (iii) or (iv) or any combination of these effects, and also a suggestion of a minimum at $t^2 > 0.8$ which may be due to effects (i) or (ii) or both. The class II behaviour (figure 5.33) is more interesting however. Thus the 1 per cent deformed specimen shows only a small negative deviation at $t^2 > 0.85$, the 2 per cent specimen a small positive deviation for $t^2 > 0.85$ and the 4 per cent specimen a stronger positive deviation beginning at $t^2 \simeq 0.5$. Now for class II $p_m \propto C_1 \propto \rho^{-1}$ (equation 5.17) and therefore the increasing positive deviation with increasing deformation (and therefore ρ) may be correlated with a decrease in $p_m[\delta\kappa]$ relative to p_m [elastic] (effects (iii) or (iv)). However, the first order elastic interaction will probably also decrease as $C_1 \propto \rho^{-1}$

approximately and the second order as $C_1^2 \propto \rho^{-2}$ approximately (see section 5.5.3(a)). A more likely explanation is that the deviation is the result of residual background class I behaviour which is a linearly increasing function of deformation and has a slightly slower variation with $B_{c2} \propto (1-t)$ than the class (ii) behaviour (see figure 5.26).

The peak effect at $b \simeq 0.8$ will now be considered. Thus according to Campbell and Evetts (1972), who give a full review of previous work and discuss various mechanisms for this effect, "the situation for pure niobium is characteristically obscure with a number of conflicting reports". There is however a general consensus that the peak effect is related to the presence of an interstitial impurity and that it is most pronounced at some intermediate stage of segregation of the interstitials at dislocations, grain boundaries or other defect features. This is certainly also the case in the present investigation (see figure 5.32 and section 5.5.2(b)). The precise role played by interstitial impurities has not previously been elucidated however.

The known mechanisms which could possibly give rise to a peak effect at intermediate or high b may be summarized as follows (see also Campbell and Evetts (loc. cit.):

(i) In two phase materials where pinning takes place at the interface boundaries between the phases, the possibility exists that for a certain field value the interaction force will go to zero thus leading to a minimum in P_v and the apparent existence of a peak at higher field values. (Evetts and Wade, 1970 and Dew-Hughes and Witcomb, 1972.) This mechanism cannot account for the present results.

(ii) The matching effect which is clearly not applicable here.

(iii) A pinning threshold effect which leads to an increase in the number of effective sites and for which the argument is similar to that for the t anomaly discussed above.

(iv) The proposal of Pippard (1969) which depends on the fact that shear modulus (C_{66}) of the fluxon lattice goes to zero quadratically as $b \to 1$. Thus since the basic pinning force varies approximately as (1-b) it is possible that a network of relatively weak line forces (for which the response of the fluxon lattice depends only on the modulus C_{66}, equation 3.52) exceeds the pinning threshold condition as $b \to 1$ and begins to pin effectively.

(v) The proposal of Campbell and Evetts (loc. cit.) and see also section 5.5.2(b)) that synchronous pinning may result, with increasing b, from a concomitant increase in the density of fluxon lattice defects which then assist the fluxon lattice to relax onto the existing pinning sites.

(vi) Finally there is the model of Kramer (1973) which is also based on a line-force response by the fluxon lattice.

The Pippard mechanism appears superficially to offer the best approach to explaining the peak effect in both class (i) and class (ii) of the present investigation.

According to Campbell and Evetts (loc. cit.) the upper limit for the magnitude of P_v (peak), for the Pippard mechanism, is given by

$$P_v^p(t) = (B/\phi_o)p_m^{\ell} \qquad 5.20a$$

$$= (k/8\pi\phi_o^{\frac{1}{2}})\left[B_{c2}^{5/2}(t)/\kappa_2^2(t)\right](1-b_p)^2\left[\ln(R_o/a_o)\right]^{-1} \qquad 5.20b$$

(see equation 3.52) where $ka_o(=u_{oc})$ is the required distortion for synchronous pinning, b_p is the value of b at the peak and R_o is the

average separation between the line pinning sites.

Campbell and Evetts suggest $k \propto 1/a_o$. Substituting $R = 10a_o$ and $p_m^{\ell} = \gamma(1-b)$ into equations 5.20a and 5.20b gives

$$(1-b_p) = (8\pi/k\phi_o^{\frac{1}{2}})\gamma(t)\left[B_{c2}^{3/2}(t)\kappa_2^2(t)\right] \qquad 5.21$$

The qualitative requirements from experiment (see for example figure 5.24) are:

(i) $(1-b_p)$ should have no significant dependence on temperature i.e. that in equation 5.21 (with $k \propto a_o^{-1} \propto B_{c2}^{1/2}(t)$) $\gamma(t) \propto B_{c2}^2(t)/\kappa_2^2(t)$. From previous considerations it will be apparent that this is consistent with the $\delta\kappa$ pinning mechanism for which (equation 3.12) $\gamma(t) \propto B_{c2}^{5/2}(t)/\kappa_1^2(t)$ which can be expressed approximately as $B_{c2}^2(t)/\kappa_2^2(t)$ for t not close to unity.

(ii) $P_v^p(t)$ should have a slightly slower variation with temperature than $P_v(t)$ in class I and class II and should have approximately the same magnitude in class (i) and class (ii). In order to compare the prediction of equation 5.20 for $P_v^p(t)$ with experiment in class (i) and in class (ii) it will be necessary to make two assumptions, viz: (a) that the predictions of the models for class I and class II for the temperature dependences of P_v are still valid for $b = b_p \simeq 0.8$ and correspond sufficiently well to the temperature dependences which would have been obtained in class (i) and class (ii) respectively if the peak effect were not present and (b) that the summation processes for the peak effect and for either class I or class II are not interdependent, i.e. that they simply sum linearly. In accordance with the above assumptions the predicted bulk pinning force will be given (for class (i) and class (ii)) by

$$\left[P_v^T(b,t)\right]_{\text{class (i), (ii)}} = \left[P_v^{I,II}(b,t) + P_v^p(b,t)\right] \qquad 5.22a$$

where $P_v^{I,II}$ are the predicted bulk pinning force densities in class I or in class II respectively. Since the absolute magnitude of P_v^p is not known it is necessary to express equation 5.22a in terms of ratios, thus:

$$\left[P_v^T(b_1,t)\right]_{\text{class (i),(ii)}} / P_v^{I,II}(b_2,t) = \left[P_v^{I,II}(b_1,t) + P_v^p(b_1,t)\right] / P_v^{I,II}(b_2,t) \qquad 5.22b$$

Now the obvious choice for b_1 is $b_1 = b_p = 0.8$ where $\left[P_v^p\right]_t$ is a maximum. If b_2 is chosen so that $P_v^p(b_2) \ll P_v^p(b_p)$ the in accordance with assumption (a) above $P_v^{I,II}(b_2) \simeq \left[P_v^p(b_2)\right]_{\text{class (i),(ii)}}$. It is apparent from figure 5.24 that this condition should be satisfied for $b_2 \leq 0.6$ in both class (i) and class (ii). Substituting into equation 5.22b for b_1, b_2 and $P_v^{I,II}$ (left hand side only) and also the temperature dependences for P_v^I (from equation 5.7) and P_v^p (from equation 5.20b) then gives the following prediction for class (i), viz:

$$\left[P_v^T(0.8,t)/P_v^T(0.6,t)\right]_{\text{class (i)}} \simeq \left[\alpha B_{c2}^3\kappa_2/\kappa_1^4 + \beta B_{c2}^3/\kappa_2^2\right] / \left[B_{c2}^3\kappa_2/\kappa_1^4\right]$$

$$\simeq \alpha + \beta\kappa_1^4(t)/\kappa_2^3(t) \qquad 5.23$$

where

$$\alpha = \left[P_v^I(0.8,t)/P_v^I(0.6,t)\right] = 0.64 \text{ (from figure 5.32)}$$

and is not dependent on the reduced temperature t and

$$\beta = \left[P_v^I(0.8,t)/P_v^p(0.8,t)\right]$$

which has only a very small dependence on t.

For class (ii), substituting for the temperature dependences of P_v^{II} and P_v^p from equations 5.19b and 5.20b (with $k \propto B_{c2}^{\frac{1}{2}}$) respectively, gives

$$\left[P_v^T(0.8,t)/P_v^T(0.6,t)\right]_{\text{class (ii)}} \simeq \left[\delta B_{c2}^3/\kappa_1^2 + \varepsilon B_{c2}^3/\kappa_2^2\right]/\left[B_{c2}^3/\kappa_1^2\right]$$

$$\simeq \delta + \varepsilon\kappa_1^2(t)/\kappa_2^2(t) \qquad 5.24$$

where

$\delta = \left[P_v^{II}(0.8,t)/P_v^{II}(0.6,t)\right] = 0.5$ (from equation 5.19 or figure 5.34)

and

$\varepsilon = \left[P_v^{II}(0.8,t)/P_v^{P}(0.8,t)\right]$

The theoretical predictions of equations 5.23 and 5.24 will now be compared with the experimental results. Thus $P_v(b = 0.8,t)/P_v(b = 0.6,t)$ as determined from experiment on the 4 per cent deformed specimens in class (i) (figures 5.16a and 5.16b) and in class (ii) (figures 5.13a and 5.13b) are plotted against $\kappa_1^4(t)/\kappa_2^3(t)$ and $\kappa_1^2(t)/\kappa_2^2(t)$ (from figure 5.6) respectively in figure 5.35. Although there is considerable scatter in the points, especially in class (i), it is possible to find a moderately accurate linear relationship (as shown by the straight lines in the figure) for each case in qualitative agreement with equations 5.23 and 5.24. [The small peak at $f(\kappa) \simeq 0.75$ in class II is related to the anomaly $P_v(b)$ at $b \simeq 0.6$ as shown by the curves of figure 5.13b.]

From these approximate straight line fits values for α, β, δ and ε have been determined. Thus: $\alpha = 0.65 \pm 0.5$ in good agreement with the model, $\beta \simeq 0.58$, $\delta = 0.44 \pm 0.4$ compared with 0.5 from theory and $\varepsilon \simeq 0.51$. Now

$$\left[\beta/\varepsilon\right].P_v^{II}(b = 0.8)/P_v^{I}(b = 0.8) = \left[P_v^P(0.8)\right]_{\text{class (ii)}} / \left[P_v^P(0.8)\right]_{\text{class (i)}} \qquad 5.25$$

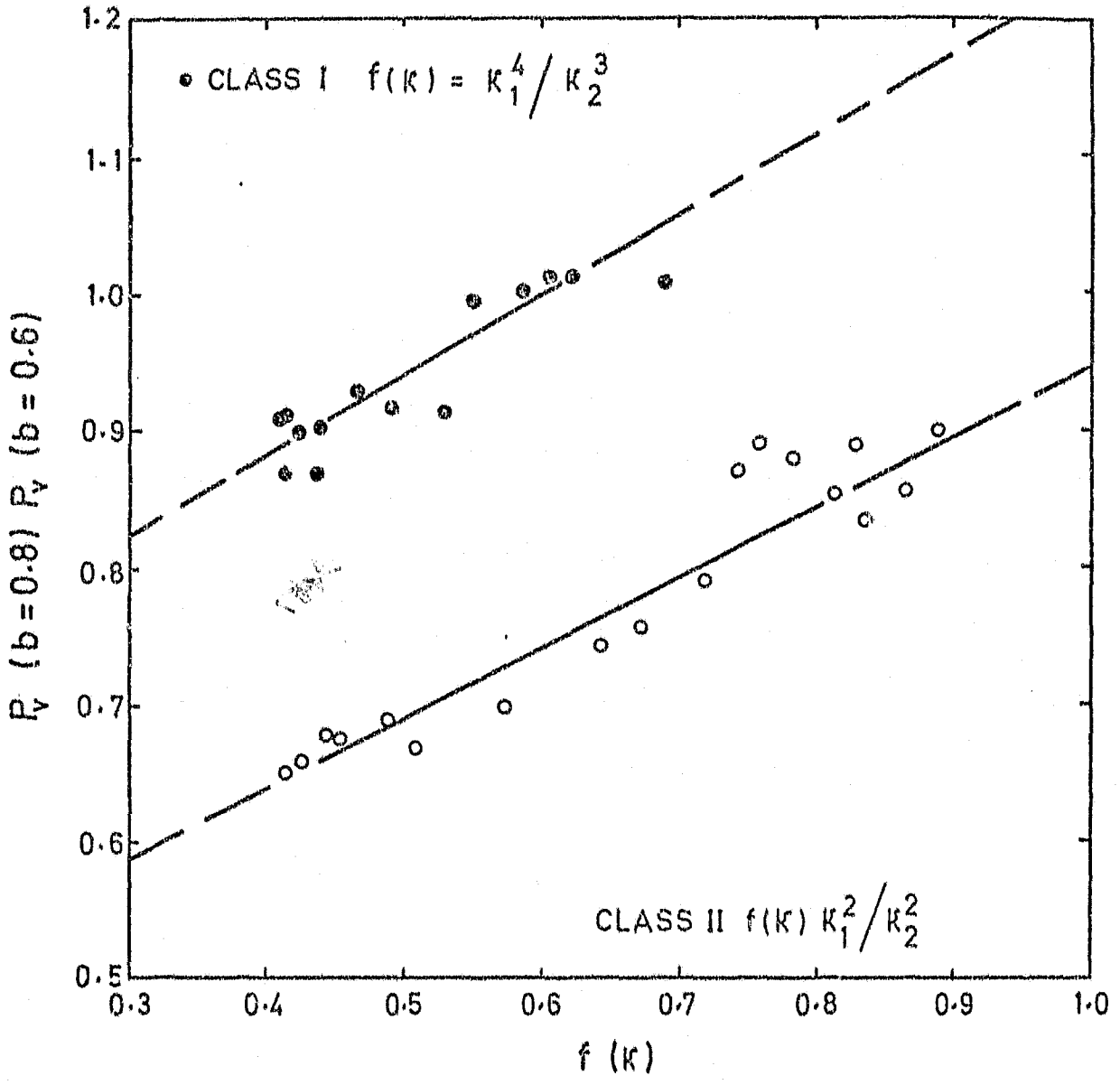


Figure 5.35. A plot of the variations of the ratio of the measured bulk pinning force density at $b = 0.6$ and $b = 0.8$ for class (i) and class (ii) against respectively $\kappa_1^4(t)/\kappa_2^3(t)$ (which is the ratio of the predicted temperature dependences for class I and the peak effect model) and $\kappa_1^2(t)/\kappa_2^2(t)$ (which is the ratio of the predicted temperature dependences for class II and the peak effect model).

which on substituting $\beta/c = 0.58/0.51$ and $P_v^{II}(0.8)/P_v^{I}(0.8) \simeq$ $\left[P_v(0.8)\right]_{\text{class (ii)}} / \left[P_v(0.8)\right]_{\text{class (i)}} = 3.3$ (figure 5.23, 4 per cent deformed specimens as-quenched gives $P_v^P[1\bar{1}0]/P_v^P[001] \simeq 3.8$. In figure 5.17 the anisotropy of $P_v(b = 0.8, T = 4.05K)$ with H_o in the $(1\bar{1}0)$ plane for the 4 per cent deformed disc is shown by the points (the ordinate scale for this plot has been chosen to facilitate inter-comparison with the solid curve (a)). This result is in approximate agreement with the above ratio and also indicates that P_v^P has a small maximum for H_o along [001] and a large maximum along the $[1\bar{1}0]$ direction.

It is concluded therefore that peak effect observed here is qualitatively consistent with the Pippard mechanism (the predicted magnitude of the effect will be examined later). The problem is now to identify the line-forces responsible for the effect. Clearly because of the relatively small difference in the magnitude of the effect in class (i) and class (ii) they cannot be dislocations or even Cottrell atmospheres on the dislocations. The effect is however definitely related to the presence of interstitial hydrogen in some ordered or sub-ordered phase. In section 3.1 previous work on pinning due to oxygen and nitrogen in niobium and vanadium was reviewed. For relatively low interstitial concentrations pinning was found to be a maximum when the fluxons were parallel to antiphase boundaries, to planes normal to crystal directions which are soft and therefore favour clustering of interstitials in these planes and to the directions along which such boundaries or planes intersect. In particular, with H_o in a {110} plane, approximately equal maxima were found for P_v when H_o was parallel to the <001> and <110> directions. It is possible therefore that the same mechanisms operate for hydrogen in niobium but in

which on substituting $\beta/\varepsilon = 0.58/0.51$ and $P_v^{II}(0.8)/P_v^{I}(0.8) \simeq \left[P_v(0.8)\right]_{\text{class (ii)}} / \left[P_v(0.8)\right]_{\text{class (i)}} = 3.3$ (figure 5.23, 4 per cent deformed specimens as-quenched gives $P_v^p[1\bar{1}0]/P_v^p[001] \simeq 3.8$. In figure 5.17 the anisotropy of $P_v(b = 0.8, T = 4.05K)$ with H_o in the $(1\bar{1}0)$ plane for the 4 per cent deformed disc is shown by the points (the ordinate scale for this plot has been chosen to facilitate intercomparison with the solid curve (a)). This result is in approximate agreement with the above ratio and also indicates that P_v^p has a small maximum for H_o along [001] and a large maximum along the $[1\bar{1}0]$ direction.

It is concluded therefore that peak effect observed here is qualitatively consistent with the Pippard mechanism (the predicted magnitude of the effect will be examined later). The problem is now to identify the line-forces responsible for the effect. Clearly because of the relatively small difference in the magnitude of the effect in class (i) and class (ii) they cannot be dislocations or even Cottrell atmospheres on the dislocations. The effect is however definitely related to the presence of interstitial hydrogen in some ordered or sub-ordered phase. In section 3.1 previous work on pinning due to oxygen and nitrogen in niobium and vanadium was reviewed. For relatively low interstitial concentrations pinning was found to be a maximum when the fluxons were parallel to antiphase boundaries, to planes normal to crystal directions which are soft and therefore favour clustering of interstitials in these planes and to the directions along which such boundaries or planes intersect. In particular, with H_o in a {110} plane, approximately equal maxima were found for P_v when H_o was parallel to the <001> and <110> directions. It is possible therefore that the same mechanisms operate for hydrogen in niobium but in

the present case are relatively weaker and therefore are able to pin effectively only by a synchronous mechanism (e.g. the Pippard mechanism). That the magnitude of the peak effect for H_o along the $[1\bar{1}0]$ direction is larger than for H_o along [001] would then indicate that the clustering effect is more important than crystallographic ordering in this case (see section 4.1). Another possibility is that the pinning sites are twin boundaries resulting from a martenistic phase transformation (see chapter 4), or, more likely, thin (order ξ) lenticular or rod-like martenistic precipitates which would pin by the $\delta\kappa$ mechanism. Such martensite precipitates are not expected to be strong pinning sites however (Campbell and Evetts, 1972). From previous considerations, and in agreement with other investigations on the peak effect the quantity of interstitial involved in the effect is very small.

Finally, putting $k = 10^{-2}$ (as suggested by Campbell and Evetts, 1972) in equation 5.20 and substituting $(1-b_p) = 0.2$ and for B_{c2} and κ_2 for niobium at 4.2K gives $P_v^p(4.2K) \simeq 2.6 \times 10^6$ dynes cm^{-3} as an upper limit. This is a factor of approximately 10^2 larger than the experimental peak. If the theoretical prediction (equation 5.20) is reduced by this factor then the predicted value for γ is approximately 2×10^{-4} dynes cm^{-1} which is the sort of order of magnitude expected.

5.5.5 Summary and conclusions

The anisotropy of the bulk pinning force density and its dependence on the configurational distribution of interstitial hydrogen in small niobium single crystal specimens containing predominantly edge dislocation arrays have been determined in a series of experiments. From these results and considerations of the deformation structure it was possible to deduce the existence of two distinct classes of behaviour which could be associated in a mutually consistent manner with the

operation of 'multiple dislocation' and 'Cottrell atmospheres' sites respectively. The multiple dislocation sites of class I consist of small (10^3 - 10^4Å diameter) roughly spherical regions of tightly tangled dislocation segments, dipoles or multipoles. The Cottrell atmosphere sites of class II consist of Cottrell atmospheres on edge dislocation segments parallel to the fluxon lattice.

Class I behaviour is similar to that found by other authors in lightly deformed type II superconducting materials. In accordance with the theoretical expectation that the interaction of isolated segments of dislocation with the fluxon lattice is too weak to satisfy Labusch's threshold requirements it is postulated that the pinning behaviour found by these other authors is also due to multiple dislocation sites of the type identified here. A proper formulation of the elementary pinning force due to a multiple dislocation site of this type and range of size (i.e. diameter $2R \sim a_o$) shows that the pinning force due to sites for which $2R \lesssim a_o$, at any instant, will be much larger than that for the others. The width of the distributions in the size and potential density (at constant $|\psi|^2$) of the multiple dislocation site is apparently sufficiently large that no significant matching effect occurs as a_o is varied. The volume density and pinning strength of effective sites apparently satisfy the dilute-limit requirements. Moreover since for these sites $R \lesssim a_o/2$ and the pinning range $d \simeq a_o/2$ a basic requirement in Labusch's point-force dilute-limit model, viz: $d \ll a_o$, is possibly also satisfied. Substitution of $d = a_o/2$ and the appropriate, properly formulated, expressions for the basic pinning force into Labusch's expression gives very good agreement with class I and apparently also with the experimental results of Good and Kramer (loc. cit.), Freyhardt (loc. cit.) and probably also Coote (loc. cit.).

In specimens containing predominantly edge dislocation arrays the multiple dislocation sites apparently pin by the $\delta\kappa$ mechanism and in Freyhardt's specimens in which the predominant dislocations are of screw type aligned normal to the fluxons the sites apparently pin by the second-order elastic interaction.

The behaviour in class II is apparently due to a form of synchronous pinning by a high volume density of Cottrell atmosphere sites which are apparently not able to pin effectively (i.e. do not satisfy the threshold criterion) at low values of b but rapidly become effective at $b \simeq 0.4$ (when the fluxon cores begin to overlap) and thereafter pin in accordance with a synchronous pinning model. This behaviour is a consequence of the nature of the proposed model for the $\delta\kappa$ interaction mechanism which apparently obtains for the Cottrell atmosphere sites and the wavy nature and high volume density of these sites. The proposed summation model for class II is in good overall agreement with experiment, and in particular for $b > 0.6$, where an explicit expression is formulated. The pinning behaviour in class II also leads to a self-consistent prediction for the coefficient of diffusion D(H, Nb) hydrogen at niobium (at 90K) which is in good agreement with the expectation value obtained by extrapolation (on an Arrhenius plot) of the well accepted higher temperature values for D(H, Nb) (see figure 4.2). By suitable ageing procedures the interstitial hydrogen in the Cottrell atmospheres can be precipitated out of solution into the dislocation cores and class II behaviour disappears leaving the much smaller class I background.

The above experiments, besides establishing the salient physical processes involved in fluxon pinning in lightly deformed, low κ materials, constitutes the first critical appraisal of Labusch's threshold criterion. It is obvious from the foregoing that clean

isolated dislocations (i.e. free of Cottrell atmospheres) are not effective as pinning sites and therefore, presumably, interact only elastically, i.e. non dissipatively with fluxons - in qualitative agreement with the threshold criterion. The fact that the dislocation density, particularly in regions of braiding, is too high for the dilute-limit model of Labusch to be applicable is obviously not relevant from a qualitative point of view.

Anomalous departures, from the predicted pinning behaviour, which were experimentally observed in the regimes $t \to 1$ and $b \to 1$ in both classes were also considered and discussed. The 'peak' effect which was found at $b \simeq 0.8$ in all the as-quenched specimens was shown to be in reasonably good agreement with Pippard's model for a synchronous line pinning-site mechanism and it was argued that the line sites were the result of some form of ordering or clustering of interstitial hydrogen on planes which intersect along the <110> and <001> directions in the niobium crystals.

CHAPTER 6

6. The Macroscopic Magnetization behaviour of Cylinders of ideal Type II Superconductors

6.1 Introduction

In any magnetic material the local values of the magnetization ($\underline{M}(r)$), the induction ($\underline{B}(r)$) and the internal or thermodynamic field ($\underline{H}_e(r)$) are related by:

$$\underline{B}(r) = \underline{H}_e(r) + 4\pi\underline{N}(r) \qquad 6.1$$

For the special case of specimens with spheroidal geometry, for which one limiting case may be considered to be very long cylinder, H_e is everywhere uniform and homogeneous inside the specimen and is given, in terms of the external field H_o by

$$H_{e_i} = H_{o_i} - 4\pi \sum_{j=1}^{3} D_{ij} M_j \qquad 6.2$$

where D_{ij} is the so-called demagnetization tensor, which can be calculated exactly for any spheroidal geometry (see for example Brailsford, 1966).

Thus if a single valued constitutional relationship is known for $B[H_e]$ or $M[H_e]$ (the square brackets will be used henceforth to denote equilibrium behaviour) the magnetization behaviour for any specimen with spheroidal geometry can be predicted. (For type II superconductors this has been done by Kulik, 1966, Fetter and Hohenberg, 1967, 1969, Cape and Zimmerman, 1967, and Zoller and Dillinger, 1969).

For shapes other than spheroidal the determination of the position dependent internal field $H_e(r)$ now usually involves a boundary value

problem which is not soluable in closed analytic form. However, for cylinders, with either very large or very small axial ratios, of normal magnetic materials (i.e. excluding superconductors*), in an axial externally applied magnetic field the internal field H_e may, to fair approximation, be considered to be uniform in the specimen. The demagnetizing coefficient is now taken to be either D_e, the demagnetizing factor for the enclosed spheriod (i.e. a spheroid having the same principal dimensions) or, more accurately, the so-called magnetometric demagnetizing factor D_m which is calculated for a solenoidal coil of the same dimensions as the specimen (see Brown, 1962). Fetter and Hohenberg (1967, 1969) argue that the above approximation does predict the reversible equilibrium behaviour in disc-specimens ($D \to 1$) of type II superconductors correctly and it has in fact frequently been used in the analysis of magnetization measurements on thin disc and short cylindrical specimens of type II superconductors. It will be demonstrated in this chapter however that this approach has only a limited validity and that the actual behaviour in such specimens can never approach equilibrium for certain external field conditions. Such non-equilibrium behaviour has been observed previously in disc-specimens and has variously been attributed to fluxon pinning or the existence of a mixed-intermediate state** in the specimen (see for

---

* This is because of the localized nature of flux tubes (in type I) and fluxons (in type II superconductors). Thin ferromagnetic specimens containing so-called 'bubble' domains are therefore also excluded.

** For a brief introduction to the mixed-intermediate state see Seeger (1970). It will become apparent later that the actual behaviour of the fluxons in a type II superconducting disc-specimen in transverse field has features in common with the so-called mixed-intermediate state but that the effect is due to the specimen geometry rather than to the existence of a long range attractive interaction between fluxons.

example Aston, Dubeck and Rothwarf, 1971 and Rothwarf, Rao and Dubeck, 1972).

In this latter case however the theory (which is essentially the same as the theory for the so-called 'Horn effect' in type I superconductors (see for example Andrew, 1948, or Kuper, 1968) predicts a size effect which will be shown to be non-existent in niobium disc-specimens. It will also be shown theoretically and experimentally that the non-equilibrium behaviour is a direct consequence of the cylindrical geometry.

Other pertinent theoretical work in respect of the magnetic behaviour of type II superconducting disc-specimens and thin films in transverse field, is that due to Pearl (1964, 1965) and Maki (1965) who uses some of Pearl's results. It will be useful to summarize briefly some aspects and conclusions of these investigations. Thus: Pearl determines the structure of a fluxon where it emerges normally from the superconductor-vacuum interface by solving the Ginzburg-Landau equation for the supercurrent density with suitable boundary conditions. Pearl finds that, within a distance λ of the interface, the electromagnetic region around the fluxon spreads and the current density $j(r)$ behaves at large r like r^{-2}. This will give rise to long range repulsive forces between fluxons. For a cylinder of radius R and thickness d Pearl (1965) calculates that the magnetic moment m, of a fluxon along the axis of the disc, is given, for $d \to 0$ by $m \simeq \phi_o R/4\pi$, for $d \to \infty$ by $m \simeq \phi_o d/4\pi$ (see also appendix 1(f)) and for intermediate d by

$$m \simeq (\phi_o/4\pi)d(1 + R/d). \qquad 6.3$$

For specimens with $d \gg \lambda$ the line tension τ of the fluxon will be given by its usual bulk value, viz: $\tau \simeq H_{c1}\phi_o/4\pi$ (see equation 1.1 and 1.2).

For the fluxon to be in equilibrium with its surroundings requires therefore an external field H_o' such that $H_o'md/4\pi$, i.e. the reduction in magnetic field energy, is equal to the line energy τd. Thus $H_o'm = H_{c1}\phi_o$ and from equation 6.3 therefore:

$$H_o' \simeq (1 + R/d)^{-1} H_{c1}$$
$$\simeq (1 - D_c)H_{c1} \qquad 6.4$$

for $R/d >> 1$ since $d/_R \simeq 1 - D_e$ (see for example Brown, 1962). Pearl however, incorrectly identifies H_o' with H_{c1}^*, i.e. the field of first penetration of fluxons into the cylinder, and therefore obtains approximately the same result for H_{c1}^* as predicted for the enclosed ellipsoid (see section 6.3.1). Pearl also makes a calculation for the long range interaction between fluxons near the surface and obtains an expression for $[dM/dH_o]_{H > H_{c1}^*}$ which varies as $(1 + d/R + R/d)$.

Maki (1965) using Pearl's result for m obtains a more accurate result which also predicts $[dM/dH_o] \to \infty$ as $R/d \to \infty$. This result is completely at variance with the expected equilibrium behaviour (Fetter and Hohenberg (loc. cit.)), viz: $[dM/dH_o]_{H_o \geq H_{c1}} = 1/De$ which tends to 1 as $R/d \to \infty$.

There is however an element of validity in both of these predictions. The discrepancy arises because of Pearl's incorrect assumptions that equilibrium conditions obtain (i.e. that $M[H_o]$ is a single valued function of H_o) and, tacitly, that m is position invariant in the cylinder or disc. The more complete analysis of the problem, which will be given here, is based on a model which sets up the aforementioned boundary conditions for a single fluxon in a cylinder explicitly. The position dependent thermodynamic field $H_e(z,r)$ (see figure 6.12) (and

hence also the moment m of a fluxon situated at a distance r_F from the cylindrical axis of the specimen) is then calculated numerically for various values of the ratio R/d. In the range of R/d investigated (viz. $0.25 \leq R/d \leq 6.25$) the predictions for $m(r_F = 0)$ are in fair agreement with Pearl's approximate prediction (equation 6.3). $m(r_F)$ however, decreases (and the energy concomitantly increases) with r_F and therefore, since flux must enter the cylinder at its perimeter ($r_F = R$) Pearl's calculation for H^*_{c1} (equation 6.4 and following) clearly predicts a value which is too small. For $R/d << 1$ an approximately correct result can be obtained from equation 6.4 if $m(r_F = R)$ is substituted from $m(0)$ however. (The exact value of H^*_{c1} will be shown to be dependent on the manner in which a fluxon penetrates the corners of the cylinder.)

The prediction of the magnetization behaviour of a cylinder after fluxons have penetrated it is problematical. However the use of certain simplifying assumptions allows the formulation of a model for the overall magnetic behaviour which is in fair agreement with experiment. This behaviour may be outlined roughly as follows: For a cylindrical specimen of ideal material, initially in the Meissner state with an external field H_o applied parallel to the cylindrical axis and increasing from zero, the magnetization increases at a rate $dM/dH_o \cong [4\pi(1 - D_m)]^{-1}$ When $H_o = H_{c1}(1 - D_m)$ the magnetization behaviour departs from equilibrium and the specimen remains completely diamagnetic (except in the regions near the sharp rims of the cylinder). Eventually at some $H_o = H^*_{c1} > H_{c1}(1 - D_m)$ the potential barrier to the entry of fluxons becomes zero and fluxons move rapidly to the moddle of the cylinder ($r = 0$) where they form a 'pool' of radius $\rho < R$. The fluxons in the 'pool' give rise to a 'back

stress' which is insufficient to expand the pool so that it fills the specimen, i.e. $\rho = R$, but which nevertheless acts at the perimeter to prevent instantaneous filling of the pool at $H_o = H_{c1}^*$. dM/dH_o (in the regime where $\rho < R$) is determined by this back-stress and is larger than the equilibrium value. At $H_o = H_{c1}$, $\rho = R$ and the overall magnetization behaviour $M(H_o)$ corresponds to equilibrium behaviour $M[H_o]$ and is therefore reversible for $H_{c1} \leq H_0 \leq H_{c2}$. In decreasing H_o, when $H_o \leq H_{c1}$, fluxon expulsion from the specimen obviously requires $\rho = R$ and therefore the magnetization might be expected to remain on the equilibrium branch until this expulsion is complete. It will however be demonstrated experimentally and theoretically that in this case the rims of the cylinder give rise to non-equilibrium behaviour. [Approximate equilibrium behaviour in decreasing H_o can be obtained if the rims of the cylinder are bevelled off.] The concept of a flux 'pool' for low B is confirmed by the magneto-optical observations of De Sorbo and Healy (1964), Baird (1964) and Baird and Wright (1972) on both type I and type II superconducting disc specimens.

6.2 Experimental

For the purpose of the investigation of this chapter a variety of experimental M-H_o results were obtained for various disc and ring-shaped single crystal specimens of niobium.

To determine the basic geometrical and possible size effects on the magnetization behaviour two series of disc-specimens were prepared as follows: A single-crystal rod (approximately 6.5mm diameter) of MARZ grade niobium supplied by the Materials Research Corporation, New York, U.S.A. with an axial orientation <111> was machined by Spark erosion to be uniformly 6mm in diameter. Six

discs of varying thickness were then spark-sliced (normal to the rod axis) from the single crystal. The rod was then successively further reduced in diameter and five more discs of various radii (R) and approximately constant thickness (d) were sliced off. The <111> faces of the discs were then spark-planed (on the finest range available on the Servomet Spark erosion machine) to be flat and parallel and the discs were finally polished in a 70:30 HNO_3-HF mixture as described in chapter 5. The final dimensions of the discs in the two series are given in table 6.1. [Some of these discs were later used in an investigation of the deformation properties of niobium in a special 'punching' experiment (Ball and Doyle, 1974 - see appendix A9). This investigation was motivated by the fluxon pinning experiments described in chapter 7.]

Details of special preparation for various other specimens will be given together with the experimental results in the next section.

6.2.1 Experimental results

Isothermal magnetization curves were obtained for the two series of <111> discs in transverse applied field H_o at a temperature $T = 4.05K$. The results are shown in figures 6.1, 6.2 and 6.3. Increasing the magnetic field sweep rate dH_o/dt by a factor of five causes no detectable change in these curves and it may be concluded therefore that they are not influenced by any spurious eddy current or other transient phenomena.

The absolute magnetization curves, obtained by normalizing the curves of figure 6.1 to 6.3 for volume, are given in figures 6.4 and 6.5. [The small hysteresis which is apparent for $H_o > 1$Koe in the curves of figure 6.4 (and absent in figure 6.5) was later found to be due to residual spark damage and therefore to insufficient chemical

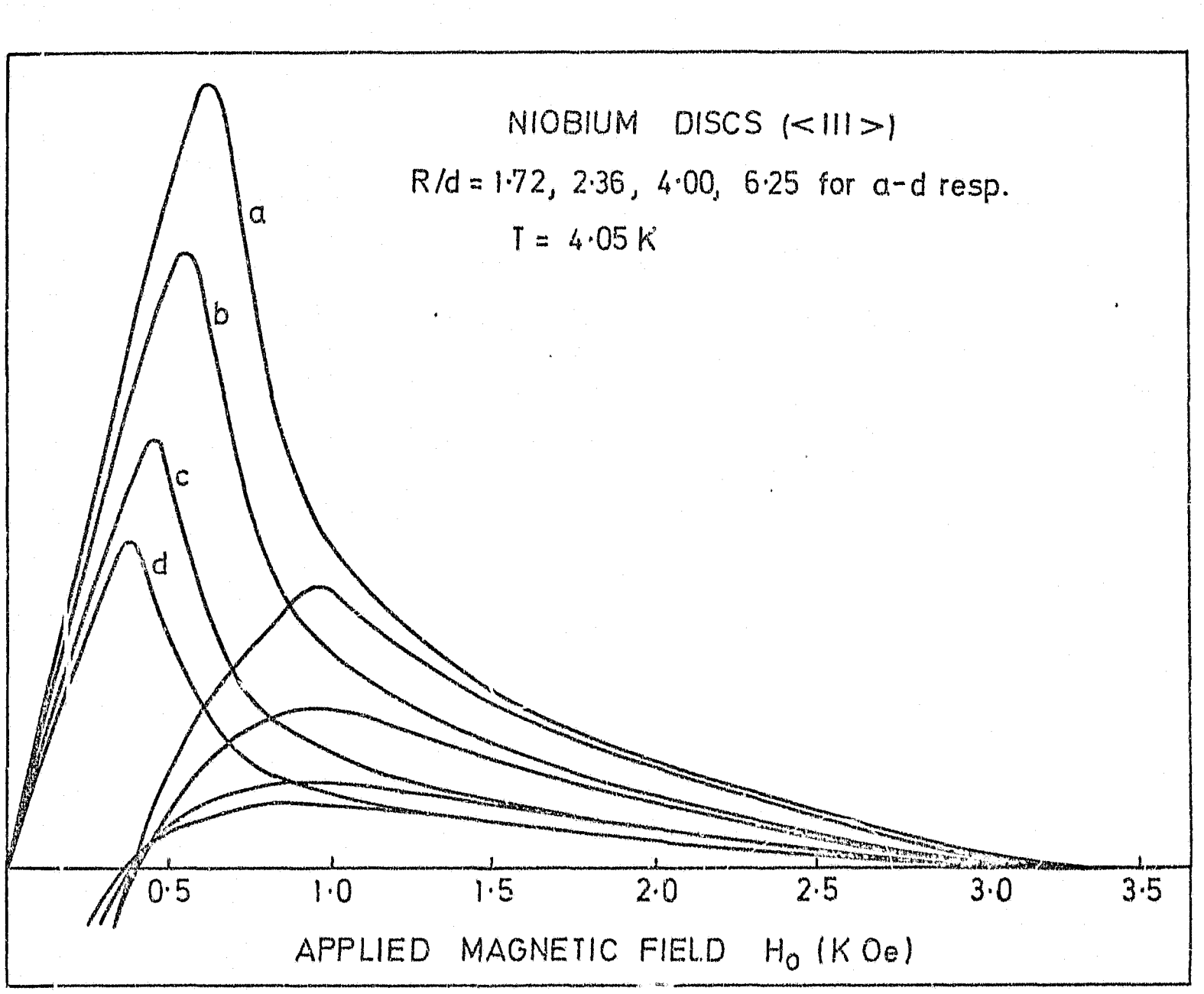


Figure 6.1. Magnetization curves obtained at T ≃ 4.05K for <111> oriented niobium disc-specimens of constant radius R ≃ 5.9mm and various thicknesses.

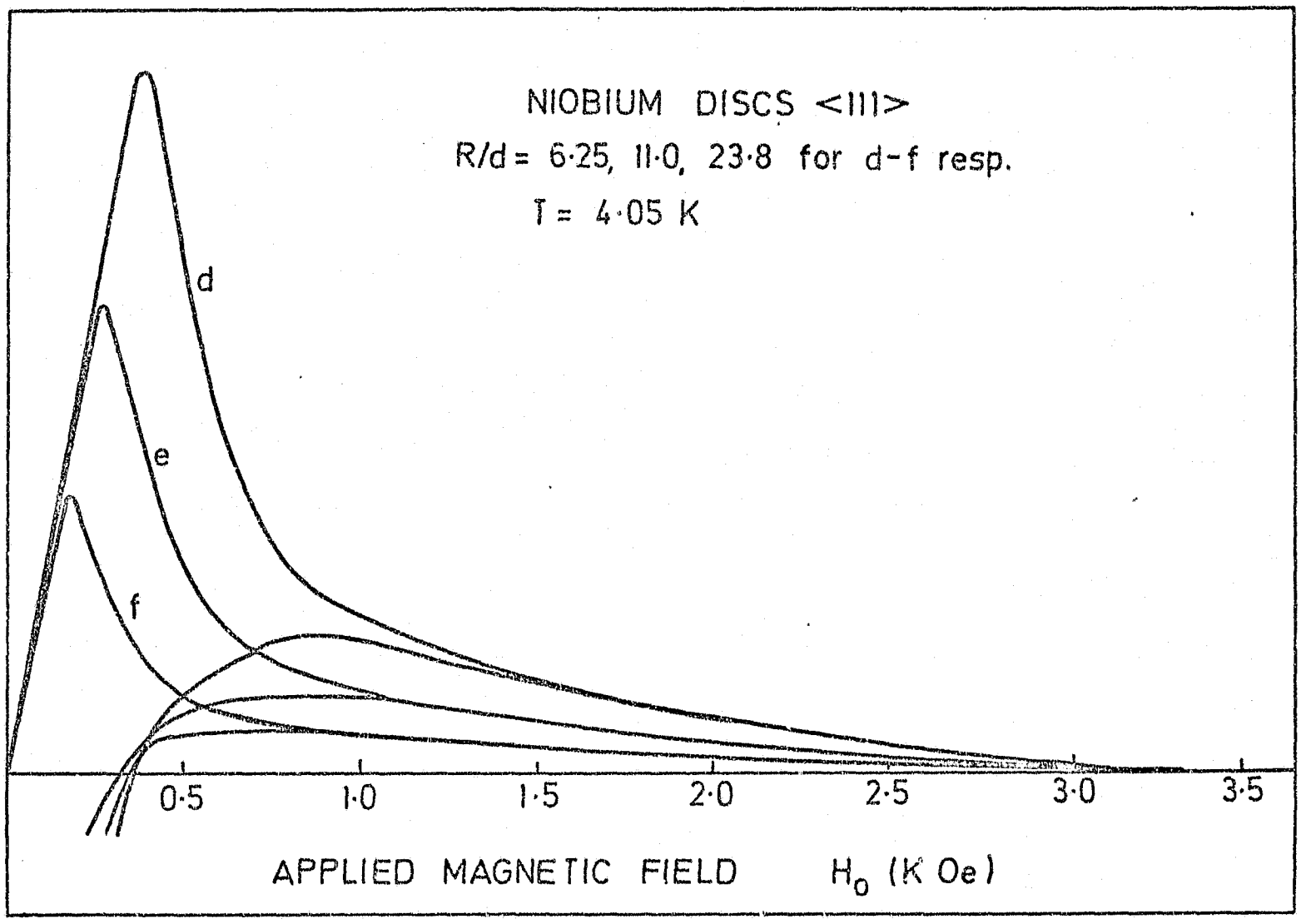


Figure 6.2. Magnetization curves obtained at T = 4.05K for <111> oriented niobium disc-specimens of constant radius R = 5.9mm and various thicknesses.

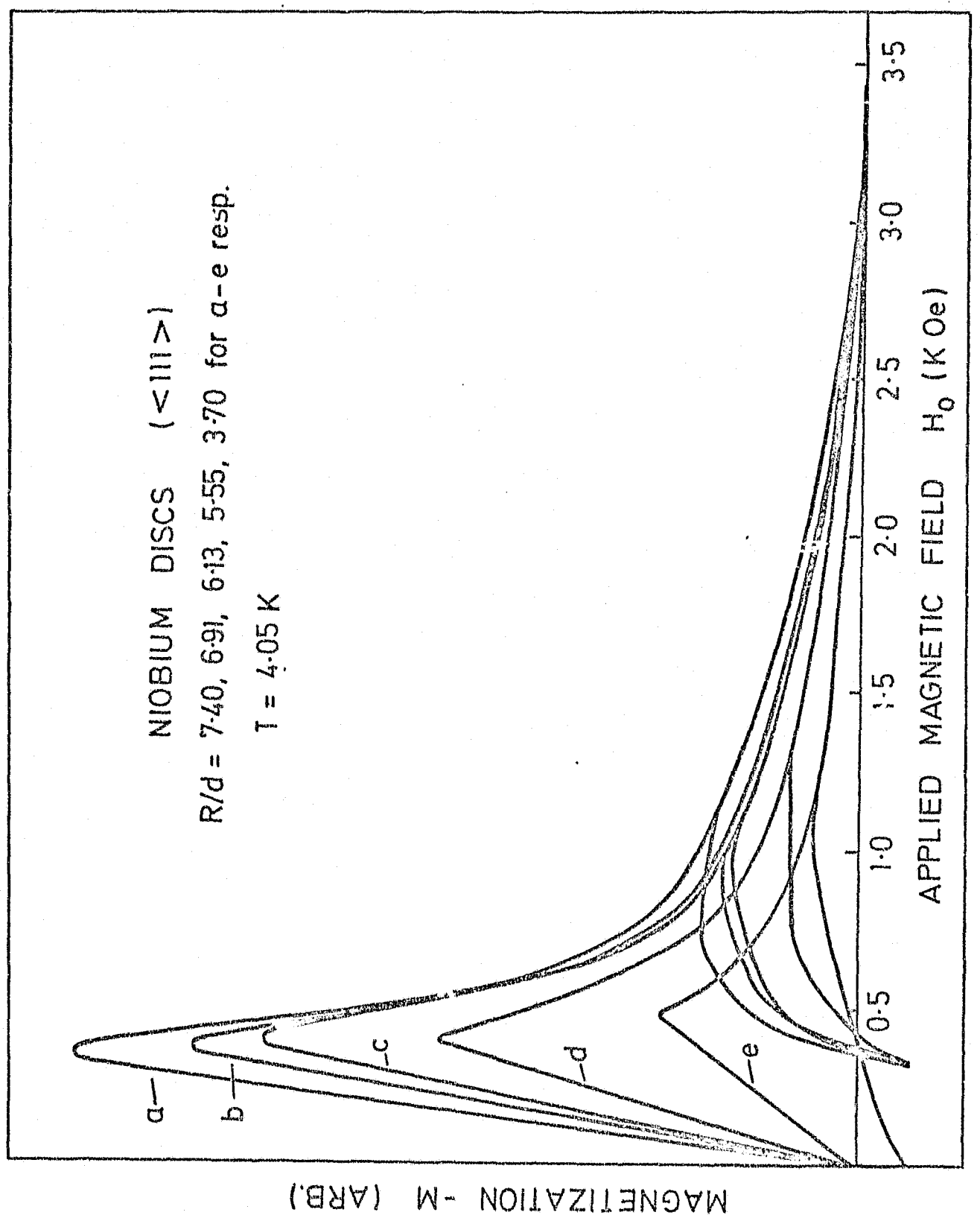


Figure 6.3. As for figure 6.1 for discs of constant thickness d ≃ 0.36mm and various radii.

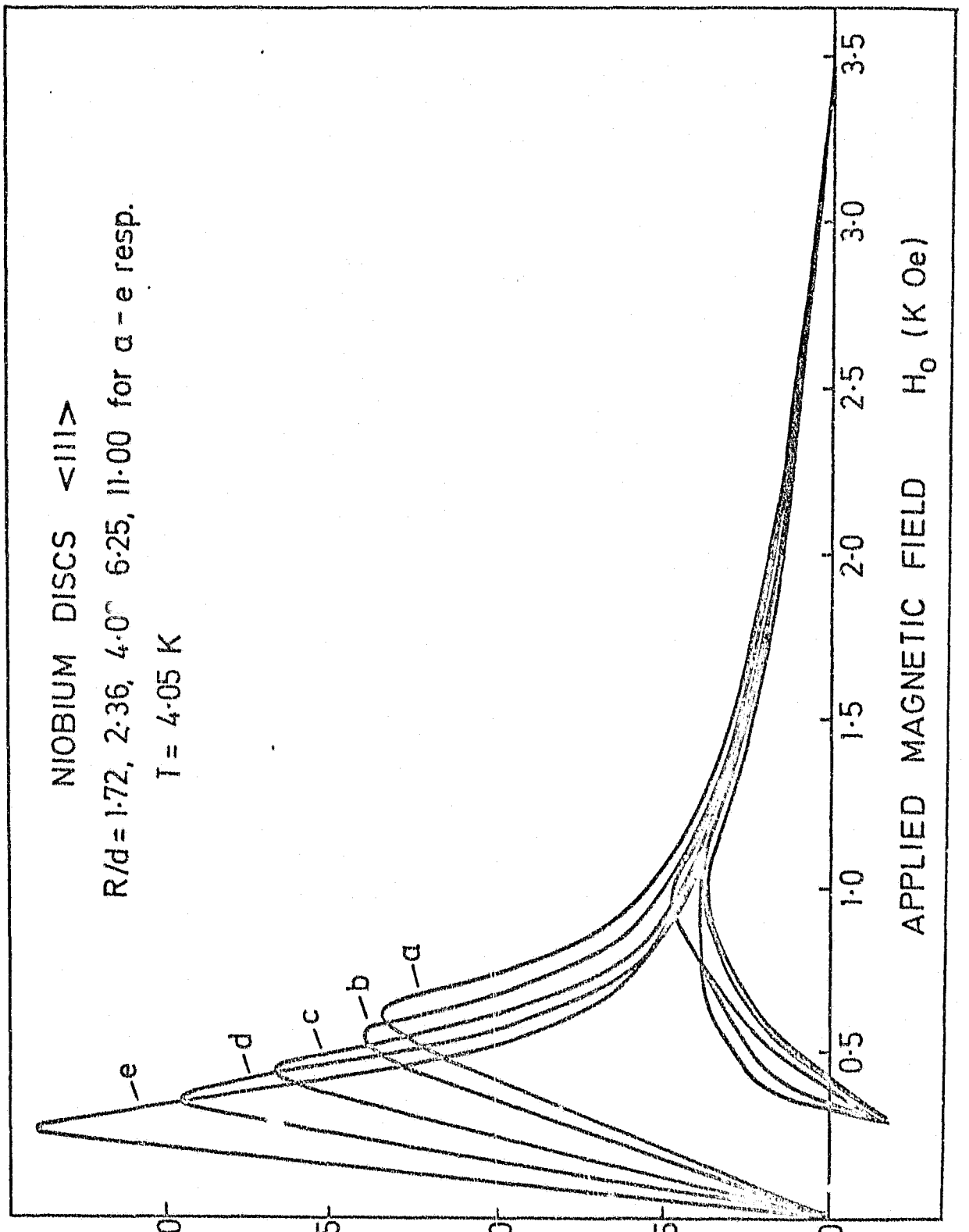


Figure 6.4. Derived absolute magnetization curves at T = 4.05K for the discs of constant radius and various thicknesses.

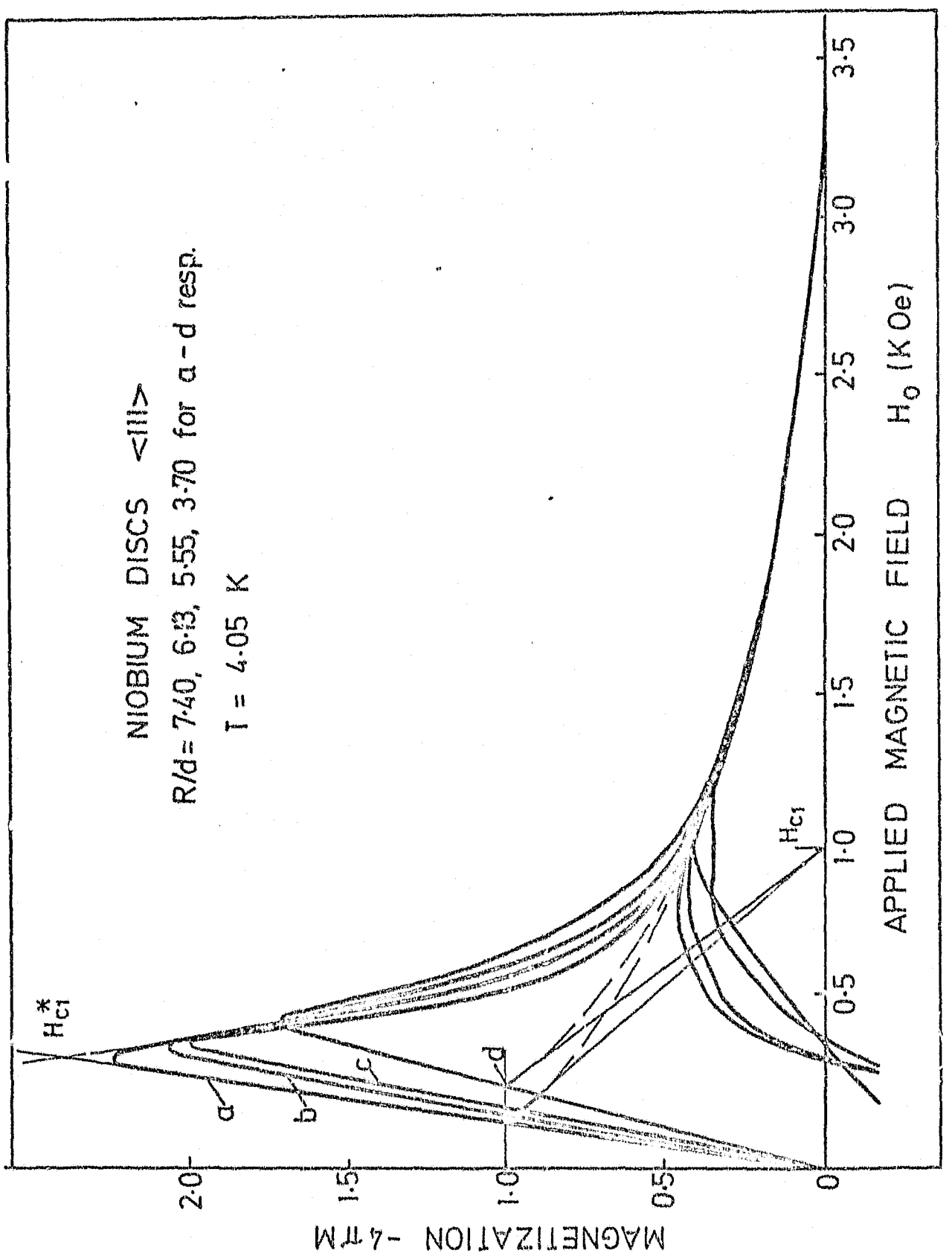


Figure 6.5. As for figure 6.4 for the discs of constant thickness and various radii. The fine and dashed curves will be referred to in the text.

polishing of these specimens.] . The field H_{c1}^{*} , denoting the onset of flux penetration into the specimens, was obtained by extrapolation as shown in figure 6.5. The values obtained for H_{c1}^{*} , $4\pi dM/dH_o$ ($H_o < H_{c1}^{*}$, H_o increasing) and ($H_o \geq H_{c1}^{*}$, H_o increasing) from the curves of figures 6.4 and 6.5 are given in table 6.1. Figure 6.6 shows the magnetization behaviour in longitudinal field for an annealed (15 hours at 1900K and 10^{-9}mm Hg) niobium disc specimen at T = 8.69K (R/d = 3, orientation <123>). The dashed curve shows the approximate behaviour after the sharp rims of the disc were bevelled off (see inset) and the specimen was chemically repolished. In figure 6.7 the magnetization curve for a disc specimen (R = 3mm, d = 0.92mm, orientation <110>) at T = 4.05K is shown (full curve) together with the curve (dashed) obtained under the same conditions after the disc was trepanned to produce a ring of average thickness $\bar{t}$ = 0.5mm. The magnetization loop in figure 6.8 is for another ring specimen (R = 2.52mm, d = 0.92mm, $\bar{t}$ = 0.2mm) at T = 4.05K. The dashed curve shows the approximate behaviour expected from consideration of the previous figure. The actual behaviour in this regime shows a premature flux penetration into the inside of the ring and will be discussed later. Figures 6.9 and 6.10 show the magnetization behaviour obtained by variously cycling a longitudinal applied field in two initially identical disc-specimens which were lightly scratched on the cylindrical surface (figure 6.9) and on the planar surfaces (figure 6.10) respectively. These results will be discussed later.

A variety of other experiments were performed which have partial relevance but will not be reported here.

TABLE 6.1

R(mm)	d(mm)	R/d	H_{c1}^{*} (Oersted)	$4\pi dM/dH_o$ (B=0)	$4\pi dM/dH_o$ ($H_o \geq H_{c1}^{*}$)	h^{*}	H_c (Oersted)
2.90	1.69	1.72	616	2.42	4.0	0.601	1435
2.90	1.23	2.36	547	2.85	4.5	0.534	1445
2.88	0.72	4.00	451	4.12	5.0	0.44	1445
2.88	0.46	6.25	377	5.88	5.8	0.368	1435
2.86	0.26	11.00	271	9.60	6.0	0.264	-
2.85	0.12	24.00	170	18.30		0.166	-
2.66	0.36	7.40	350	6.80	7.1	0.341	-
2.42	0.35	6.92	373	6.64	7.1	0.364	-
2.30	0.375	6.14	396	5.80	5.7	0.386	-
2.00	0.36	5.55	400	5.35	4.8	0.390	-
1.41	0.38	3.70	478	3.92	4.0	0.466	-

$T_c = 9.295 \pm 0.005K$ FOR $T = 4.05K$ $H_c = 1440\ O_e$ $H_{c2} = 3320\ O_e$ $H_{c1} = 1025\ O_e$ $K_1 = 1.6$ $K_2 = 2.2$

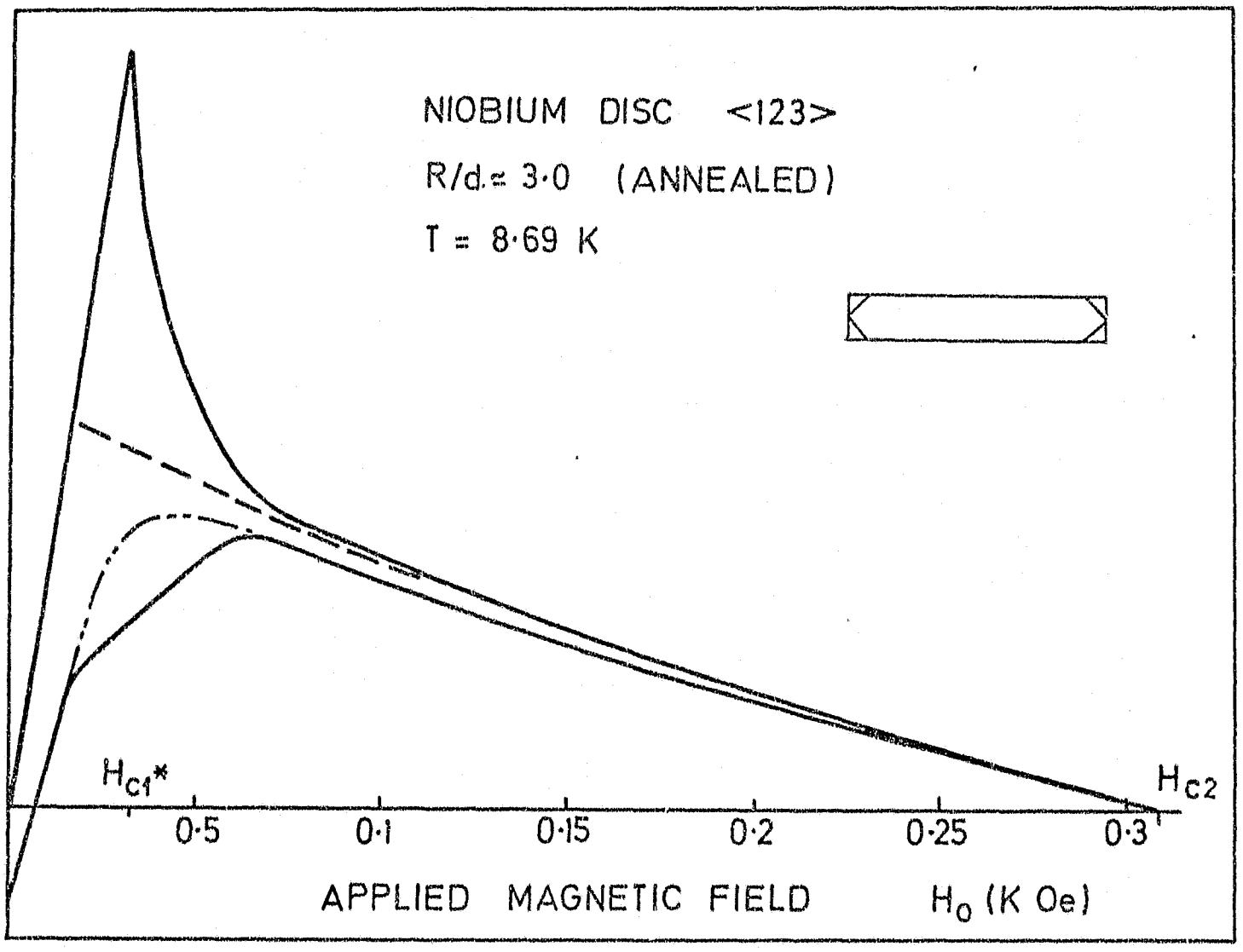


Figure 6.6. Magnetization curve for a niobium disc-specimen (orientation <123> along the cylindrical axis and R/d ≃ 3.0) at T ≃ 8.69K after annealing at 1900K for 15 hours in a vacuum of 10^{-9}mm Hg (solid curve) and subsequently after bevelling off the rims as shown.

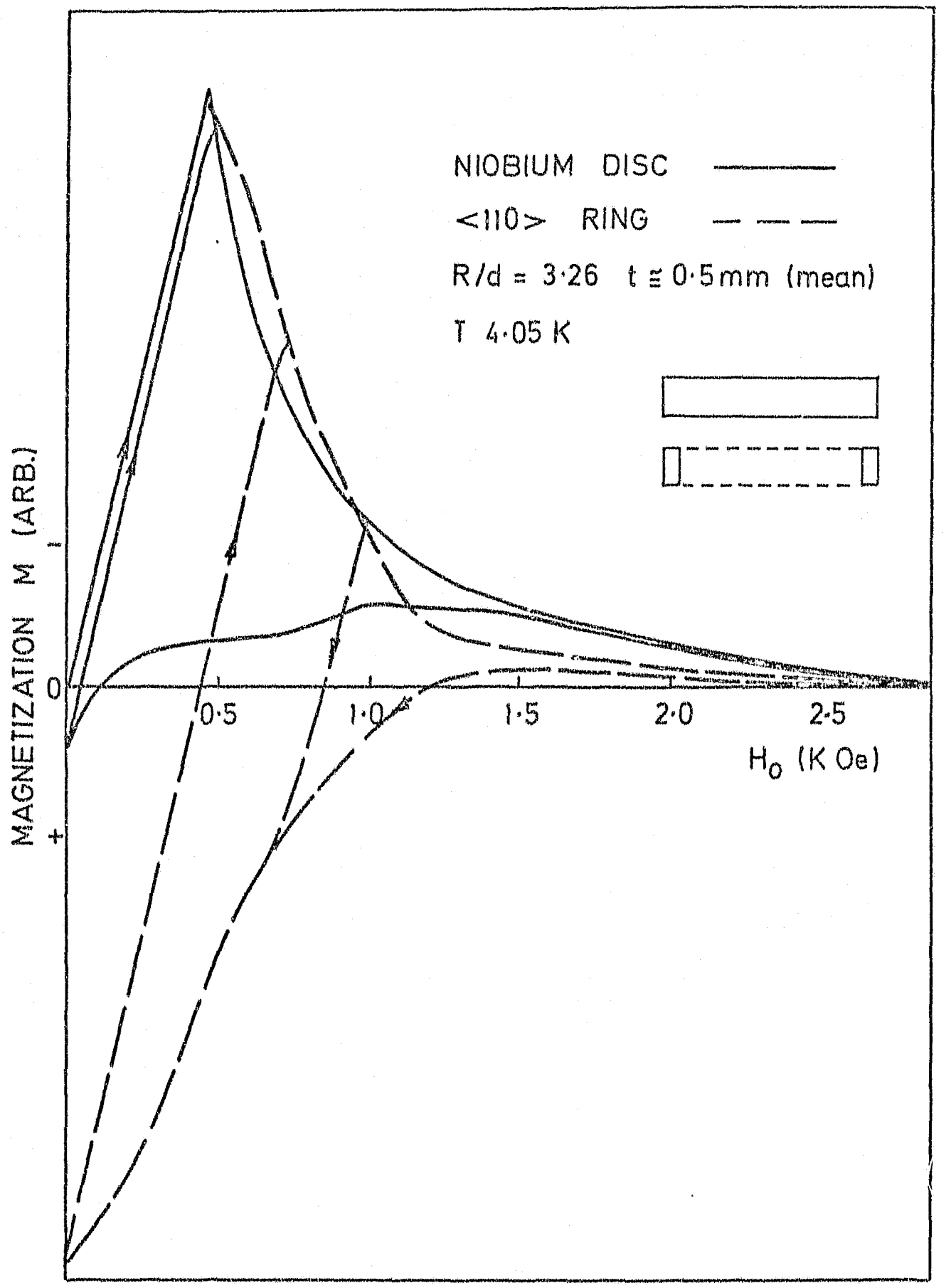


Figure 6.7. Magnetization curves at T = 4.05K for a disc-specimen (solid curve) and for a ring specimen (R/d = 3.26-mean ring thickness 0.5mm) (dashed curve) obtained by trepanning the disc-specimen. The field of first penetration H_{c1}^{*} is apparently the same for both specimens.

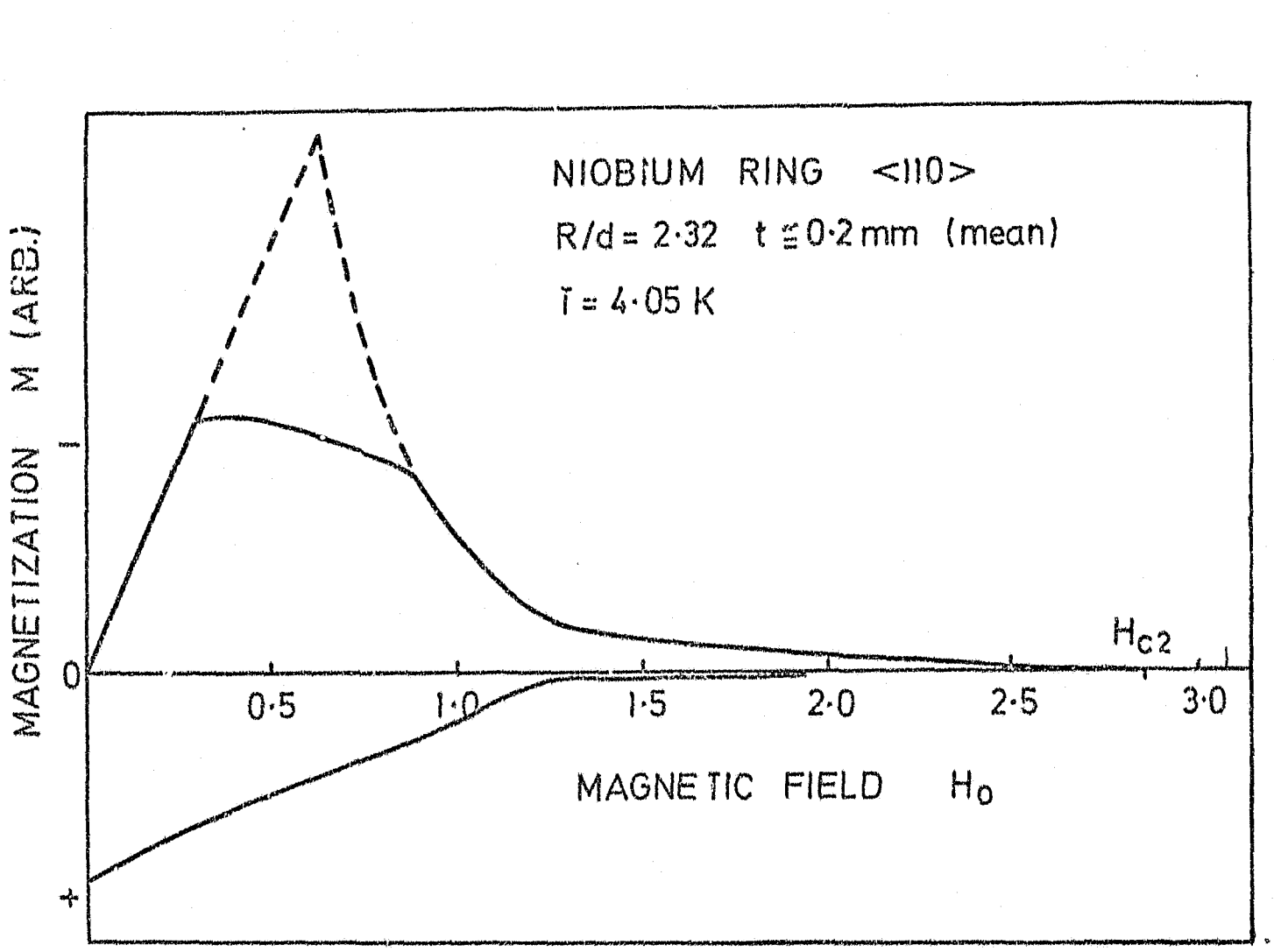


Figure 6.8. Magnetization curves at T = 4.05K for a ring specimen (R/d = 2.32, mean t = 0.2mm). In this case t is apparently too small (at some point along the ring) to allow usual behaviour (dashed curve).

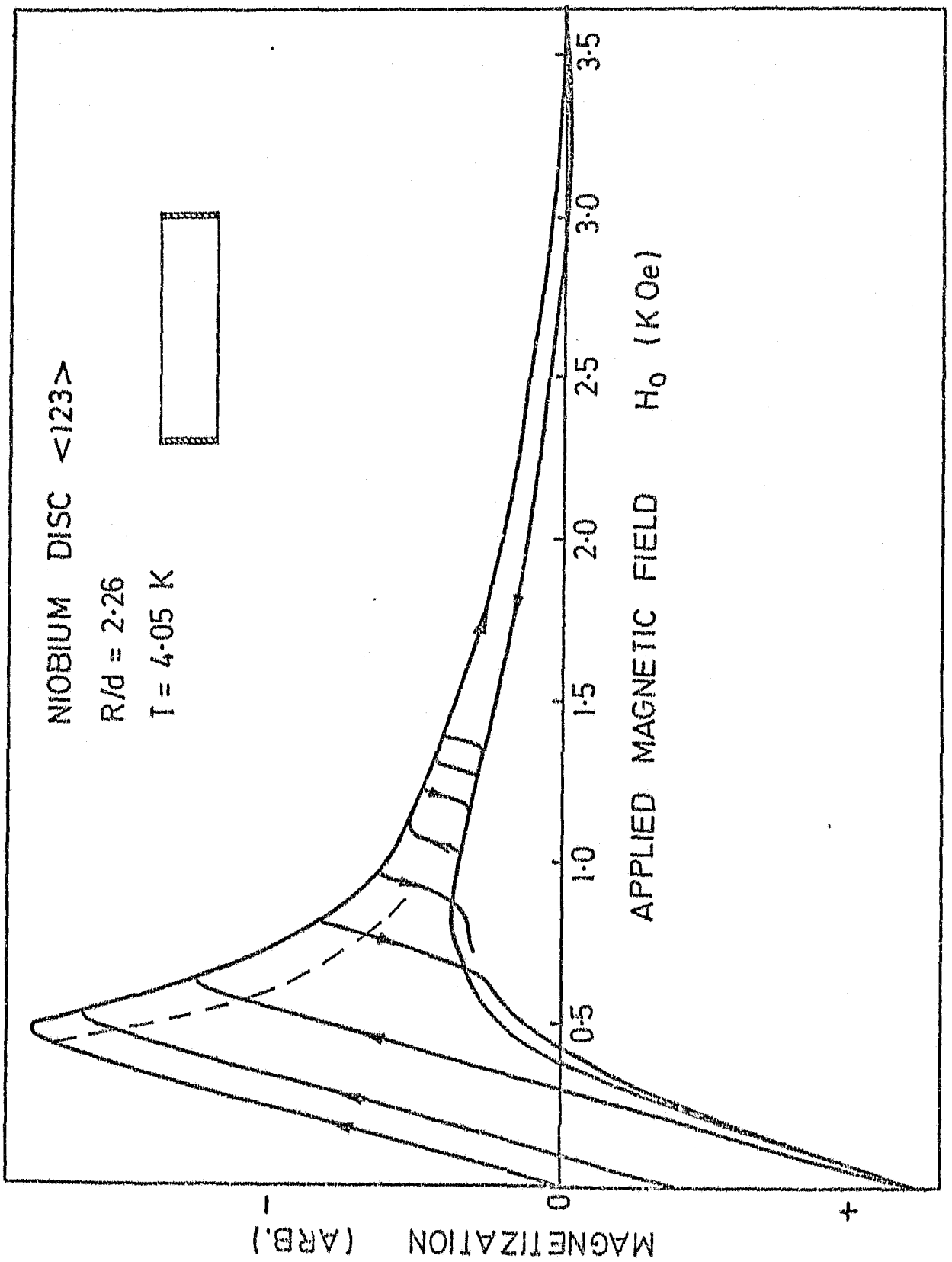


Figure 6.9. Magnetization curves at T = 4.05K for a disc-specimen (R/d = 2.26, orientation <123>) which was scratched on its peripheral surface.

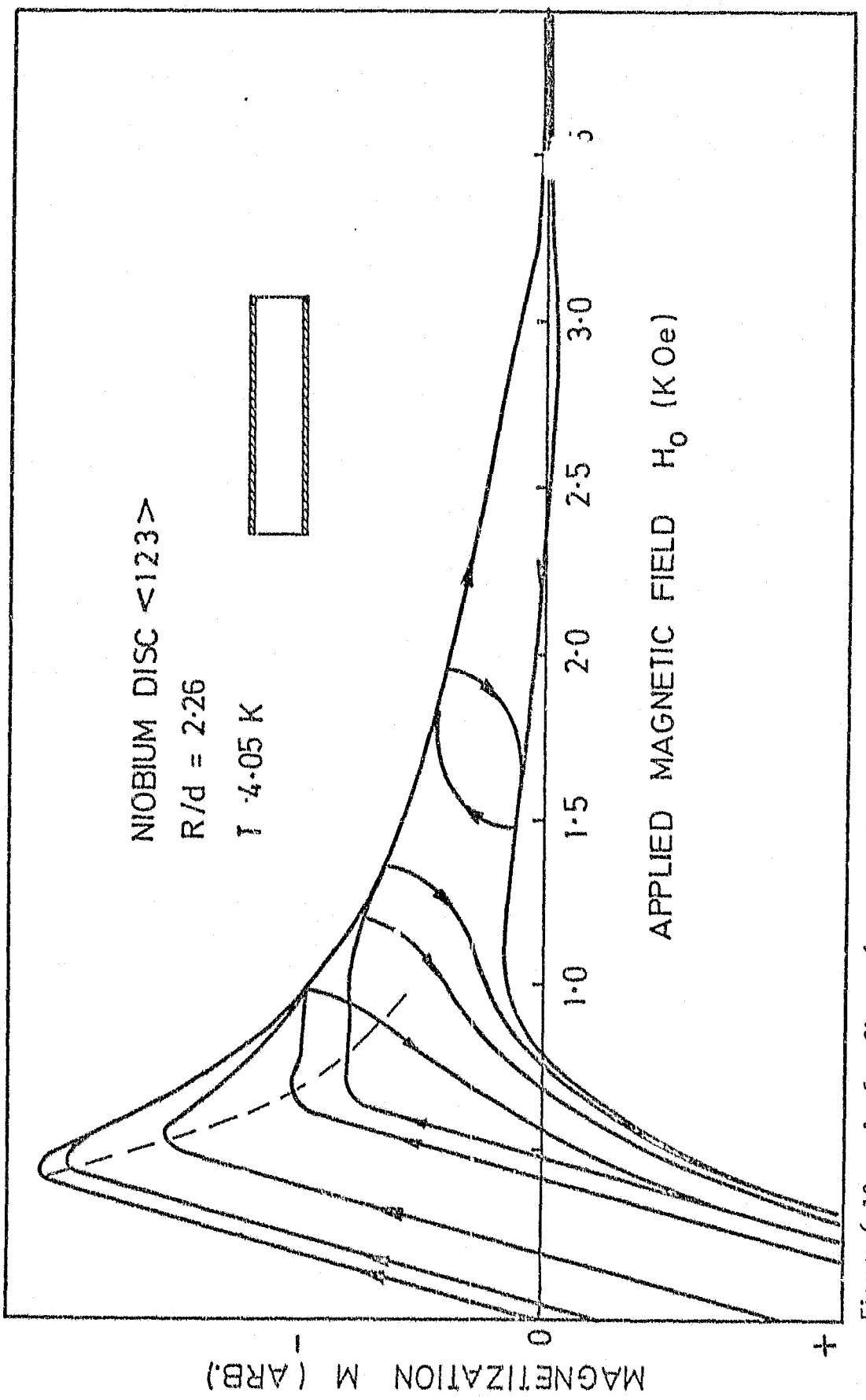


Figure 6.10. As for figure 6.9 with the specimen scratched on its planar surfaces.

6.3 Theory

6.3.1 Equilibrium magnetization behaviour for a type II superconducting spheroid

In this section a brief review will be given of the theoretical predictions for the M-H_o behaviour of spheroidal specimens of a type II superconductor for which the constitutive relaxation $B[H_o]$ (for long thin specimens in longitudinal fields) is known. (For references see section 6.1.)

The general behaviour for spheroidal specimens with a demagnetizing coefficient D along a principal axis in the direction of the applied field H_o is given (see equations 6.1 and 6.2) by

$$B = H_e + 4\pi M \qquad 6.5$$

and

$$H_e = H_o - 4\pi MD \qquad 6.6a$$

or

$$H_e = H_o - D(B - H_e) \qquad 6.6b$$

or

$$H_e = (H_o - DB)(1 - D)^{-1} \qquad 6.6c$$

where B and M are now the macroscopic induction and magnetization in the spheroid respectively and H_e is the internal or thermodynamic field.

For a spheroidal specimen in the Meissner state $B = 0$ and therefore from equations 6.5 and 6.6c,

$$4\pi M = -H_e = H_o(1 - D)^{-1}$$

and therefore

$$4\pi [dM/dH_o]_{B=0} = (1 - D)^{-1} \qquad 6.7$$

Initial fluxon penetration occurs when $H_e = H_{c1}$. The applied field $H_o = H^*_{c1}$ at which this just occurs is given by equation 6.6c on substitution for H_e and H_o with $B = 0$ and is

$$H^*_{c1} = H_{c1}(1 - D) \qquad 6.8a$$

so that

$$h^* = H^*_{c1}/H_{c1} = (1 - D) \qquad 6.8b$$

The induction B in a spheroidal specimen is in equilibrium with the thermodynamic field in accordance with Abrikosov's constitutive relation (see chapter 1) and is reversible with variations in H_o. From equation 6.6c

$$B[H_e] = B[(H_o - BD)/(1 - D)] \qquad 6.9$$

The transition to the mixed state at $H_e = H_{c1}$ in a long thin specimen in longitudinal field is either a first order or a λ type second order transition (see for example Finnemore, Stromberg and Swenson, 1966) with $dB/dH \to \infty$ (so that $dM/dH_o \to 0$) as $H_o \to H_{c1}$ from above. In this case $D = 0$ and therefore $H_e = H_o$ (equation 6.6a) and the transition requires $dM/dH_o \to 0$ as $H_o \to H_{c1}$ from above. When $D \neq 0$: from equation 6.6a

$$dH_e/dM = dH_o/dM - 4\pi D$$

and therefore fore

$$H_o \to H_{c1} \quad \text{or} \quad B \to 0$$

$$4\pi[dM/dH_o] = D^{-1} \qquad 6.10a$$

or

$$dB/dH_o = D \qquad 6.10b$$

The behaviour for $H_o \lesssim H_{c2}$ will be taken directly from the results of Cape and Zimmerman (1967) and is given (see also equation 1.6) by

$$4\pi[dM/dH_o]_{H_o \to H_{c2}} = [\beta(2\kappa_2^2 - 1) + D]^{-1} \qquad 6.11$$

It is obvious from equation 6.6a that the upper critical field H_{c2} will not depend on D since $M \to 0$ at $H_o \to H_{c2}$.

Finally the superconducting condensation energy per unit volume ($-H_c^2/8\pi$ - see chapter 1) is obviously invariant with specimen geometry and therefore

$$\int_0^{H_{c2}} M(H_o)\,dH_o = \int_0^{H_{c2}} M[H_e]\,dH_e = -H_c^2/8\pi \qquad 6.12$$

where the square brackets imply equilibrium behaviour.

The above equations for obtaining the magnetization behaviour for a specimen of demagnetizing factor D from the constitutive $M[H_e]$ relation are equivalent to shearing the reversible $M\text{-}H_o$ curve for a specimen with $D = 0$ so that each point on the curve moves a distance $4\pi MD$ along the H_o axis. Figure 6.11 shows the behaviour (dashed curve (a)) for a spheroid with $R/d = 11.0$ ($D_e = 0.909$) as predicted from the $M(H_o)$ behaviour (dashed curve(b)) for a <111> long cylinder at $T = 4.05K$. Also shown in the figure is the actual experimertal $M\text{-}H_o$ curve for the disc specimen. It is apparent that for H_o increasing initial flux penetration is delayed until well past the value predicted by curve (a). At $H_o = H_{c1}^*$ (H_{c1}^* will henceforth be used only for the cylindrical case), there is a very sharp second order (see later) transition and the magnetization decreases almost linearly with H_o initially. For $H_o \geq H_{c1}$ the magnetization is apparently in equilibrium and reversible. The behaviour for $H_o \lesssim H_{c1}$ in decreasing fields is due to the sharp rims of the disc and fluxon pinning in the specimen. For an ideal specimer there should be no trapped flux at $H_o = 0$ (see later).

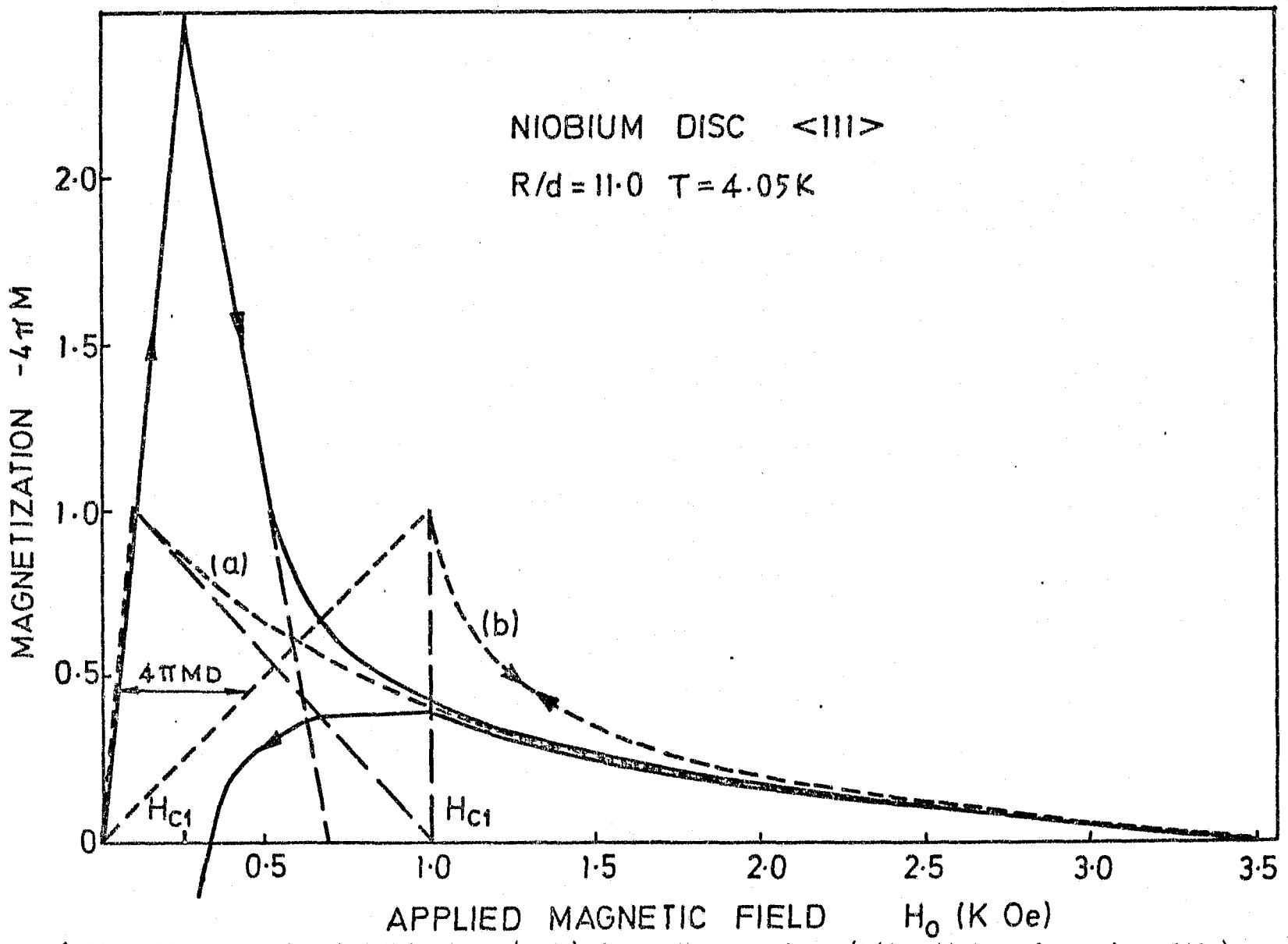


Figure 6.11. The magnetization behaviour (M-H_o) for a disc-specimen ($R/d = 11.0$, orientation <111>) at $T = 4.05K$ (solid curve) is compared with the behaviour for a spheroidal-specimen (dashed curve (a)) of the same axial ratio and volume as the disc specimen, derived by 'shearing' the curve for an infinite long specimen (shown approximately by dashed curve (b)) by an amount $4\pi MD$ as shown.

6.3.2 Macroscopic equations for the description of non-reversible superconductors of arbitary shape

The results of the previous section, inter alia, have been generalized by Labusch (1973) in a rigorous manner, to type I and type II superconductors of arbitrary shape.

In essence Labusch formulates an explicit expression for the Gibbs free energy δG required to create a fluxon (or flux tube) in a macroscopic specimen containing an arbitrary but fixed distribution of other fluxons. Terms of order λ/Δ, ξ/Δ and a_o/Δ where Δ is the smallest characteristic dimension of the superconducting specimen and the other parameters have their usual meaning, are neglected. The remaining terms are then rationalized and the final result for δG is given as

$$\delta G = (\phi_o/4\pi) \int (\underline{H}_r(r) - \underline{H}_e(r))\underline{d}\ell \qquad 6.13$$

where H_r is just the magnetic field in equilibrium with the local induction $B(r)$ in accordance with Abrikosov's constitutive relationship and $H_e(r)$ is the local value of the thermodynamic field (see below). The term in H_r obviously contains (i) the line energy of the fluxon, i.e. $H_{c1}\phi_o/4\pi$ (see chapter 1) which is the sum of the kinetic energy of the current vortex around the fluxon and the loss of condensation energy inside the fluxon and (ii) the short range interaction energy between the fluxon and its neighbours (see section 6.3.5). As the induction B tends to zero, $H_r \to H_{c1}$.

The thermodynamic field $H_e(r)$ is the usual* internal magnetic field in a magnetic material. It is position dependent here because

---

* For a spheroidal specimen of ideal reversible type II superconducting material $H_e(r) = H_e = H_r$ and $\delta G = 0$ everywhere in the specimen.

of the arbitary shape of the specimen and the boundary condition requirements.

The boundary conditions for a superconductor are (i) that the tangential component of H is continuous through the superconductor-vacuum interface (ii) that the normal component of B is continuous through the surface (iii) curl $H = 0$ inside the specimen and (iv) div $B = 0$. These conditions can be satisfied, in theory, for the applied field and the self field of a fluxon in a superconducting specimen by the well known method of substituting a suitable magnetic charge distribution over the surface of the specimen in place of the actual field sources. This charge distribution then gives rise to the external field and inside the specimen $H_e(r)$ is defined to be the vacuum field due to these charges. In equilibrium the creation of a fluxon parallel to and in the specimen surface requires $\delta G = 0$ and therefore

$$H_{e_{11}} = H_{r_{11}} \qquad 6.14$$

at the surface. Providing that there is no surface barrier mechanism (see chapter 1) this result applies equally in reversible and irreversible superconducting specimens.

The boundary conditions above obviously also require

$$B_{\perp}(H_r) = H^{o}_{e_{\perp}} \qquad 6.15$$

at the surfaces where $H^{o}_{e_{\perp}}$ is the perpendicular component of the field outside the specimen. Equations 6.14 and 6.15 effectively constitute all the boundary conditions for a specimen of arbitrary shape and $H_e(r)$ is now obtainable from the differential equation

$$\text{div } \underline{H}_e(\underline{r}) = \sigma(\underline{s}).\ \delta(\underline{r} - \underline{s}) \qquad 6.16$$

where $\sigma = H^{o}_{e_\perp} - H^{i}_{e_\perp}$ and $H^{i}_{e_\perp}(\underline{s})$ is the field just inside the superconductor surface at a point $\underline{s}$. δ is the Dirac delta function. Also: H_e tends to the applied external field H_o as $r \to \infty$.

Finally Labusch derives an expression for the driving force per unity length of fluxon in the non-equilibrium situation and obtains

$$f_o = (\phi_o/4\pi)\left[\int(\text{curl } \underline{H}_r \times \underline{d\ell}) + \sum_{i=1}^{2}{}' \pm \delta(\underline{r} - \underline{s}_i)(H_r(\underline{s}_i) - H_e(\underline{s}_i))_{11}\right] \qquad 6.17$$

where the first term is a line integral along the unit length of fluxon under consideration and is identical with the usual expression obtaining in the bulk in long specimens, i.e. with $D = 0$ (see for example Campbell and Evetts, 1972). The second term is for the force on the fluxon in the surface of the specimen if the unit length of the fluxon under consideration emerges from the surface at points $\underline{r} = \underline{s}_1$ and/or $\underline{r} = \underline{s}_2$. $(H_r(\underline{s}_i) - H_e(\underline{s}_i)_{11}$ is then the component parallel to the surface at $\underline{r} = \underline{s}_i$.

In the following section $H_e(r)$ for a cylindrical specimen will be evaluated. The treatment was done in collaboration with Professor R. Labusch who outlined the theory.

6.3.3 Calculation of the field $H_e(r)$ in a cylindrical specimen

In accordance with the considerations of the previous section the fluxon is assumed to consist of two monopole magnetic charges $\pm\phi$ on the opposite planar ends of a cylindrical surface as shown in figure 6.12a. The problem is now (1) to find a charge distribution function $\sigma(r)$ over the surfaces of the cylinder such that the boundary conditions required by a superconductor are satisfied and

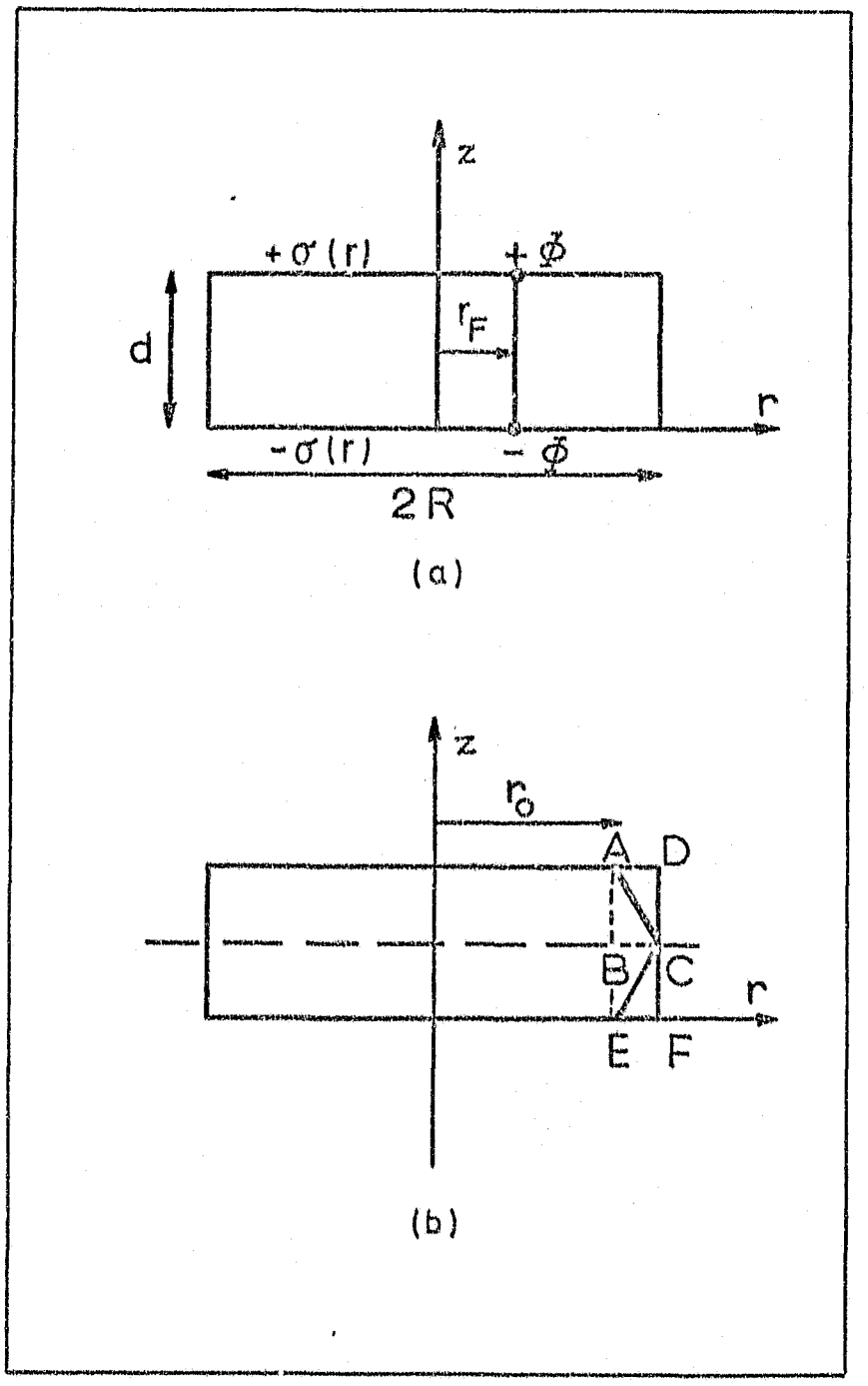


Figure 6.12a. Co-ordinate system for the description of the charge distribution over the surface of a disc-specimen (radius R, thickness d) when a fluxon is situated at $r = r_F$.

Figure 6.12b. Schematic diagram to illustrate the manner in which a fluxon penetrates the rims of a cylindrical or disc specimen.

(ii) to specify ϕ so that the quantization condition for a fluxon is satisfied. Thus:

Thus: The magnetic field due to a dipole of strength ϕd situated at $r = r_F$ is given, in cylindrical co-ordinates (see figure 6.12a), by

$$\underline{H}(z,r) = -\nabla\phi[(|\underline{r} - \underline{r}_F|^2 + (d - z)^2)^{-\frac{1}{2}} - (|\underline{r} - \underline{r}_F|^2 + z^2)^{-\frac{1}{2}}] \quad 6.18$$

The superconducting boundary condition requires that just outside the superconductor the field component, normal to the surface, due to the dipole should be zero everywhere except at $r = r_F$ (i.e. $H_z(z = -\varepsilon$ and $z = d + \varepsilon$, $0 \leq r \leq R$, $r \neq r_F) = 0$ and $H_r(r = R + \varepsilon$, $0 \leq z \leq d) = 0$ as $\varepsilon \to 0$). The surface charge distribution σ required to satisfy the boundary condition will usually be greater than zero everywhere except at the equator of the cylinder (i.e. $z = d/2$, $r = R$). However in the limits $R/d \to 0$ and $R/d \to \infty$ the charges over the curved surface ($r = R$) will tend to zero. For intermediate R/d it is assumed that these charges will make only a relatively small contribution to the total surface charge, and may therefore be neglected (but see later). Thus introducing equal and opposite surface charge distributions $\sigma(|\underline{r}_1 - \underline{r}_F|, z = 0)$ and $\sigma(|\underline{r}_1 - \underline{r}_F|, z = d)$ into equation 6.18 and evaluating only for $H_z(-\varepsilon, r)$ gives

$$H_z(-\varepsilon, r) = 2\pi\phi\Big[\gamma(-\varepsilon, |\underline{r} - \underline{r}_F|) - \gamma(d + \varepsilon, |\underline{r} - \underline{r}_F|) + \int_0^R \sigma(|\underline{r}_1 - \underline{r}_F|)\,\gamma(-\varepsilon, |\underline{r} - \underline{r}_1|)\,d^2r_1 - \int_0^R \sigma(|\underline{r}_1 - \underline{r}_F|)\,\gamma(d + \varepsilon, |\underline{r} - \underline{r}_1|)\,d^2r_1\Big] \quad 6.19$$

where $\gamma(z, r) = (z/2\pi)(z^2 + r^2)^{-3/2}$ and the integration is to be taken

over the planar surface of the cylinder. Now in the limit $\varepsilon \to 0$, $\gamma(\varepsilon, r) = \delta(r)$ - the Dirac delta function, and therefore fror equation 6.19

$$[H_z(-\varepsilon, r)]_{\varepsilon \to 0} = 2\pi\phi[-\delta(|\underline{r} - \underline{r}_F|) - \gamma(d, |\underline{r} - \underline{r}_F|) + \sigma(|\underline{r} - \underline{r}_F|) - \int_o^R \sigma(|\underline{r}_1 - \underline{r}_F|)\gamma(d, |\underline{r} - \underline{r}_1|)d^2r_1] \quad 6.20$$

The boundary conditions can now be satisfied by choosing

$$\sigma(|\underline{r} - \underline{r}_F|) = \gamma(d, |\underline{r} - \underline{r}_F|) + \int_o^R \sigma(\underline{r}_1 - \underline{r}_F)\,\gamma(d, |\underline{r} - \underline{r}_1|)d^2r_1 \quad 6.21$$

since equation 6.20 now gives

$$[H_z(-\varepsilon, r)]_{\varepsilon \to 0} = 2\pi\phi\,\delta(|\underline{r} - \underline{r}_F|) = 0 \text{ for } r \neq r_F \quad 6.22$$

as required.

The quantization condition for the fluxon requires that for

$$\varepsilon \to 0: \quad \int_o^R H_z(-\varepsilon, r)d^2r = 2\pi\phi = \phi_o \quad 6.23$$

and therefore

$$\phi = \phi_o/2\pi \quad 6.24$$

Substituting for ϕ and replacing $-\varepsilon$ by z in equation 6.19 gives

$$H_z(z, r, r_F) = -(\phi_o/2)\int_o^R \psi(|\underline{r}_1 - \underline{r}_F|)[\gamma(z, |\underline{r} - \underline{r}_1|) + \gamma(d - z, |\underline{r} - \underline{r}_1|)]d^2r_1 \quad 6.25$$

where it is easily shown that

$$\psi(|\underline{r} - \underline{r}_F|) = 2[\sigma(|\underline{r} - \underline{r}_F|) + \delta(|\underline{r} - \underline{r}_F|)] \quad 6.26$$

The thermodynamic field $H_e(z, r_F)$ can now be formulated in terms of $H_z(z, r)$ by turning on a longitudinal applied field H_o and determining the magnetostatic energy contribution of the fluxon ($E_m(r_F)$) which is given by

$$E_m(r_F) = -(H_o/4\pi) \int_{\text{all space}} [B_z(z, r, r_F) - H_z(z, r, r_F)]d^3r \qquad 6.27$$

Outside the superconductor $B = H$ and $E_m = 0$. Inside the superconductor $B_z dr^3 = \phi_o \int_o^d dz$ (from the quantization condition) and H_z is given by equation 6.25. Substituting for B and H into equation 6.27 gives

$$E_m(r_F) = -(H_o\phi_o/4\pi) \left[\int_o^d dz + \tfrac{1}{2} \int_o^d \int_o^R \int_o^R \psi(\underline{r}_1 - \underline{r}_F)|\gamma(z, |\underline{r} - \underline{r}_1|) \right.$$

$$\left. + \gamma(d - z, |\underline{r} - \underline{r}_1|)]d^2r_1, d^2r\, dz \right] \qquad 6.28a$$

which may be simplified (see appendix A1(g) as follows:

$$E_m(r) = -(H_o\phi_o/4\pi) \int_o^d [1 + \tfrac{1}{2} \int_o^R \psi_o(r_1)[\gamma(z, |\underline{r} - \underline{r}_1|)$$

$$+ \gamma(d - z, |\underline{r} - \underline{r}_1|)d^2r_1]dz] \qquad 6.28b$$

where

$$\psi_o(r) = \int_o^R \psi(|\underline{r} - \underline{r}'|)d^2r'$$

and therefore from equation 6.26

$$\psi_o(r) = 2\int_o^R [\sigma(|\underline{r} - \underline{r}'|) + \delta(|\underline{r} - \underline{r}'|)]d^2r'$$

$$= 2[1 + \int_o^R \gamma(d, |\underline{r} - \underline{r}'|)d^2r' + \int_o^R\int_o^R \gamma(d, |\underline{r} - \underline{r}'|)$$

$$\gamma(d, |\underline{r}' - \underline{r}''|)d^2r'd^2r'' + \ldots]$$

$$= 2 + \int_o^R \psi_o(r')\,\gamma(d, |\underline{r} - \underline{r}'|)d^2r' \qquad 6.29$$

now $E_m(r) = -(\phi_o/4\pi)\int_o^d H_e(r_1,z)$ by definition

and from equation 6.28b the reduced thermodynamic field is therefore deined by

$$H_e(z, r) = H_o\Psi(z, r) \qquad 6.30$$

where

$$\Psi(z, r) = 1 + \tfrac{1}{2}\int_o^R \psi_o(r_1)[\gamma(z, |\underline{r} - \underline{r}_1|) + \gamma(d - z, |\underline{r} - \underline{r}_1|)]d^2r_1 \qquad 6.31$$

In the following section values for the functions $\Psi(0, r) = \Psi(d, r)$ $\Psi(d/2, r)$ and $(1/d)\int_o^d \Psi(z, r)dz$ will be required.

These are given by

$$\Psi(0, r) = \Psi(d, r) = 1 + \tfrac{1}{2}\int_o^R \psi_o(r_1)[\delta(|\underline{r} - \underline{r}_1|) + \gamma(d, |\underline{r} - \underline{r}_1|)]d^2r_1$$

$$= 1 + \psi_o(r)/2 + \int_o^R \psi_o(r_1)\,\gamma(d, |\underline{r} - \underline{r}_1|)d^2r_1$$

and from equation 6.29 therefore

$$\Psi(0, r) = 1 + \psi_o(r)/2 + (\psi_o(1) - 2)/2$$

$$= \psi_o(r) \qquad 6.32$$

$$\Psi(d/2,\ r) = 1 + \int_o^R \psi_o(r_1)\ \gamma(d/2,\ |\underline{r} - \underline{r}_1|)d^2r \qquad 6.33$$

and

$$\frac{1}{d}\int_o^d \Psi(z,\ r)dz = 1 + (1/2\pi) \int_o^R \psi_o(r_1)[(r_{c0} + |\underline{r} - \underline{r}_1|)^{-1}$$

$$- (d^2 + |\underline{r} - \underline{r}_1|^2)^{-\frac{1}{2}}]d^2r_1 \qquad 6.34$$

where r_{c0} is some cut-off radius which must be suitably chosen (see later). $\Psi_o(r)$ in equation 6.29 has been evaluated numerically as a function of r/R in steps of 0.1 for various values of R/d (see appendix A8) and then substituted into equations 6.32, 6.33 and 6.34. These latter expressions were then evaluated by further machine calculations. The final results for $\Psi(d,\ r)$, $\Psi(d/2,\ r)$ and $\frac{1}{d}\int_o^d \Psi(z,\ r)dz$ are shown as a function of r/R for the various values of R/d in figure 6.13. The cut-off radius r_{c0} in equation 6.34 was kept constant for all values of R/d and was chosen so that the value of $\frac{1}{d}\int_o^d \Psi(z,\ r)dz$ would be midway between the values of $\Psi(d,\ r)$ and $\Psi(d/2,\ r)$ for a disc with $R/d = 6.25$ as shown in figure 6.13. This choice (i.e. $r_{c0} \simeq 0.014R$) is reasonable but arbitrary and the results for equation 6.34 may be somewhat in error.

The other source of error, previously alluded to, is the neglect of the charge distribution over the curved surface of the cylinder. The results of figure 6.13 show that the magnitude of $\Psi(d/2,\ r)$ is smaller than that of $\Psi(d,\ r)$, particularly as $r \to R$, so that the magnetic field lines bulge out and must cut the cylindrical surfaces. The model is therefore more accurately applicable to suitably 'barrelled' specimens. [In practice for cylinders the flux will

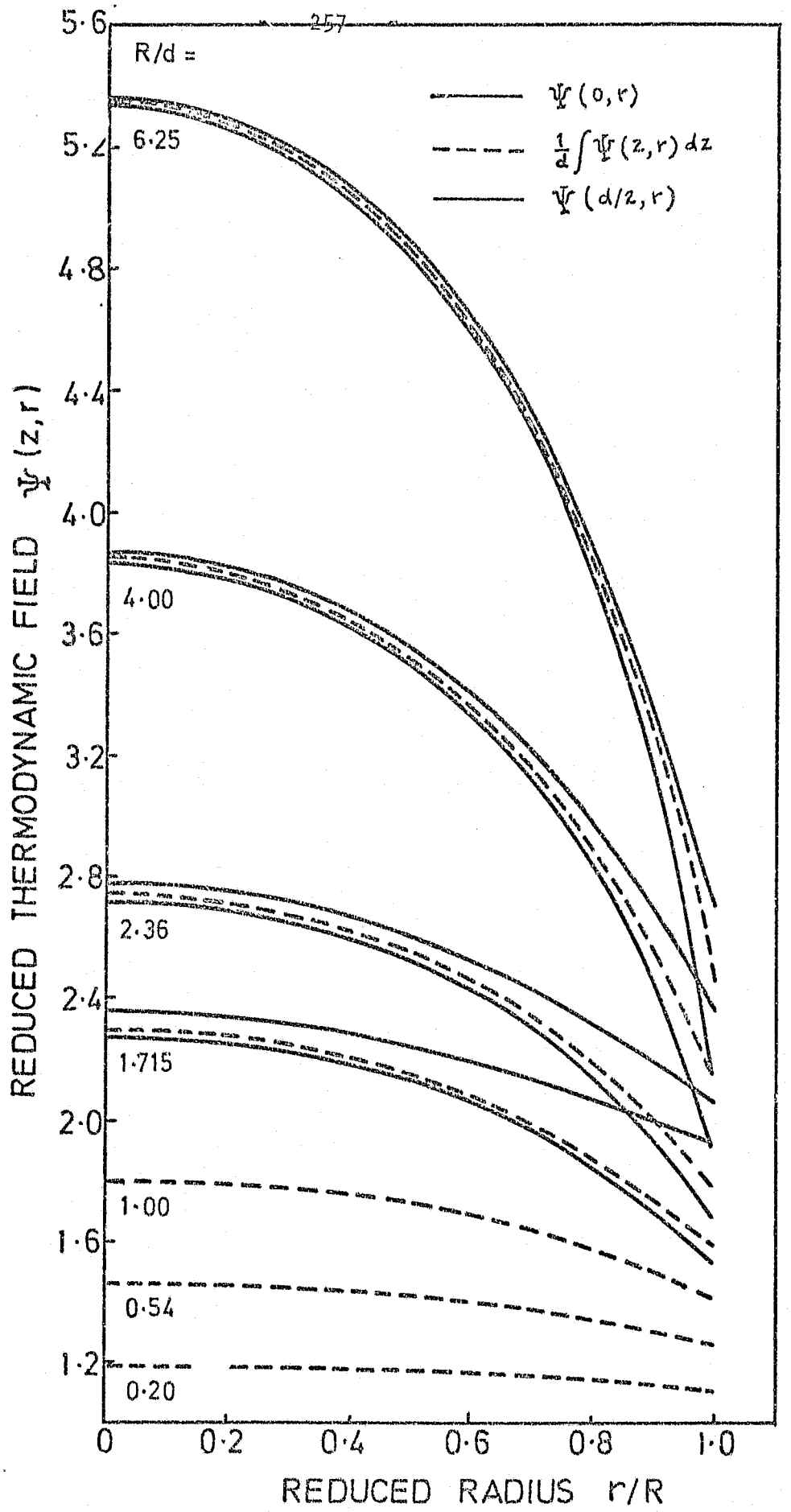


Figure 6.13. The variation of the reduced thermodynamic field Ψ on the end and the equatorial planes of a cylinder as a function of the reduced radial position of a fluxon for various values of R/d. The dashed curve shows the mean value of $\Psi(r_F)$.

penetrate the sharp rims at low values of the applied field H_o and possibly even drive them completely normal at high H_o. It will be shown later that this has a relatively small effect on the magnetization behaviour in increasing H_o however.]

6.3.4 Calculation of the reduced field $h^* = H^*_{c1}/H_{c1}$ for fluxon penetration into a cylindrical specimen

In the previous section the magnetostatic energy component for a fluxon (E_m) was formulated and the reduced thermodynamic field ($\Psi = H_e/H_o$) was evaluated.

The Gibbs free energy for an isolated fluxon (see section 6.3.2) is given by the line integral

$$\delta G = (\phi_o/4\pi)\int (H_{c1} - H_e)\,d\ell \qquad 6.35$$

where the integration is to be taken over the length of the fluxon. (The first term under the integral gives the line energy and the second the magnetostatic energy.)

For a superconducting cylinder in a longitudinal field, increasing from zero, fluxon penetration will begin at the sharp rims (indicated by points D and F in figure 6.12b - H_o along z) and proceed until eventually the leading fluxon which penetrated at D, emerges from the cylinder at some point A and at point C and the leading fluxon which penetrated at F emerges at E and C. (Providing these fluxon segments are not strongly curved, which is most unlikely, it may be assumed without significant loss of accuracy, in the following analysis, that the segments are straight and lie along AC and EC as shown in figure 6.12b). The two segments of fluxon may now join at C and the fluxon along ACE will collapse dissipatively to lie along ABE and then, since H_e is a decreasing function of r, move towards $r = 0$. The field at which this occurs will be defined as H^*_{c1}.

For a fluxon segment along AC the Gibbs free energy is given by

$$\delta G = (\phi_o/4\pi)\left[H_{c1}(d^2/4 + \Delta r^2)^{\frac{1}{2}} - H_o \int_{AC} \Psi(z, r)\, d\ell\right] \qquad 6.36a$$

and since the line integral is path independent curl $\Psi = 0$) and the radial component of Ψ on the $z = d/2$ plane is zero, so that

$$\delta G = (\phi_o/4\pi)\left[H_{c1}(d^2/4 - \Delta r^2)^{\frac{1}{2}} - (H_o/2) \int_o^d \Psi(z, r_o)\, dz\right] \qquad 6.36b$$

where $\Delta r = R - r_o$. The determination of the critical conditions, viz: $H_o = H_{c1}^*$ and $\Delta r = \Delta r_c$, by minimizing δG with respect to Δr is problematical. However, it is reasonable to assume that a fluxon segment penetrating the rim will do so in such a manner that $\delta G = 0$ at all times. On this assumption H_{c1}^* will be given by the minimum value of H_o which satisfies this condition in equation 6.36. Rewriting equation 6.36b in terms of the reduced field $h = H_o/H_{c1}$ gives

$$h = (1 + (2\Delta r/d)^2)^{\frac{1}{2}} \left(\frac{1}{d}\int_o^d \Psi(z, r_o)\, dz\right)^{-1} \qquad 6.37$$

Using the results obtained for $\frac{1}{d}\int \Psi dz$ in the previous section (see figure 6.13), h has been determined as a function of r_o for the various values of R/d and is plotted against r_o/R in figure 6.14 which shows definite minima from which $h^*(R/d)$ and $|\Delta r_c/R|_{R/d}$ can easily be measured. These values are given in table 6.2. Included in the table is the prediction for the enclosed spheroid, viz: $h^* = (1 - D_e)$ (see section 6.3.1) and also $(1 - D_m)$. It is apparent from the table that the present model predicts a considerable delay in initial fluxon penetration compared with the prediction for the enclosed spheroid (or, in particular, with the predicted equilibrium behaviour). Detailed comparison with experiment will be given in section 6.4.

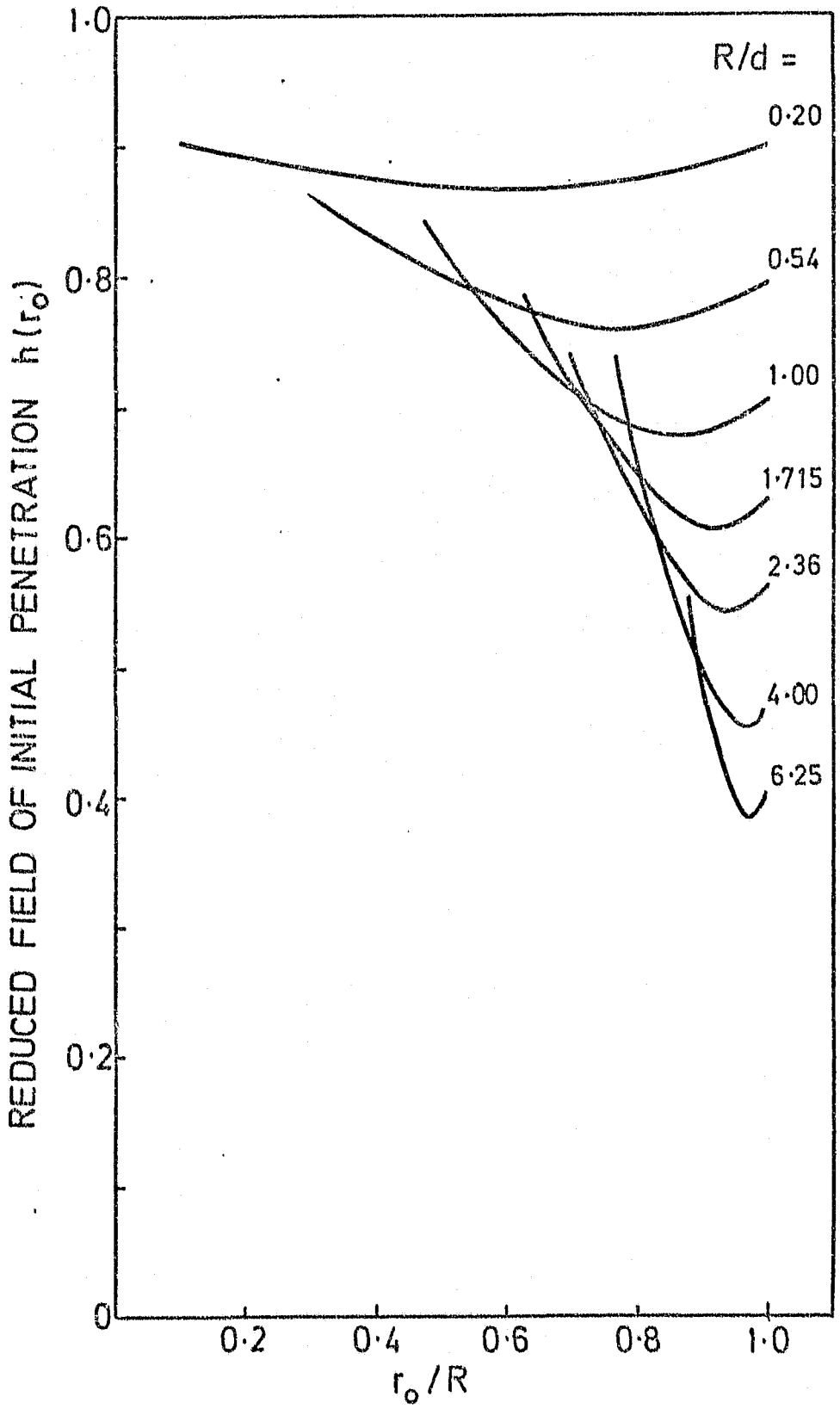


Figure 6.14. A plot of the reduced field of initial penetration of fluxons into the bulk of a cylindrical specimen versus the reduced radius of penetration for a flux spot on the planar end-surface of the specimen (see figure 6.12b) for the various values of R/d for which numerical calculations were made. The figure shows minima in $h(r_o)$ which are expected to be the critical $h^*(r_c)$.

TABLE 6.2

R/d	$\Delta r_c/R$	h^* (theory)	h^* (exp)	$(1+R/d)^{-\frac{1}{2}}$	D_m	D_e	$(1-D_m)$	$(1-D_e)$	$\zeta(K)$
0.20	0.35	0.868	-	0.913	0.14	0.132	0.86	0.868	-
0.54	0.22	0.760	-	0.806	0.33	0.358	0.67	0.642	1.38
1.00	0.13	0.680	-	0.707	0.475	0.522	0.525	0.478	1.63
1.72	0.80	0.605	0.601	0.607	0.60	0.668	0.40	0.332	1.96
2.36	0.60	0.540	0.535	0.546	0.672	0.739	0.328	0.261	2.29
4.00	0.35	0.450	0.44	0.447	0.766	0.831	0.234	0.169	3.07
6.25	0.25	0.385	0.368	0.371	0.830		0.170		4.12

6.3.5 Magnetization behaviour of a type II superconducting cylinder in a longitudinal applied field

In this section a model for the salient physical processes involved in the overall magnetization behaviour of an ideal superconducting cylinder in a longitudinal applied field will be proposed. A rigorous analysis of the model will not be attempted here but a few of the more important predictions will be considered.

Thus: In the previous section it was found that initial fluxon penetration into the cylinder is delayed to an externally applied field which is in excess of that for which a fluxon is energetically favoured in the bulk of the cylinder. The first fluxons to overcome this effective barrier are able to reduce their Gibbs energy by moving towards the middle of the cylinder. (In real specimens fluxon pinning mechanisms will, to some extent, prevent this. This will be discussed in section 6.4.)

A consideration of the results of the previous sections leads to the proposal that in the initial stages of fluxon penetration the fluxons form a 'pool', centered on the cylindrical axis of the specimen, of radius $\rho < R$. The existence and stability of such a pool requires (i) that the spatial gradient of the interaction energy between any fluxon and all the other fluxons in the pool is equal and opposite to the gradient of its magnetostatic energy and (ii) that there is a long-range back-stress, due to the fluxons in the pool acting at the perimeter ($r = R$) of the cylinder, which prevents the instantaneous growth of the pool to $\rho = R$ at $H_o = H^*_{c1}$. The Gibbs free energy for the fluxons in the pool is given by

$$G = (\phi_o d/4\pi) \int_o^\rho (H_{c1} - H_o \frac{1}{d} \int_o^d \Psi(z, r)dz)\ n(r)d^2r$$

$$+ \int_o^\rho n(r_1)d^2r_1 \int_o^\rho n(r_2)n(\underline{r} - \underline{r}_1)d^2r_2$$

$$+ d \int_o^\rho \omega(n(r))d^2r \qquad 6.38$$

where $n(r)$ is the local flux line density, $n(\underline{r}_1 - \underline{r}_2)$ is the long range surface interaction energy between two fluxons at $\underline{r}_1$ and $\underline{r}_2$ respectively (resulting in accordance with the model of section 6.3.3 from the surface magnetic charge distribution, or in accordance with Pearl (see section 6.1), from the long range (r^{-2}) currents associated with a fluxon at the superconducting-vacuum interface) and $\omega(n(r))$ is the usual short-range interaction between fluxons in the bulk of the specimen.

The terms in H_{c1} and H_o are respectively the line energy and the magnetostatic energy of the fluxons.

$\omega(|\underline{r}_1 - \underline{r}_2|)$ is given (see for example de Gennes, 1966) for low fluxon densities by

$$\omega(|\underline{r}_1 - \underline{r}_2|) = (\phi_o/4\pi)^2.(z/\lambda^2).K_o(|\underline{r}_1 - \underline{r}_2|/\lambda)$$

$$\simeq (\phi_o/4\pi)^2.(z/\lambda^2).[\pi\lambda/(|\underline{r}_1 - \underline{r}_2|)]^{\frac{1}{2}} \exp(-|\underline{r}_1 - \underline{r}_2|/\lambda)$$

6.39

where $z = 6$ is the number of nearest fluxon neighbours and K_o is the zero-order modified Bessel function. From the considerations of sections 6.3.2 and 6.3.3 the long range interaction energy between two fluxons at $\underline{r}_1$ and $\underline{r}_2$ is given by

$$n(|\underline{r}_1 - \underline{r}_2|) = (\phi_o/4\pi) \int_o^d H_z(z, |\underline{r}_1 - \underline{r}_2|)dz \qquad 6.40$$

where $H_z(z, |\underline{r}_1 - \underline{r}_2|)$ is given by equation 6.19 and is the field resulting from the surface charge distribution of a fluxon at $\underline{r}_1$ acting at a point $\underline{r}_2$ (or vica versa).

It seems reasonable, but difficult to justify, that $n(r)$ should be independent of r for $r < \rho$. Making this assumption allows the Gibbs free energy (equation 6.38) to be evaluated and minimized with respect to ρ at constant

$$B(r \leq \rho) = (\phi_o/\pi\rho^2) \int_o^\rho n(r) d^2r = N\phi_o/\pi\rho^2$$

(where N is the total number of fluxons in the pool) and at constant H_o to determine the equilibrium $\rho(B, H_o)$ behaviour. This will however be done only for the limit $\rho \to R$ where the required numerical integrations are available from section 6.3.3 (see later). Qualitatively the behaviour of $\rho(B, H_o)$ can be ascertained by consideration of equation 6.38. Thus for constant N a decrease in H_o will cause the magnetostatic energy term, which is negative, to decrease in absolute magnitude relative to the positive interaction terms so that the pool radius ρ will increase. Eventually ρ will become equal to R and, if edge effects are neglected (see later), fluxons will begin to leave the specimen. If H_o is now increased ρ will become less than R again and will decrease in equilibrium with H_o at constant N until eventually the back stress, due to the long range repulsive force of the fluxons in the pool acting at the perimeter $r = R$, is insufficient to prevent the penetration of more fluxons. Further increase in H_o therefore causes ρ to increase until at some $H_o = H_R$; $\rho = R$. For $H_{c2} \geq H_o \geq H_R$ fluxons should move reversibly in and out of the specimen and N should therefore be in thermodynamic equilibrium with H_o.

Now on the assumption that $n(r)$ is indeed independent of r the

long range surface interaction term in equation 6.38 is given, on substitution for η from equation 6.40 by

$$U_T^{\rho} = (\phi_o N^2/8\pi) \int_o^d \int_o^{\rho} \int_o^{\rho} \int_o^R \psi(|\underline{r}_1 - \underline{r}_2|)[\gamma(z, |\underline{r} - \underline{r}_1|) + \gamma(d - z, |\underline{r} - \underline{r}_1|] \, d^2r_1 d^2r_2 d^2r dz \qquad 6.41a$$

Putting $\rho = R$ and using the result of appendix A1(g) gives

$$U_T^{R} = (\phi_o N^2/8\pi) \int_o^d \int_o^R \int_o^R \tfrac{1}{2}[\psi_o(r_1)[\gamma(z, |\underline{r} - \underline{r}_1|) + \gamma(d - z, |\underline{r} - \underline{r}_1|)]] \, d^2r_1 d^2r dz$$

which may be reduced using equation 6.32 to give

$$U_T^{R} = (\phi_o N^2/8\pi) \int_o^R [\int_o^d [\psi(z, r) - 1] dz \, dr^2]$$

$$= (\phi_o N^2/8\pi)\pi R^2[\zeta(R) - 1] \qquad 6.41b$$

where

$$\zeta(R) = (1/\pi R^2) \int_o^R [\tfrac{1}{d} \int_o^d (\Psi(z, r)dz)] d^2r \qquad 6.42$$

[$\zeta(R)$ has been numerically evaluated from the results of section 6.3.3 (for $\frac{1}{d}\int_o^d \Psi(z, r)dz$ at the various values of R/d) and is included in table 6.2.]

It will now be assumed that for $\rho \simeq R$, R may be replaced by ρ in equation 6.41b and 6.42 without significant error. Substituting for U_T^{ρ} from equation 6.41b into equation 6.38 for the Gibbs free energy of the pool gives

$$[G]_{\rho \to R} = (d\rho^2/4)[B(H_{c1} - H_o\zeta(\rho)) + (B^2/2)(\zeta(\rho) - 1) + \alpha(B)] \qquad 6.43$$

where $B = N\phi_o/\pi R^2$ is the average induction in the specimen (assumed uniform) and $\alpha(B)$ is related to $\omega(n(r))$ and is the contribution from the short range forces. Minimizing with respect to B at constant H_o and with $\rho = R$ gives

$$[\partial G/\partial B]_{H_o,\ \rho = R} = 0 = H_{c1} - H_o\zeta(R) + B(\zeta(R) - 1) + \partial\alpha(B)/\partial B \qquad 6.44$$

and therefore the value of B in equilibrium with H_o is given by

$$B[H_o] = (H_o\zeta(R) - H_{c1} - \partial\alpha(B)/\partial B)/(\zeta(R) - 1) \qquad 6.45$$

and also

$$dB[H_o]/dH_o = (\zeta(R) - \partial^2\alpha(B)/\partial^2 B.dB[H_o]/dH_o)/(\zeta(R) - 1)$$

$$= \zeta(R)/(\zeta(R) - 1 + \partial^2\alpha(B)/\partial^2 B) \qquad 6.46$$

These predictions will now be compared with the equilibrium predictions for a spheroidal specimen with a demagnetizing coefficient D. It will be convenient and sufficient (see later) to make this comparison for a pool with $\rho = R$ in the limit $B \to 0$ (from above) where $\alpha(B)$, $\partial\alpha/\partial B$ and $\partial^2\alpha/\partial B^2$ also tend to zero. In this limit, from equation 6.45,

$$H_o[B \to 0] = H_{c1}/\zeta(R) \qquad 6.47$$

and from equation 6.46

$$[dB[H_o]/dH_o]_{B \to 0} = \zeta(R)/(\zeta(R) - 1) \qquad 6.48$$

For a spheroidal specimen (see section 6.3.1) $H_o(B \to 0, \text{from above})/H_{c1} = h^* = (1 - D)$ and $[dB[H_o]/dH_o]_{B \to 0, \text{from above}} = D$. It is therefore obvious that a direct comparison of the predictions for the cylindrical and spheroidal cases can be made from a plot of $\zeta(R)/(\zeta(R) - 1)$ versus D fo specimens of various axial ratios. This has been done in figure 6.15 where $D = D_m$ has been used (see later).

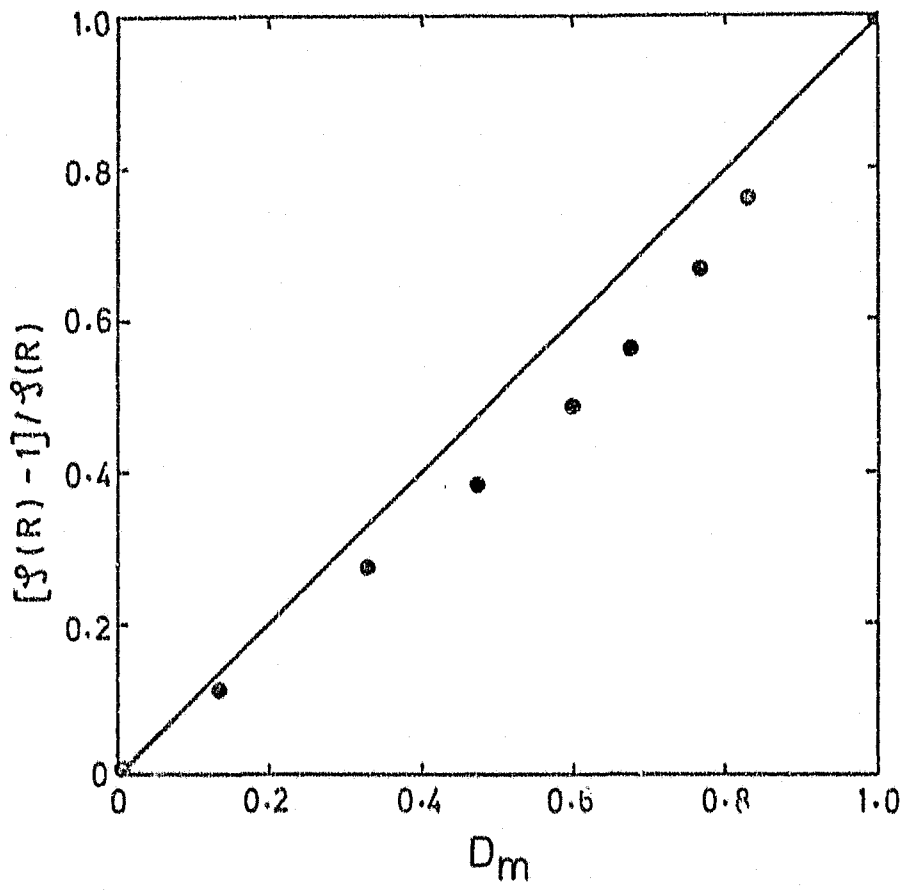


Figure 6.15. A comparison of the predictions of the present model for the equilibrium behaviour in cylindrical specimens with the prediction for a spheroidal specimen with demagnetizing factor D_m - in the limit $B \to 0$ from above (points).

In the limits $D \to 0$ and $D \to 1$ agreement between the two predictions is exact. However, for intermediate D there is a maximum discrepancy of about 20 per cent which does not necessarily imply that the model is inaccurate since it is easily demonstrated that for H_o decreasing in the range $0 < H_o < H_{c2}$ the model predicts $\int_0^{H_{c2}} M dH_o = -H_c^2/8\pi$. The field H_R, at which $\rho \to R$ and the magnetization just becomes reversible in increasing H_o, may be determined from the following considerations. Thus for $\rho \leq R$ the Gibbs free energy of the fluxons in the pool (equation 6.43) must be zero. Also for ρ to be stable the magnetostatic energy due only to the induced surface charges (which drive the fluxons into the cylinder), i.e. $BH_o(\zeta(R) - 1)$, must exactly compensate for the repulsive interaction terms, thus:

$$BH_R[\zeta(\rho) - 1]_{\rho \to R} = (B^2/2)[\zeta(\rho) - 1]_{\rho \to R} + \alpha(B)$$

which on substitution into equation 6.43 for G and equating to zero gives

$$[G]_{\rho \to R} = 0 = B(H_{c1} - H_R\zeta(R)) + BH_R(\zeta(R) - 1)$$

and therefore

$$H_R = H_{c1} \qquad 6.50$$

Finally an approximate prediction can be made for dH_o/dB ($H_o \gtrsim H_{c1}^*$, H_o increasing) when $\rho << R$ if it is assumed that the 'back stress' on the penetrating fluxons due to the fluxons already in the pool can be calculated for this situation by taking the limit $\rho \to 0$, i.e. by assuming all the fluxons in the pool to be at $r = 0$. In this approximation, from equation 6.36b and 6.40, the Gibbs free energy for a penetrating fluxon is given by

$$\delta G \simeq (\phi_o d/4\pi)\left[H_{c1}(1 + (2\Delta r/d)^2)^{\frac{1}{2}} - H_o \frac{1}{d}\int_o^d \Psi(z, r_o)dz\right.$$

$$\left. + (B/2)\frac{1}{d}\int_o^d \psi(0 - r_o)[\gamma(d, r) + \gamma(d - z, r)]d^2rdz\right] \quad 6.51$$

In the critical condition $\delta G = 0$ and $[\Delta r = R - r_o] \rightarrow [\Delta r_c^1 = R - r_c^1]$, where $r_c^1 \rightarrow \Delta r_c$ in the limit $B \rightarrow 0$ (see section 6.3.3), and dB/dH_o is given by

$$\left[dB/dH_o\right]_{H_o \gtrsim H_{c1}^*} \simeq \left[\frac{1}{d}\int_o^d \Psi(z, r_c^1)dz\right] / \left[\frac{1}{2d}\int_o^d\int_o^R \psi_o(0 - r_c^1)[\gamma(d, r)\right.$$

$$\left. + \gamma(d - z, r)]d^2rdz\right] \quad 6.52$$

The evaluation of this expression requires additional numerical calculation which will not be done here.

6.4 Discussion and comparison with experiment

Summarising the results thus far: predictions have been made for the reduced field h^* of initial penetration of fluxons into a cylindrical specimen and a model has been proposed for the non-equilibrium behaviour which occurs in increasing applied field in the range $H_{c1}^* \leqslant H_o \leqslant H_{c1}$. This model also predicts that in decreasing H_o the specimen induction $B(H_o)$ will be in thermodynamic equilibrium.

In order to compare the predicted results for $h^* = H_{c1}^*/H_{c1}$ with experiment it is necessary first to obtain H_{c1} (i.e. the field of initial penetration in an infinitely long specimen). H_{c1} can be obtained approximately from the results of chapter 5 but it was found that a more accurate result could be obtained from the results for the two series of <111> discs (see figures 6.4 and 6.5), in a self consistent manner, if the shearing process described in section 6.3.1. (and see

figure 6.11) is used in reverse* (i.e. each point on the magnetization curves of figures 6.4 and 6.5 is moved a distance $|4\pi MD|$ along the positive H_o direction). To demonstrate this it will be necessary to digress for a while. Thus: the magnetization behaviour for $H_o \leq H^*_{c1}$, H_o increasing, when the specimen is fully in the Meissner state (apart from the regions near the sharp rims) must be in thermodynamic equilibrium. For $H_{c2} \geq H_o \geq H_{c1}$, with H_o increasing or decreasing, equilibrium behaviour is also predicted and apparently obtains in the experimental results (see figures 6.4 and 6.5b which show approximately reversible behaviour for $H_{c2} \geq H_o \geq$ 1Koe ($T = 4K$)). The reverse shearing process on the various magnetization results of figures 6.4 and 6.5 (taking the average values, in each case, of $4\pi M$ in the regime $H_{c2} \geq H_o \geq 1$ Koe) should therefore produce a single curve (corresponding to that for a specimen with $D = 0$) in the field regimes $H_o \leq H^*_{c1}$ (H_o increasing from zero) and $H_{c2} \geq H_o \geq 1$ Koe if the correct demagnetization coefficient (i.e. either D_e or D_m - see section 6.1) is chosen. In agreement with the consideration that the predicted relative distance ($\Delta r_c/R$) of flux penetration into the rims of the disc specimen is small (see table 6.2 and also figure 6.16) such a single curve was obtained when D_m was used. In figure 6.17 the results obtained from figures 6.4 and 6.5 for the slope $-4\pi dM/dH_o$ in the Meissner regime are compared with the prediction of equation 6.7 when either D_m or D_e is substituted. (The use of the factor 2/3 in the latter case is required to compensate for the volume ratio between the enclosed ellipsoid and the disc.) The results of the

---

* For the specimen with the largest value of R/d (viz: 11.0) this shearing process causes the point $M(H^*_{c1})$ to move to a value $M(H^*_{c1} + 4\pi MD)$ such that $H^*_{c1} + 4\pi MD \geq H_{c2}$.

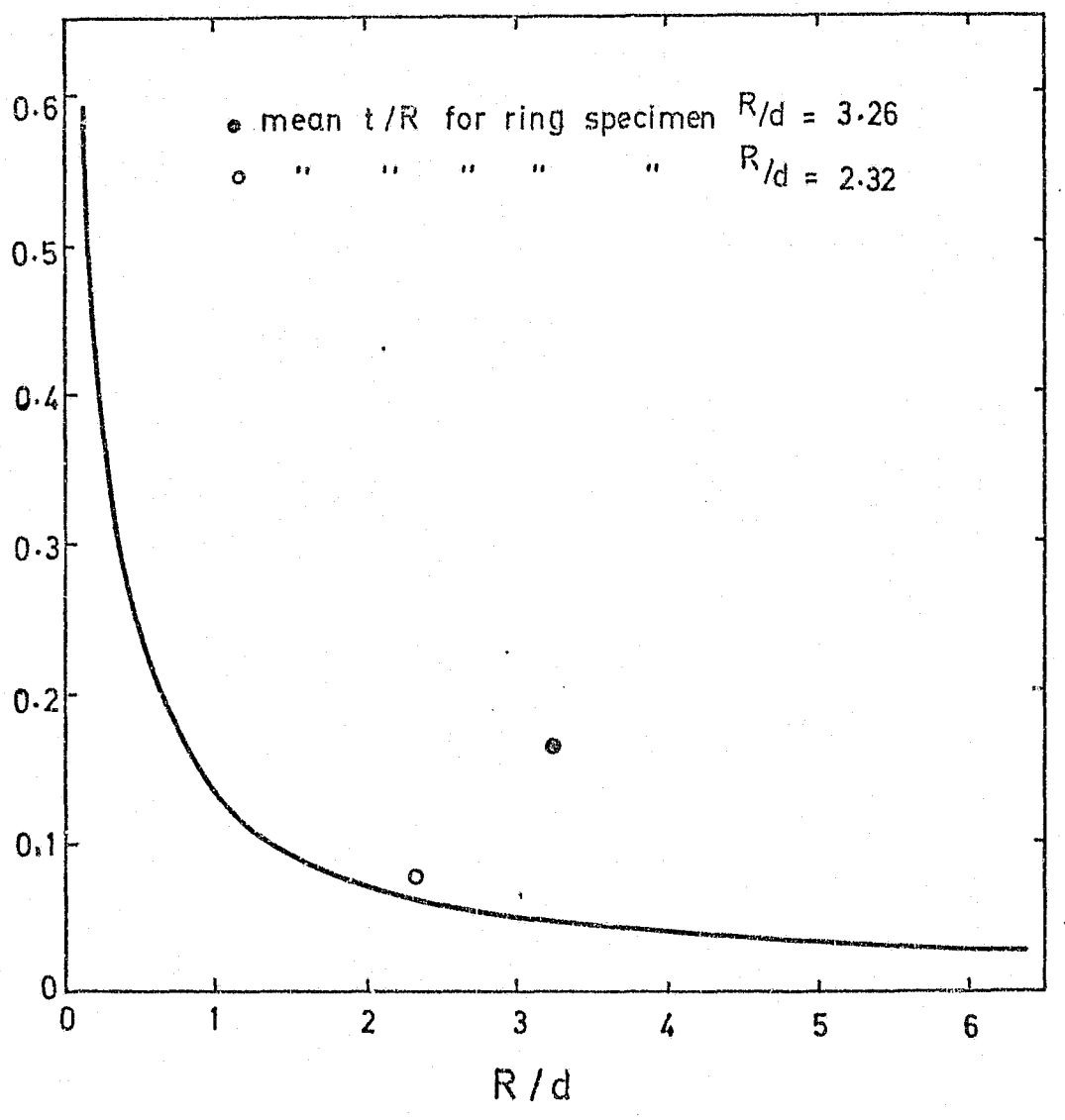


Figure 6.16. The predicted (see figure 6.14) reduced penetration distance as a function of R/d showing that for most of the range of R/d this distance is small · and o show the mean reduced ring thicknesses for the two ring specimens.

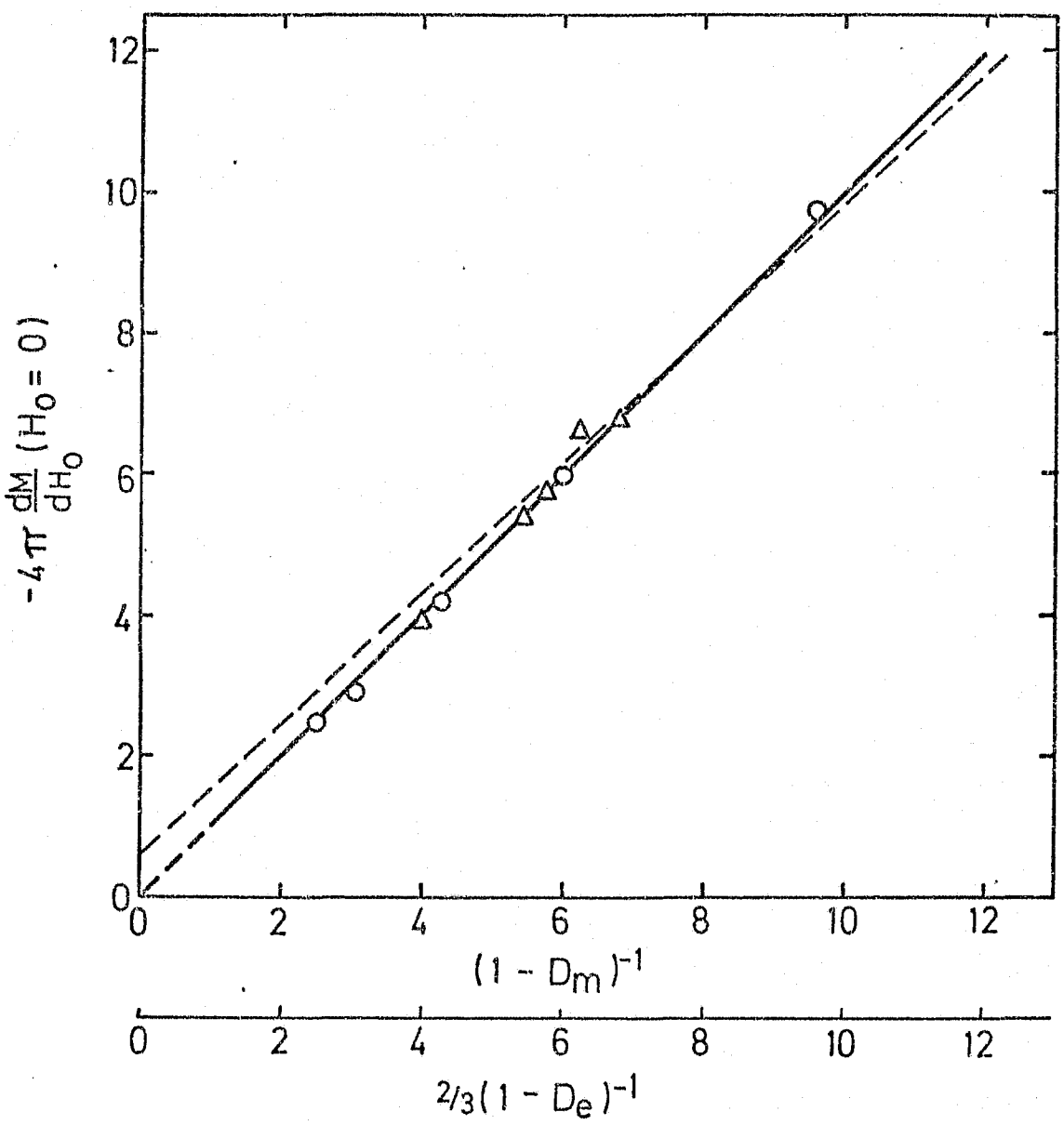


Figure 6.17. A comparison of the experimentally determined slopes of the magnetization curves in the Meissner regime ($B = 0$) with the equilibrium predictions using $D = D_m$ (solid curve) and $D = D_e$ (dashed curve) respectively (see text). The figure shows that the use of $D = D_m$ is the better approximation.

figure confirm that the use of D_m rather than D_e is the better approximation. H_{c1} is now readily obtainable, in a self consistent manner, by an iterative process which involves (i) choosing some value for H_{c1} (obviously the value from chapter 5) and marking it on the H_o axis of figures 6.4 and 6.5 (actually much enlarged as in the original experimentally obtained results). (ii) drawing a series of lines through this point with slopes D_m^{-1} (see equation 6.10a and figure 6.5 and noting their points of intersection with the magnetization curves in the Meissner regime and finally (iii) moving the point on the H_o axis until these points of intersection occur at a constant value of $-4\pi M$ which should (and in fact did) have a value corresponding to the point on the H_o axis which is therefore H_{c1}. The final value obtained for H_{c1} in this way is given in table 6.2 and $h^* = H^*_{c1}/H_{c1}$ has been calculated and included in the table.

These results are also shown as a function of d/R in figure 6.18 where the theoretical prediction (section 6.3.3) is shown by the solid curve (which has been smoothly drawn through the calculated values for h^* from table 6.12). The agreement is apparently very good. A remarkably simple empirical formula has also been found for h^*, in terms of R/d - in the range investigated, which is given by

$$h^* = (1 + R/d)^{-\frac{1}{2}} \qquad 6.53$$

The prediction of this formula is compared with the experiment, the present theoretical treatment and the equilibrium prediction for the enclosed ellipsoid, viz: $h = (1 - D_e)$ (equation 6.8b) in figure 6.19.

A remarkable feature of the transition at h^* in the $M\text{-}H_o$ curves for the disc-specimens (see figure 6.1 to 6.5) is that it is very

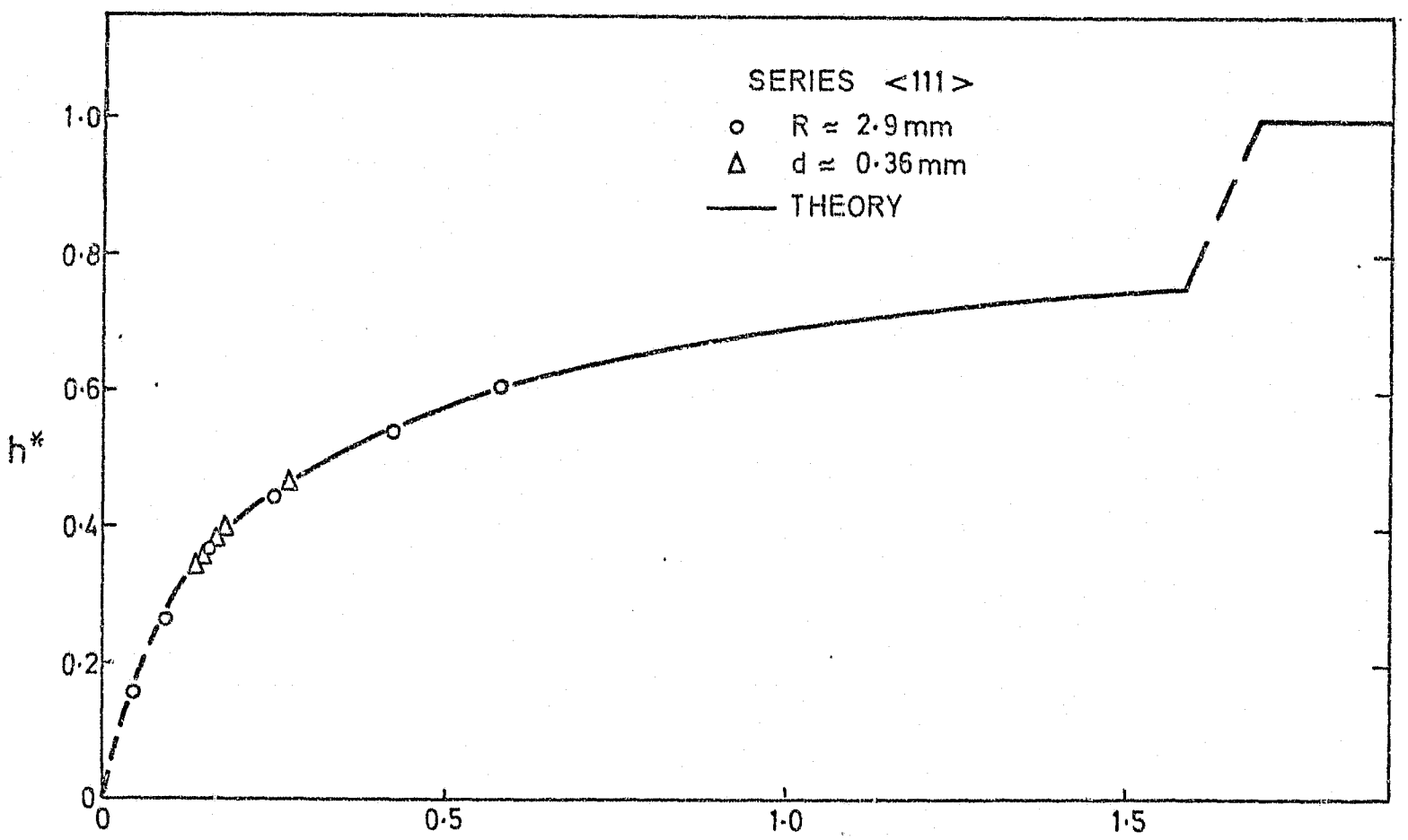


Figure 6.18. A comparison of the critical reduced field of initial fluxon penetration as a function of d/R determined from the model (solid curve) with the experimentally determined values for the two series of <111> disc-specimens (O and Δ).

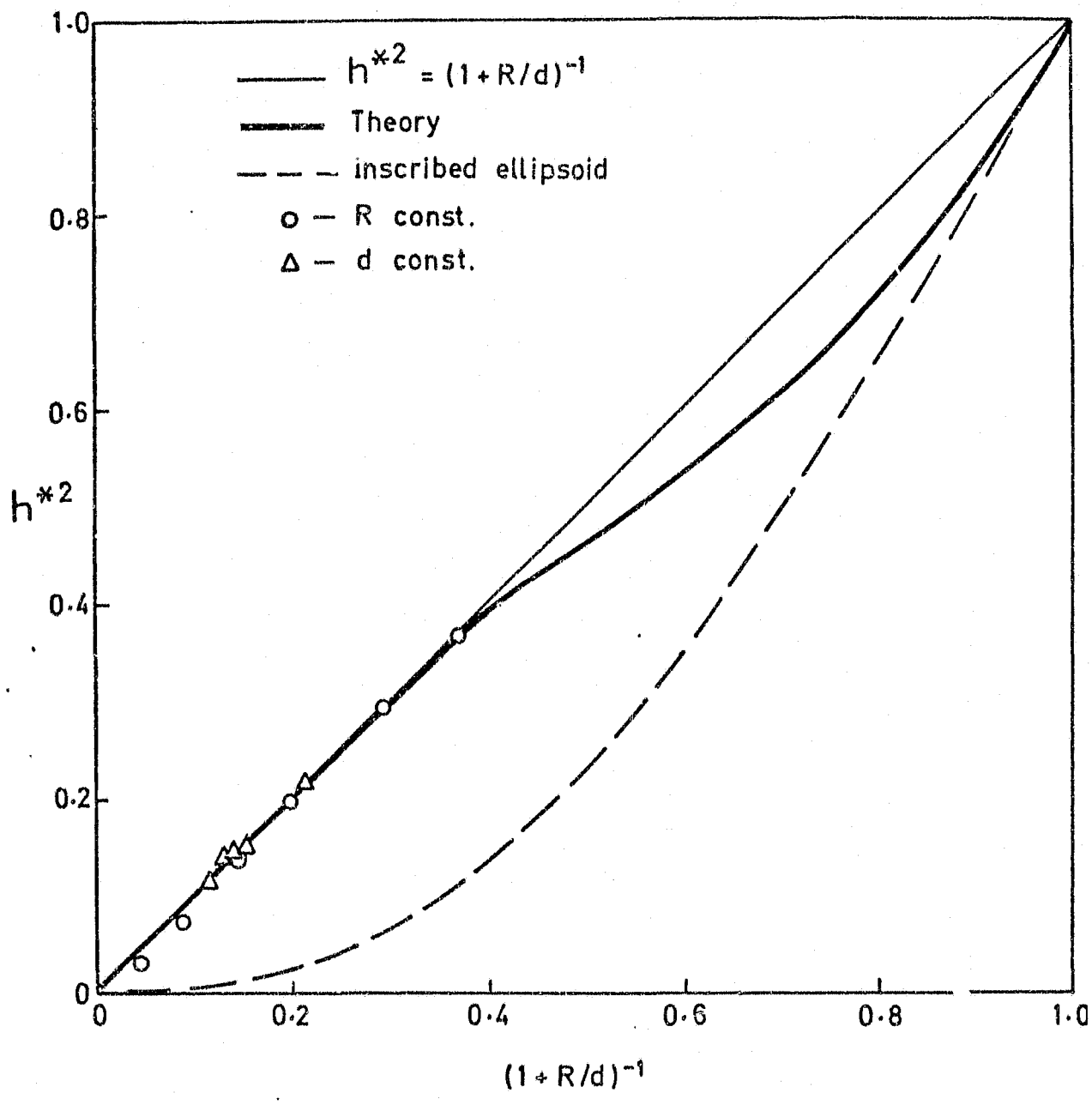


Figure 6.19. The variation of the square of the reduced field of initial penetration as determined experimentally (0 and Δ) is compared with the predictions of the model (heavy curve) as a function of $(1 + R/d)^{-1}$ showing the remarkable empirical relationship $h^{*2} = (1 + R/d)^{-1}$ over the range of R/d investigated. [The predictions for a spheroid (from section 6.3.1) are shown by the dashed curve.]

sharp. (It is probably a second-order λ type transition on account of the 'back-stress' due to the fluxons in the pool.) If the model for the prediction of h^* is considered to be sufficiently accurate the sharpness of this transition may be of use in the determination of κ_3 (see equation 1.7) when H_{c1} is not easily obtainable because of fluxon pinning imperfections in the material or because of the requirement of a long thin specimen for the direct measurement of H_{c1}. Values for κ_1, κ_2 and κ_3 at 4.05K obtained from equations 1.5 to 1.7 on substituting experimental values for the various parameters are given in table 6.1.

It is apparent from the results of figures 6.18 and 6.19 that there is no consistent 'offset' between the results on the two different series of <111> discs. This implies that there are no size effects in the range of R/d investigated.

The bulk critical field H_c (see chapter 1) can now also be obtained approximately from the curves of figures 6.4 and 6.5 by the simple expedient of (i) smoothly extrapolating the magnetization curves from the equilibrium behaviour in the regime $H_o > H_{c1}$ back to the point $-4\pi M = H_{c1}$ on each curve so that its slope is D_m^{-1} at this point (reference to figures 6.5 and 6.11 will make this clear) and (ii) measuring the area $\int_0^{H_{c2}} M dH_o = -H_c^2/8\pi$ (equation 6.12) under the resulting curve. Values determined for H_c from some of the curves are included in table 6.1.

In agreemer with the theoretical prediction that $H_R = H_{c1}$ (section 6.3.5) the magnetization curves of figures 6.4, 6.5 and 6.11 show that the onset of reversible behaviour occurs in increasing H_o at H_{c1}. However, in contrast to the theoretical prediction, it is apparent

from the above figures that in decreasing H_o the magnetization curves depart from equilibrium behaviour at $H_o \simeq H_{c1}$. This behaviour is a consequence of the sharp rims of the disc specimens and is aggravated by fluxon pinning due to defects in the bulk and on the surface of the specimen. (The effect of sharp rims in causing hysteresis in the magnetization curves of type I superconductors was first reported by Schoenberg (1937).)

Qualitatively this effect may be explained as follows: Consider figure 6.20b which is a schematic representation of the flux distribution in the r-z plane of an ideal disc specimen for various external field conditions as shown on the idealized M-H_o curve of figure 6.20a. For $H^*_{c1} < H_o < H_{c1}$, H_o increasing (point 1), figure 6.20b - 1 shows the flux to be confined to a pool (radius ρ - front AB) and to the triangular areas (CEO and ODF) in the rims where the applied external field is strongly concentrated. With increasing H_o fluxon segments along CO and OD join at O, collapse dissipatively loosing line energy to lie along CD, and then more dissipatively down the magnetostatic potential gradient to join the pool along AB. The pool grows, $M(H_o)$ moves along the M-H_o curve between point 1 and 2 and eventually at point 2 the pool touches the penetration fronts in the rims, i.e. A → C and B → D (figure 6.20b - 2), leaving a narrow region which is devoid of flux. At $H_o = H_{c1}$ this region also disappears as the pool front just touches the lateral surface of the disc at the equator (point υ). With further increase in H_o the density of the fluxons in the pool increases reversibly and the curvature of the fluxons (convex outward - which is a consequence of the mutual repulsive interaction between fluxons in the bulk of the specimen and the fact that $H_e(z, r)$ is lower in the equitorial plane than on the planar surfaces

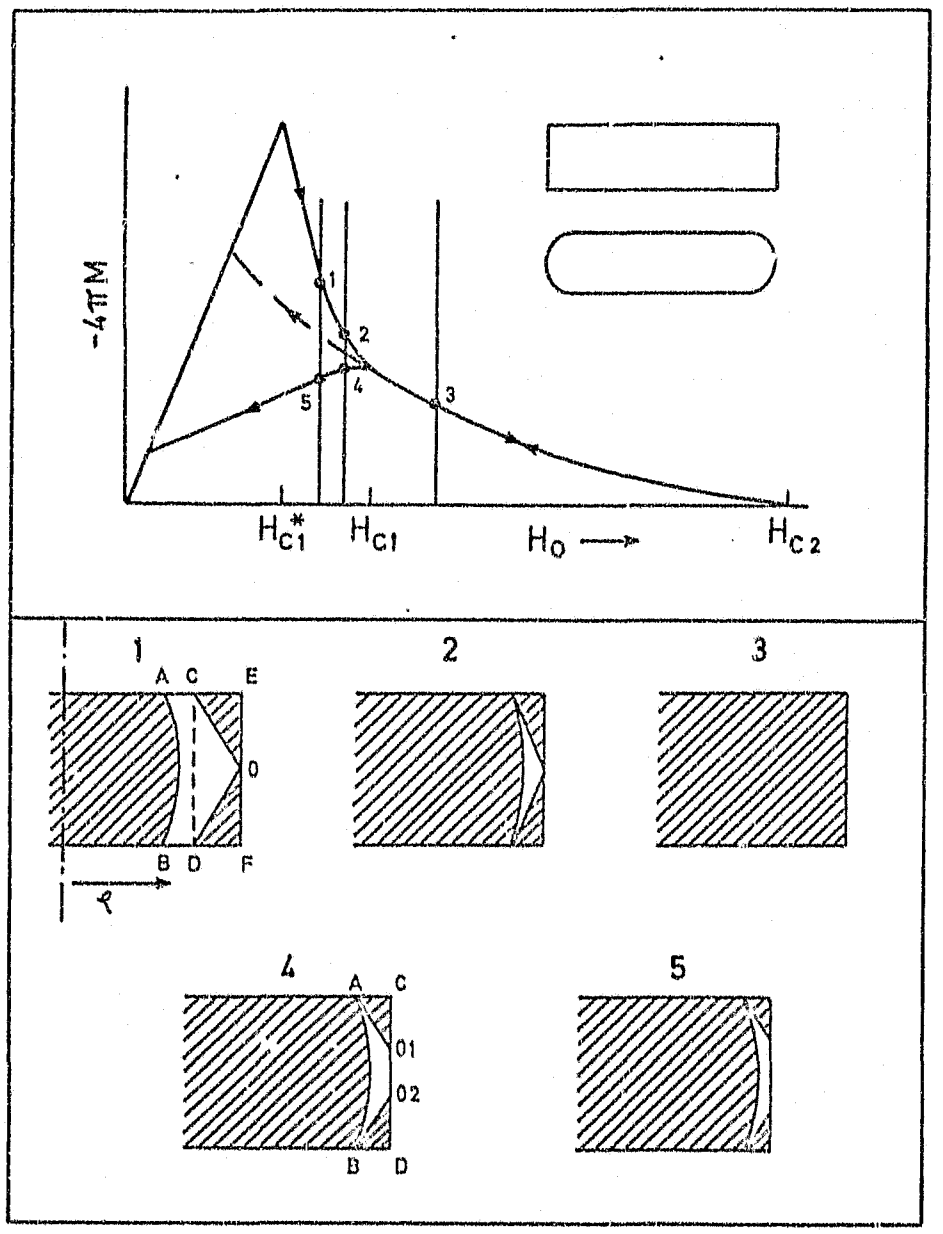


Figure 6.20 A schematic diagram illustrating the behaviour of the fluxon lattice pool and the penetration regions in the rims of a disc specimen with increasing and decreasing applied field H_o in the range $H_o \leq H_{c1}$.

(see section 6.3.3)) decreases until as $H_o \rightarrow H_{c2}$ it tends to zero. If H_o is now decreased fluxons leave the specimen reversibly again until $H_o = H_{c1}$. At this point the pool is only just in contact with the lateral surface of the specimen at its equator. With further decrease in H_o, neglecting surface barrier effects, it would be energetically favourable for the pool to remain in contact with the surface and for fluxons to escape in equilibrium with H_o. $M(H_o)$ would then move along the dashed curve of figure 6.20a and $\bar{B}(H_o)$ (H_o decreasing) would be slightly larger than $\bar{B}(H_o)$ (H_o increasing). The pool radius ρ is the former case is also larger than in the latter and the mutual repulsion between the fluxons in the pool and in the penetration regions in the rims is therefore also larger. The equilibrium flux distribution is therefore as shown in figure 6.20b - 4 (compare with figure 6.20b - 2 for H_o increasing). The penetration fronts (CO_1 and CO_2) in the rims no longer meet at the equator and the pool front (AB) does not touch the equator either. Fluxon escape now requires a fluxon along AB (figure 6.20b - 4) to jump dissipatively and split into two segments (of lower total Gibbs energy) along CO_1 and CO_2 respectively. $M(H_o)$ moves along the $M\text{-}H_o$ curve from points 4 to 6 (figure 6.20a), with $B(H_o) > B[H_o]$. At point 6 all the flux has been expelled. (It will be apparent from the above discussion that the presence in the specimen of regions which are devoid of flux is associated with non-equilibrium $M(H_o)$ behaviour. For a suitably 'barrelled' specimen (see section 6.3.3) for which the calculations for $H_e(z, r)$ are strictly appropriate such devoid regions will not occur in decreasing H_o and equilibrium $M(H_o)$ behaviour is predicted for this case.)

The above behaviour is well illustrated by the magnetization curve of figure 6.6 if the small residual trapped moment resulting from fluxon pinning is overlooked*. The dashed curve shows the result of removing the rims by bevelling (see inset). As expected from the above considerations the curve for the bevelled disc is closer to the thermodynamic equilibrium behaviour. Moreover the bevelling does not significantly affect the value of h^*.

In the region of non-equilibrium behaviour, i.e. for $H_o \leqslant H_{c1}$, the model predicts that $\rho \leqslant R$ and therefore any movement in the $M\text{-}H_o$ phase diagram between the $M(H_o)$ branches for H_o increasing and H_o decreasing can only occur along lines of constant average induction $(B = (1/\pi R^2) \int_o^R B(r) 2\pi r dr)$, i.e. diamagnetics with $4\pi dM/dH_o = (1 - D_m)^{-1}$. With reference to figure 6.20b, it will be apparent that along these diamagnetics the fluxon distribution will be intermediate between that shown by the limiting case (e.g. figures 6.20b - 1 and 4 for H_o increasing and decreasing respectively). This was confirmed experimentally. The concept of the formation of a fluxon pool in cylindrical, or in particular, disc-specimens is well illustrated by the magneto-optical studies referred to in section 6.1. The results obtained in these studies on type I superconductors are more convincing because the flux tubes, which are macroscopic in this case, are less easily pinned by defects and consequently their behaviour is closer to ideal. The effect of fluxon pinning on fluxon penetration and pool

---

* The change in dM/dH_o at $H_o \simeq H_{c1}(1 - D_m)$, H_o decreasing (point A in the figure), occurs because $B[H_e]$ in the lateral surface ($r = R$) tends to zero at this point and the remaining pinned flux in the specimen cannot be further reduced by decreasing H_o to zero.

formation in type II superconductors is significant even in the most highly annealed niobium specimens investigated magneto-optically (De Sorbo and Healy, 1964). These results show large balloon-like projections of flux penetration into the specimen. The overall behaviour is however consistent with the present model and considerations.

The experiments of figures 6.9 and 6.10 were conducted to investigate the affect of fluxon pinning on the magnetization curve of disc-specimens. The specimen which was scratched on its lateral surface ($r = R$) (figure 6.9) shows (i) a slightly larger value for the field of initial fluxon penetration than the predicted value (i.e. H^{*}_{c1}), (ii) diamagnetic behaviour for magnetization paths in the $M(H_o\uparrow)$ and $M(H_o\downarrow)$ envelope and (iii) for H_o decreasing, an excursion by these paths out of the envelope if $H_o < H_{c1}$. The former two observations are consistent with fluxon pinning in the lateral surface and the latter is probably a consequence of fluxon pinning in the bulk of the specimen and therefore of different distributions $B(r)$ depending on the previous magnetic history of the specimen.

The disc specimen which was scratched on the plane surfaces (figure 6.10) shows (i) a field H_o of initial fluxon penetration which is approximately the predicted value (i.e. H^{*}_{c1}), (ii) diamagnetic paths only within the expected $M(H_o\uparrow)$ and $M(H_o\downarrow)$ envelope for an equivalent specimen with no pinning sites and (iii) hysteretic minor $M\text{-}H_o$ loops outside this envelope.

This behaviour is characteristic of fluxon pinning in the bulk of the specimen. The dashed curve in the figure is the estimated $M\text{-}H_o$ curve (H_o increasing) for the equivalent undeformed specimen and

therefore represents the M-H_o locus for which fluxon penetration is possible.

The experimental results on the ring specimens (figures 6.7 and 6.8) are included to confirm that h^* is the same as that for a disc-specimen of the same dimension if the ring thickness (t) exceeds Δr_c (see section 6.3.4) as obtains for the specimen of figure 6.7 (see figure 6.17). This is a necessary consequence of the fact that the boundary conditions for the ring in the Meissner state, with no trapped flux threading it, must effectively be the same as for a disc (in transverse external fields). For $t < \Delta r_c$ fluxon penetration must obviously begin sooner than predicted by the theory for a disc specimen. This is shown by the results of figure 6.8 where the mean ring thickness which was not uniform is $\bar{t} \simeq \Delta r_c$ (see figure 6.17) so that presumably $t < \Delta r_c$ at some point on the ring.

6.5 Conclusions

By using the method of replacing circulating currents by distributed surface magnetic charges which satisfy the boundary conditions for a cylindrical superconducting specimen the position dependent thermodynamic field $H_e(r)$ has been calculated for cylindrical specimens of various axial ratios (R/d). These calculations show that the free energy of a fluxon, parallel to the cylindrical axis of the cylinder, is an increasing function of radial displacement from the axis. This gives rise to non-equilibrium behaviour, in increasing applied field H_o, which is manifest by a delay in initial fluxon penetration to a field above that expected for the enclosed spheroid and to an applied field regime when the fluxons form a 'pool' of radius $\rho < R$ in the cylinder. Predictions are made for the field $H_o = H^*_{c1}$ of initial fluxon penetration and the field $H_o = H_R$ ($= H_{c1}$) at which $\rho \to R$, H_o increasing, which are in excellent agreement with experiment. The

behaviour in decreasing H_o and the effect of the cylinder rims is also considered. If the rims are removed by bevelling the specimen remains in thermodynamic equilibrium in decreasing H_o. The predicted $B[H_o]$ behaviour in this case is not identical with the predictions for the enclosed spheroid.

It is therefore concluded, contrary to previous and current expectation, that the overall magnetization behaviour of cylindrical specimens in longitudinal applied field, even with their rims bevelled off, cannot in general be considered to correspond, even approximately, to the behaviour predicted for the enclosed spheroid. This is of particular relevance in current investigations on the order of the transition from the Meissner to the mixed state and on the so-called mixed-intermediate state in cylindrical-specimens in longitudinal applied field (see section 6.1).

CHAPTER 7

7. Fluxon Pinning in Deformed Disc-shaped Niobium Single-Crystal Specimens

7.1 Introduction

The investigation described in this chapter constitutes, in essence, the preliminary work of this thesis which was an attempt to determine the approximate relative importance of bulk and surface pinning mechanisms*. Two types of experiment were envisaged, viz: (i) to measure the pinning force density P_v in variously deformed disc-shaped niobium specimens as a function of their axial ratios, and (ii) to lightly deform a disc-shaped single crystal specimen by means of a punch and die so as to create a narrow annular region of deformation concentric with the disc axis and then to determine P_v in this region. In both cases measurements would be made in a transverse applied magnetic field. In the former experiment, for discs of constant radius R, a plot of P_v versus d (the disc thickness) would indicate the relative contribution due to the bulk and to the planar surfaces of the specimens. In the latter experiment the pinning forces due to a dislocation network not in close proximity to the lateral surface (which is parallel to the applied field - see footnote) could be investigated.

---

* At the time of inception there was some suggestion and apparent experimental evidence (see for example Schweitzer, Garber and Bertman, 1967) that near surface effects in surfaces parallel to the applied field were responsible for most of fluxon pinning in low κ (e.g. niobium) specimens.

Preliminary investigation on disc-shaped specimens of niobium however, immediately revealed the presence of the geometry effect which was the subject of chapter 6. This development led to a curtailment of the investigation pending an adequate understanding of this geometry effect. Subsequently some of the objectives of this project were achieved and published by other authors (see for example Das Gupta and Kramer, 1972) and it had become apparent that various surface pinning effects could be virtually eliminated by suitable specimen preparation techniques.

This chapter will consequently be confined to the description and approximate analysis of the 'punched' disc experiment which is not particularly successful but nevertheless has some interesting and useful features. The experiment consists basically in the measurement of the magnetization behaviour of a disc-shaped specimen in transverse field both before and after the deformation process outlined above. For a sufficiently narrow annular band (width Δr) of deformation the local fluxon gradient dB/dr in the band may be taken to be its mean value in the band and therefore relatively easy to obtain from the magnetization curves providing that the rest of the specimen is relatively free of pinning sites. Consideration of the critical state model (see chapter 3) obviously requires that dB/dr in the deformed band will be determined by the 'weakest' section along its length, i.e. the section with the lowest potential value of P_v (which is proportional to dB/dr).

7.2 Experimental

7.2.1 Specimen preparation and deformation

The method of preparation of disc-shaped specimens has been described in chapter 6. The specimens used in this investigation were bevelled

discs (see figure 7.2a) of single crystal niobium with the cylindrical axis along <111>, diameter 6mm and thickness 0.65mm (R/d = 4.62).

Deformation was performed with the use of an assembly which comprised a cylindrical stainless steel, flat-ended punch (diameter 3mm), a mating brass die (diameter 3.5mm) and a jig to hold the punch, die and specimen coaxial. The jig was designed so that the punch could be pressed into the flat surface of the specimen in a controllable manner using the tensometer mentioned in chapter 5. The specimens were deformed at a rate of 0.175mm per minute and the resulting deformation, i.e. the depth of the indentation, in the specimen to be considered herein, was 0.065mm.

The dislocation arrangement resulting from this deformation procedure is fairly complex but is nevertheless predominantly confined to a narrow annular region around the punch perimeter. This was evident in deformed specimens which were planed, by spark erosion, to remove the indentation and mound and then subsequently chemically polished for etch pit studies. The polishing gave rise to a very rapid preferential disolution of the specimen, along the punch perimeter ($r = r_o$), in a band which was less than approximately 0.5mm wide and attempts to prepare foils for the electron microscope were not successful. Much can be inferred about the actual dislocation type and arrangement from the results of a separate study by Ball and Doyle (1974 - and see appendix A9) where <111> discs were placed on a flat soft metal bed (e.g. lead) rather than over a die, and 'punched' as described above. In essence the dislocation debris consists mainly of a high density of screw dislocation and screw dislocation dipoles parallel to the <111> axis of the disc. (In the present experiment, where the magnetization behaviour of the disc specimen is measured in transverse applied field, the fluxons are parallel to the screw

dislocations). Regions of dislocation tangling should also be prevalent.

Cross section diagrams for the two specimens, i.e. as prepared and deformed, are shown schematically in figures 7.2a and 7.2b.

7.2.2 Magnetization measurements

Magnetization loops were obtained, for one sense of the external field, applied parallel to the cylindrical axis of the as-quenched (300 - 4k) disc-specimens, initially fully in the Meissner state at various temperatures in the range $4K < T < 9.3K$.

7.2.3 Experimental results

Only the results on two initially identical bevelled disc-specimens, as described in section 7.2.1, will be reported here. From the magnetization curves for the undeformed and deformed specimens the upper critical field H_{c2} and the field of initial fluxon penetration H^{*}_{c1} (see chapter 6) were measured and are shown as a functions of temperature in figure 7.1. The critical temperature, obtained from figure 7.1 by extrapolating $H_{c2}(T)$ and $H^{*}_{c1}(T)$ to $H_o = 0$, is $T_c = 9.31 \pm 0.01K$. In figures 7.2a and 7.2b magnetization loops, normalized at H^{*}_{c1} and $M(H^{*}_{c1})$ for various reduced temperatures $t = T/T_c$ are shown for the as-prepared undeformed and for the deformed specimens respectively. For direct comparison the loops obtained at $t = 0.435$ in each case have been superimposed in figure 7.3a. In figure 7.3b the ideal reversible magnetization curve is shown for a specimen with zero demagnetizing coefficient at $t = 0.435$. This curve has been derived from curve (a) in figure 7.3a as explained in chapter 6.

The curves of figure 7.3a show the expected increase in the magnetic hysteresis with deformation. However, the increase is significant only for $H_o < H_{c1}$ and for $H_o > H_{c1}$ is too small for accurate

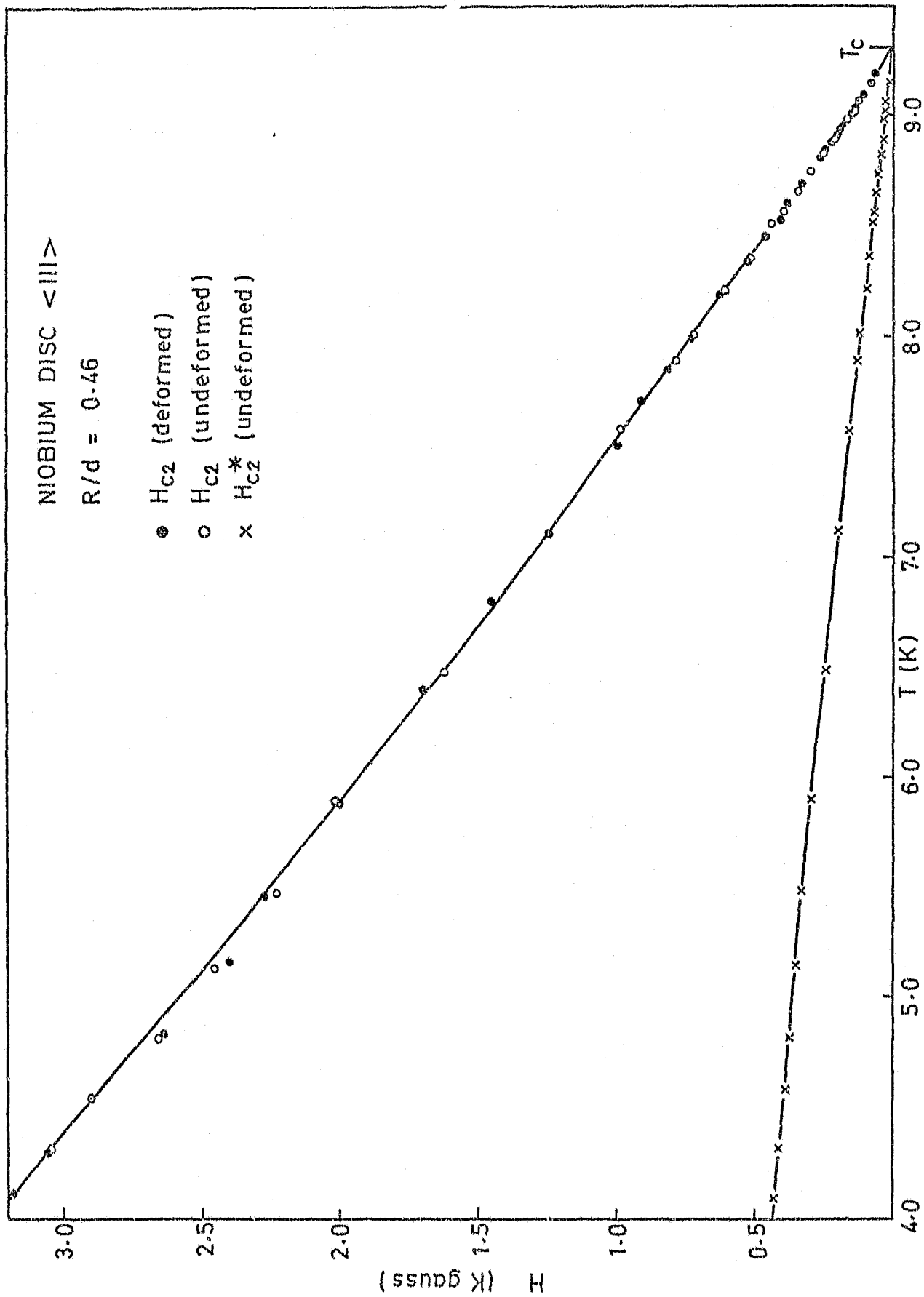


Figure 7.1. The experimentally determined variations of the upper critical field and the field of initial flux on penetration with temperature in bevelled niobium single crystal disc-specimens (R/d = 0.46 oriented <111>) as-prepared and after deformation by punching (see text).

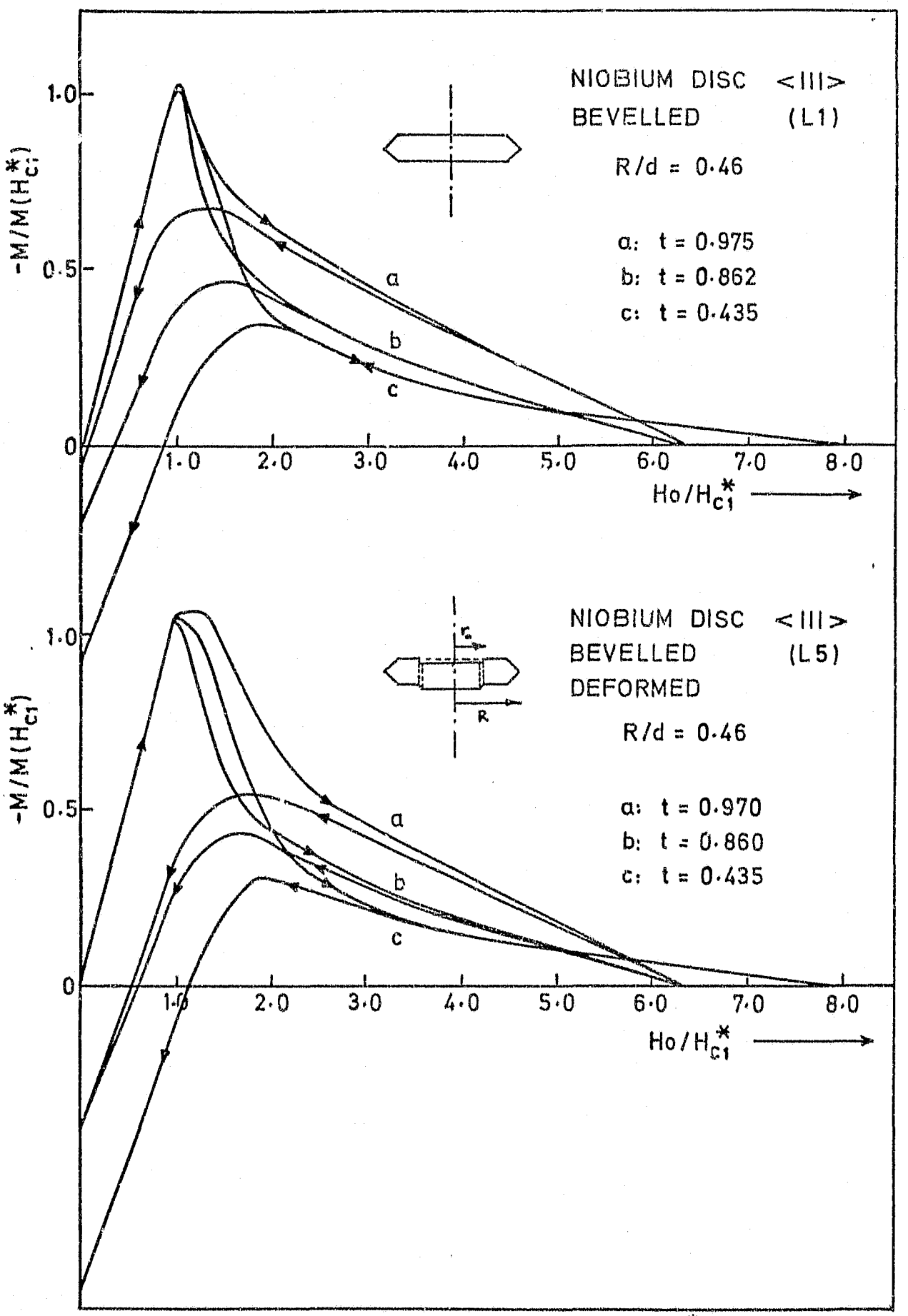


Figure 7.2a. Magnetization curves normalised to H^*_{c1} for the disc-specimen (figure 7.1) at reduced temperatures t = 0.975, 0.862 and 0.425.

Figure 7.2b. As for (a) in the specimen deformed by punching (see text) for t = 0.970, 0.860 and 0.435.

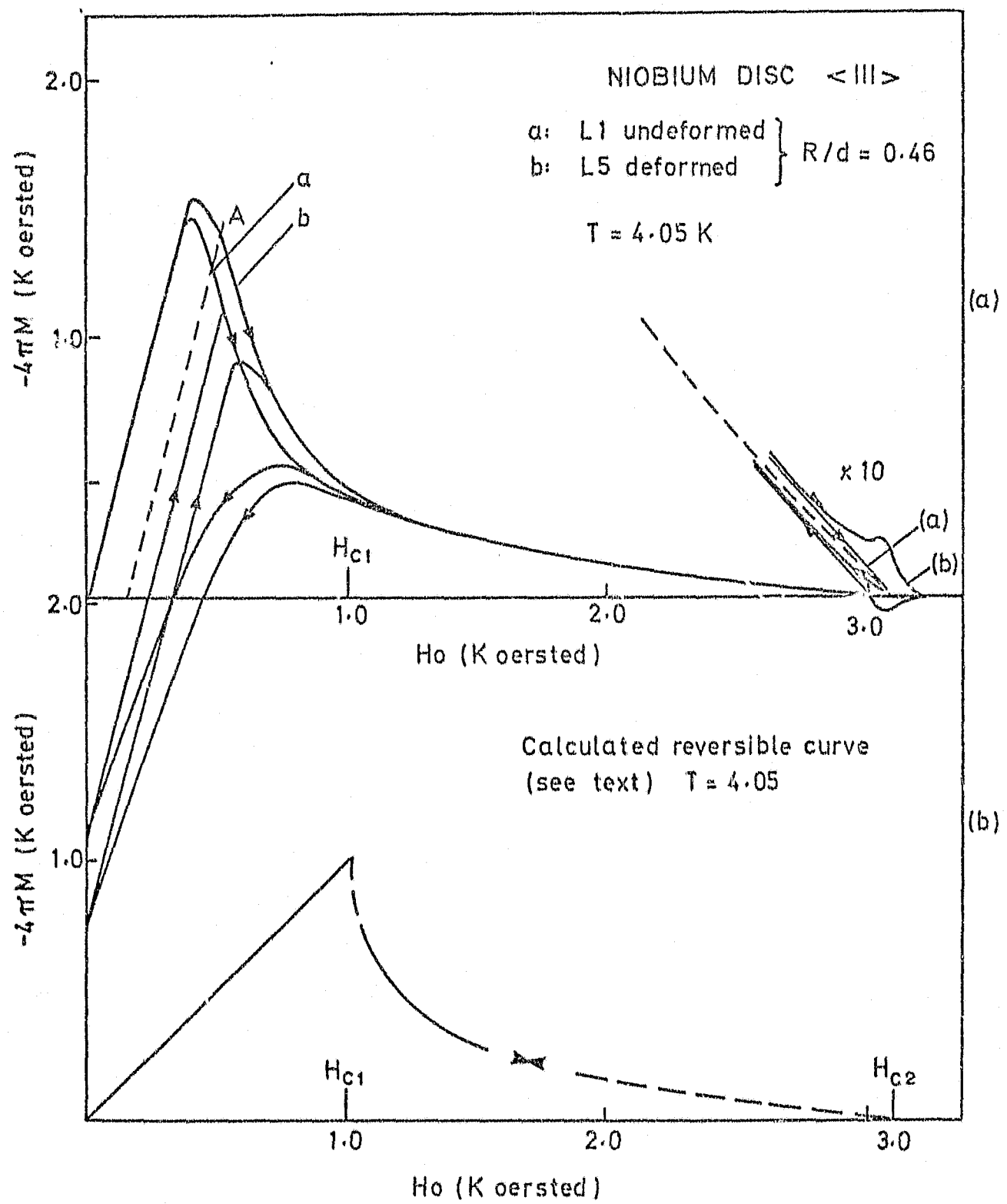


Figure 7.3a. A direct comparison of the magnetization curves at $t \simeq 0.435$ in the disc-specimen as-prepared (curve (a)) and deformed (curve (b)) showing the increase of hysteresis in the deformed specimen. For $H_o \lesssim H_{c2}$ the deformed specimen shows a small peak affect.

Figure 7.3b. The calculated reversible curve for a very long specimen in longitudinal applied field ($D \to 0$ - see text).

measurement. This constitutes an ineluctable disadvantage of the present experiment since to increase the magnitude of the hysteresis requires one or more of the following, viz: (i) an increas- in the strain in the deformed annulus (this is not practical since the specimen geometry will become significantly altered and moreover there is a tendency for the specimen to bend at higher strains so that the background (i.e. away from the annular region) fluxon pinning increases), (ii) an increase in the width of the annular deformed region (in this case the use of the mean gradient dB/dr in the deformed annular region will no longer give a reasonably accurate result) and (iii) an increase in the radius of the deformed annulus (this is also not practical since it becomes difficult to deform the specimen without concomitant bending and also complicates analysis - see later). At higher magnetometer sensitivity it became evident (see figure 7.3a) that the hysteresis in the undeformed specimen is almost as large as in the deformed specimens for $H_o > H_{c1}$. However, with suitable U.H.V. annealing of specimens before deformation it might be possible to obtain results, albeit not very accurately, in this field regime.

7.3 Theory

The magnetization behaviour for a disc-shaped specimen of ideal type II superconducting material was discussed in some detail in chapter 6. For the deformed disc-specimen under ideal conditions, i.e. with P_v non-zero and constant in a narrow annular region concentric with disc, and zero everywhere else, and neglecting possible surface barrier effects an exact analysis of the magnetization curves and hence a prediction of P_v could in principle be made using the methods of chapter 6, and in particular, equation 6.17.

In practice the situation is too complex for an exact analysis and in any case it will become apparent that the geometry effect need

not be explicitly considered - but see later comments. Only a much simplified treatment will therefore be attempted here. Thus for the determination of $P_v(B,T)$ in the deformed annular region it is apparent from equations 6.17, A1 Ae.7 that a knowledge of the local values of B, dB/dr and dH[B]/dB is required. dH[B]/dB is obtainable from calculated reversible magnetization curves for D = 0 at various temperatures (see section 7.2). B and dB/dr can be determined approximately in various regimes of H_o from the magnetization curves for both the deformed and undeformed disc-specimens as follows: Consider the magnetization behaviour in a deformed disc with the applied field H_o increasing from zero. After initial fluxon penetration at $H_o = H^*_{c1}$ the fluxons move into the specimen and pile up against the pinning sites in the deformed annular region. dB/dr in the region will attain a critical value (see section 3.1) but initially will not be non-zero through the entire width of the annular region and consequently no fluxons will penetrate to the middle ($r = 0$) of the specimen. Eventually, with further increase in H_o, penetration will occur at the 'weakest' point along the length of the deformed annular region and fluxons will rapidly begin to fill the interior ($r < r_o$) of the specimen*. The M-H_o curve should show a discontinuous change in slope at this point and such behaviour is indeed evident in the experimental M-H_o curve of figure 7.3a (curve b - point A). With further increase in H_o, and therefore in the average induction in the

---

* In accordance with the considerations of chapter 6 the first fluxons to penetrate the annular region will move to the middle of the specimen and form a pool of radius $\rho < r_o$. However the pool will expand to $\rho = r_o$ already at a relatively small value of the average induction $\bar{B}$ in the specimen.

specimen, it will be assumed that the fluxons are able to redistribute continuously so that dB/dr is non-zero only in the deformed anulus and since the width Δr, relative to R, and the pinning effectiveness of the deformed annular region are small, that dB/dr may be considered to be independent of r across the region. This behaviour will continue until H_o reaches H_{c2}. Reducing H_o from H_{c2} will cause dB/dr to change sign and eventually at $H_o = 0$ there will be a residual trapped flux in the interior ($r < r_o$) of the specimen. The above assumptions together with the definitions $B_o = B(r > r_o + \Delta r/2)$ and $B_i = B(r < r_o - \Delta r/2)$ then lead to the following results, in the regime where $dB/dr \neq 0$ anywhere in the annular region, viz:

$$\langle dB/dr \rangle = \Delta B/\Delta r = (B_o - B_i)/\Delta r \qquad 7.1$$

and

$$\langle B \rangle = (B_o + B_i)/2 \qquad 7.2$$

where the bras and ketts indicate the average values in the annulus. The problem now is to obtain B_o and B_i in terms of the average measured inductions $B_u(H_o)$ and $B_d(H_o)$, on either the increasing or decreasing branch of the M-H_o curves, for the undeformed and deformed specimens respectively. For the deformed specimens

$$\bar{B}_d = (1/\pi R^2) \int_o^R B(r) d^2R$$

$$= [B_i r_o^2 + B_o(R^2 - r^2)]/R^2$$

$$= B_o - (B_o - B_i)/\rho^2 \qquad 7.3$$

where $\rho = r_o/R$. For the undeformed specimen when $H_o \geq H_{c1}$ (see chapter 6) $\bar{B}_u = B[H_o]$ i.e. $\bar{B}_u$ is uniform over the specimen and is equal to the thermodynamic equilibrium value. It is reasonable to assume that B_o for the deformed specimen, in this field regime, where the magnetic hysteresis is small (see figure 7.3), will tend to

to the equilibrium value $B[H_o]$ since it is apparent that $(B_o - B_i)/B_o << 1$ and in any event variations in B_i only contribute approximately ρ^{-2} (i.e. 0.25 in the present case) times as effectively as B_o to the overall magnetization behaviour. It will therefore be assumed for large $\bar{B}_u$, $(H_o \gtrsim H_{c1})$ that

$$B_o(H_o) = \bar{B}_u(H_o) \qquad 7.4$$

Substituting for B_o into equation 7.3 gives

$$(B_o - B_i) = \Delta B = [\bar{B}_u(H_o) - \bar{B}_d(H_o)]\rho^2 \qquad 7.5$$

The average values for dB/dr and B in the annular region from equations 7.1 and 7.2 respectively may now be expressed in terms of $\bar{B}_u$ and $\bar{B}_D$ for H_o either increasing or decreasing. Thus:

$$\langle dB/dr \rangle = (\bar{B}_u(H_o) - \bar{B}_d(H_o))\rho^2/\Delta r \qquad 7.6$$

and

$$\langle B \rangle = \bar{B}_u(H_o) - (\bar{B}_u(H_o) - (\bar{B}_u(H_o) - \bar{B}_d(H_o))\rho^2/2 \qquad 7.7$$

These expressions are strictly valid (neglecting the geometry and possible surface barrier effects) only in the limit $\Delta B \to 0$ and/or $\Delta r \to 0$. They should nevertheless be a reasonable approximation in the regime $H_o \gtrsim H_{c1}$ where $[\bar{B}_u - \bar{B}_d]$ is small and consequently not accurately obtainable from experiment. For $[\bar{B}_u - \bar{B}_d]$ larger and measurable the use of these expressions to determine P_v in the deformed annulus is not expected to give better than an order of magnitude estimate but is nevertheless expected to give the functional dependences of P_v on B and T with reasonable accuracy. When applied to actual specimens the above treatment is also expected to be more accurate, at low $\bar{B}$, for H_o increasing rather than for H_o decreasing since in the former case the tendency for fluxons to move to the middle of the specimen (see chapter 6) will partly overcome the

small background pinning due to centres not in the annulus and in the latter case this tendency will assist these pinning sites. It has been estimated from the results of chapter 6 that in the region of the deformation the bulk driving force due to the tendency for fluxons to move to the middle of the specimen is of the order 10^3 dynes cm^{-2} in the low $\bar{B}_d$ regime at $T \simeq 4K$. This will later be seen to be nearly two orders of magnitude smaller than the value of P_v determined for the deformed annular region at approximately the same temperature. This justifies the neglect, in the above treatment, of the geometry effect. Since, however the forces due to the geometry effect operate over entire disc their overall effect outside the annular region is appreciable.

7.4 Determination of the bulk pinning force density $P_v(b,t)$

The determination of $P_v(b)$ fo[illegible]e deformed annular region will be confined to $t = T/T_c = 0.435$. $\bar{B}_u(H_o)$ and $\bar{B}_d(H_o)$, H_o increasing, have therefore been measured from the M-H_o curves of figure 7.3a and ΔB and <B> have been calculated from these results using the analysis of the previous section. In figure 7.4 ΔB is shown as a function of <B>. The maximum in $\Delta B(<B>)$ at <B> = 160 gauss corresponds with point A on curve (b) of figure 7.3a and clearly demonstrates the onset of fluxon penetration through the deformed annular region. For <B><160 gauss, H_o increasing, therefore $B_i = 0$ and figure 7.4 shows that $\Delta B \propto <B>$ as expected from equations 7.1 and 7.2 However, disregarding inaccuracies, in the magnitude of ΔB and <B>, which are now obviously significant in this regime, it will be apparent that since the fluxon penetration front does not extend through the entire width Δr of the deformed annular region equations 7.1 and 7.6 are no longer even approximately valid. Δr in these equations should now

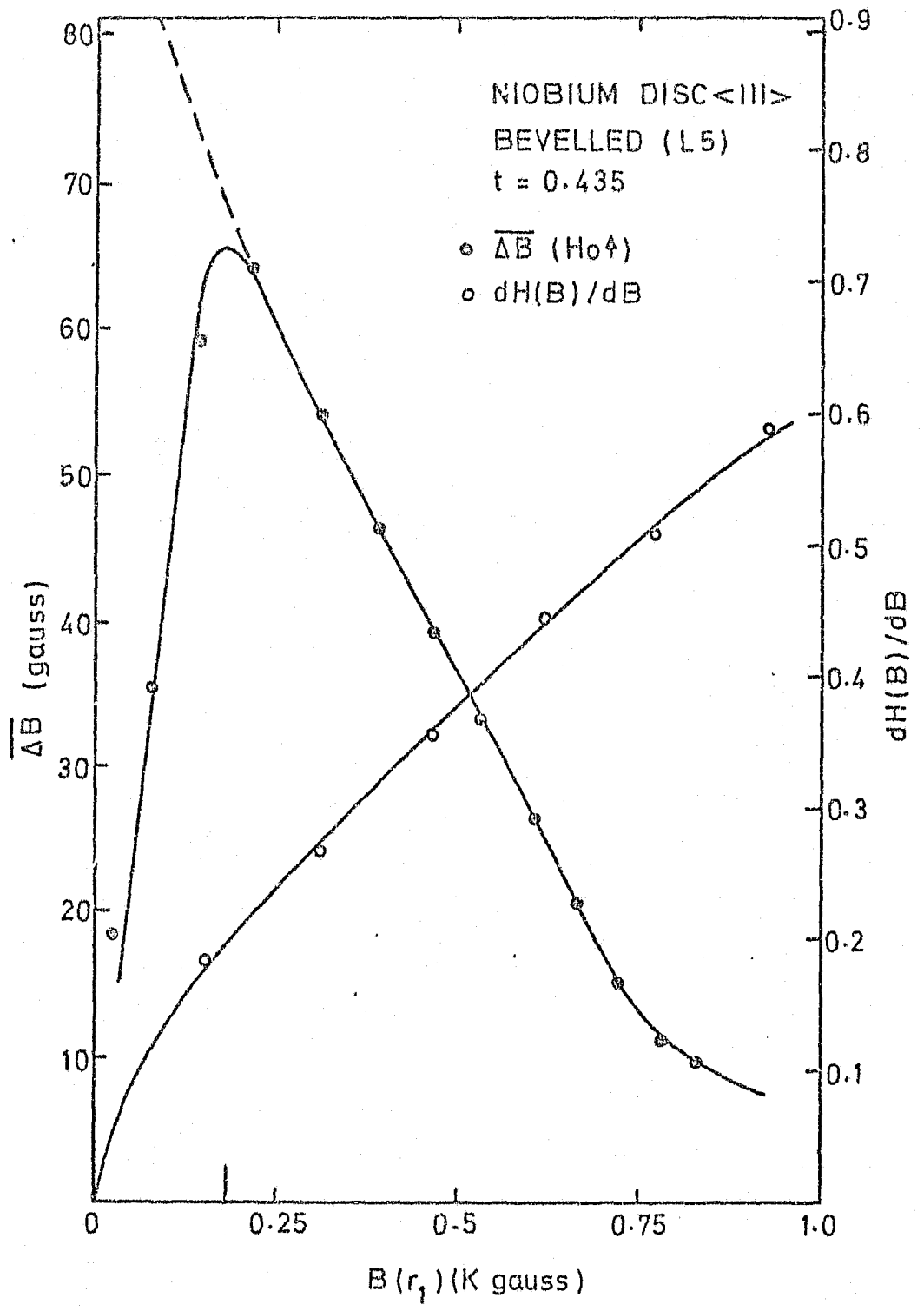


Figure 7.4. The variation with the induction, in the deformed region, of the difference in the induction across the deformed annular region, as determined from the magnetization curves for the deformed and undeformed disc-specimens at $t \simeq 0.435$ and the equilibrium $dH(B)/dB$ as determined from the magnetization curve of figure 7.3b. The behaviour for $B(r_o) < 160$ gauss is explained in the text.

be replaced by the actual field dependent distance over which B is non-zero in the annular region. The calculation of this distance is problematical and for the present purposes it will be sufficient to assume that equation 7.6 will have a limited validity if $\Delta B(\langle B \rangle)$ is taken to be the dashed (see figure 7.4) extrapolation of the behaviour at high <B> into this low <B> regime. Also shown in figure 7.4 is a plot of $dH[B]/dB$ versus <B> as obtained from the reversible curve, for a specimen with D = 0, shown in figure 7.3b. Using the results of figure 7.4 and equation 7.6 for <dB/dr>, with $\Delta r = 0.5$mm (see section 7.2.1), P_v has been determined as a function of $b = \langle B \rangle / B_{c2}$ from equation Ae8 and is plotted against b in figure 7.5 (from figure 7.1 : $B_{c2}(t = 0.435) = 3250$ gauss)

The dependence of P_v on t has been determined for $b = 0.1$. In figure 7.6 values for $-4\pi M$ (H_o increasing) at $b = 0.1$ from the $M\text{-}H_o$ curves for the deformed and undeformed specimens, are shown as a function of temperature. $\Delta B(T)$ as determined from these results is also shown in the figure. Now $dH[B]/dB$ for $b = 0.1$ is almost invariant with temperature and $P_v(t)$ has therefore been calculated using the value of this parameter from figure 7.4. In figure 7.7 $\log P_v(t)$ is shown as a function of $\log B_{c2}(t)$. This plot is characterised by two linear sections with the change in slope occurring at $t = 0.883$ ($B_{c2} = 520$ gauss, $\langle B \rangle = 52$ gauss). For $t < 0.883$: $P_v(t) \propto B_{c2}^{2.3}(t)$ and for $0.883 < t < 1$: $P_v(t) \propto B_{c2}^{1.3}(t)$.

7.5 Discussion and Conclusion

The result obtained for $P_v(b, t < 0.885)$ in the deformed annular region is apparently consistent with the multiple dislocation site dilute-limit model which was formulated in chapter 5. Thus according to the model $P_v(t) \propto B_{c2}^3(t)\kappa_2(t)/\kappa_1^4(t)$ which, for t not

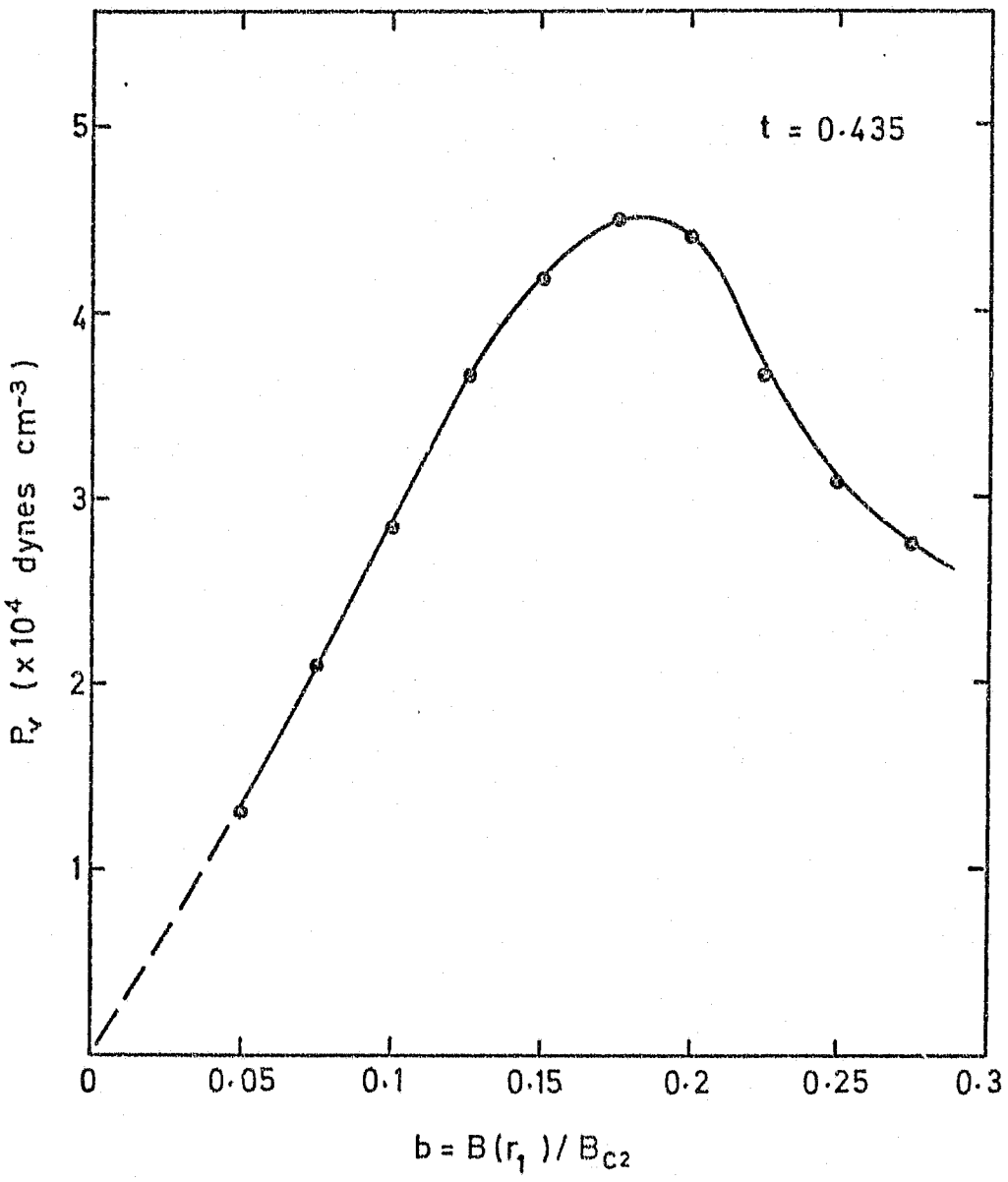


Figure 7.5. The calculated variation in the bulk pinning force density with reduced induction at $t = 0.435$ in the deformed annular region. The maximum in P_v occurs at $b \simeq 0.18$.

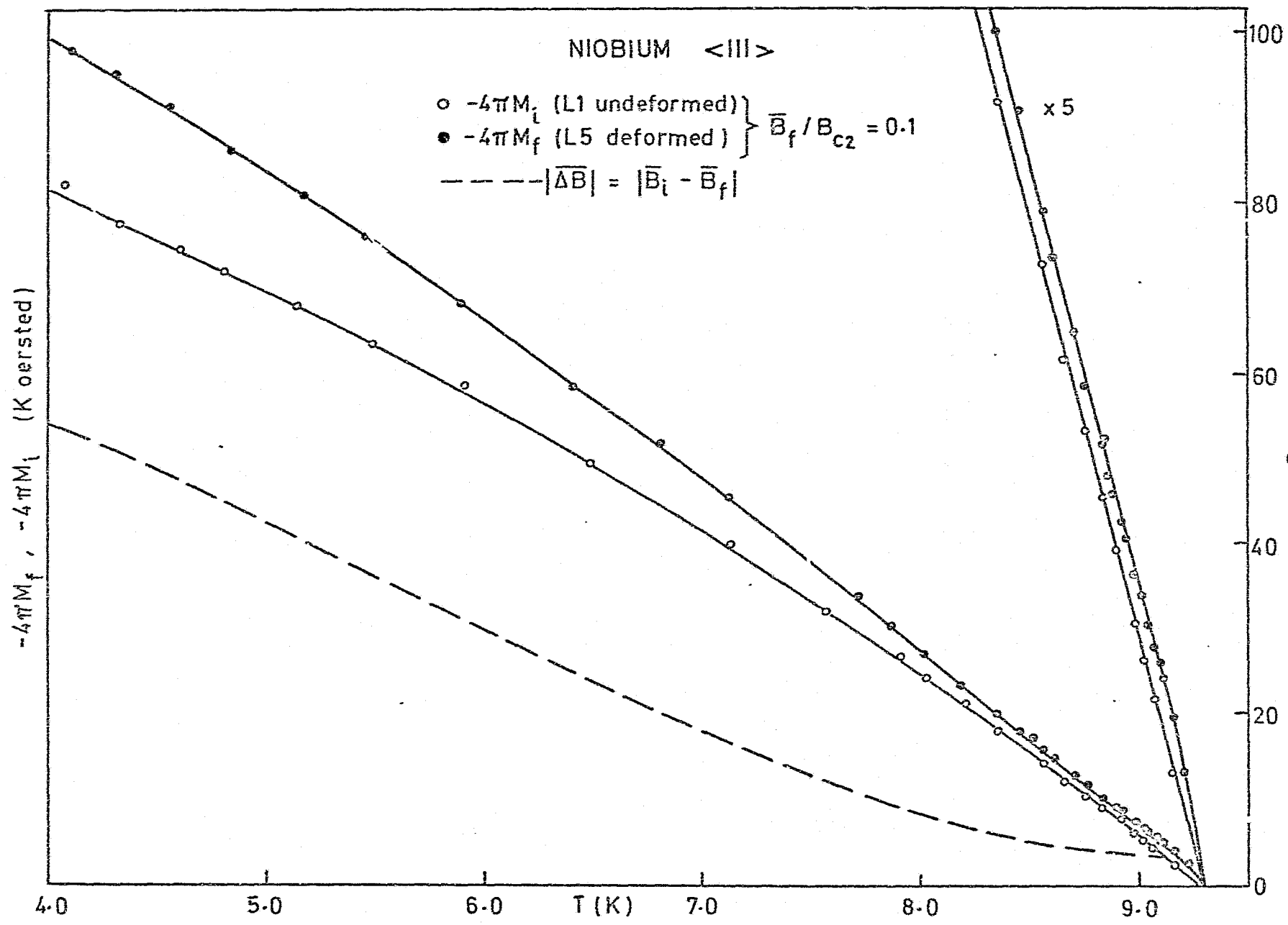


Figure 7.6. The variation with temperature, determined from the magnetization curves of the deformed and undeformed specimens, of the difference in the magnetic moment at constant H_o (and hence in ΔB across the deformed annular region (see text) of radius r_o at such a field that $b(r_o) = 0.1$).

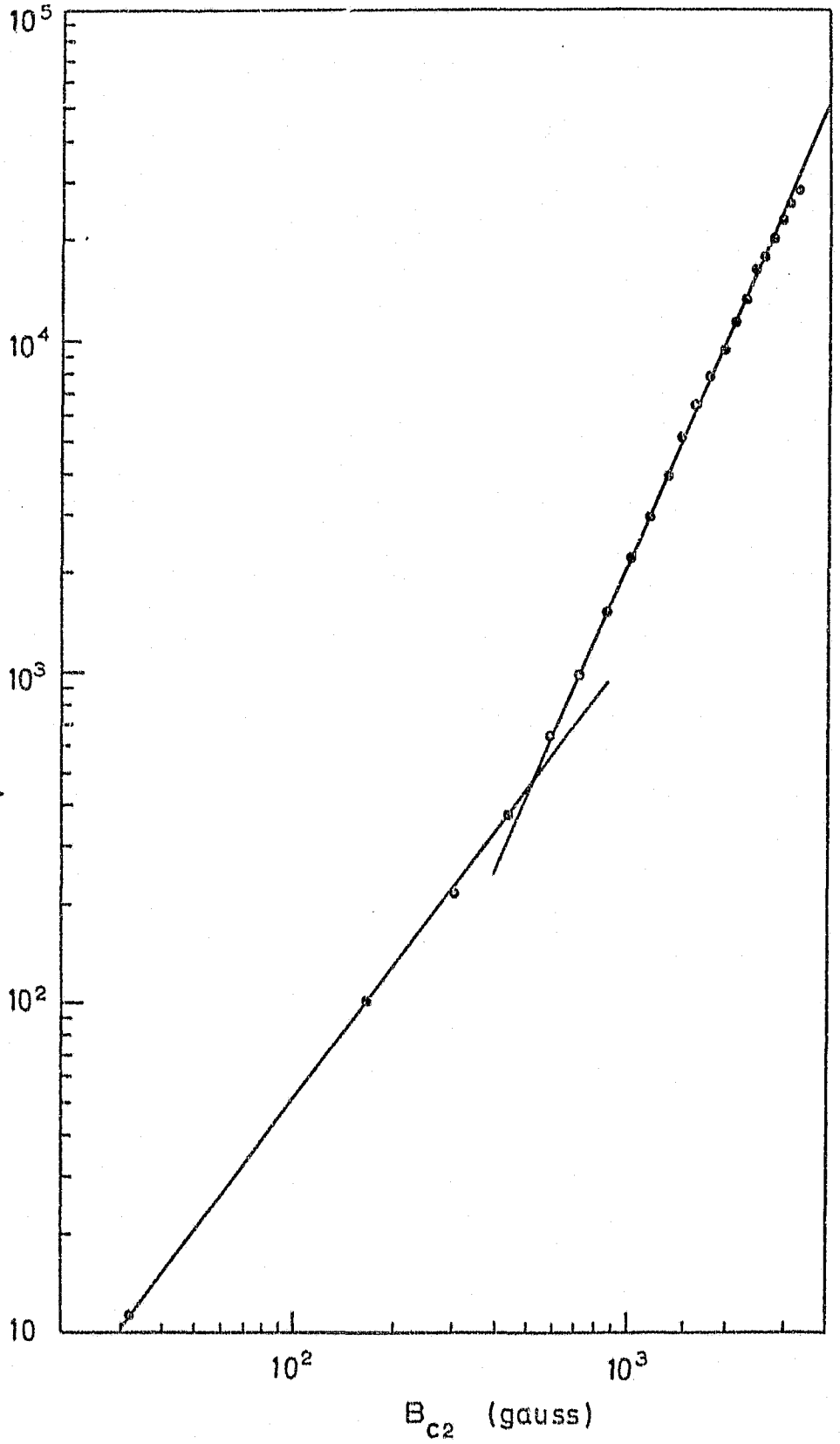


Figure 7.7. A log-log plot of the bulk pinning force density at $b(r_o) = 0.1$ in the deformed annular region versus the upper critical field (induction). The plot shows two linear regions, for $t < 0.885$ $P_v \propto B_{c2}^{2.3}$ and for $t > 0.885$ $P_v(t) \propto B_{c2}^{1.3}$.

close to 1, varies approximately as $B_{c2}^{5/2}(t)$ in approximate agreement with the present findings for $t < 0.885$. The $P_v(b)$ behaviour obtained here (see figure 7.5) is very similar in its limited range, i.e. $0 < b < 0.3$, to the result obtained by Coote (1970 - and see also, Campbell and Evetts 1972) which for $b > 0.4$ was shown in chapter 5 to be consistent with the dilute-limit multiple dislocation site model. In particular the value of b for which $P_v(b)$ is a maximum was found by Coote to be $b \simeq 0.22$ which compares reasonably with $b \simeq 0.18$ in the present investigation.

The transition, in increasing t, from $P_v \propto B_{c2}^{2.3}$ to $P_v \propto B_{c2}^{1.3}$ at $t \simeq 0.89$ is remarkably sharp (see figure 7.7) and is therefore not readily accounted for by any of the mechanisms mentioned in section 5.

APPENDIX 1(a)

The Ginzburg-Landau expression for the free energy

The Ginzburg-Landau expression for the free energy per unit volume in the superconducting state is given (Ginzburg and Landau, 1950) by

$$F_s = F_n + \alpha|\Psi|^2 + \frac{\beta}{2}|\Psi|^4 + \frac{1}{2m^*}\left|\left(-ih\nabla - \frac{e^*}{c}\Lambda\right)\Psi\right|^2 \; ; \; h^2/8\pi \qquad a1$$

where F_n is the free energy in the normal state, α and β are constants of the superconducting material, Ψ is the order parameter or wave function which must be suitably defined, e^* and m^* are the effective charge and mass respectively for the Cooper pairs, $\underline{A}$ is the vector potential ($h = \text{curl } \underline{A}$) and h is the local field.

Minimization by variational calculation of the integral $\int_{\text{specimen}} (F_s - F_n)dv$ with respect to local variations in Ψ or in $\underline{\Lambda}$ gives the two so-called Ginzburg-Landau equations and the following results are obtained from these equations and a1

$$|\Psi_o|^2 = -\alpha/\beta \qquad a2$$

$$H_c^2/8\pi = \alpha^2/2\beta \qquad a3$$

$$\xi^2 = h^2/2m^*\alpha \qquad a4$$

and $$\lambda = [\beta m^* c^2/16\pi e^{*2}\alpha]^{\frac{1}{2}} \qquad a5$$

where ξ is related to the Pippard coherence length and λ is identical with the London penetration length (λ_L) if α/β in equation a5 is replaced by the number of superconducting electrons n_s per unit volume. [A particular normalization for the order parameter $|\Psi|^2 = n_s/n_{TOTAL}$.] The so-called Ginzburg-Landau parameter is defined as

$$\kappa = \lambda/\xi \qquad a6$$

APPENDIX 1(b)

The relationship between the stress tensor in cartesian and cylindrical co-ordinates

In cartesian co-ordinates: The stresses, in terms of a stress function ϕ which is invarient along the z axis, are given (see for example Jaeger, 1956) by

$\sigma_{xx} = \partial^2\phi/\partial y^2$, $\sigma_{yy} = \partial^2\phi/\partial x^2$ and $\sigma_{xy} = -\partial^2\phi/\partial x\partial y$.

In cylindrical o-ordinates: The stresses, again in terms of the stress function ϕ, are given by

$$\sigma_{rr} = \frac{1}{r}(\partial\phi/\partial r) + \frac{1}{r^2}(\partial^2\phi/\partial\theta^2)$$

$$\sigma_{\theta\theta} = \partial^2\phi/\partial r^2$$

and $\sigma_{r\theta} = \tau_{r\theta} = \frac{1}{r^2}(\partial\phi/\partial\theta) - \frac{1}{r}(\partial^2\phi/\partial r\partial\theta) = -\frac{\partial}{\partial r}(\frac{1}{r}\partial\phi/\partial\theta)$

The relationship between the stresses in cartesian and cylindrical co-ordinates, with r in the x-y plane and $\theta = 0$ along the x axis, are given by the following simple geometrical identities:

$$\sigma_{xx} = \sigma_{\theta\theta}\cos^2\theta + \sigma_{rr}\sin^2\theta + 2\tau_{r\theta}\sin\theta\cos\theta$$

$$\sigma_{yy} = \sigma_{\theta\theta}\sin^2\theta + \sigma_{rr}\cos^2\theta - 2\tau_{r\theta}\sin\theta\cos\theta$$

and $\sigma_{xy} = \sigma_{\theta\theta}\cos\theta\sin\theta - \sigma_{rr}\cos\theta\sin\theta + \tau_{r\theta}\sin^2\theta$.

APPENDIX 1(c)

The second-order elastic interaction between the fluxon lattice and a perpendicular screw dislocation

The effective second-order interaction force for fluxon collinear with the z direction in cartesian co-ordinates is given according to equation 3.3.6 by

$$f_m(t) = (\sqrt{2}\, H_{c2}(t)/\kappa_1(t) h_c(0)\ (\underline{i}\frac{\partial}{\partial x} + \underline{j}\frac{\partial}{\partial y}) \iiint (n_v^2 \delta C_B(0) \times (n_{xz}^2 + n_{xy}^2)\delta C_{44}(0) |\psi_o|^2 dxdydz]_{max} \qquad c1$$

For a screw dislocation, along the x direction at $y = y_o$ and $z = 0$ in an isotropic crystal, the displacements u, v and w (collinear with the x, y, and z axis respectively) are given by

$$u = (b_o/2\pi)\tan^{-1}[(y - y_o)/z|$$

$$v = 0$$

$$w = 0$$

where b_o is the Burgers vector. The non-vanishing components of the resulting stress are given by

$$\eta_{xy} = \mu(\partial v/\partial x + \partial u/\partial y) = (\mu b_o/2\pi) z/[(y - y_c)^2 + z^2] \qquad c2$$

and

$$\eta_{xz} = \mu(\partial w/\partial x + \partial u/\partial z) = -(\mu b_o/2\pi)(y - y_o)/[(y - y_o)^2 + z^2] \qquad c3$$

where $\mu = C_{44}$ is the shear modulus.

Substituting for η_{xy}, η_{xz} and $|\psi_o|^2$ from equation c2, c3 and 3.9 respectively into equation c1 gives the pinning force per unit length of dislocation as

$$\underline{p}_m^{\ell} = \underline{j}A\left[\partial/\partial y_o \int_{-a_o/2-\infty}^{+a_0/2+\infty}\int_{-\infty}^{+\infty}\left[z^2 + (y - y_o)^2\right]^{-1}\left[1 - 1/3(\cos\{2\pi(x + y/\sqrt{3})\}\right.\right.$$

$$\left.\left. + \cos\{2\pi(2y/\sqrt{3})/a_o\} + \cos\{2\pi(x - y)\sqrt{3})/a_o\}\right]dxdydz\right]_{max} \qquad c4$$

where

$$A = (C_{44}\ b_o/2\pi)^2\left[\sqrt{2}H_{c2}(t)/\kappa_1(t).H_c(0)\right]\delta C_{44}(0)(1 - b)/a_o$$

Integrating:

$$p_m^{\ell} = A\left[\partial/\partial y_o \int_{-\infty}^{+\infty}\int_{-\infty}^{+\infty}\left[z^2 + (y - y_o)^2\right]^{-1}\left[x - \frac{a_o}{6\pi}\sin\{2\pi(x + y/\sqrt{3})/a_o\}\right.\right.$$

$$\left.\left. - \frac{x}{3}\cos\{\frac{2\pi}{a_o}(2y/\sqrt{3})\} - \frac{a_o}{6\pi}\sin\{2\pi(x - y/\sqrt{3})\}\right]_{-a_o/2}^{+a_o/2}dydz\right]_{max}$$

$$= A\left[\partial/\partial y_o \int_{-\infty}^{+\infty}\int_{-\infty}^{+\infty}\left[z^2 \quad y - y_o)^2\right]^{-1}\left[a_o(1 - \frac{1}{3}\cos\{\frac{2\pi}{a_o}(2y/\sqrt{3})\}\right]dydz\right]_{max}$$

$$= Aa_o\left[\partial/\partial y_o \int_{-\infty}^{+\infty}\left[\pi/(y - y_o)\right]\left[1 - \frac{1}{3}\cos\{\frac{2\pi}{a_o}\,2y/\sqrt{3}\}\right]dy\right]_{max}$$

Now putting

$\alpha = 4\pi/a_o\sqrt{3}$ and $(y - y_o) = y_1$ so that $dy = dy_1$ gives

$$p_m^{\ell} = Aa_o\left[\partial/\partial y_o \int_{-\infty}^{+\infty}(\pi/y_1)\left[1 - \frac{1}{3}\cos\{\alpha(y_1 + y_o)\}\right]dy_1\right]_{max}$$

$$= Aa_o\left[\partial/\partial y_o\left(\pi\int_{-\infty}^{+\infty}dy_1/y_1 - \frac{1}{3}\cos(\alpha y_o)\int_{-\infty}^{+\infty}\frac{\cos(\alpha y_1)}{y_1}\,dy_1\right.\right.$$

$$\left.\left. - \frac{1}{3}\sin(\alpha y_o)\int_{-\infty}^{+\infty}\frac{\sin(-\alpha y_1)}{y_1}\,dy_1\right]\right]_{max}$$

$$p_m^{\ell} = -Aa_o\left[\partial/\partial y_o\left(\frac{\pi}{3}\sin(\alpha y_o)\right)\right]_{max}$$

$$= -A\,(4\pi^2(3\sqrt{3}) \quad \text{for } y_o = a_o\sqrt{3}/4 \qquad \text{c5}$$

Substituting for A from equation c5 with

$$p_m^{\ell} = (1/3\sqrt{3})\left[C_{44}b_o\right]^2\left[\sqrt{2}\,H_{c2}(t)/\kappa_1(t)H_c(0)\right]\delta C_{44}(0)\times$$

$$(1 - b)\,b^{\frac{1}{2}}.(B_{c2}/\phi_o)^{\frac{1}{2}} \qquad \text{c6a}$$

or

$$p_m^{\ell}(t, b) \propto \left[B_{c2}^{3/2}(t)/\kappa_1(t)\right].\,b^{\frac{1}{2}}(1 - b) \qquad \text{c6b}$$

APPENDIX 1(d)

The elastic properties of the fluxon lattice

The mutual interactions between the discrete fluxons in a hexagonal lattice gives rise to an elastic behaviour which is isotropic in the basal plane. In the equations which are given below anisotropy in κ_1 and κ_2 for the superconducting matrix are ignored.

Early calculations on the elastic constants of the fluxon lattice were made by Silcox and Rollins (1963) and Friedel, de Gennes and Matricon (1963). More recently Labusch (1968, 1969a) has derived all the elastic constants in terms of parameters which can be experimentally obtained from the reversible magnetization curve ($M - H_o$) for a very long specimen in longitudinal applied field H_o.

The non vanishing component of the elastic moduli C_{ij} are C_{11}, C_{12}, C_{44} and C_{66} with the condition $2C_{66} = C_{11} - C_{12}$. According to Labusch*

$$C_{11} = (1/4\pi)B^2(\partial H[B]/\partial B) + C_{66} \qquad d1$$

$$C_{44} = (1/4\pi)B\ H[B] \qquad d2$$

$$C_{66} = (1/8\pi)\int_0^B B_1^2(\partial^2 H[B_1]/\partial B_1^2)dB_1 \qquad d3a$$

for $b = B/B_{c2} \geq 0$ and

---

* The expression for C_{66} (equation d3b) is usually expressed in terms of some unspecified κ. The approximate Maki parameters (i.e. κ_1 and κ_2) have however been substituted because of their relatively stronger temperature dependences in low κ materials (e.g. niobium).

$$C_{66} = (1/4\pi)H_c^2[\kappa_1^2(2\kappa_2^2 - 1)/[1 + (2\kappa_2^2 - 1)\beta_A]]0.48(1-b)^2 \qquad d3b$$

for $b \lesssim 1$,

where $\beta_A = 1.14$ for a triangular fluxon array and $H[B]$ is the value of H in equilibrium with B (for a long specimen $H[B] = H_o(B)$). Equation d3b for C66 is expected to be reasonably accurage in the regime of b for which there is some fluxon core overlap. For niobium this is $b \gtrsim 0.4$ (see for example Freyhardt, 1971 and also section 3.2.1).

The effective modulus for the fluxon lattice response to a point like force is given (Labusch, 1969b) by

$$C_e^p = (1/\beta\pi^{\frac{1}{2}})[(C_{44}C_{11})^{-\frac{1}{2}} + (C_{44}C_{66})^{-\frac{1}{2}}]^{-1} \qquad d4a$$

where $\beta = 1.07$.

Values for κ_1 and κ_2 as functions of the reduced temperature t in niobium are obtainable from the results of chapter 5. In table A1 values for κ_1, κ_2 $H[B]/B$, $\partial H[B]/\partial B$ and C_{11}, C_{44} and C_{66} from equation d1, d2, d3b, and d4a respectively are given for niobium at $T = 4.05K$ for various values of b in the range $0.4 < b < 1$. C_{11}, C_{44} and C_{66} are also shown as functions of b in figure A1.1. It is apparent that $C_{66} << C_{44}$ and therefore equation d4a for C_e^p may be expressed more simply as

$$C_e^p = (1/\beta\pi^{\frac{1}{2}}).(C_{44}C_{66})^{\frac{1}{2}} \qquad d4b$$

Also since C_{66} (equation d3b) may be expressed approximately by $C_{66} \propto B_{c2}^2(1 - b)^2/\kappa_2^2$ and C_{44} (equation d2) by $C_{44} \propto b^2B_{c2}^2$ the variation of C_e^p with t and b is given approximately by

$$C_e^p \propto [B_{c2}^2(t)/\kappa_2(t)]\, b.(1 - b) \qquad d5$$

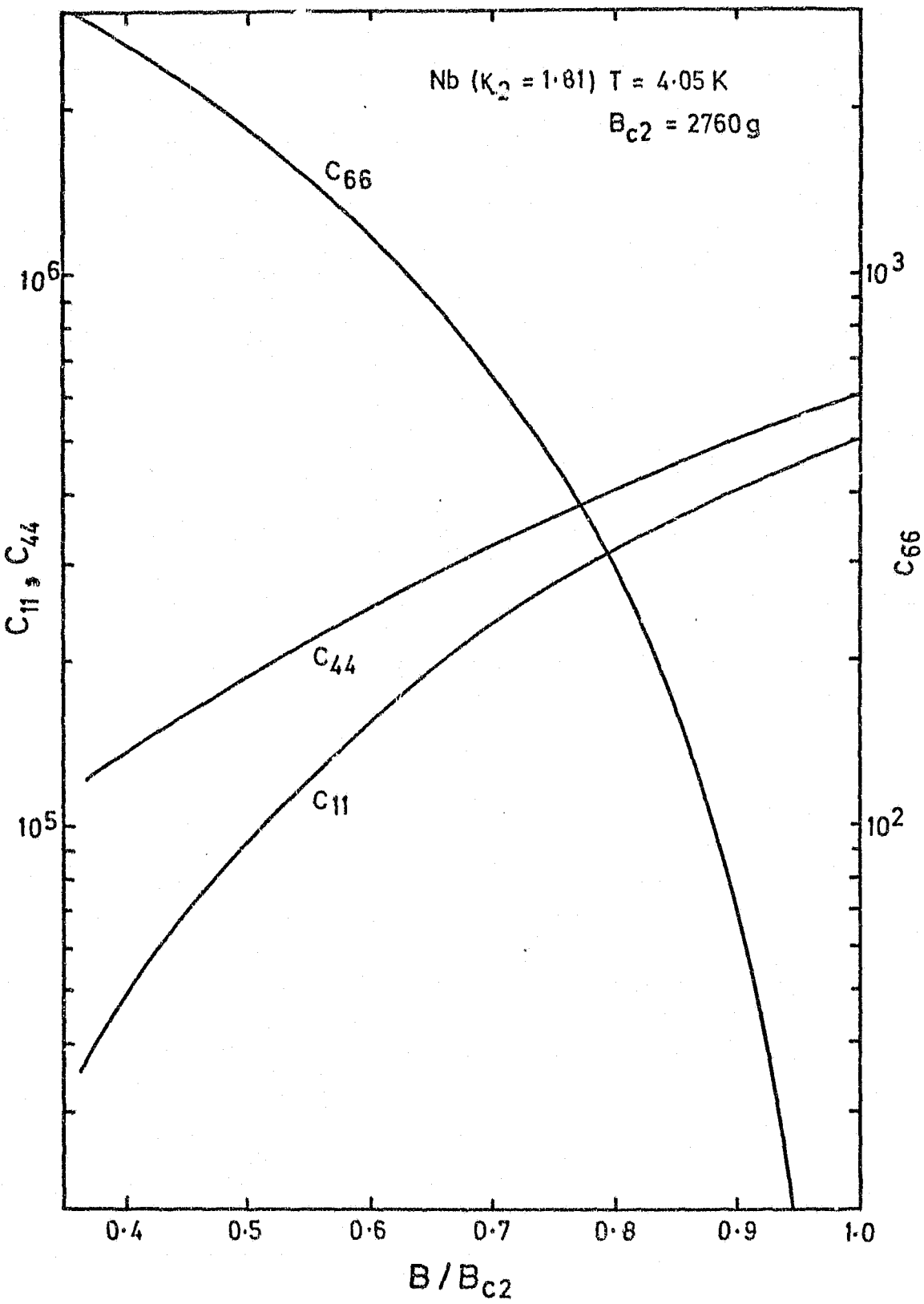


Figure A1.1. The experimentally determined variation of C_{11}, C_{44}, and C_{66} with reduced induction in the range $0.35 < b < 1.0$.

TABLE A.1

Nb [001], T = 4.05K, $B_{c2}(4.05)$ = 2760 gauss, $\kappa_2(4.05)$ = 1.81

b	$\frac{\partial H_e(B)}{\partial B}$	$\frac{H_e(B)}{B}$	C_{11}	C_{44}	C_{66}	$C_{44}^{-\frac{1}{2}}[C_{66}^{-\frac{1}{2}} + C_{11}^{-\frac{1}{2}}]$
0.4	0.48	1.40	$0.49.10^5$	$1.35.10^5$	$2.62.10^3$	$6.53.10^{-5}$
0.45	0.55	1.29	0.70	1.59	2.20	6.30
0.5	0.62	1.23	0.95	1.86	1.82	6.17
0.55	0.67	1.17	1.24	2.15	1.47	6.24
0.6	0.70	1.13	1.54	2.47	1.16	6.39
0.65	0.73	1.10	1.88	2.83	0.89	6.73
0.7	0.78	1.08	2.32	3.20	0.66	7.29
0.75	0.80	1.05	2.73	3.60	0.46	8.15
0.80	0.81	1.04	3.15	4.04	0.29	9.48
0.85	0.82	1.03	3.59	4.50	0.16	11.89
0.9	0.83	1.02	4.06	5.01	0.07	16.72
0.95	0.83	1.01	4.54	5.49	0.02	32.02

APPENDIX 1(e)

Analysis of the experimental magnetization curves for the determination of $P_v(B,T)$

The method which will be employed here is based on that of Fietz and Webb (1969) and is applicable to a long cylindrical specimen in a longitudinal applied field (H_o).

It will be apparent from the considerations of chapter 6 that the specimens of chapter 5, which for the present purposes may be considered to be cylindrical (see Campbell and Evetts, 1972, p. 270) with $d/R = 12$ where d the length and R is half the side of the square cross section, may be considered to behave, to good approximation, like infinitely long specimens. The experimental results of chapter 5 on the undeformed specimens are in reasonable agreement with this conclusion.

For a specimen with reversible magnetization behaviour therefore (see section 6.3.1).

$$B[H_o] = H_o + 4\pi M[H_o] \qquad e.1$$

everywhere in the bulk of the specimen.

If the magnetization is not reversible B and M will not be uniform in the specimen. However, in the absence of barrier effects in the surface parallel to H_o, it is usual to assume that the value of the induction B just inside the surface is in equilibrium with H_o, i.e. $B[H_o]$ (see section 6.3.1). Since no such barrier effects were detectable in the specimens of chapter 5 the analysis according to

Fietz and Webb (loc. cit.) should be applicable here.

Thus: Using the boundary condition $B = B[H_o]$ in the surface and critical state model (see section 3.1) Fietz and Webb relate the average magnetic moment $\tilde{M}$ of the specimen to a critical current $J_c(B[H_o])$ evaluated near the surface. Thus consider a specimen, initially in the Meissner state ($\bar{B} = 0$), in increasing H_o. When H_o has reached some value H_o^1 such that $H_{c1} \leq H_o^1 < H_{c2}$ flux will have penetrated into the specimen and $B(r = R) = B[H_o^1]$ and $B(r)$ will be a smoothly varying single valued function of r as shown schematically by curve $B_-(r)$ in figure A.1.2(a). If H_o is now increased so that $H_o > H_{c2}$ and then decreased again to $H_o = H_o^1$ the resulting distribution of B in the specimen will be as shown schematically by curve $B_+(r)$ in the figure. Associated with the finite gradient dB/dr in the specimen in increasing and decreasing H_o are critical currents $J_-(r)$ and $J_+(r)$ respectively which have a parametric dependence on $B[H_o^1]$ in the surface.

Fietz and Webb expand J_- and J_+ in a Taylor series about the point $r = R$ and then integrate to obtain $B_-(r)$ and $B_+(r)$ respectively. The average magnetization $\bar{M}$ in the specimen is then obtained from the integral equation

$$4\pi\bar{M}(H_o) = \frac{2}{R^2}\int_o^R [B(r) - H_o]rdr \qquad \text{e.2}$$

The final results are then expressed by

$$4\pi(\bar{M}_+ - \bar{M}_-) = 2kJ_+R/3 + 4kJ_+'''R^3/5! + \ldots \qquad \text{e.3}$$

$$4\pi(\bar{M}_+ + \bar{M}_-) = 2(4\pi M[H_o]) - kJ_+'R^2/3! + \ldots \qquad \text{e.4}$$

where $k = 4\pi/10$ and the derivatives of J are to be evaluated at $r = R$. For H_o not close to H_{c1} so that B is not small the series

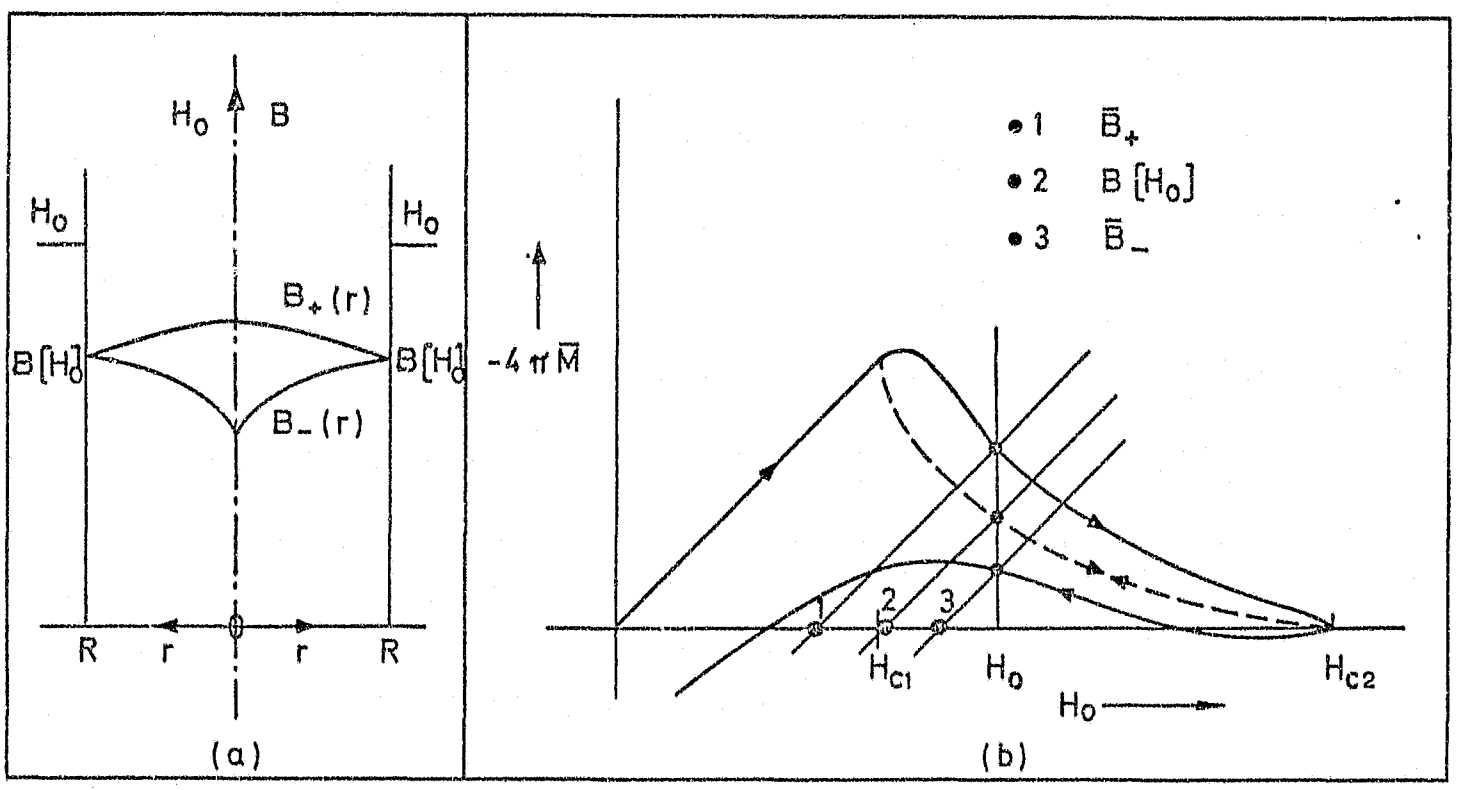


Figure A1.2a. Schematic representation of the distribution of the induction inside a long superconducting specimen in longitudinal field.

Figure A1.2b Schematic representation of the magnetization curve for a deformed specimen showing the method for obtaining the average induction in increasing and decreasing applied field.

in equations e.3 and e.4 converge rapidly and the results are more conveniently expressed by

$$\bar{B}_+ - \bar{B}_- \simeq 2kJ_cR/3 \qquad e.5$$

and

$$\bar{B}_+ + B_- \simeq 2B[H_o] \qquad e.6$$

where $\bar{B}$ is the average specimen induction (in gauss) and $J_c = J_+$ is the critical current (in amps. cm^{-2}) corresponding to $B = B[H_o]$. When B is small equation e.6 becomes inaccurate much faster than does equation e.5 and $B[H_o]$ is preferably obtained from the magnetization curve for a reversible specimen. (In the present investigation the magnetization curves for the undeformed specimens were used.)

The bulk pinning force density $P_v(B,T)$ is given (see section 3.1) by

$$P_v(B,T) = -(1/4\pi)\underline{B} \times \nabla \times \underline{H} \qquad e.7$$

which in the present case may be expressed as

$$P_v(B,T) = (J_c.B[H_o]/10).dH_o[B]/dB \qquad e.8$$

in practical units (amps cm^{-2} and gauss). $B[H_o]$ and dB/dH_o have been determined from the magnetization curves for the undeformed [001] rod specimen. These are shown in figures A.1.3 and A.1.4 respectively as functions of temperature for values of H_o and the reduced induction $b = B/B_{c2}$ in the range $0.3 \leq b \leq 0.95$ respectively. $J_c(B,T)$ was then obtained from the magnetization curves (see figure A.1.2.(b)) using the analysis outlined above and $P_v(B,T)$ was then finally obtained using equation e.8.

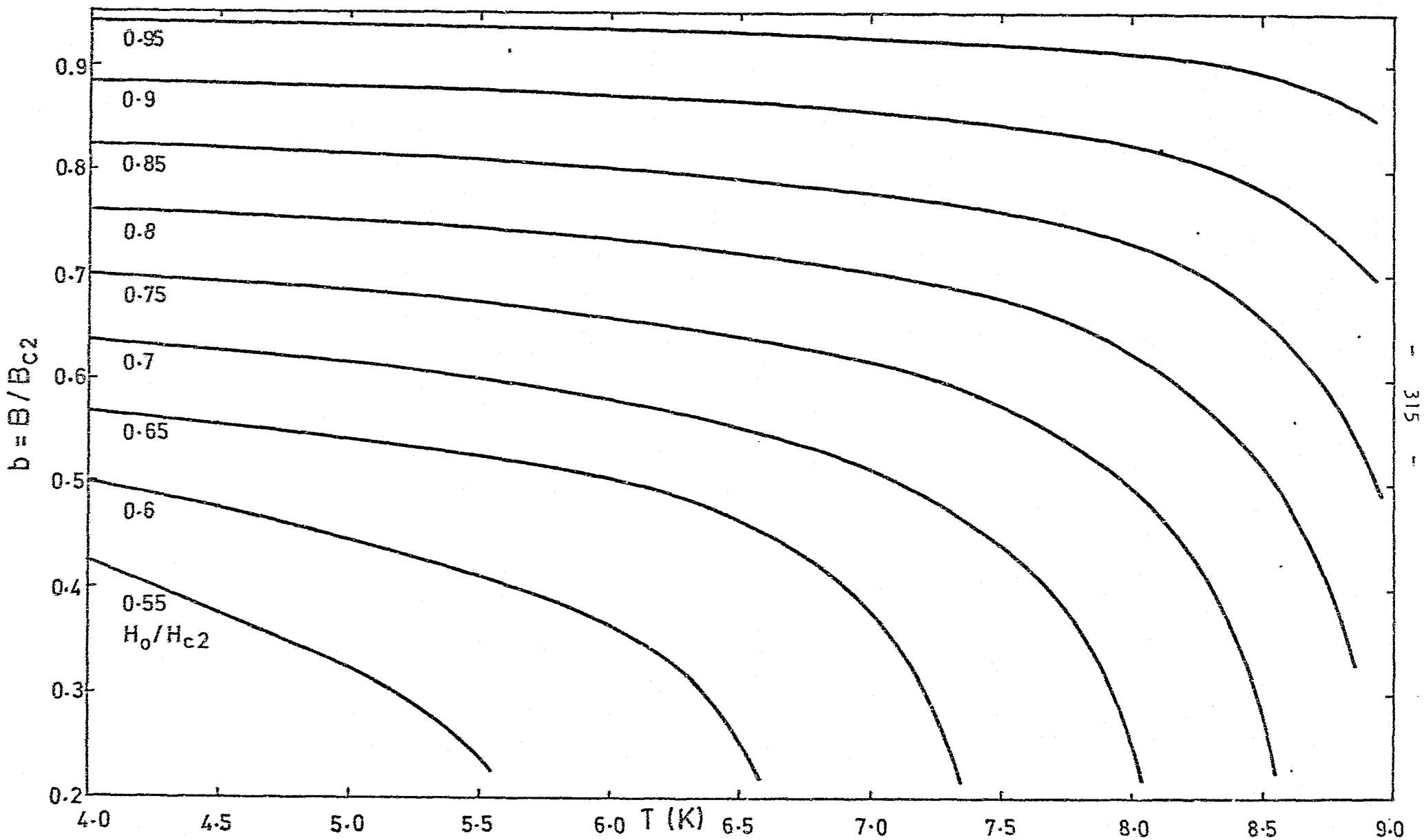


Figure A1.3. The variation of the reduced induction with temperature for various values of the reduced applied field H_o/H_{c2} in the range $0.55 < H_o/H_{c2} < 0.95$.

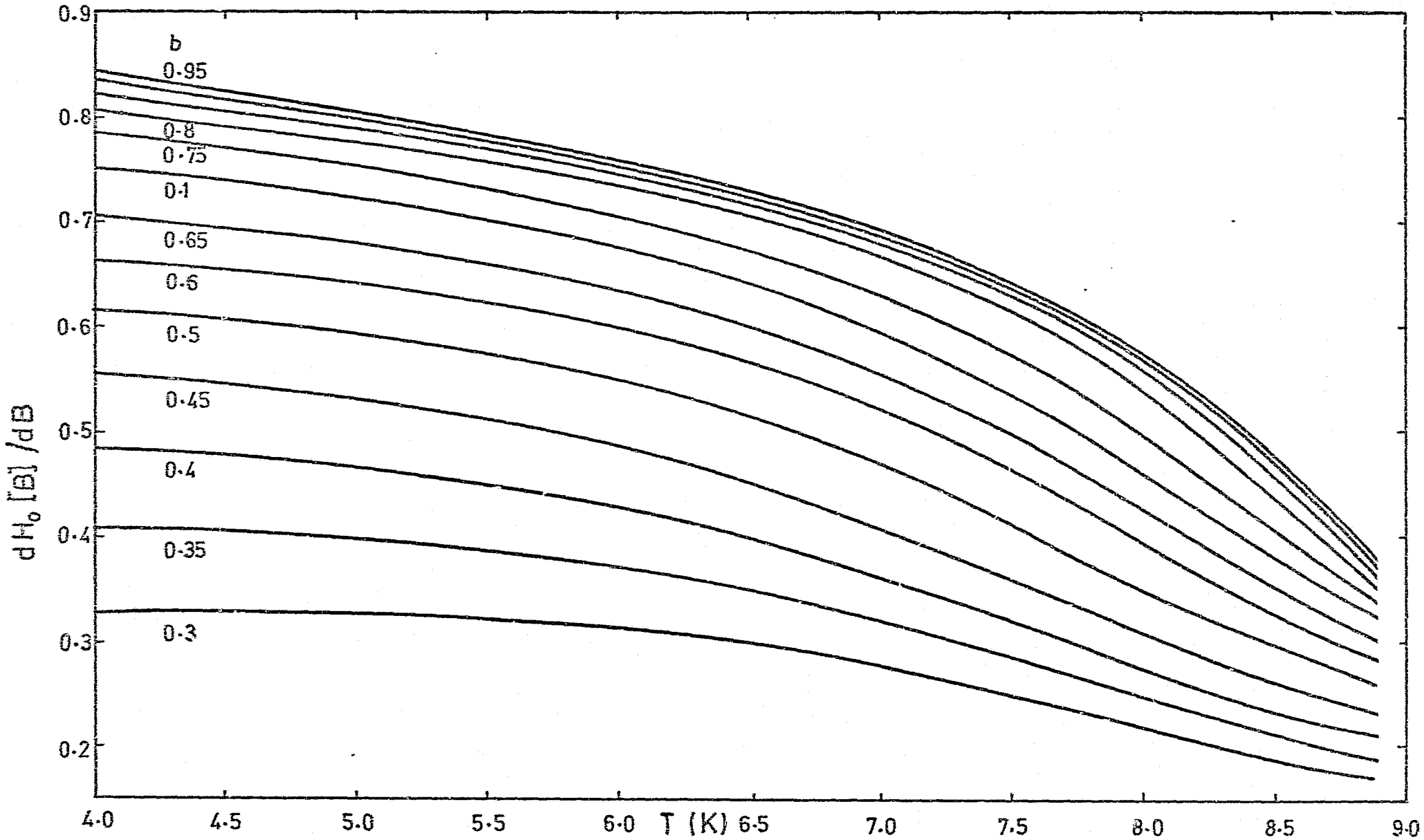


Figure A1.4. The variation with temperature of the equilibrium value of dH/dB for various values of the reduced induction in the range $0.3 < b < 0.95$.

APPENDIX 1(f)

The magnetic moment of a fluxon

By definition, for a current density j(r), the magnetic moment m is given by

$$m = \frac{1}{2c} \times \int_{\text{all space}} [\underline{r} \times \underline{j}(r)]\, d^3r$$

For a fluxon of length d, substituting $\underline{j}(r) = (c/4\pi)[\nabla \times \underline{H}]$ gives

$$m = (d/4\pi)\int_0^\infty\int_0^\infty [\underline{r} \times (\nabla \times \underline{H})]d^2r$$

$$= (d/4\pi)2\pi\int_0^\infty [\cancel{\nabla(\underline{H}.\underline{r})}^{0} - (\underline{r}.\nabla)\underline{H} - (\underline{H}.\nabla)\underline{r} - \underline{H} \times \cancel{(\nabla \times \underline{r})}^{0}]\, rdr$$

$$= (d/4\pi)2\pi\int_0^\infty [-\underline{r}\partial H/\partial r - \underline{H}]rdr$$

$$= -(d/4\pi)2\pi\int_{r=0}^\infty \underline{r}d(r\underline{H}) = -(d/4\pi)2\pi\left| \underline{r}.r\underline{H} - \int r\underline{H}.dr \right|_{r=0}^\infty$$

$$= -(d/4\pi)2\pi\int_0^\infty r\underline{H}dr \quad \text{and finally}$$

$m = \phi_o d/4\pi$ for any reasonable H(r) which is quantized.

This expression for m is only valid if the fluxon is collinear with the long axis of the needle shaped specimen (length d, radius R) in the limit $d/R \to \infty$ (and therefore $D \to 0$ where D is the demagnetizing coefficient for the specimen). For finite d/R the return paths, for

the flux outside the fluxon, which are constrained by the boundary conditions for the superconductor, to be outside of the superconductor, are now different from the usual dipole configuration. This has the effect of enhancing the magnetic moment. For the limit $d/R \to 0$ Pearl (1965) gives $m \approx \phi_o R/4\pi$.

APPENDIX 1(g)

Proof of the exact equivalence of:

$$A = \int_o^R \psi_o(\underline{r}_1)[\gamma(z, |\underline{r} - \underline{r}_1|) + \gamma(d - z, |\underline{r} - \underline{r}_1|)]d^2r_1$$

and

$$B = \int_o^R \int_o^R \psi(|\underline{r}_1 - \underline{r}'|)[\gamma(z, |\underline{r}_2 - \underline{r}_1|) + \gamma(d - z, |\underline{r}_2 - \underline{r}_1|)]d^2r_1 d^2r_2$$

where

$$\psi_o(r') = \int_o^R \psi(|\underline{r}'' - \underline{r}'|)d^2r''$$

Thus: Substituting for ψ_o above into the expression for A and integrating with respect to d^2r over the same limits gives

$$\int_o^R Ad^2r = \int_o^R \int_o^R \int_o^R \psi(|\underline{r}_1 - \underline{r}_2|)[\gamma(z, |\underline{r} - \underline{r}_1|) + \gamma(d - z, |\underline{r} - \underline{r}_1|)]d^2r_1 d^2r_2 d^2r$$

which is symmetrical in the 'subscripted' variables r_i (which can therefor be freely interchanged) and consequently it is easily seen that

$$\int_o^R Ad^2r = \int_o^R Bd^2r$$

Now since R can have any value

$$A \equiv B$$

[Sincere thanks are due to Dr A.G. Every of this department for suggesting this elegantly simple proof.]

APPENDIX A1(h)

An approximate calculation of the interaction force on the fluxon lattice as a function of the dimensions of a spherical or cylindrical region of uniform potential density

The final expressions of chapter 3 for the basic pinning force p_m due to regions, in which either the Ginzburg-Landau parameter κ or the elastic constants C_{ij} for the crystal are different from their values in the surrounding matrix, are valid only if the dimensions of these regions, normal to the fluxons, is small with respect to the range of variation in the order parameter $|\psi|^2$. This is a consequence of the assumption in the formulation of these expressions that, for example,

$\left[\frac{\partial}{\partial r}\int \delta\kappa[|\psi|^2 - |\psi|^4]d^3r\right]_{max}$ could be approximated by $V\delta\kappa\left[\frac{\partial}{\partial r}[|\psi|^2 - |\psi|^4]\right]_{max}$

where $\delta\kappa$ is the difference in κ between the region and the surrounding matrix and V is the volume of the region.

In this appendix an approximate calculation will be made to generalize the above mentioned expressions for p_m to arbitrarily large dimensions. It will be assumed in the calculation that the potential density Ω within the site (for a given $\delta\kappa$ or δC_{ij}) is size invariant. [However, as discussed in chapter 4 the effective minimum dimension for a region of non-zero potential can never be less than the coherence length $\xi(t)$. The treatment given here is therefore valid only for sites with diameters (normal to the fluxons) $2R > \xi(t)$. For $2R < \xi(t)$ the effective potential density (for a given $\delta\kappa$ or δC_{ij} in the

region) is assumed to be given by $\Omega(R^2/4\xi^2(t))$.]

(i) Spherical sites

The co-ordinate system which will be used here is as shown in figure 3.2. The spatial variation of the pinning potential density for a spherical site of radius R situated at $x = z = 0$ and $y = y_o$ is chosen, for convenience, to be given by the gaussian function*

$$g(x,y,z) = \Omega \exp - [(x^2 + (y - y_o)^2 + z^2)/R^2]. \qquad h1$$

The spatial variation of the order parameter $|\psi|^2$ for the fluxon lattice may be taken, to fair approximation for $b = B/B_{c2} > 0.5$, to be given, neglecting any be dependence, by

$$\Psi(x,y) = 1 - \frac{1}{3}\left[\cos \frac{2\pi}{a_o}(x+y)\sqrt{3} + \cos \frac{2\pi}{a_o}(2y/\sqrt{3}) + \cos \frac{2\pi}{a_o}(x-y/\sqrt{3})\right] \qquad h2$$

(This will also be a reasonable approximation for the spatial variation of $|\psi|^2 - |\psi|^4$, for $b > 0.5$ but see later.)

The interaction energy is therefore

$$I = \int_{-\infty}^{\infty}\int_{-\infty}^{\infty}\int_{-\infty}^{\infty} g(x,y,z)\Psi(x,y)\,dx\,dy\,dz \qquad h3$$

Using the formula $\cos\theta = \frac{1}{2}(e^{i\theta} + e^{-i\theta})$ and substituting from equations h1 and h2 into equation h3 gives

$$I = \Omega \int_{-\infty}^{\infty}\int_{-\infty}^{\infty}\int_{-\infty}^{\infty}\left[1 - \frac{1}{6}(e^{i\theta_1} + e^{i\theta_2} + e^{i\theta_3})e^{\theta_4} + C.C.\right]\right] dx\,dy\,dz \qquad h4$$

where $\theta_1 = \gamma(x + y/\sqrt{3})$, $\theta_2 = \gamma(2y/\sqrt{3})$, $\theta_3 = \gamma(x - y/\sqrt{3})$,

$\theta_4 = -\left[(x^2 + (y - y_o)^2 + z^2)/R^2\right]$ and $\gamma = 2\pi/a_o$

---

* Sincere thanks are again due to Dr A.G. Every for suggesting the use of a gaussian function therefore also the method of integration.

The interaction force along the y axis is therefore

$$F_y = dI/dy_o = (\Omega/6)\frac{d}{dy_o}\left[\sum_{i=1}^{3}\int_{-\infty}^{\infty}\int_{-\infty}^{\infty}\int_{-\infty}^{\infty}(e^{i\theta_i}\, e^{\theta_4} + C.C.)dxdydz\right.$$

$$= (\Omega/6)\frac{d}{dy_o}\left[\sum_{i=1}^{3} I_i\right] \qquad h5$$

Now

$$I_1 = \int_{-\infty}^{\infty}\int_{-\infty}^{\infty}\int_{-\infty}^{\infty}(e^{i\gamma(x+y/\sqrt{3})-(x^2+(y-y_o)^2+z^2)/R^2} + C.C.)dxdydz$$

$$= \int_{-\infty}^{\infty}(e^{i\gamma x - x^2} + C.C.)dx \int_{-\infty}^{\infty}(e^{i\gamma y/\sqrt{3} - (y-y_o)/R^2} + C.C.)dy.$$

$$\int_{-\infty}^{\infty} e^{-z^2/R^2}dz$$

and using the formulae $\int_{-\infty}^{+\infty} e^{ikx - (x-b)^2/2a}\, dx = 2(2\pi a)^{\frac{1}{2}} e^{ikb} e^{-ak^2}$

and $\int_{-\infty}^{+\infty} e^{-r^2x^2}dx = \sqrt{\pi}/r$ $(r > 0)$ gives

$$I_1 = \pi^{3/2}R^3\; e^{-(2/3)(R\gamma)^2}\left[e^{i\gamma y_o/\sqrt{3}} + C.C.\right]$$

Similarly

$$I_2 = \tfrac{1}{2}\pi^{3/2}R^3 e^{-(1/6)(R\gamma)^2}\left[e^{i\gamma(2y_o/\sqrt{3})} + C.C.\right]$$

and $I_3 = \pi^{3/2}\, R^3\, e^{-(2/3)(R\gamma)^2}\left[e^{-i\gamma y_o/\sqrt{3}} + C.C.\right]$

Substituting for I_1 back into equation h5 and reverting to trigonometric notation gives

$$F_y = (\Omega/3)\,\pi^{3/2}R^3.\,\frac{d}{dy_o}\left[2e^{-(2/3)(R\gamma)^2}.\,\cos(\gamma y_o/\sqrt{3}) + e^{-(1/6)(R\gamma)^2}.\right.$$

$$\left.\cos(2\gamma y_o/\sqrt{3})\right]$$

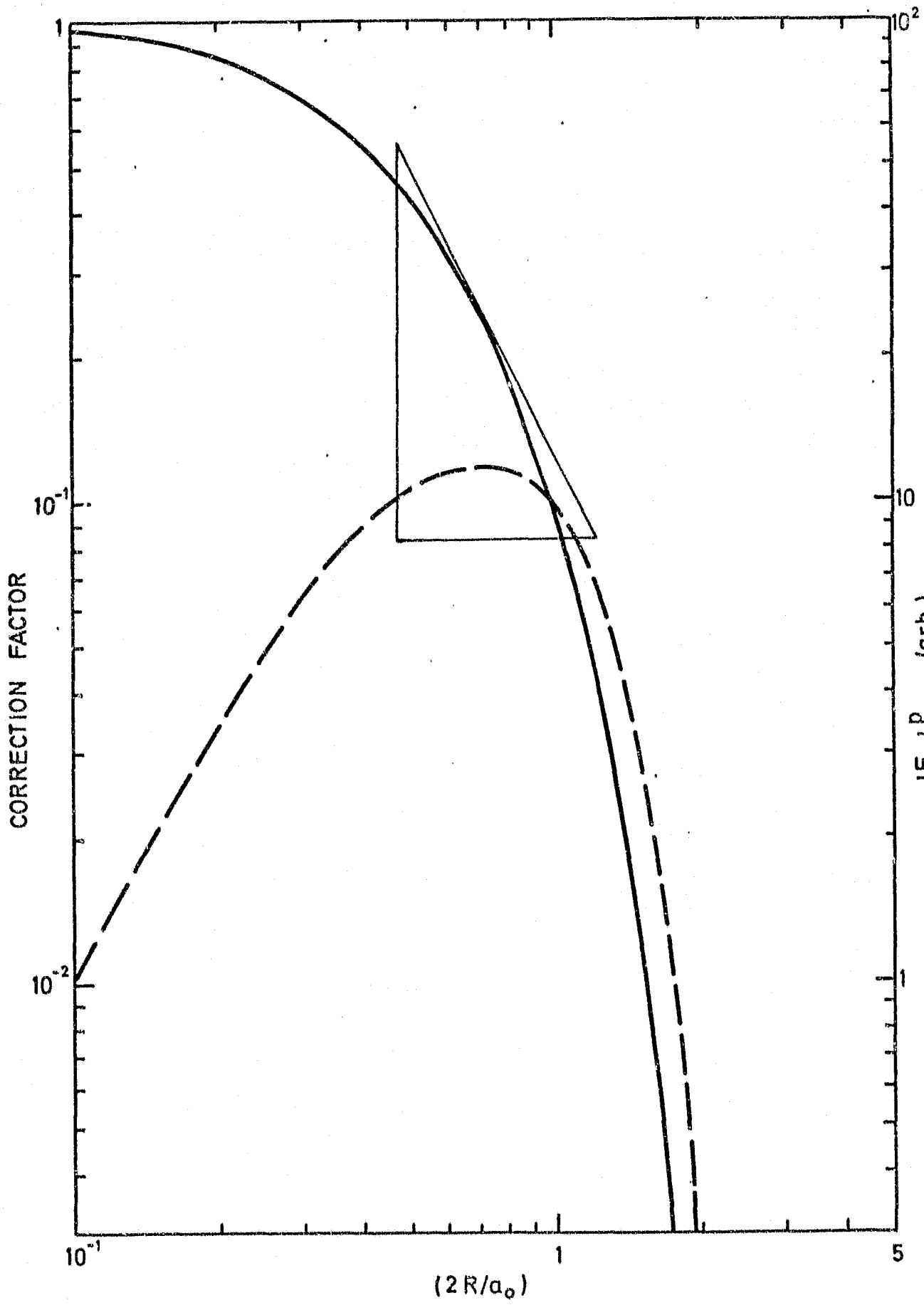


Figure A1.5 . The maximum pinning force due to a spherical site of uniform non-zero pinning potential density, within a radius R, is shown as a function of $2R/a_o$ (dashed). The solid line is a plot of the 'correction factor' required for generalizing the pinning force as calculated for a site with $R << a_o$ to arbitrary R.

$$F_y = -\Omega(2/3)\pi^{3/2}R^3.(2\gamma/\sqrt{3})\left[e^{-(2/3)(R\gamma)^2}.\sin(\gamma y_o/\sqrt{3}) + e^{-(1/6)(R\gamma)^2}\right.$$
$$\left.\sin(2\gamma y_o/\sqrt{3})\right] \qquad h6$$

Now for a particular value of R $|F_y|$ will be close to its maximum value when $\sin(\gamma y_o/\sqrt{3}) = \sin(2\gamma y_o/\sqrt{3})$ and $y_o \simeq a_o\sqrt{3}/6$. Thus finally

$$|F_y|^p_{max} \propto \Omega(R^3/a_o)\left[e^{-(8\pi^2/3)(R/a_o)^2} + e^{-(2\pi^2/3)(R/a_o)^2}\right] \qquad h7$$

The term in the square brackets is the required correction factor for generalizing the pinning force p_m due to a vanishingly small site to a site with radius R. This term and $|F_y|^p_{max}$ are shown as functions of $(2R/a_o)$ on a log-log plot in figure A1.5. The curve for $|F_y|^p_{max}$ shows a sharp maximum at $2R/a_o \simeq 0.7$ with half maximum values at $R/a_o \simeq 0.15$ and 0.63 respectively. At $R/a_o = 1$ the value of $|F_y|^p_{max}$ has become negligible. In the region of the maximum in $|F_y|^p_{max}$ the average slope in the curve for the correction factor term is approximately 2 so that the correction factor in this regime is proportional to $(a_o/R)^2$.

(ii) Cylindrical sites

For a cylindrical site of length L and radius R which is perfectly straight and collinear with the z direction and is centred at $x = 0$ and $y = y_o$ the pinning potential is given (see also equation h1) by

$$g(x,y,z) = \Omega \exp - \left|(x^2 + (y - y_o)^2/R^2\right| \qquad h8$$

and it is easily shown that the maximum force along the y direction is now given (see equation h7) by

$$|F_y|^{\ell}_{max} \propto (L/R)|F_y|^p_{max} \qquad h9$$

Thus finally the basic pinning force for spherical or cylindrical sites will be given by

$$|F_y|_{max} = A\Omega\beta \times (\text{correction factor}) \qquad h10$$

where A is a constant which includes geometrical factors and is proportional to R^3 for a spherical site and R^2L for a cylindrical site and β is a factor which has been included to take into account the dependence of Ψ on b. For $\Psi \propto |\psi|^2$, $b > 0.4$: $\beta = (1 - b)$ and for $\Psi \propto (|\psi|^2 - |\psi|^4)$, $b \gtrsim 0.5$: $\beta \simeq b(1 - b)$. Since β is already included in the expressions of chapter 3 for p_m equation h10 may be rewritten in terms of these p_m as

$$|F_y|_{max} = p_m \times (\text{correction factor}) \qquad h11$$

APPENDIX A2

A2 The Magnetometer

A2.1 The detection coils

With reference to figure A2.1 the scalar potential Ω of a fixed dipole of moment M situated at the origin and pointing along the z direction is given by

$$\Omega = (\underline{M}\cdot\underline{r})/r^3$$

$$= M\cos\theta/r^2$$

$$= Mz/r^3 \qquad \text{A2.1}$$

If the dipole is vibrated along the z direction with a sufficiently small amplitude a and with a frequency ω the time varying potential $\Omega_1(t)$ in the surrounding space is given by

$$\Omega_1(t) = -a(\partial\Omega/\partial z)\,e^{i\omega t}$$

and therefore from equation A2.1

$$\Omega_1(t) = -Ma[1/r^3 - 3z^2/r^5]\,e^{i\omega t} \qquad \text{A2.2}$$

The field H(t) associated with this time varying potential is given by

$$\underline{H}(t) = -\text{grad}_p\,(\Omega_1(t))$$

$$= -\left[\frac{\partial\Omega_1}{\partial r}\,\underline{a}_r + \frac{1}{r}\,\frac{\partial\Omega_1}{\partial\theta}\,\underline{a}_\theta\right]$$

$$= -\frac{1}{r}\,\frac{\partial\Omega_1}{\partial\theta}\,\underline{a}_\theta$$

so that from equation A2.2

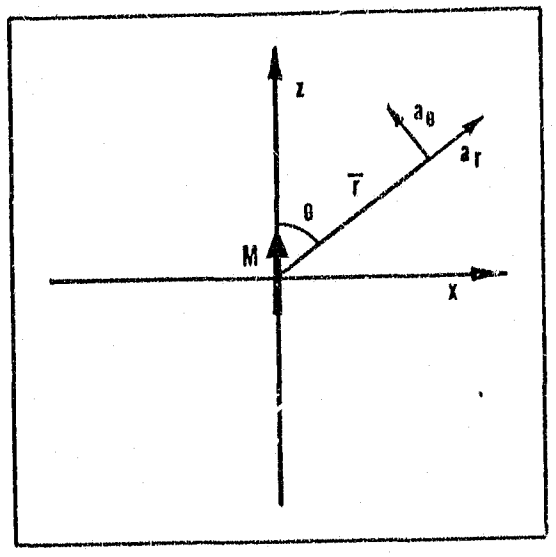


Figure A2.1. Co-ordinate system for the description of the scalar potential of a dipole M situated at the origin pointing along the z axis.

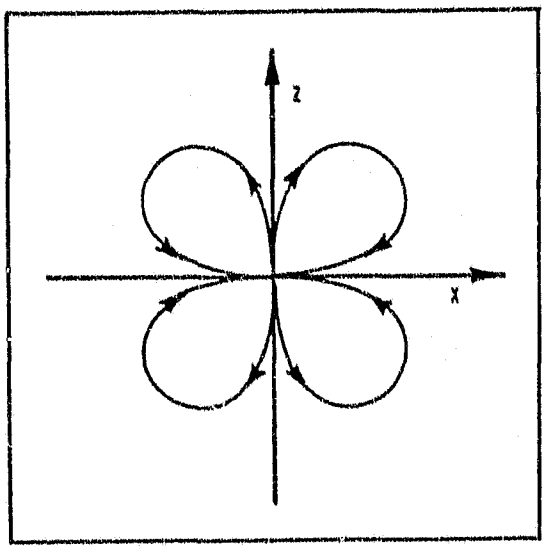


Figure A2.2. The spatial configuration in the x-z plane of the time varying component of the magnetic field due to a dipole pointing and vibrating along the z direction.

$$\underline{H}(t) \simeq (3Ma/r^4)\,\frac{\partial}{\partial\theta}\left[(\cos^2\theta)\,\ell^{i\omega t}\right]\underline{a}_\theta$$

$$\simeq (3Ma/r^4)\sin\theta\cos\theta\,\ell^{i\omega t}\,\underline{a}_\theta \qquad \text{A2.3}$$

$\underline{H}(t)$ is symmetric about the z axis and its spatial configuration is shown in figure A2.2

The optimum coil configuration to detect H(t) consists of two cylindrical coils connected in series opposition, co-axial with the z axis, and symmetrically disposed with respect to the sample as shown in figure A2.3. The signal induced in the detection coil is given by

$$v_s \propto dH(t)/dt$$

and therefore from equation A2.3

$$v_s = \alpha\nu aM\cos(2\pi\nu t) \qquad \text{A2.4}$$

where $\nu = \omega/2\pi$ and α is a constant which is proportional to the total turns area of the coils and depends on their geometry.

The noise signal $\bar{v}_n(T)$ from the coils depends on their total resistance R and is given by

$$\bar{v}_n(T) = (4R(T)kTB)^{\frac{1}{2}} \qquad \text{A2.5}$$

when kT is the thermal energy and B is the bandwidth of the detection system. Now $R = 4\rho L/\pi d^2$ where ρ is the resistivity of the copper winding, L is the total length and d the diameter of the wire. For any particular fixed coil geometry with a total number of turns n: $n \propto d^{-2}$ and Ld^2 is a constant. Therefore $R \propto \rho/d^4 \propto n^2\rho$ and substitution into equation A2.5 gives

$$\bar{v}_n(T) \propto n\left[\rho(T)kTB\right]^{\frac{1}{2}} \qquad \text{A2.6}$$

From equations A2.4 and A2.6 the signal to noise ratio is given by the expression

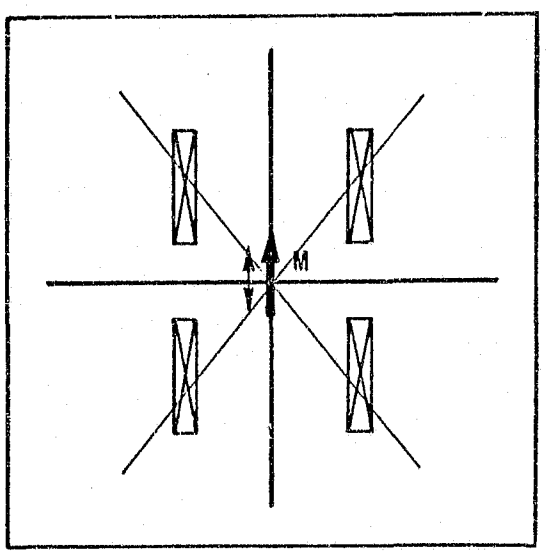


Figure A2.3. The coil configuration for optimal detection of the time varying field of the vibrating dipole as shown.

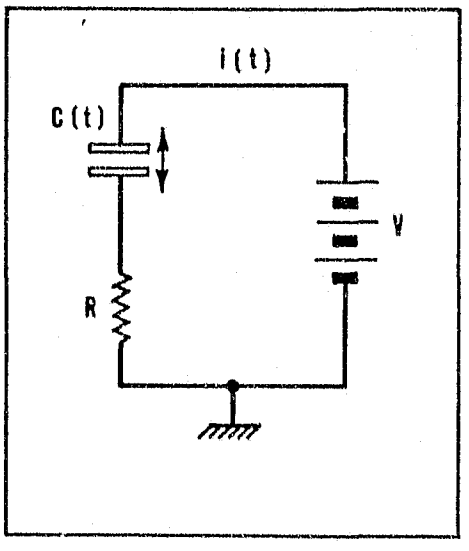


Figure A2.4. Equivalent circuit for the vibrating capacitor reference system.

$$\bar{v}_s/\bar{v}_n \propto \alpha v a M/[n(\rho kTB)^{\frac{1}{2}}]$$

$$\propto \nu a M/(\rho(T)kTB)^{\frac{1}{2}}$$

(since $\alpha \propto n$ for fixed coil geometry).

$\bar{v}_s/\bar{v}_n$ is therefore independent of the total number of turns n. In practice the product νa is limited by mechanical and power considerations in the electromechanical transducer and the system bandwidth B has a lower practical limit which is determined by the rate at which measurements are to be made. Maintaining the detection coils at a temperature of about 4K rather than 300K ($\rho_{300}/\rho_4 \simeq 100$ for the copper windings) increases the signal to noise ratio by nearly two orders of magnitude. An upper limit for the number of turns n is therefore determined by the criterion that the noise signal from the coils ($\bar{v}_n$) be equal to the detection system noise signal referred to the input of the system. In the present system this criterion could not be realized because of the necessarily small space available for the detection coil windings. The final specifications for the coils are as follows:

Inner diameter:	10.5mm
Outer diameter:	15.2mm
Length: per coil:	30mm
Coil separation:	(centre to centre) : 34mm
Wire:	48 S.W.G. formvar insulated copper
Number of turns:	18,300 per coil
Inductance:	2.42Henry per
Resistance:	5.6K-ohm (T=300K), 50 ohm (T=4.0K)

A2.2 The vibrating capacitor system

The equivalent circuit for one half of the vibrating plate capacitor assembly and the associated electronic system is shown

schematically in figure A2.4. C(t) is the capacitance of the vibrating capacitor and R is the effective impedance of the system which, in practice, is the input impedance of the reference channel amplifiers.

Assuming the capacitor plates to have an effective area A, separation d and a modulation amplitude a then the capacitance C(t) is given by

$$C(t) = A/4\pi[d + a\cos(2\pi\nu t)]$$

$$\text{Now } dC(t)/dt = Aa\nu \sin(2\pi\nu t)/2[d + a\cos(2\pi\nu t)]^2 \qquad \text{A2.8}$$

$$= i(t)/V$$

$$= v(t)/RV$$

Rearranging and expanding the denominator in equation A2.8 ($d >> a$) gives for v(t)

$$v(t) = (RA/2d^2)Va\nu \sin(2\pi\nu t)\left[1 - \frac{2a}{d}\cos(2\pi\nu t) + \frac{3a^2}{d^2}\cos^2(2\pi\nu t)\right]$$

In the present system $a \simeq 0.1$ and $d \simeq 5$mm, i.e. $d/a \simeq 50$ and therefore the reference signal v_R is given to good approximation by

$$v_R = -\beta Va\nu \cos(2\pi\nu t + \pi/2) \qquad \text{A2.9}$$

with $\beta = A/2d^2$

A2.3 Magnetometer circuit

The electronic circuit for the magnetometer (excluding the lock-in-amplifier and the transducer drive amplifier) is shown in figure A2.5. The labels (blocked) refer to the various controls and sockets. A1 is a low noise, high input impedance, wide band amplifier designed by Fairchild (Fairchild application report number 159). The circuit and specifications for the amplifier are given in figure A2.6. The transducer drive amplifier is a standard D.C.-A.C.

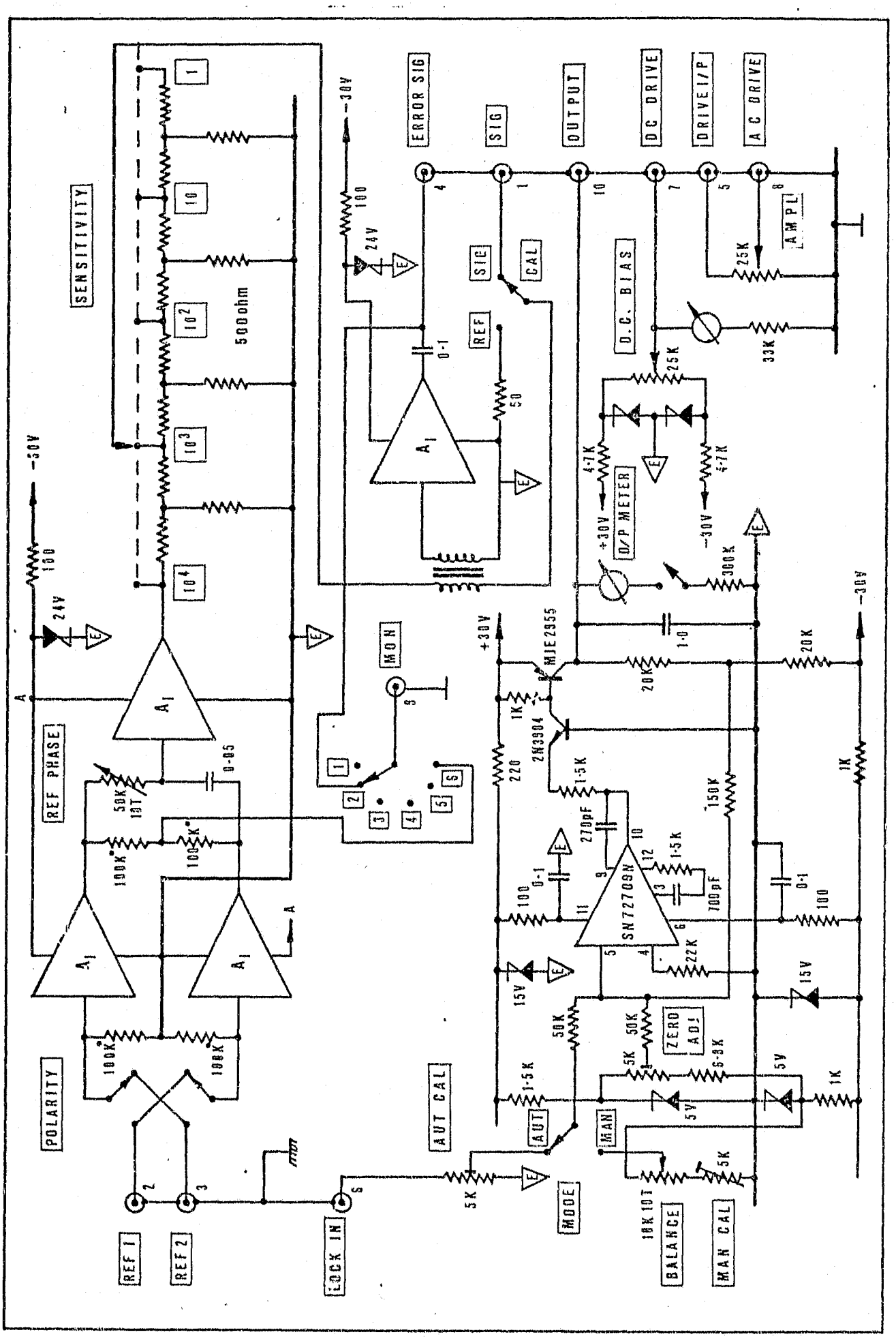
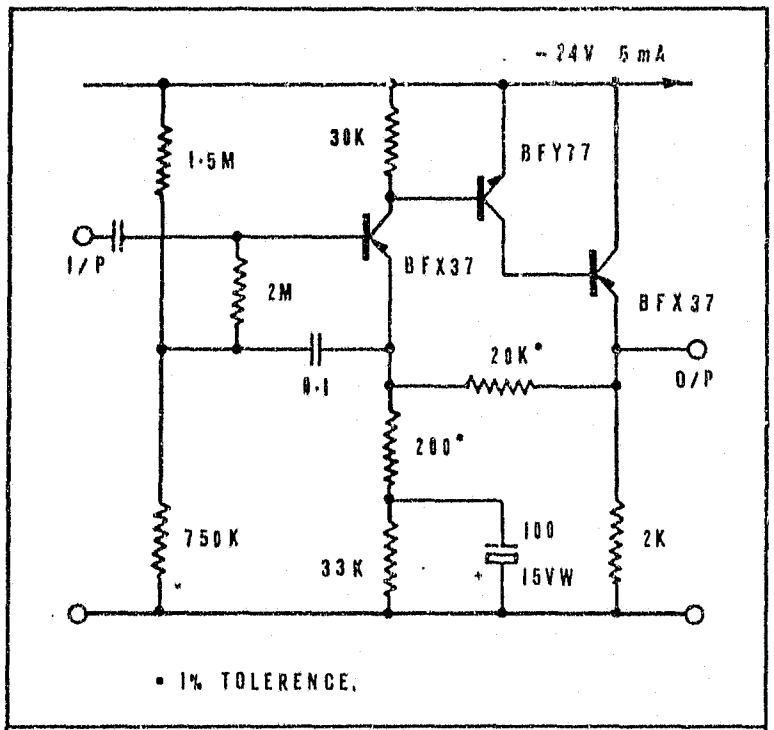


Figure A2.5. Schematic circuit diagram for the comparator unit of the magnetometer.



from FAIRCHILD APPL REPORT 159
low noise high input impedance preamplier
NOISE FIG: 1·2dB for a source imp. of 100K.
INP. IMP: 9M (f≤1KHz). OUTP. IMP: 50ohm.
O/L GAIN: 73 (10Hz≤f≤10KHz).

Figure A2.6. The low noise preamplifier circuit (A1 in figure A2.5) (from Fairchild Application Report 159).

power amplifier and the design is due to D.L. James of this department. The power supply for the magnetometer is an Advance-Type P.P.3.

A2.4 Magnetometer set-up procedure

Having inserted a specimen (which may be a reference sample for calibration purposes - see later) into the magnetometer and having pumped the magnetometer to the desired exchange gas pressure the set up procedure is as follows:

The magnetometer controls are set as indicated below and the system is allowed to 'warm up' for about 30 minutes.

TRANSDUCER AMPLIFIER	:	GAIN	:	MAXimum
MAGNETOMETER	:	MON.	:	6
		CAL.	:	REFerence
		MODE	:	MANual
		BALANCE	:	5.0
		SENSITIVITY*	:	1, 10, 10^2, 10^3, 10^4
LOCK-IN-AMPLIFIER	:	SENSITIVITY*	:	0.05, 0.5, 5, 50, 500mV
		SIGNAL Q	:	10-15
		FREQUENCY	:	8.1-8.4
		FREQ. MULTIPLIER	:	X10
		REF. ATTEN	:	0.5
		TIME CONSTANT	:	300ms
		MODE	:	INTernal
		METER/MONIT	:	SIGnal
		ZERO SUPRESS	:	OFF.
		ROLL OFF	:	6dB/OCTAGE

* The SENSITIVITY settings depend on the specimen and will be discussed later. At this stage any vertical pair may be chosen. (Usually X10^3 and 50mV respectively).

MAGNET POWER SUPPLY : FIELD : MINIMUM

(It is assumed that the Lock-in-amplifier has been previously checked for correct functioning.)

After the warm-up period the AMPlitude control is adjusted for an approximately half full-scale reading on the Lock-in-amplifier (LIA) meter. The POSITION control is adjusted to give a minimum (virtually zero) signal on the C.R.O. The FREQ. TRIM. control (LIA) is finely adjusted for maximum deflection on the LIA meter. The POSITION and AMPlitude controls are finely adjusted to give a reading of precisely 5.0 on the LIA meter for either position of the POLARITY switch.

The magnetometer CALibration switch is now set to SIG. and the magnet current (FIELD) is manually increased to a value which is expected to give a specimen magnetic moment which is just greater than half its maximum value. (If this field is not known it may be easily established.)

If during this procedure the LIA meter reading increases the POLARITY switch must be reversed. The BALANCE and REF. PHASE controls on the magnetometer are now alternatively adjusted to obtain a minimum deflection on the LIA meter while increasing the LIA SENSITIVITY by a factor of 100 (or 50 on the most sensitive range). If the BALANCE reading is now less than 1.0 or if no balance setting can be found a different pair of SENSITIVITY settings for the SENSITIVITY of the magnetometer and LIA are chosen and the procedure is repeated. The minimum reading on the meter should now be less than 5 per cent of f.s.d. (and is due mainly to the 1st harmonic from the reference capacitor). With the MONitor switch set to either position 2 or 6 there should be virtually no signal on the CRO. The lock-in-

amplifier has, up to this point, been used as a voltmeter. To obtain synchronous rectification the METER/MONITOR switch is set to OUT. The meter reading should now be virtually zero. The TIME CONSTANT is set to 1 Sec. and the MODE switch on the magnetometer to AUTomatic. The PHASE controls on the LIA are adjusted to give a steady on-scale reading on the LIA meter, the magnetometer MODE switch is returned to MANual and the BALANCE control is adjusted (by about 1 per cent) to give this meter reading. The LIA PHASE control is now switched through 90^{o} and is then finely adjusted for zero deflection on the LIA meter. The PHASE is now switched back through 90^{o} and the magnetometer MODE switch is returned to the AUTomatic position. The magnetic field is reduced to zero and the magnetometer is set-up. Note: for a 'first-time' set-up or if the phase controls have for some reason been adjusted far from their usual operating positions it is advisable, due to some slight parasitic dependences between the various controls to repeat the entire set up procedure once more.

Calibration. Although the instrument may be calibrated against a single specimen over its entire sensitivity range it is more accurate to calibrate against a known specimen suitable for the sensitivity range required for the unknown specimen. A superconducting specimen is usually most suitable for this purpose. For a strongly ferromagnetic sample a pure nickel stand is best employed.

Manual operation. After the above set-up procedure the magnetometer MODE is left on the MANual position. To obtain the magnetic moment of the specimen the BALANCE control is adjusted to give a null reading on the LIA meter and the magnetic moment is obtained from the output on the DVM or from the BALANCE control setting.

Miscellaneous. The MAN. CAL. and AUT. CAL. controls on the magnetometer have been adjusted so that the O/P METER on the magnetometer gives a reading which corresponds to that of the LIA meter.

A2.5 Specimen rods and holder stage

A general purpose specimen rod with various specimen stages and a temperature controllable specimen stage and rod are shown schematically in figure A2.7. Crystalline quartz is used for the stages where possible because of its good thermal conductivity is low temperatures and its very small magnetic susceptibility. Otherwise the rods and stage are designed to be of low mass to reduce reaction forces.

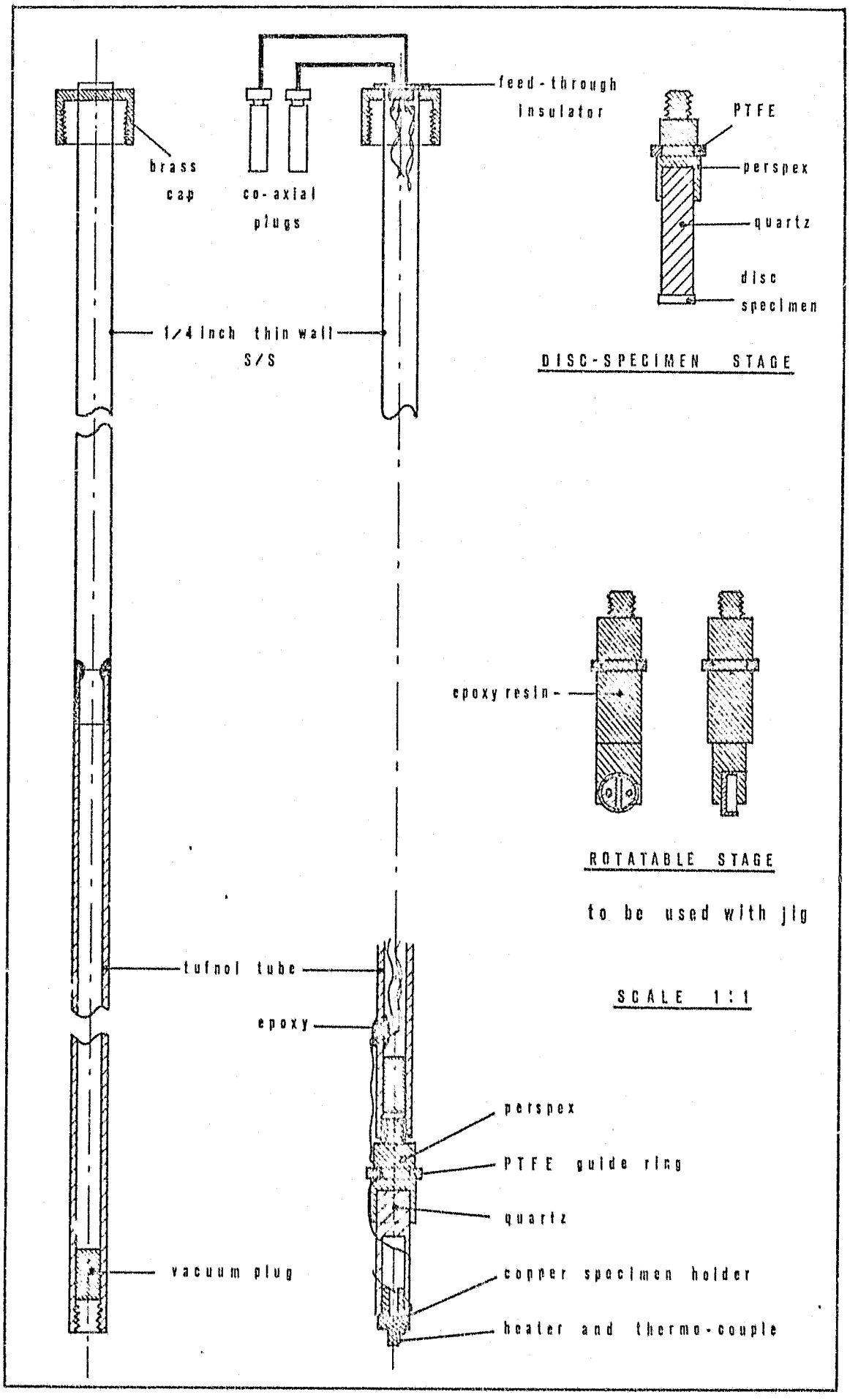


Figure A2.7. Various specimen rods and stages (including the temperature regulated stage) for use with the magnetometer.

APPENDIX A3

A3 Temperature regulation

A3.1 A.C. bridge temperature regulator

The electronic circuitry for the regulator is given in figure A3.1.

Transistors Q1 and Q2 are the active elements of a phase shift oscillator, Q3 and Q4 of a buffer amplifier, Q5, Q6, Q7 and Q8 of a two stage phase shift circuit, Q9 of an amplifier, Q10, Q11, Q12 and Q13 of a D.C. power amplifier, Q14 and Q15 of a low noise input amplifier and Q16 and Q17 of a phase sensitive detector.

The frequency of oscillation of the phase shift oscillator is given by:

$$f = 1/[(24)^{\frac{1}{2}}\pi C_2 R_3]$$

$\simeq$ 295Hz for the present circuit.

The tuned amplifier (op. amp. SN 72709N and associated circuitry) was suggested by D.L. James and has the following characteristics:

Taking $C_5/C_6 = a$ and $Z_i = bR_9$ (where Z_i is the source impedance) then the pass frequency f_o, the Q factor and the gain A_o at f_o are given by:

$$f_o = 2\pi/(R_9 C_5 a^{\frac{1}{2}})$$

$$Q = 1/(2a^{\frac{1}{2}})$$

$$A_o = 1/(2ab)$$

The total gain in the signal channel [i.e. due to the low noise amplifier and tie tuned amplifier] is approximately 10^6. The gain of the D.C. amplifier may be varied between 0 and approximately 50. The

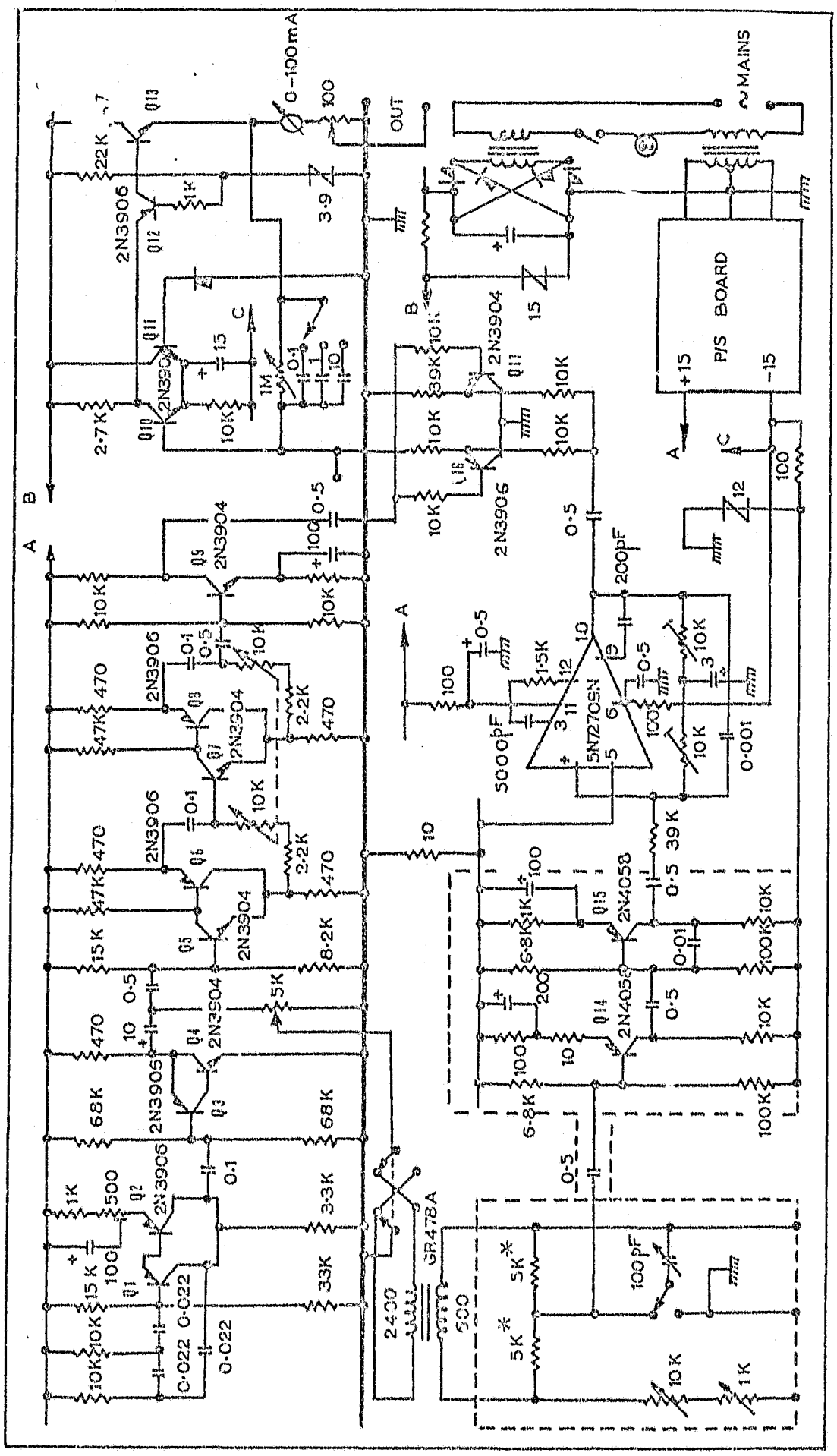


Figure A3.1. Electronic circuit diagram for the A.C. bridge temperature regulator.

bandwidth of the electronic part of the circuit is determined primarily by R_6 and C_4.

Set-up procedure. The initial set-up procedure involves setting up the oscillator, balancing the reactive component of the bridge and adjustment of the tuned amplifier. To do this the oscillator is monitored on a CRO and the trim potentiometer R is adjusted until the oscillator just begins to oscillate - producing an undistorted sinusoidal signal. The circuit is then broken at point x. The BRIDGE CURRENT is set to maximum and point Y is monitored on the CRO. The bridge is now adjusted by means of R COARSE to give an unsaturated sinusoidal signal on the CRO. Resistors R_9 are adjusted to maximize this signal. The bridge is now balanced (to give zero signal on the CRO) by adjusting R COARSE, R FINE and C. The circuit is reconnected at x and the C.R.O. is connected to the MONitor socket. The regulator is now permanently set-up for routine use and the adjustments which will be described now depend on external circumstances.

The BRIDGE CURRENT is set for the desired maximum dissipation in the thermometer. With the bridge adjusted to be slightly off-balance the PHASE is now adjusted to give a symmetric unipolar output from the phase sensitive detector (as monitored on the CRO). If this signal is negative going a deflection will be obtained on the output meter. The SENSE switch is set so that for a re-adjustment of the bridge corresponding to the thermometer temperature decreasing the output current increases as indicated on the meter, R. COARSE and R.FINE are now adjusted to a desired value and the D.C. gain (D.C. GAIN and O/P Attenuator) are increased as far as possible consistent with no hunting instability in the system. Adjustment of the TIME CONSTANT to higher values permits a large D.C. gain to be used but does not

necessarily improve the overall stability.

Stability. The ultimate stability of a servo-loop regulator depends on the open-loop gain of the system. If this is increased beyond a certain limit, then; under certain conditions, regenerative feedback or hunting will occur in a closed loop configuration (i.e. when the thermometer is thermally coupled to the heater). The stability of the servo-loop against regenerative feedback depends on the difference between the slopes of the open-loop and closed-loop frequency-gain characteristics at their point of intersection. This in turn depends on the bandwidth of the electronic system, on the coupling between the thermometer and heater and on the thermal mass of temperature regulated system. If this difference in slopes is less than 20dB per decade the system is inherently stable. Also if the thermal coupling between thermometer and heater is perfect the closed loop gain will be unity and the system will be stable under all conditions. The thermal mass of the regulated system effectively behaves as an integrating capacitor in parallel across the thermometer-heater feedback link. Thus, unless this link is perfect, the closed loop gain-frequency characteristic falls off more rapidly leading eventually, with increasing thermal mass, to instability. In the present system therefore, facility has been made for altering the system gain - frequency characteristics and the thermal system has been designed, consistent with its other functions, to be of low mass and to afford close thermometer-heater coupling.

Finally the control stability is degraded slightly by various sources of drift in the electronics (for example in the oscillator). However, for the present purposes the short term (15 minute) stability of ±1mK in the range $T < 10K$ which is obtainable is more than adequate.

A3.2 Thermo-couple temperature regulator

The thermo-couple potential is monitored on a Hewlett-Packard Differential Voltmeter (HP 3420B) in the differential mode (as discussed in Chapter 3). The output signal from the voltmeter is fed to a unipolar power amplifier to provide the heater current.

The stability criteria are obviously similar to those already discussed for the D.C. bridge regulator. However, because the system is D.C. throughout performance is considerably degraded by drift and by spurious thermal e.m.f.'s along the thermo-couple leads and at the input of the voltmeter.

APPENDIX A4

A4 Temperature sensors and measurements

A4.1 Carbon resistor

Carbon resistor thermometers are often insufficiently reproducible, with cycling from room temperature to 4K, to make good secondary thermometers. However, they have the advantage of having only a very slight magneto-resistance and are therefore eminently suitable for temperature regulation purposes in varying magnetic fields. The dependence of resistance on temperature vary over a wide range from one process or manufacturer to another.

The resistor used here is a 47Ω (T = 300K) Allen Bradley type TR ⅛ watt with most of its insulating sheath ground off and the tin plating removed from its copper leads.

The magneto-resistance for a similar resistor (Allen Bradley 100Ω ⅛ watt) has been measured by Hudson (1968) for temperatures in the range $4K < T < 30K$ and for magnetic fields up to 40K gauss. Hudson's results show an almost linear dependence of magneto-resistance on magnetic field. At a field of 40K gauss the percentage change in resistance varies from approximately +0.6 per cent to -2.8 per cent from T = 4.19K to T = 12.2K respectively and then apparently drops to -2.3 per cent at T = 28.7K. These results indicate that in the experiments on niobium in the present investigation, where the magnetic field rarely exceeds 3 kilogauss, the magneto-resistance of the carbon resistance thermometer should be negligibly small. This was confirmed experimentally.

A4.2 Gold-iron chromel thermo-couple

The thermo-electric properties of very dilute alloys of iron in gold have been extensively studied (see for example Berman, Brock and Huntley, 1965).

The advantage of this alloy is its very high thermopower (10-15μV/K) at low temperatures. Its disadvantages are its strong paramagnetism and the effect of magnetic fields on the thermopower which increases with decreasing temperature. The former disadvantage is partially overcome by using very fine thermo-couple wires and the latter was not important in the present investigation since the thermo-couple was only used for annealing experiments in zero magnetic field.

The material used in this investigation (Au - 0.3 per cent Fe) and chromel (wire diameter 0.08mm) was supplied by Johnson Matthey Limited.

An approximate calibration curve for the thermo-couple is shown in figure A4.1.

A4.3 Germanium resistance thermometer

The thermometer is a Solitron Devices Incorporated Series 5, model number SP5401 (thermometer number 1814) and is He^3 filled for operation at temperatures below 1K. The thermometer encapsulation can (gold plated copper) is approximately 12mm long and 3mm in diameter and fits snugly into a cylindrical hole in the 'calorimeter'. Good thermal contact with the calorimeter is achieved by the use of Apiezon N grease and by thermally anchoring the thermometer leads (which are fine, varnish insulated copper wires - the original multi-strand tin-plated copper leads having been cut off fairly close to the device).

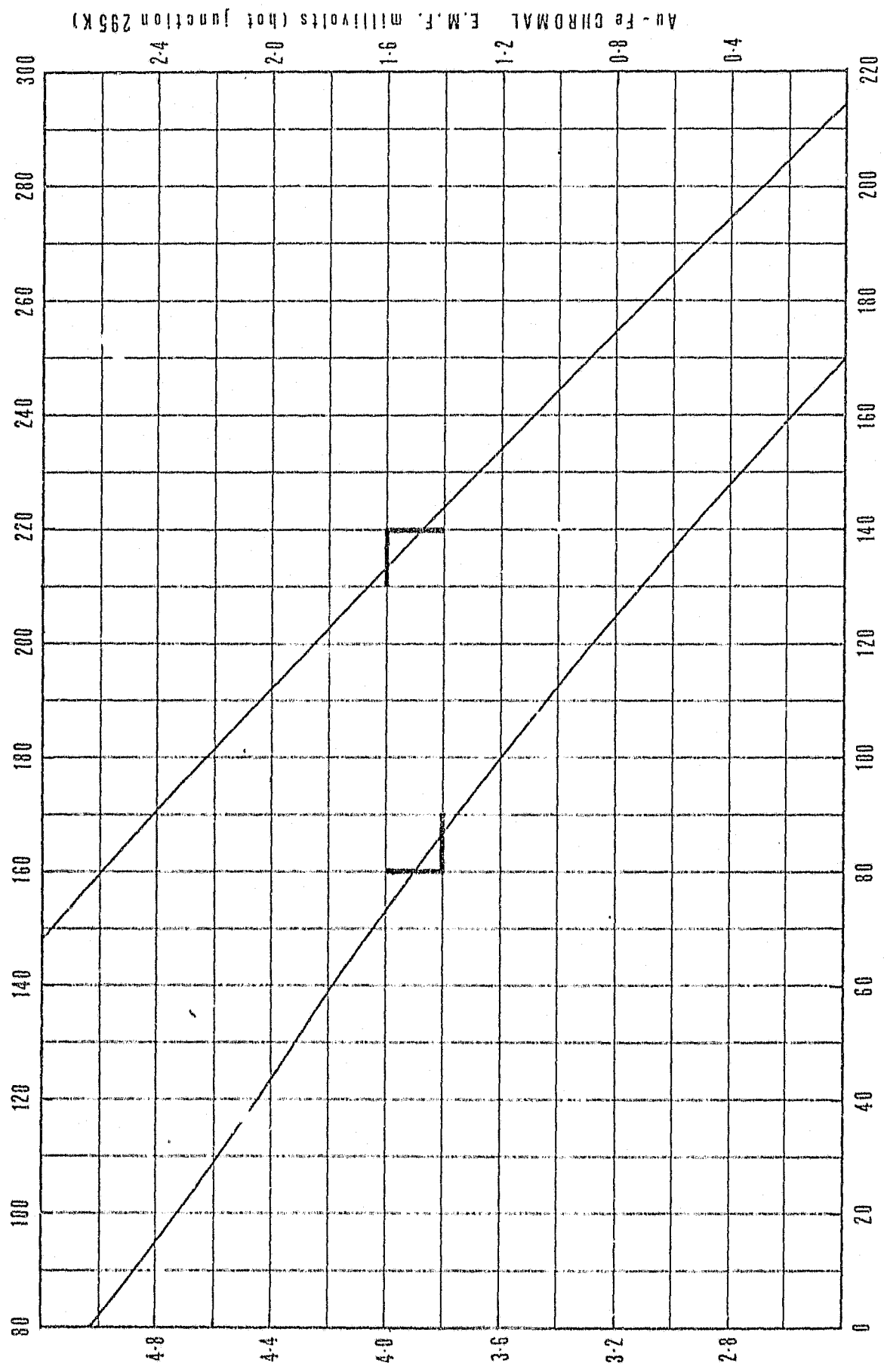


Figure A4.1. Calibration curve for the $(Au-0.03\% Fe)$-Chromel Thermocouple in the range $0 < T < 295K$.

The small sensing element of the germanium thermometer has a very low thermal mass, fast response time, high sensitivity and very high reproducibility with repeated cycling between room temperature and liquid helium temperatures (e.g. Low, 1961, Lindenfeld, 1961 and Sarner and Blakemore, 1967). Germanium resistance thermometers have a relatively large magneto-resistance and temperature measurements should therefore be made in zero magnetic field.

The present thermometer was calibrated (along with several others) against two secondary standards which were supplied by Professor N.E. Phillips, Department of Chemistry, University of California, Berkley, U.S.A. These standards were calibrated as follows:

$0.3 < T < 1.5K$: Susceptibility of CeM_9NO_3 substandard, against He^4 vapour pressure ($1.2K < T < 4.2K$) using linear extrapolation of $1/\chi$ versus T to lower temperatures.

$1.2 < T < 4.2K$: T58 He^4 vapour pressure scale.

$4.2 < T < 25K$: He^4 gas pressure (fully compensated) in parallel with He^4 vapour pressure and platinum resistance standard calibrated by the N.B.S. (U.S.A.).

Calibration against these substandards was done by J.C.F. Brock (ex this Department) and the author as follows:

The thermomete s, including the secondary standards, were clamped into a custom made copper block (with adequate precautions to obtain near perfect thermal contact) which was attached by means of a weak thermal link to the He^3 can of a cryostat designed by J.C.F. Brock for operation at temperatures between 0.3K and 30K. (This cryostat is described by Vandersande, 1974.) The copper block was also provided

with a carbon resistance thermometer (Spear 100 ohm 1/4 watt) and a 100 ohm manganin heater winding for use with the A.C. bridge temperature regulator which has been described in chapter 3 and in appendix A3.1.

Resistance measurements were taken for all the thermometers at close temperature intervals in the range $0.3K < T < 30K$ using the temperature regulator and the Data Acquisition System. The measuring currents through the thermometers were 1μA for $0.3K < T < 2K$ and 10μA for $2K < T < 30K$.

Finally, by inter-correlation with the substandards, using the method of least squares (numerical computation by J.L. Crawford), the resistance-temperature data for each unknown thermometer were fitted to a polynomial of the form

$$(T)^{-1} = \sum_{i=1}^{n} A_i (\log_{10} R)^{i-2}$$

The final value chosen for n was 7.

Polynomials of the form above are too simple* to give a good fit over a wide temperature range and show a tendency to oscillate. The polynomial coefficients were therefore calculated for three temperature ranges, viz. $0.3 < T < 4$, $1.5 < T < 12$ and $2.5 < T < 25K$. In the present investigation the coefficients for the range $1.5 < T < 12K$ are used. In this case the fitting errors due to oscillation range between ±3mK with an R.M.S. deviation of 0.34mK. The computer program for converting current and voltage data for thermometer 1814 in the temperature range $1.5K < T < 12K$ is given in appendix A8. A calibration curve for approximate use is given in figure A4.2.

The circuit diagram for the thermometer current source is shown in figure A4.3. The measuring current is 10μA and provision is made

* or too complicated!

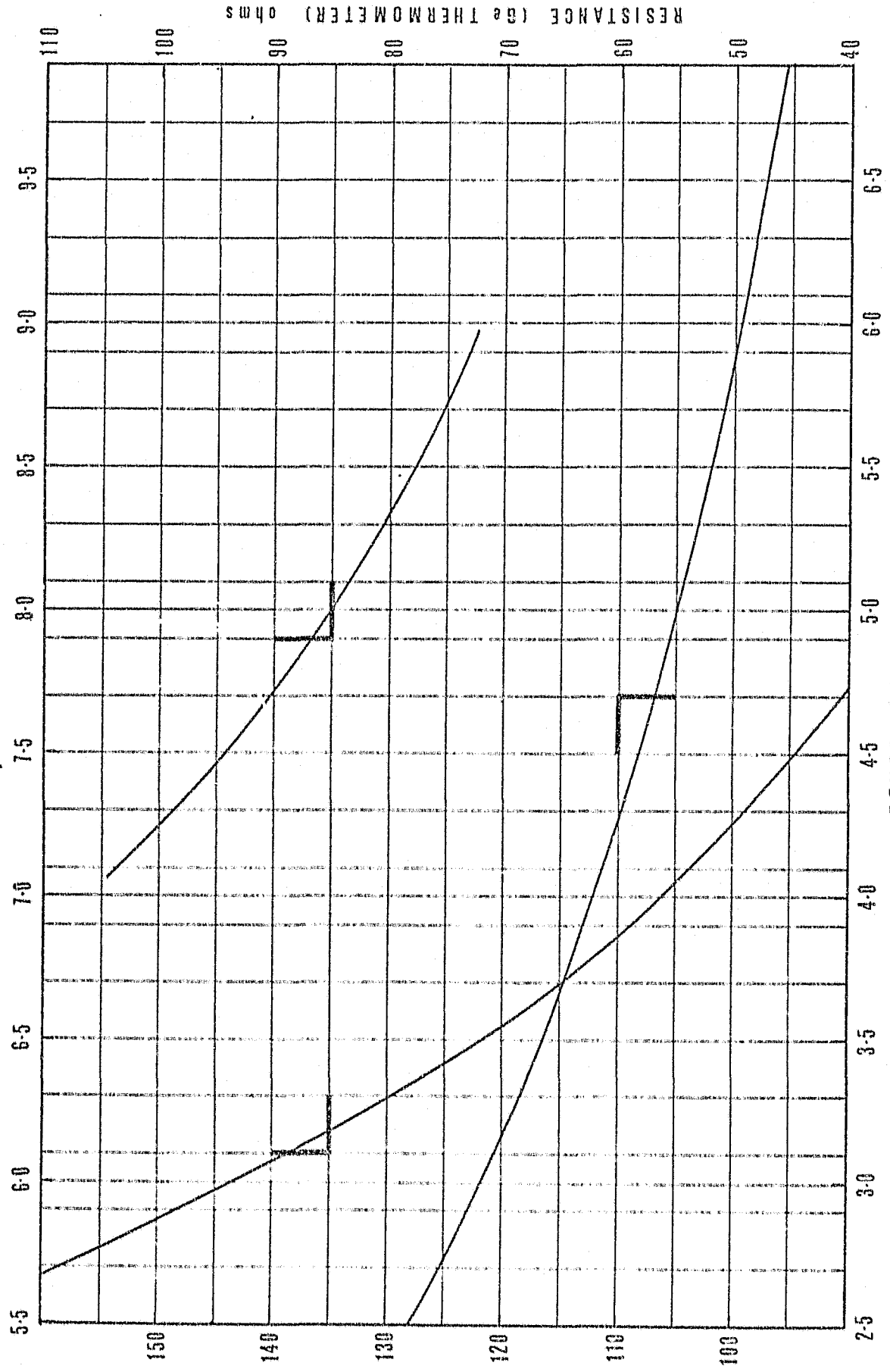


Figure A4.2. Calibration curve in the range 2.5 < T < 10K for the germanium resistance thermometer (Solatron Devices Incorporated, Series 5, Model SP5401= 1814).

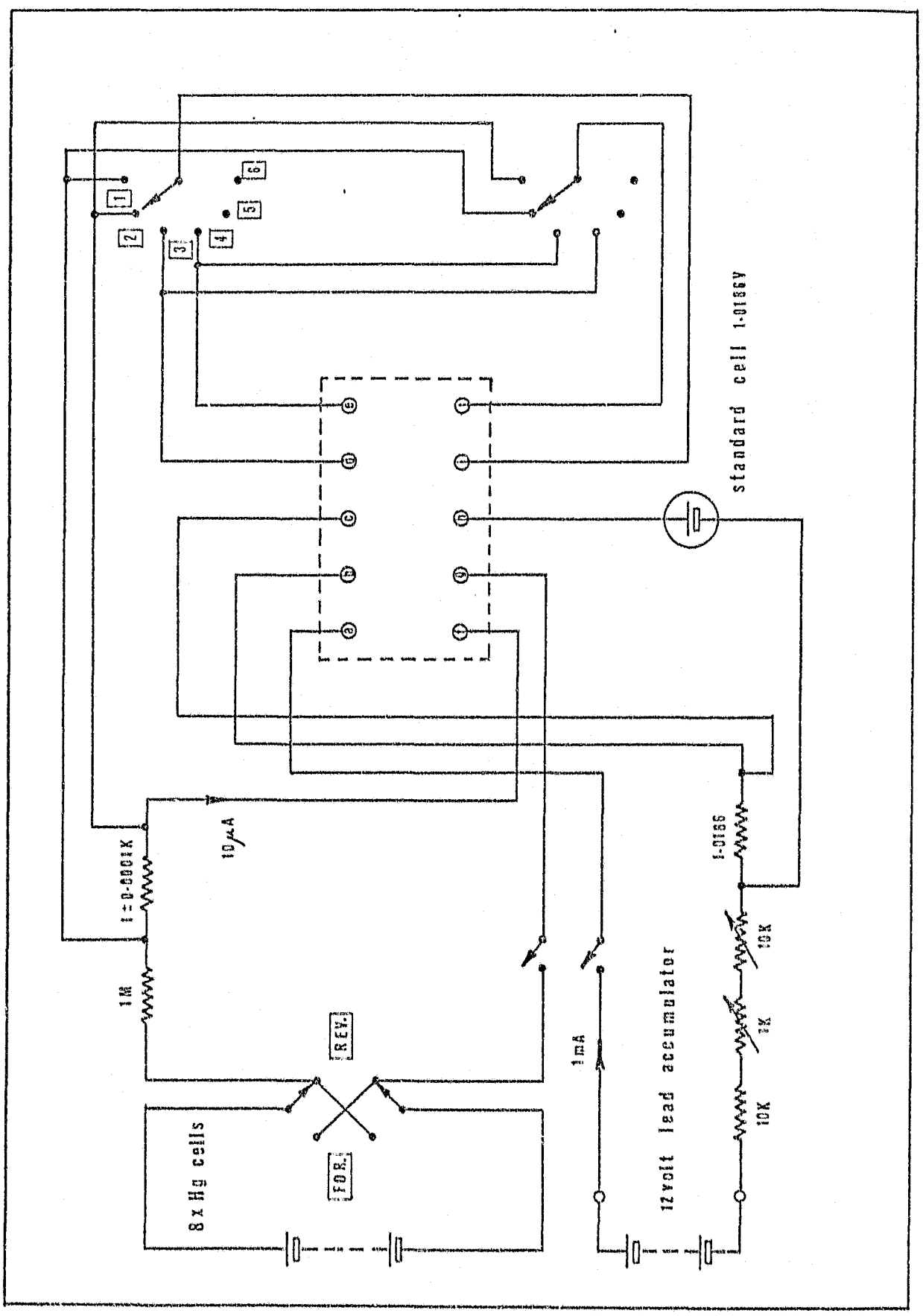


Figure A4.3. Circuit diagram for the germanium resistance thermometer constant current source and power supply for a potentiometer circuit.

for reversing the current. Each resistance measurement is made with either current sense to eliminate spurious thermal e.m.f.'s. Also shown in the circuit is the current source for a standard potentiometer which may be used if a D.V.M. is not available.

APPENDIX A5

A5 Superconducing Magnet and Ancillary Apparatus

A5.1 Coil design

The analysis which follows, for the magnetic field of a thick solenoid, is due to Barker (1950,.

Consider first the general case: With reference to figure A5.1 the magnetic field components due to a system of pairs of coil windings of vanishingly small cross section, situated co-axially with respect to the z axis and symmetrically with respect to the origin, are given by

$$H = 2\pi C_1[1 + (C_3/C_1)(z^2 - y^2/2)+(C_5/C_1)(z^4 - 3z^2y^2 + 3y^4/8)+. .] \quad A5.1$$

and

$$h = -2\pi zyC_1[(C_3/C_1)+\tfrac{1}{2}(C_5/C_1)(4z^2 - 3y^2)+ . . .] \quad A5.2$$

where H and h are the z and y components of the field strength at the point $\delta(z,y)$ and

$$C_n = 2\sum_{jn} i_j \sin^2\theta_j . r_j^{-n} P_n^1(\cos\theta_j) \text{ for n odd}$$

and

$$C_n = 0 \text{ for n even}$$

where P_n^1 is the Legendre polynomial and i_j is the current (in abamperes) in the jth loop.

For a thick solenoid of length 2b, outer-diameter $2a_2$ and inner diameter $2a_1$ carrying a current I amperes the coefficients C are given by

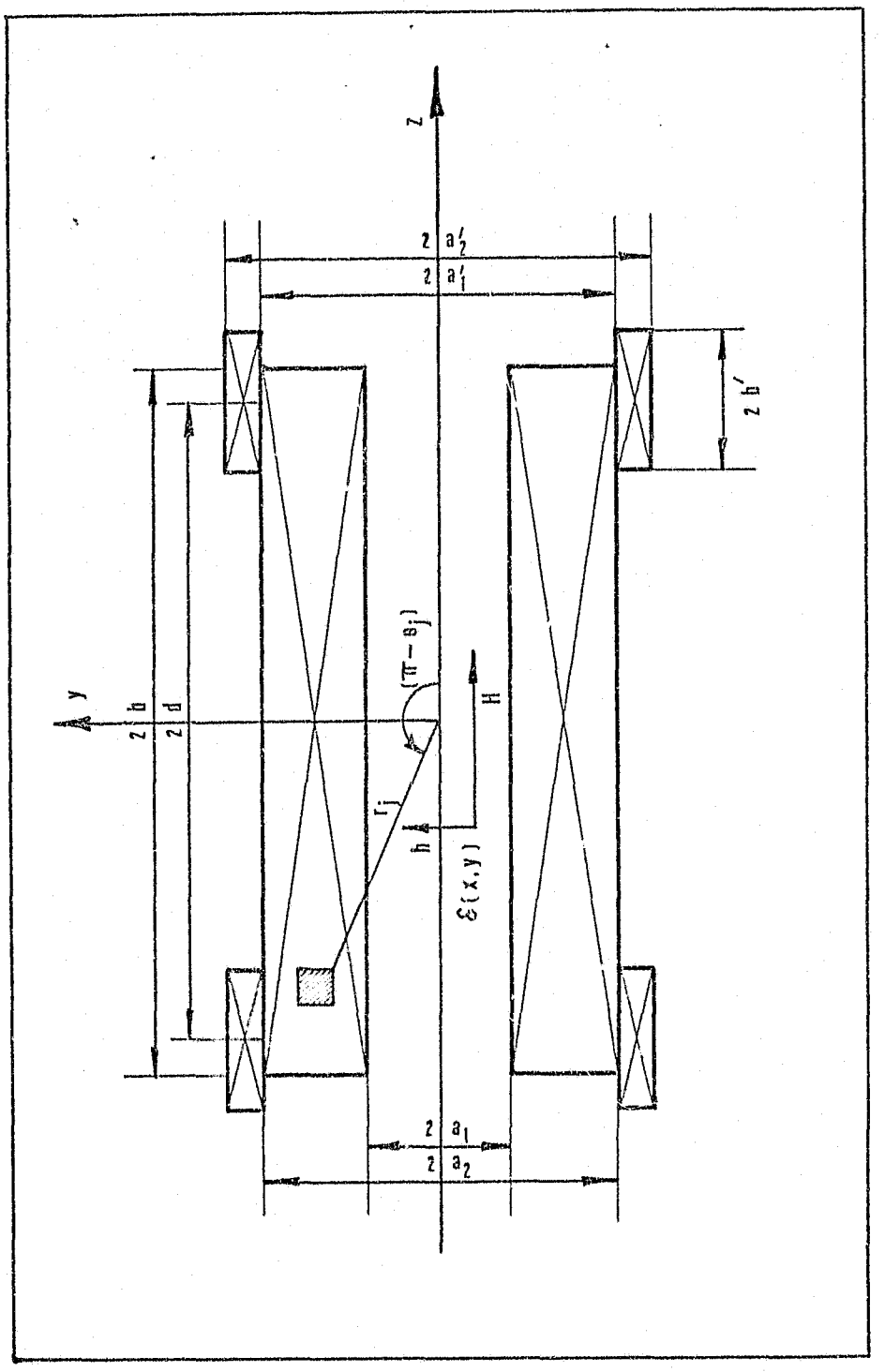


Figure A5.1. Schematic diagram of the superconducting magnet coils showing parameters and the co-ordinate system for the calculation of the spatial configuration of the magnetic field.

$$C_1 = (21b/10)\left[\ln((b^2+a_2^2) + a_2) - \ln((a_1^2+b^2)+a_1)\right] \qquad A5.3$$

$$C_3 = (1/10b)\left[a_2^3(a_2^2 + b^2)^{-3/2} - a_1^3(a_1^2 + b^2)^{-3/2}\right] \qquad A5.4$$

$$C_5 = (1/120b^3)\left[a_2^3(2a_2^4 + 7a_2^2b^2 + 20b^4)(a_2^2 + b^2)^{-7/2} - a_1^3(2a_1^4 + 7a_1^2b^2 + 20b^4)(a_1^2 + b^2)^{-7/2}\right] \qquad A5.5$$

Equations A5.1 and A5.2 do not give the field at a point (c,y) unltess $(c^2 + y^2)^{\frac{1}{2}} < a$. However an expansion can be developed about a point (c,0) which is convergent if $y < a$ for all value of c. Thus:

$$H(c,y) = \pi\left[C_1(b + c) + C_1(b - c) - (y^2/2)(C_3(b + c) + C_3(b - c)) + (3/8y^4)(C_5(b + c) + C_5(b - c)\right] \qquad A5.6$$

and

$$h \simeq H(0,0) - H(0,y) \qquad A5.7$$

Consideration of equations A5.6 and A5.7 indicates that high homogeneity and an optimum value for the field H(0,0) (for a given current) are not compatible. For the latter requirement, which is important for superconducting magnets because of the high cost of material, the ratio b/a_2 should be approximately unity. For the former requirement the ratio b/a_2 should be much larger than unity. As this ratio decreases the axial homogeneity decreases rapidly while the radial homogeneity however does so much less rapidly. High axial homogeneity may however be obtained over a useful proportion of the solenoid length (near its centre) by the simple expedient of using suitable correction coils. The design of a practical superconducting solenoid therefore is a compromise between high field per unit length of wire and high radial field homogeneity and includes correction coils for axial field homogeneity.

The final dimensions chosen for the main coil in the present design (i.e. $2b = 10cm$, $2a_2 = 5cm$ and $2a_1 = 2cm$ - see figure A5.1). give a radial homogeneity ($1 : H(0,0)/H(0,a_1)$ of approximately $1 : 10^4$ and a field $H(0,0) \simeq 40Kgauss$ at a current of 30amperes (which is the manufacturers expected critical current for the Supercon A25 wire at 40Kgauss when wound into a solenoid of this size).

The correction coil geometry and configuration were calculated for optimum axial homogeneity along the $y = 0$ axis over $Z = \pm 1.5cm$ as follows:

From equation A5.6 including the correction coil parameters (see figure A5.1) the field at any point (c,0) is given by

$$H(c,0) = \pi[\ C_1(a_2,a_1,b + c) + C_1(a_2,a_1,\ b-c) \ + \ 2\ C_1(a_2',a_1',\ b+d+c) \ + \ C_1(a_2',a_1',\ B+d-c)\ ] \qquad A5.8$$

Now putting $a_1' = a_2$ and starting with reasonable values for a_2', b' and d a consistent fine scale numerical search was made to optimize these values. This was done by calculating $H(c,0) - H(0,0) = \Delta(c_j)$ for $0 < c_j < 1.5cm$ in steps of 0.01 and finding the correction coil parameter values which gave the minimum square derivation $\sum_{j=1}^{150} (\Delta(c_j)^2)$. The computer program (for which the author is indebted for assistance to J.L. Crawford) is included in appendix A8. The method is tedious and inelegent but is justified for a once only application since it is not unreasonably long in execution. The final values obtained for the correction coil are: $a_2' = 3.05cm$ ($a_1' = 2cm$), $b^1 = 1,0cm$ and $d = 4.5$ cm.

The total length of wire ℓ required for a coil of dimensions b, a_2 and a_1 is given by

$$\ell = 2\pi a_1^3(\alpha^2 - 1)\beta/A$$

where $\alpha = a_2/a_1$, $\beta = b/a_1$ and A is the effective cross sectional area of the conductor ($1.45 \times 10^{-3} cm^2$ for the present case). Substituting values for the main coil and also for the correction coils gives $\ell_m + 2\ell_c = \ell_{TOTAL} = 1670m$. The inductance L of the solenoid is given (Terman, 1943) by

$$L = a_1^5[\beta(\alpha - 1)+A]^2(\alpha + 1)[\theta - \lambda(\alpha-1)/\beta] \times 10^{-6}$$

where θ and λ are functions of α and β and in this case for the main coil are $\theta = 0.01197$ and $\theta = 0.01188$. Substitution into the equation above gives $L = 0.78$ henries. The total resistance in series with the magnet (with the 0.1ohm standard resistor) is $R \approx 0.5$ ohm and therefore the time constant for energising the magnet is $\tau \approx 0.5$ seconds. However, in the event of the superconductivity of the magnet being rapidly quenched the rate at which the energy will be dumped will not depend on τ but will depend on the time constant of the effectively coupled L-R circuit comprising the magnet bobbin and the aluminium retaining sheath (see figure 2.6).

A5.2 NMR calibration of the magnet

The NMR probe and the electronic layout is shown schematically in figure A5.2. The probe may be positioned accurately at any point along the axis of the solenoid. The sample is a small cylinder (3mm in diameter and 3mm long) of pure aluminium powder in a matrix of epoxy resin. [From Higgins and Yung Kwan Chan (1968): The $^{27}A\ell$ NMR frequency is 11.112MHz at 10Kgauss. The free atom NMR frequency is 11.094MHz at 10Kgauss which is corrected by adding a virtually temperature independant Knight shift of 0.162 per cent.] The marginal oscillator circuit is due to Robinson (1959) (frequency range 200KHz to 20MHz at levels between 1 and 250mV). The

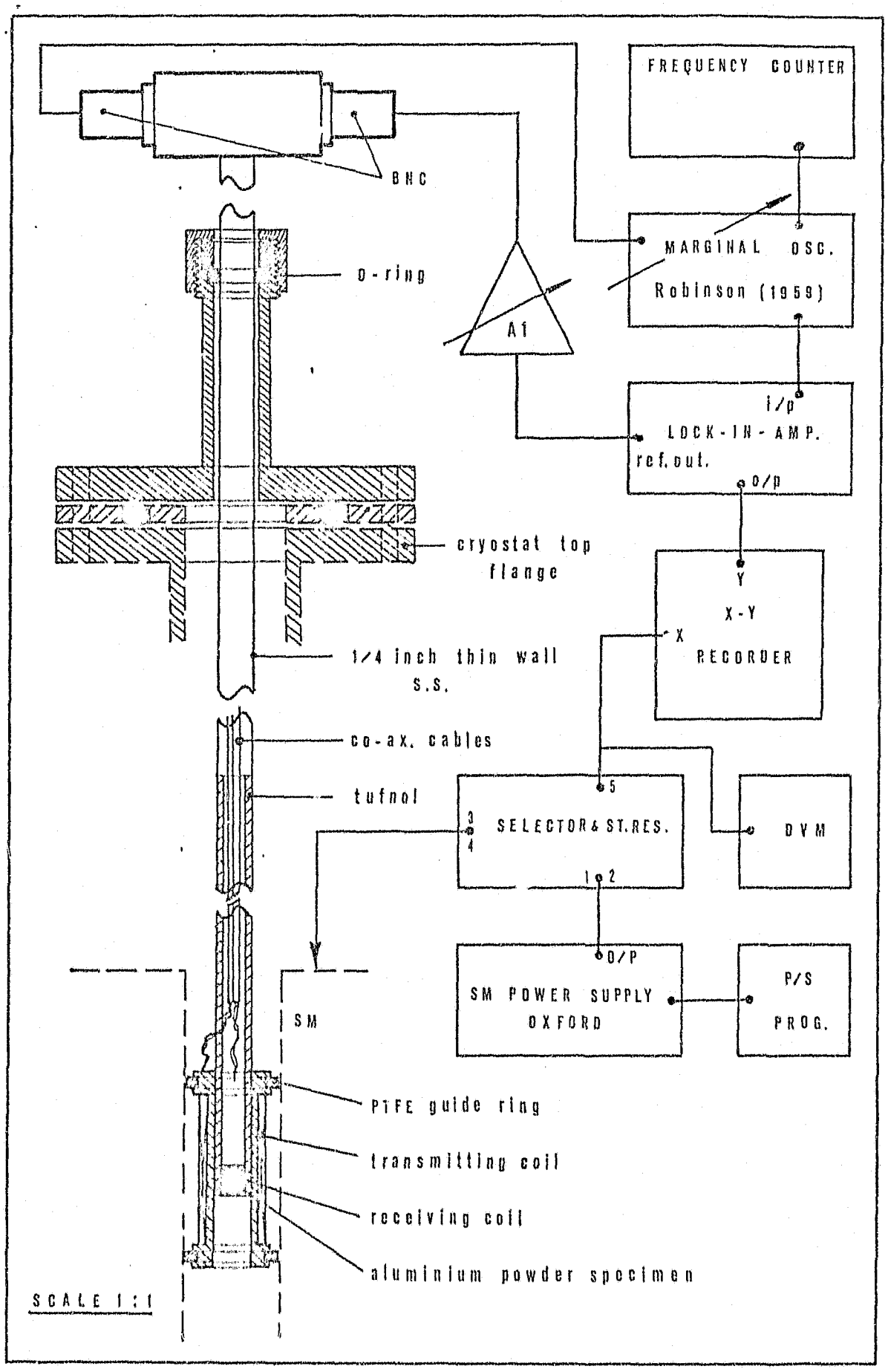


Figure A5.2. Schematic diagram of the NMR probe and electronics for the calibration of the superconducting solenoid magnet.

amplifier A1 is the same power amplifier which is used to drive the transducer of the magnetometer. The frequency and magnitude of modulation used were 33Hz and approximately 10gauss respectively.

Procedure: With the marginal oscillator tuned to a particular frequency the NMR line was located by sweeping the magnetic field in the anticipated range. After optimization by adjustment of the LEVEL of the marginal oscillator the NMR line was plotted on the X-Y recorder and the frequency and magnet current corresponding to the line centre were noted. This process was repeated for increasing fields up to approximately 15Kgauss and then in decreasing fields down to zero field. The NMR line was found to be approximately symmetrical with a half height width of approximately 2.5gauss. The results are shown in figure A5.3 where the frequency readings have been converted to field values. The exact calibration figures for the magnet in increasing and decreasing fields (0-15Kgauss) respectively are:

1.3958Kgauss/amp and

1.3892Kgauss/amp

Axial homogeneity was subsequently determined by moving the probe along the z axis of the solenoid in measured steps with the magnet current held constant at 2.55amps. A graph of B(z)/B(0) versus z is plotted in figure 2.8. The small asymmetry and lack of homogeneity ($\sim 2{:}10^4$) along the positive z direction at $z \simeq 1.5$cm is probably due to slight flux trapping after cycling the magnet to 15Kgauss.

A5.3 Hall probe and ancillary apparatus

The electronic circuitry for the Hall probe and for the superconducting magnetic power supply programmer are contained in a single unit (which also houses the liquid helium depth gauge) and are shown

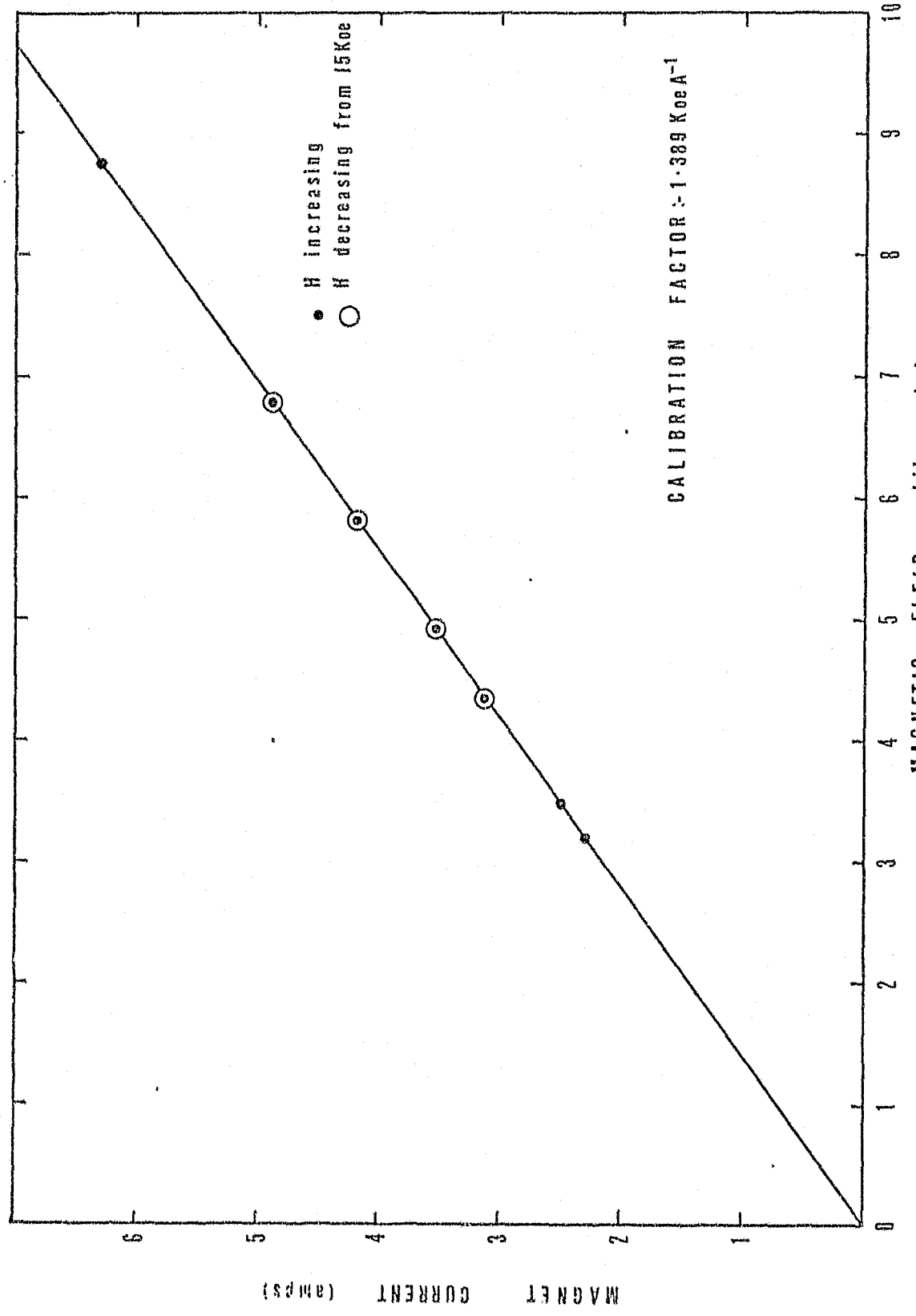


Figure A5.3. The calibration H-I curve for the superconducting magnet obtained from the NMR results in increasing and decreasing I.

schematically in figure A5.4.

The electronics for the Hall probe consists, in essence, of a constant current source and circuitry for linearizing the Hall probe output and for compensating for the small zero field potential which appears across the Hall probe due to slight asymmetry of the potential contacts. The Hall probe element is a Siemens Model RHY18 which is especially suitable for low temperature operation.

The magnet power supply programmer provides an output voltage which may be adjusted manually or may be swept up or down linearly with time at various present rates. The dynamic range of the sweep may be varied between 10 per cent and 100 per cent by adjustment of R_5 (RANGE).

The circuit for the 'selector unit', containing the standard resistors for monitoring the magnet current, is shown in figure A5.5.

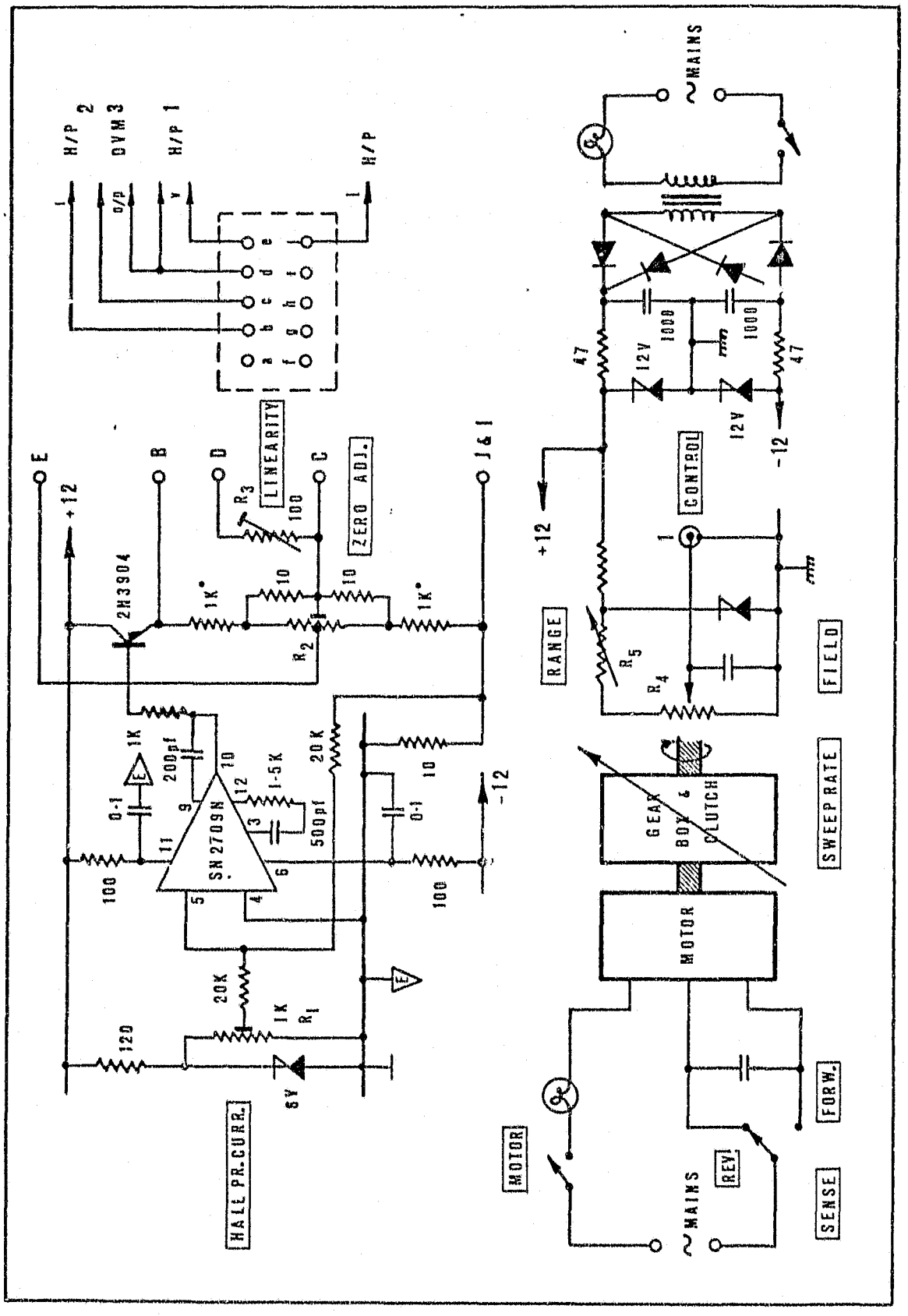


Figure A5.4. Circuit diagram for the Hall probe electronics and the magnet power supply programmer.

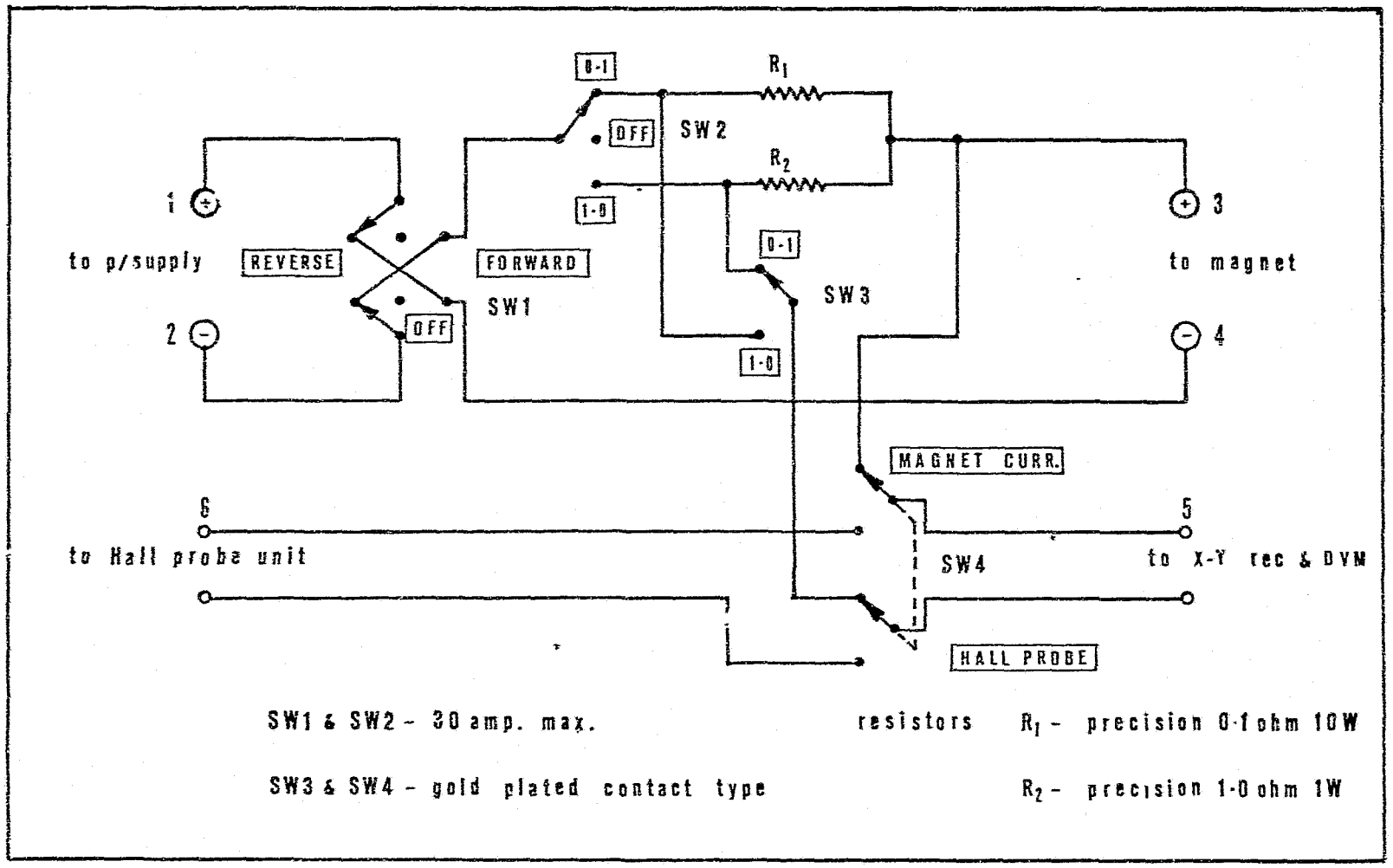


Figure A5.5. Circuit diagram for the magnet current monitor and selection unit.

APPENDIX

A6 Continuous Reading Depth Gauge for Liquid Helium

The design of such a gauge of moderate accuracy seemed to be too trivial to warrant a literature search. The present design is included to complete the description of the apparatus. The gauge probe and its associated electronic circuitry are shown schematically in figure A6.1. The principle of operation depends on the relatively large difference in the thermal conductivity between helium liquid and vapour. The sensitive portion of the probe consists of a tufnol tube (6mm diameter and 35cm long) into which a shallow double spiral groove has been cut to accommodate a non-inductively wound sensing wire (see figure A6.1). The sensing wire consists of a 42 S.W.G. manganin wire which is very lightly 'tinned' with ordinary radio solder over most of its length. This makes the wire superconducting with a critical temperature Tc in the range $5K < T < 7K$. The untinned portions are at the top of the probe at the two ends of the wire where it is soldered to copper leads.

If the probe is totally immersed in liquid helium the sense wire is superconducting and the resistance virtually zero. If a portion of the probe is above the level of the liquid helium an electric current can be found for the wire which will thermally quench the superconductivity in this portion. The value of this current depends on the thermal conductivity of the surrounding medium and the electrical and thermal conductivity of the manganin wire. (The layer of normally conducting solder is too thin to affect the result appreciably.) The

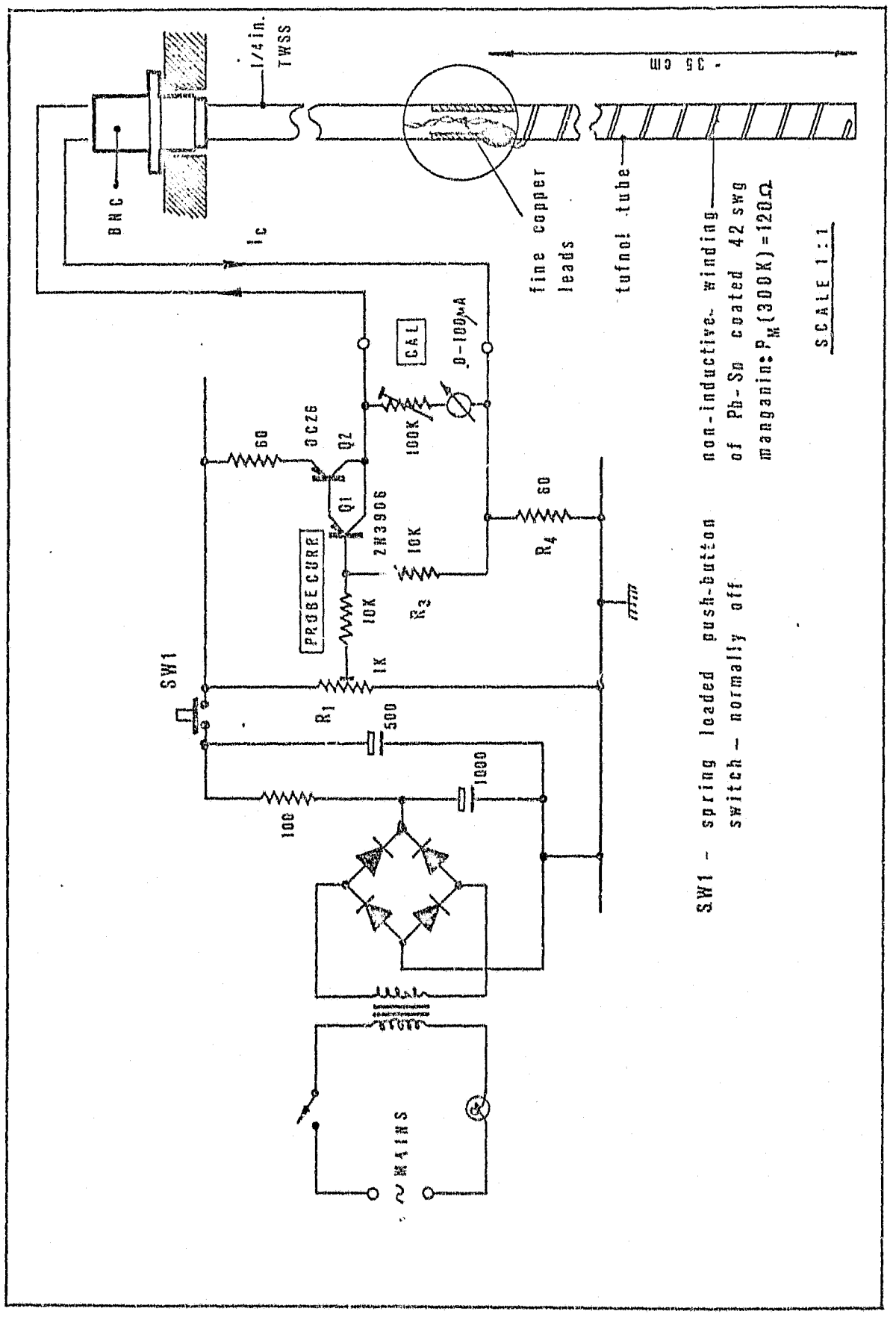


Figure A6.1. Schematic diagram of the continuous reading liquid helium depth probe and associated electronics.

short untinned sections of wire at the top of the probe ensure that nucleation of the quenching process takes place in this region. The low thermal conductivity of the manganin wire and the relatively higher thermal conductivity of the LHe prevents the quenching process from propagating below the helium liquid level. The electrical resistivity of the manganin wire is virtually independent of temperature and therefore the resistance of the sense probe R_m increases linearly with decreasing liquid helium level below the top of the probe.

The electronic circuitry is designed to monitor the probe resistance R_m and to maintain a constant current I_c through the probe. Thus with reference to figure A6.1: I_c is determined by the bias, on the base of transistor Q1, which in turn depends on the setting of the potentiometer R_1 and on feedback via R_4 via R_3. Thus I_c is held constant at a value which is determined by the setting of R_1. The resistance R_m is monitored on the meter which measures the potential drop across the probe.

Set up of procedure: With the probe in-situ in the cryostat helium transfer is commenced until the cryostat just cools to 4K and transfer of liquid commences. The PROBE CURRENT is now increased from minimum with the switch SW1 held close until the meter indication just reaches a flat maximum. (It may be necessary to adjust the CALibration control to keep the meter on scale.) The CALibration control is now adjusted to give full scale deflection on the meter. The cryostat is filled with liquid helium and the meter will, with the switch SW1 closed, read approximately zero when the liquid reaches the top of the probe.

The present gauge was found to be very nearly linear when tested in a transparent glass dewar.

APPENDIX A7

A7 Resistivity Measurement

A very brief outline is given here of the theory of the impulse eddy current decay method from the paper by Bean, de Blois and Nesbitt (1959).

Thus: If a magnetic field is suddenly applied to a conductor eddy currents are induced which tend to oppose the changing magnetic field in the conductor. The average induction $\bar{B}$ therefore does not immediately reach its equilibrium value in the conductor but does so exponentially with a time constant which is characteristic of the resistivity and permeability of the conducting material. If these properties are uniform in the conductor, then, neglecting displacement currents in Maxwell's equation, the time rate of change in B is given by

$$\partial\bar{B}/\partial t = (10^9 \rho/4\pi\mu)\nabla^2\bar{B} \qquad \text{A7.1}$$

where ρ is the resistivity in ohm. cm and μ is the permeability.

An extensive tabulation of solutions to equation A7.1 for various specimen geometries has been given by Carslaw and Jaeger (1959). For rods of constant cross section the voltage at long times after a change in field ΔH_o, induced in a coil of N turns wound around this section is given by

$$v(t) = 10N(\Delta H_o)\rho \exp(-t/\tau_R)$$

where $\tau_R = 2.17 \times 10^{-9}\mu R^2/\rho$

for a circular cross section of radius R and

$$v(t) = [160N(\Delta H_o)\rho \exp(-t/\tau_{ab})]/\pi^3 ab$$

where $\tau_{ab} = [\, 1.27 \times 10^{-9} \mu a^2 b^2 \,] / \rho(a^2 + b^2)$

for a rectangular cross section of sides a and b.

For any arbitrary cross section or overall sample shape, resistivity ratios are still obtainable from time constant (τ) ratios without a knowledge of the geometrical function, thus:

$$\rho(T_1)/\rho(T_2) = \tau(T_2)/\tau(T_1)$$

Method: A schematic diagram of the electronic apparatus (from Clarke and Mordike, 1966) is given in figure A7.1. The principle of operation is as follows. The multivibrator acts as a master timer which switches (i) the current in the primary coil (via amplifier A1) to provide the changing magnetic field (ii) the precision R-C network (via A_2) and (iii), a relay switch which alternately allows the C.R.O. to sample the exponentially varying signals from the secondary coils and from the R-C network. By adjusting the PRE-PULSE generator these two signals can be synchronised, both increasing or both decreasing, on the C.R.O. Finally, by adjusting the REF. AMPlifier, SIG. AMPlifier and R and C the two traces on the C.R.O. can be made to coincide exactly over most of their length (as stated previously the eddy currents are exponential only at long times after the impulse). R and C may then be read off to give the decay time constant $\tau = RC$. An example is given in figure A7.2 where τ has been determined experimentally for various values of R and C on a single specimen held at constant temperature.

For very good conductors it is necessary to compensate for the inherent relaxation time of the primary pulsing coil. This is easily done by measuring the time constant with and without the specimen in the coils and then subtracting to obtain the difference (Stern, Levy, Kagiwada and Rudnick, 1962).

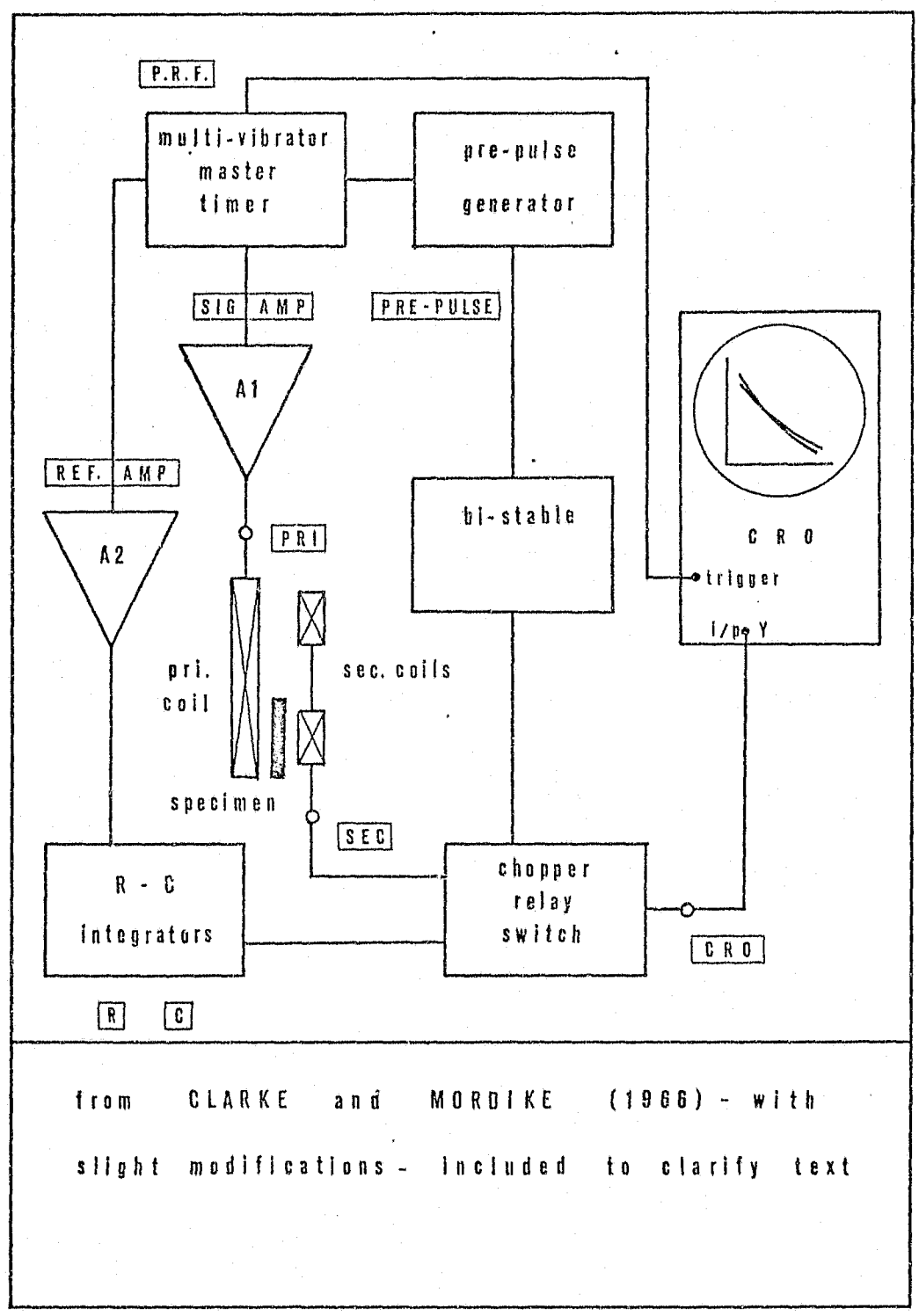


Figure A7.1. Schematic diagram of the apparatus and electronics for measurement of resistivity by the eddy current decay method (from Clarke and Mordike, 1966).

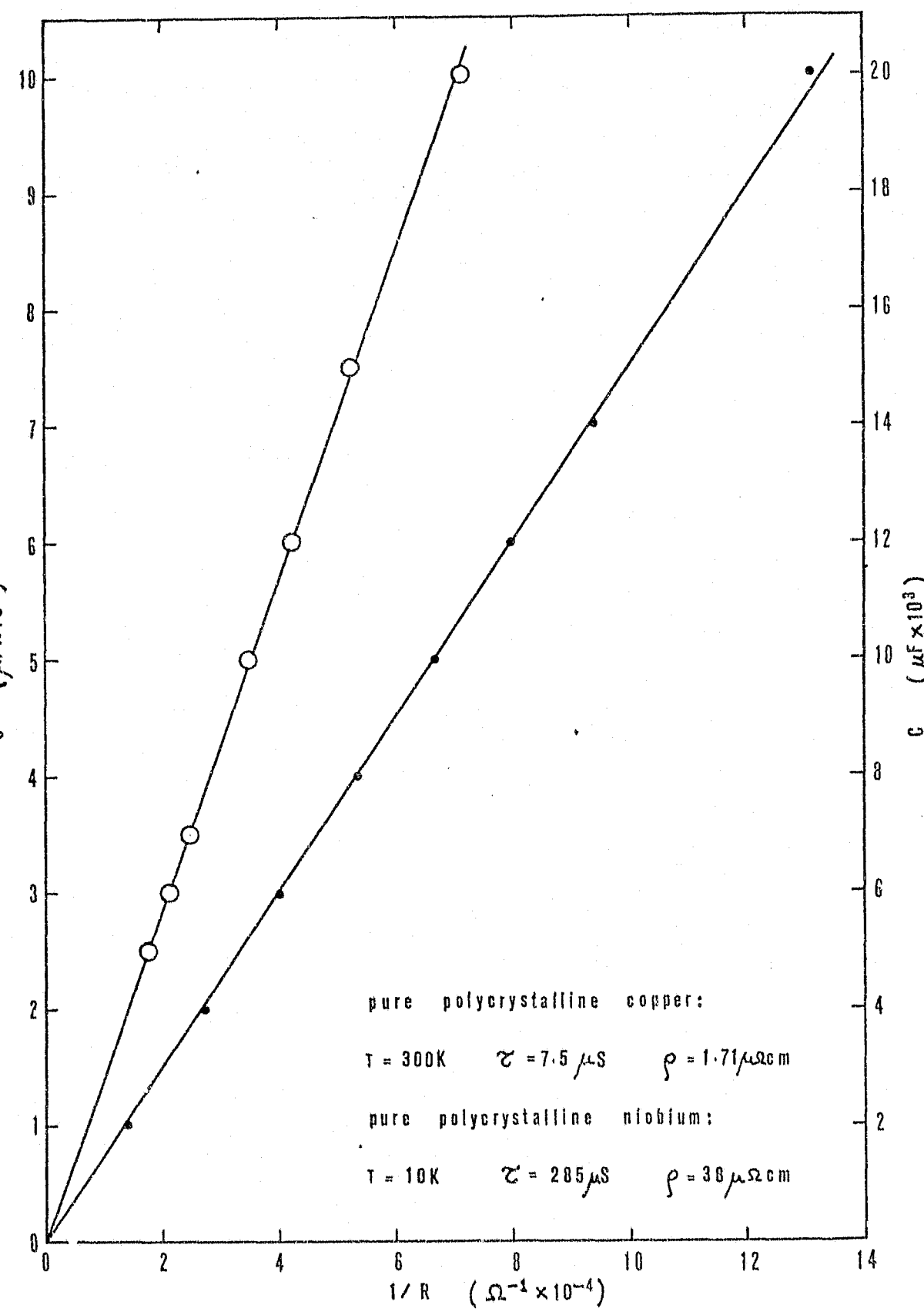


Figure A7.2. The results of experiments to determine the resistivity of a copper and a niobium specimen by the eddy current decay method and to demonstrate the relative accuracy obtainable.

APPENDIX A8

Computer programs

The programs which follow are all written in FORTRAN IV.

1. Resistance to temperature fit for Germanium resistance thermometer No. 1814 (in the range 2.5K < T < 12K)

Programs to read list of voltage v and current c and to write list of corresponding temperature t.

```
1          real*4 r,t
2          real*8 dr, dt, dz, d1, d2, d3, d4, d5, d6, d7
3    1     format(2y)
4    2     format(4x,'t')
5    3     format(1y)
6          write(6,2)
7    4     read(5,1) v,c
8          r=v/c
9          dr=r
10         dz=dlog10(dr)
11         d1=+18.451208170231/dz
12         d2=-65.682517688506
13         d3=+93.641900933404*dz
14         d4=-68.744309674618*dz*dz
15         d5=+27.456806656060*dz*dz*dz
16         d6=-5.6484892581927*dz*dz*dz*dz
17         d7=+0.4721052835856*dz*dz*dz*dz*dz
18         dt=d1+d2+d3+d4+d5+d6+d7
```

```
19          t=1/dt
20          write(6,3)t
21          go to 5
22          stop
23          end
```

2. Calculation of $H_e(r,0)$

Programs to read the radius ro≡R and the thickness d≡d for the cylinder and write $H_e(r, 0)$ in steps of r=R/10 between r=0 and r 1.

```
 1          double precision a2,xx(21,21),y(21,21),p(21),rho(21,21),pm,dy(21)
 2          double precision a1,xr(21),om,rho(21,21),q(21)reslty,dyl,dyj
 3          double precision rho2(21,21),reslx,rho3(21,21),r(21),dp,ro,d,ds
 4          double precision s(21),p1,r1,a,b,c,x(21),oy,yo
 5          real mr
 6          integer z
 7    1     format(2f10.4)
 8          read(5,1)ro,d
 9          z=0
10          pi=3.14159
11          ds=d*d
12          dp=d/(pi+pi)
13          r1=2.0
14          jj=idint(ro+1.0)
15          jk=idint(2.0*ro+1.0)
16          jl=idint(ro+r1)
17          do 12 i=1.2
18          r1=r1+1.0
19          if (z.gt.0) go to 60
20          c=1.0
```

```
      do 6 j=1,jk
      a=-1.0
      b=-1.0
      c=c+1.0
      dy=2.0*ro*c-c*c
      yo=dsqrt(oy)
      dy(j)=yo/ro
      do 6 k=1,jk
      a=a+1.0
      b=b+1.0
      y(k,j)=-yo+b*dy(j)
      if (j.gt.1) go to 2
      x(k)=-ro+a
    2 xx(k,j)=(x(j))-x(k)*(x(j)-x(k))+ds
    6 continue
  110 format(10x,'radius of disc=',f3,0,10x,'thickness of disc=',f7.4)
      write(6,110) r0.0
  111 format(10x,'radial distance',16x,'ratio md/mo')
      write(6,111)
   60 z=0
      do 13 j=1,jk
      do 13 k=1,jk
      if (j.gt.1) go to 13
      xr(k)=(x(k)-r1)*(x(k)-r1)+ds
   13 rho3(j,k)=0.0
  600 do 8 j=1,jk
      do 8 k=1,jk
      do 70 l=1,jk
      do 7 m=1,jk
```

```
      if (z.gt.0) go to 66
      a1=xr(1)+y(m,1)*y(m,1)
      om=1.0/dsqrt(a1)
      rho1(m,1)=om*om*om*dp
      rho(m,1)=rho1(m,1)
   66 a2=xx(1,j)+(y(k,j)-y(m,1))*(y(k,j)-y(m,1))
      pm=1.0/dsqrt(a2)
    7 p(m)=rho1(m,1)*pm*pm*pm*dp
      dy1=dy(1)
      call simpsn(jk,p,dy1,reslty)
   70 q(1)=reslty
      call simpsn(jk,q,1.0,resltx)
      z=1
    8 rho2(k,j)=resltx
      do 9 j=1,jk
      do 9 k=1,jk
      rho1(k,j)=rho2(k,j)
    9 rho3(k,j)=rho3(k,j)+rho2(k,j)
      if (rho2(j1,j1).lt.1.0d-5) go to 90
      go to 600
   90 do 11 j=1,jk
      do 10 k=1,jk
   10 r(k)=rho3(k,j)+rho(r,j)
      dyj=dy(j)
      call simpsn(jk,r,dyj,reslty)
   11 s(j)=reslty
      call simpsn(jk,s,1.0,resltx)
      mr=resltx
  112 format(14x,f3.0,26x,f8.4)
```

```
79          write(6,112) r1,mr
80      12  continue
81          stop
82          end
```

Calculates superconducting solenoid correction coil parameters for optimum axial homogeneity

For definition of parameters see figure A5.1. Program reads search field for correction coil parameters, viz: bpin≡a_2^1 (minimum), bpfin≡a_2^1 (maximum), lpin≡b^1((minimum), lpfin 6^1 (maximum), dpin≡d (minimum) and dpfin≡d (maximum) and the search resolutions dbp≡Δa_-^1, dlp≡Δb_-^1 and ddp≡Δd and finds correction coil geometry for optimum axial homogeneity over central 60 per cent of solenoid length. Main coil parameters are a≡a_1=1, ap≡a_2=2.5, b≡a_1^1=2.5 and l≡b=5. Program also plots final reduced axial field $B_z(z)/B_z(z=0)$ as a function of distance z along the axis of the solenoid.

```
Real l,lp,lpin,lpfin,lpmin,min,meang,lpe,lmz,ll
dimension 99(53), z(53),data(1000),y(5),g(51),cc(51)
 1      1   format(3(f4.2,1x))
 2      2   format(3(f6.4,1x))
 3      3   format(3(f4.2,1x))
 4      4   format(20 x 'a=',f5.2,5x,'ap='f5.2,5x,'b='f5.2,5x'd='.
 5      1   20x'values for min. sq. dev:', 5x'bp=',f5.2,
 6      2   5x'lp=',f7.4,5x,'dp='f5.2/
 7      3   40x,'sum of dev. sq=',(pe10.311)
 8      5   format(15x,f5.1,1pse15.3)
 9      6   format(18x,'z',s(f13.1,2x)/)
10      7   format('1',20x,'bp searched from',f5.2,'to',f5.2,'bt',f5.2)
11      8   format(20x,'lp searched from',f7.4,'to'f7.4,'be',f7.4)
```

```
12      9   format(20x,'dp searched from',f5.2',to',f5.2,bt',f5.2///)
13          f(x,p) alog(sqrt(***+p*p)+x)
14          cp(bb,p)=p*(f(bb,p)-f(ap,p))
            gf(bb,ll,ss,dd)=cp(bb,ll+dd)+cp(bb,ll-dd)+cp(bb,ll+ss)
                                        + cp(bb,ll-ss)
15          nin=5
16          nout=6
17          a=1.0
18          ap=2.50
19          b=2.50
20          l=5.0
21          read(nin,1)bpin,bpfin,dbp
22          read(nin,2)lpin,lpfin,dlp
23          read(nin,3)dpin,dpfin,ddp
24          min=1.e50
25          do 101 i=1.51
26          z(i)=(i-1)/1
27          lpz=l+z(i)
28          lmz=l-z(i)
29          lmz=l-z(i)
30    101   cc(i)=lpz*(f(b,lpz)-f(a,lpz))+lmz*(f(b,lmz-f(a,lmz))
31          bp=bpin
32     21   lp=lpin
33     22   dp=dpin
34     23   sum=0
35          do 24 i=1,16
36          s=dp+z(i)
37          d=dp-z(i)
38          g(i)=cc(i)+gf(bp,lp,s,d)
```

```
      24    sum=sum+g(i)
            meang=sum/16.0
            sumsq=0.0
            do 25 i=1,16
            dev=g(i)-meang
      25    sumsq=sumsq+dev*dev
            if(sumsq-min)26,27,27
      26    min=sumsq
            bpmin=bp
            lpmin=lp
            bpmin=dp
      27    dp=dp+ddp
            if(dp-dpfin)23,23,29
      29    lp=lp+dlp
            if(lp-lpfin)22,22,30
      30    bp=bp+dbp
            if(bp-bpfin)21,21,34
      34    write(nout,7)bpin,bpfin,dbp
            write(nout,8)lpin,lpfin,dlp
            write(nout,9)dpin,dpfin,ddp
            write(nout,4)a,ap,b,1,bpmin,lpmin,dpmin,min
            do 35 i=1,51
            smin=dpmin+z(i)
            smin=dpmin+z(i)
            dmin=dpmin-z(i)
      35    g(i)=cc(i)+gf(bpmin ,lpmin,smin,dmin)
            do 40 k=1,5
      40    y(k)=k/10.0
```

```
      write(nout,6)(y(k),k=1,5)
      do 3t i=1,51
37    gg(i)=g(i)/g(1)
      do 36 j=1,46,5
      jm1=j-1
      yy=jm1/10.0
      k1=jm1+11
      k2 jm1+5
36    write(nout,5). . .(gg(kk),kk=k1,k2)
      call plots(data(1),4000)
      call plot(0.0,-11.0-3)
      call plot(0.6,0.5,-3)
      call symbol(4.5,6.5,0.1,'jlcforo7',0.0,8)
      call scale(gg,5.0,51,1,10.0)
      z(52)=0.0
      z(53)=0.5
      call axis(0.0,0.0,'z',-1,10.0,0.0,0.0,0.5,10.0)
      call axis(0.0,0.0,'99',2,5.0,90.0,99(52),99(53),10.0)
      call line(z,99,51,1,0,0)
      call line(z,99,51,1,0,0)
      call plot(15.0,0.0,999)
      end
      1*
      11 lked syslib dd
      11 do dsname=sys7,load,disp old
      11 go plo .erc dd unit=plotterc,disp(old,delete)
      11 go sysin,dd*
      call plot(0.0,-11.0,-3)
      call plot(0.6,0.5,-3)
```

```
96          call symbol(4.5,6.5,0.1,'jlcforo7',0.0,8)
97          call scale(99,5.0,51,1,10.0)
98          z(52)=0.0
99          z(53)=0.5
100         call axis(0.0,0.0,'z',-1,10.0,0.0,0.0,0.5,10.0)
101         call axis(0.0,0.0,'99',2,5.0,90.0,99(52),99(53),10.0)
102         call line(z,99,51,1,0,0)
103         call plot(15.0,0.0,999)
104         end
105         1*
106         11 lked syslib dd
107         11 do dsname sys7,load,disp=old
108         11 go plotterc dd unit plotterc disp=(old,delete)
109         11 go sysin,dd*
            3.00,3.50,0.05
            1.0000,2.0000,0.0375
            3.00,4.50,0.01
            1*
            11
```

Materials Science and Engineering, 16 (1974) 125—132
© Elsevier Sequoia S.A., Lausanne — Printed in The Netherlands

A New Experiment to Study the Deformation of Body-Centred Cubic Crystals

A. BALL
Department of Metallurgy and Materials Science, University of Cape Town (S. Africa)
T.B. DOYLE
Department of Physics, University of Witwatersrand, Johannesburg (S. Africa)

(Received August 7, 1973; in revised form January 8, 1974)

SUMMARY

The results of an experiment which produces an equal shear stress on all planes of a [111] zone of a body-centred cubic niobium crystal are discussed with reference to the deformation behaviour in uniaxial tension.

An asymmetry of the critical resolved shear stress for slip in niobium crystals on {112} planes has been inferred from the observation that the transition from (101) [111] slip to (1$\bar{1}$2) [$\bar{1}$11] slip is displaced in opposite senses for uniaxial compressive and tensile loading from the locus of orientations having equal resolved shear stresses on the two systems. It has been deduced that the critical resolved shear stress for slip on the {110} planes is intermediate between the smaller stress required for shear in the twinning sense on the {112} planes and the stress to cause shear in the anti-twinning direction on {112} planes. This asymmetry is reported to increase with decreasing temperatures [3]. The slip line observations on iron - silicon crystals by Taoka, Takeuchi and Furubayashi [4] and by Šesták and Zárubová [5] demonstrate asymmetry and more recent works by Statham, Vesely and Christian [6] and by Šesták and Blahovec [7] investigate the phenomenon in Nb - Mo and Fe - Si alloys respectively. Hirth and Lothe [8] and Foxall *et al.* [3] have suggested that this behaviour is indicative of an asymmetry of cross slip probability.

Bowen, Christian and Taylor [9] pointed out the difficulty of demonstrating the asymmetry of slip directly in a convincing manner. Yield stress values are not sufficiently accurate or reproducible and the bending experiments of Šesták and Libovicky [10] and Šesták, Sladek and Zárubová [11] can be difficult to interpret because slip traces, other than those indicating the asymmetry, are always present.

1. INTRODUCTION

The crystallography and rate-controlling mechanisms of dislocation slip in body-centred cubic metals have been the subject of numerous papers. A discussion of the topic has recently been given by Christian and Vítek [1] and by Christian [2]. The rapid increase in the critical resolved shear stress with decreasing temperature below room temperature has, in turn, been attributed to the lattice friction stress, impurities, cross slip probability and the movement of jogs. The observation by electron microscopy of a high remanence of screw dislocations after deformation at ambient temperatures and below, indicates that these dislocations are less mobile than edge dislocations and their motion may therefore determine the flow stress of the body-centred cubic metals.

The slip lines produced during deformation are generally wavy and the observation of non-crystallographic slip, especially at elevated temperatures, has been interpreted as resulting from microscopic cross slip of dislocations with Burgers vectors $b = a/2\langle 111\rangle$ between the {110} and {112} glide planes.

The experiment described in this paper follows from the work of Smakula and Klein [12] and Rachinger and Cottrell [13]. These authors examined the slip systems in compounds with the caesium chloride-type structure by analysing the shape of the bump produced on the underside of thin crystals by indentation of the upper surface. If material was 'punched through' on {100} planes along a common ⟨001⟩ direction to produce a well-defined square bump when the crystal plane was close to a cube plane, the experiment established that slip was confined to the {100} ⟨001⟩ system. Since niobium is known to slip on planes of a given ⟨111⟩ zone, the application of a flat circular punch normal to a thin (111) crystal may provide information with regard to preferred slip planes of the zone and cross slip around the cylinder of maximum shear stress. Although the results are qualitative, the experiment is unique in the sense that it examines the effect of an equal applied shear stress on all slip planes of a given a/2 [111] dislocation and clearly shows an asymmetry of slip behaviour.

2. EXPERIMENTAL

A single crystal rod (approximately 6.5 mm diameter) of MARZ grade niobium supplied by the Materials Research Corporation, New York (interstitial content less than 310 p.p.m., substitutional content less than 50 p.p.m. excluding tantalum, which is approximately 200 p.p.m.) with an axial orientation [111], was spark sliced into discs 1 mm to 3 mm thick. The (111) faces of the discs were spark planed flat and parallel and then chemically polished in a 70:30 HNO_3,HF mixture at room temperature.

The specimen disc was placed flat on a 5 mm thick piece of lead, which had been covered with a thin piece of surgical rubber. (For the high temperature experiment aluminium was used without the rubber.) The deformation was produced by pushing a flat polished 3 mm diameter cylindrical punch into the (111) face of the disc at a rate of 0.175 mm per minute. A special jig, which ensured that the punch moved normal to the disc, was placed between the faces of a compression machine and the load was continuously recorded. The impression produced was typically 0.1 mm to 0.3 mm deep. The experiment was performed at 77K, 159K, 300K, 450K and 600K. A number of specimens were 'double punched' by using a 2 mm diameter punch in the reverse direction and concentric with the deformation mound produced by the initial punch. An optical examination of the deformation was made before the dislocation content and arrangement were determined by etch pitting. The replaned and polished (111) surfaces of the disc are ideal for the production of etch pits in niobium. A prior decoration heat treatment at 600°C for half an hour in acetylene at a pressure of 5×10^{-6} mm Hg was found to be necessary. The etching was produced in a 18:9:9 H_2SO_4, HF, H_2O_2 mixture in the manner described by Nembach [14].

3. RESULTS

At all temperatures, except 77K, the deformation with the solid punch resulted in a flat well-defined cylindrical impression (Fig. 1a) on the top surface, and a flat roughly triangular mound on the lower surface of the disc (Fig. 1c). The load required for the deformation increased rapidly with strain and there was no initial yield or easy glide behaviour. The truncated triangular outline of the mound lies just inside the projection of the punch perimeter (*i.e.* the truncated triangle is inscribed by the projection of the circular impression as drawn in Fig. 2). It was found that the triangular shape of the mound was more pronounced for increasing sample thickness and for lower deformation temperatures (Fig. 3). At 77K the specimens deform by twinning.

The crystallography of the deformation, as determined by X-ray Laué photographs, is shown in Fig. 2. The long sides of the truncated triangle lie along traces of the three {112} planes normal to the plane of the disc. The applied shear in the [111] direction on these three {112} planes corresponds to shear in the twinning sense for the body-centred cubic lattice. The 'double punching' experiment resulted in the 180° rotation about the axis normal to the disc of the triangle with respect to the $[\bar{1}\bar{1}2]$ direction marked in the perimeter of the disc as shown in Figs. 1c and 1d. Hence, the long sides of the smaller

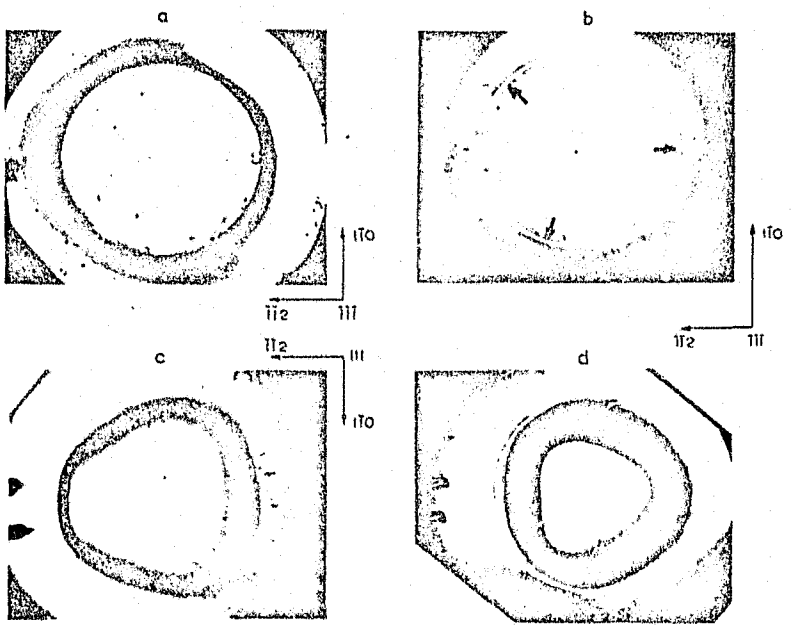


Fig. 1. (a) Upper surface of a punched disc. Punch diameter 3 mm. (b) Upper surface of a punched disc after spark planing and acid polishing. Arcs of rapid dissolution are indicated. (c) Lower surface of punched disc showing triangular mound. (d) Triangular mound produced by 'double punching'. The $[\bar{1}\bar{1}2]$ direction was marked on the perimeter on both sides of the disc.

triangle also correspond to shear on the {112} planes in the twinning direction.

After spark planing the *upper* surfaces of the specimens which had been deformed with the punch (*i.e.* until the impression was just removed), chemical polishing caused the formation of three arcs of rapid dissolution on the shear circle (see Fig. 1b). These arcs have mid-points on the poles of the $(1\bar{2}1)$, $(\bar{2}11)$ and $(11\bar{2})$ planes marked in Fig. 2. The shear as applied in the [111] direction corresponds to shear in the twinning sense on these planes. The rapid chemical dissolution in these areas must be a consequence of high remanence of dislocations after deformation.

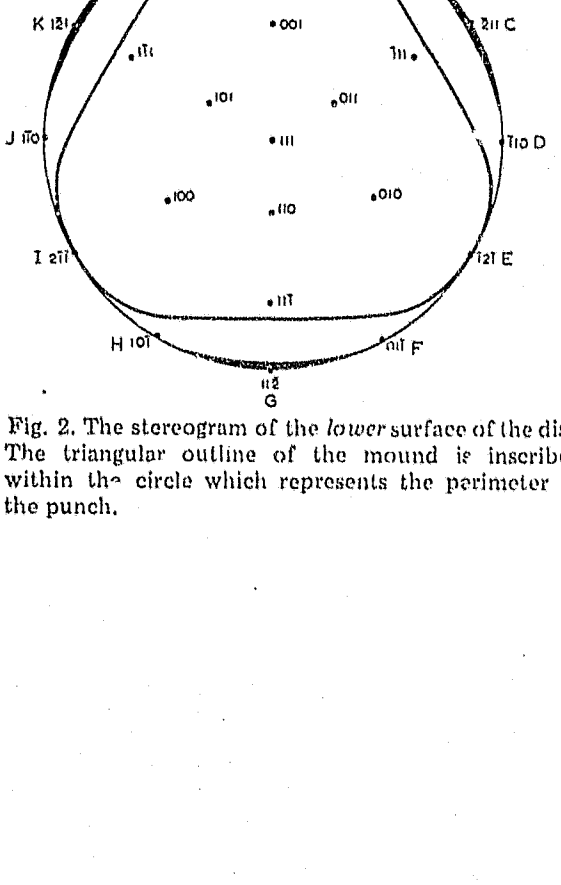


Fig. 2. The stereogram of the *lower* surface of the disc. The triangular outline of the mound is inscribed within the circle which represents the perimeter of the punch.

Etch pitting the *upper* surface of the specimens produced a dense ring of unresolvable pits on and near the punch circle with bands of pits extending outside the circle along traces of the 'twinning' {112} planes (see Fig. 4). On the *lower* surfaces (which were also spark planed flat) some pits were produced on the shear circle, but bands of pits were observed to emanate from the inside of the shear circle along traces of the 'twinning' {112} planes (see Fig. 5). Etch pit patterns intermediate between these limiting cases were found at different levels in the sample obtained by spark planing.

128

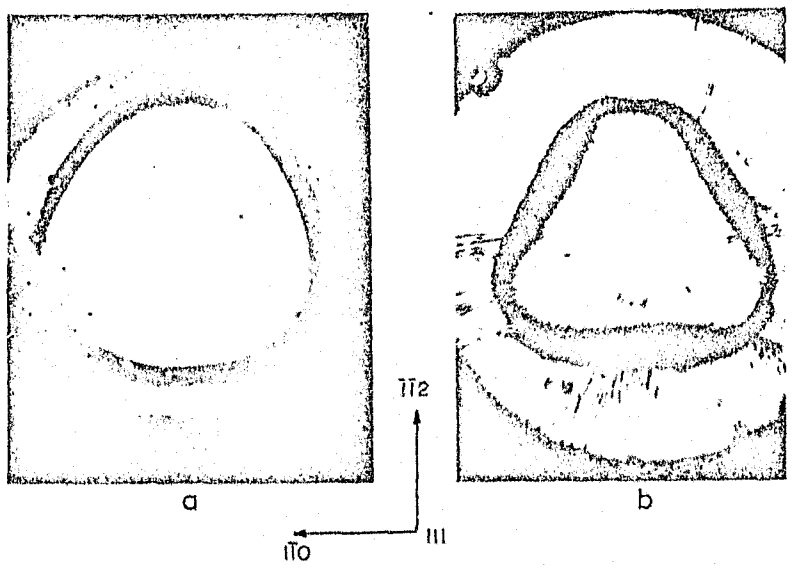


Fig. 3. (a) Typical mound produced either by punching a thin disc ($\lesssim 1$ mm), or by punching at elevated temperatures ($T \gtrsim 450°$K). (b) Typical mound produced by punching a thick disc at 298K (> 1 mm).

4. DISCUSSION

The elastic stress distribution due to a rigid flat cylindrical punch being pressed into a semi-infinite elastic solid has been determined by Boussinesq [15], by Harding and Sneddon [16] and by Sneddon [17]. A pertinent re-

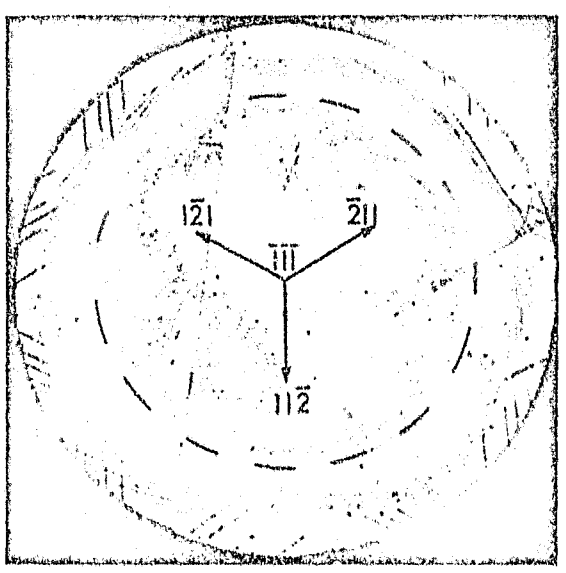
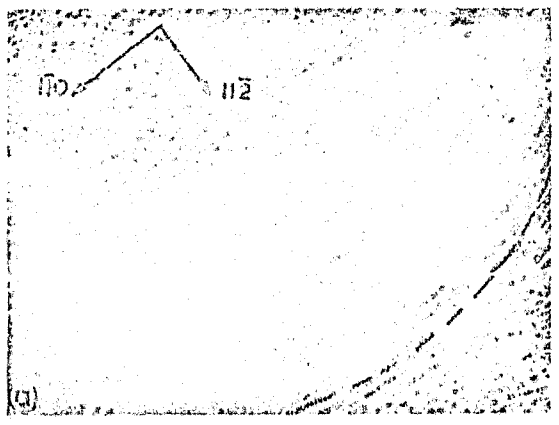


Fig. 4. The etch pit pattern on a polished *upper* surface of a punched disc. The perimeter of the punch is marked as a dotted circle (diam. 3 mm). Slight bending of the specimen is responsible for the etch pit bands at the perimeter.



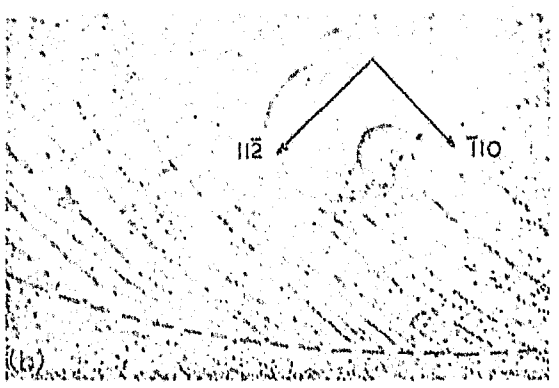


Fig. 5. Etch pit patterns produced on the polished *lower* surfaces of punched discs. The bands of etch pits follow a $\{112\}$ 'twinning' plane which lie within the circle of maximum shear stress which is marked. (a) Magn. × 52. (b) Lightly deformed specimen. Magn. × 200.

sult is the infinite value of the pressure at the perimeter of the punch on the upper surface. Thus, initial yielding should occur at the perimeter. However, for the punch to move into a *semi-infinite* solid, the complete volume immediately under the punch must be displaced by plastic flow. Movement of the punch into the solid will only commence when the plastic zones around the perimeter have spread over the total contact area. Material will then be transferred by plastic flow from under the punch to the free surface outside its edges and volume is conserved. In the case of a plate of *finite* thickness, material can be punched through to the underside if the plastic zones around the perimeter of the punch grow to form a completed cylindrical shear surface through the total thickness of the plate.

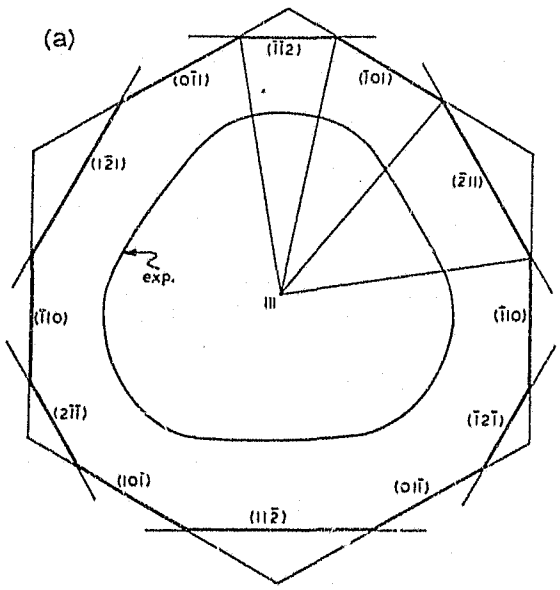
The usual theory of plasticity applies to isotropic homogeneous materials and macroscopic shear occurs along directions which are determined by the externally applied forces and constraints only. In single crystals, however, considerations such as dislocation energies, the relative friction stress for dislocation movement on discrete glide planes, cross slip probability and the relative work hardening of different glide systems indicate that macroscopic shear will not, in general, follow lines of maximum applied shear stress. (The requirement of constant volume will obviously still apply.) For example, the strong ordering forces in the b.c.c. compounds studied by Smakula and Klein [12] and Rachinger and Cottrell [13] favour shear by the glide of dislocations with b = a ⟨001⟩ on cube planes. The confinement of shear to these {100} ⟨001⟩ systems results in square bumps on the underside of thin {001} plates when the upper surfaces are subjected to indentation.

The lowest energy dislocation for body-centred cubic niobium has the Burgers vector a/2 ⟨111⟩ and glide occurs on {110} and {112} planes. In the experiment described, the imposed shear will favour deformation using dislocations with the b = a/2 [111] (see Fig. 2). Dislocations with Burgers vectors in the remaning three ⟨111⟩ directions only experience a shear stress of approximately one-third of this maximum value.

Cross slip of screw dislocations has been shown by many authors to be a process inherent to the deformation of body-centred cubic metals. It might, therefore, have been anticipated in the present experiment that the material under the punch would move through the niobium disc as a result of the repeated cross slip of screw a/2 [111] dislocations around the cylinder of maximum shear stress. This would create circular edge dislocations, which could glide prismatically to produce a *circular* flat mound on the underside of the disc. Deviation from a circular shape could be due to variations in the lattice friction stress, cross slip probability and hardening of the various planes of the [111] zone around the glide cylinder. Planar facets would result if any one type of slip plane was favoured for any one of these reasons. For example, a hexagonal bump would result if the {110} [111] system operated in preference to all others. Chin [18] has examined the situation in theory by analysing the yield loci for various values of the critical resolved shear stresses, for the {110}, {112} and {123} ⟨111⟩ slip modes. The treatment predicts a truncated triangular yield locus if {112} slip is preferred to {110} and {123} and the critical resolved shear stress for shear in the 'twinning' sense is less than that for shear in the 'anti-twinning' sense. If the orientation dependence of the slip geometry, observed by Foxall *et al.* [3] and discussed by Duesbery [19] for uniaxial tensile deformation of niobium is used to derive the c.r.s.s. for the various slip systems then a twelve-sided polygon may be expected for room temperature punching. The {112} 'twinning', {110} and {112} 'anti-twinning' sides would have lengths in the ratio of 7.2:4.9:4. At 228K the corresponding ratio would be 9:5.4:1.4. At 175K the resulting shape would be a truncated triangle with long sides along the {112} 'twinning' planes and short facets along the {110} planes, the ratio of lengths being 16.2:2. The yield loci for 298K and 175K are drawn in Fig. 6 and for comparison the outlines of the bumps experimentally observed at 300K and 159K have been drawn from the photographic images. The general shape is in good agreement but it should be noted that the 'corners' of the triangles are rounded and follow the outline of the punched circle. The 'twinning' facets are nearly planar and lie inside the punch circle. The following discussion attempts to establish the deformation mechanisms.

The truncated triangular mound is in-

130



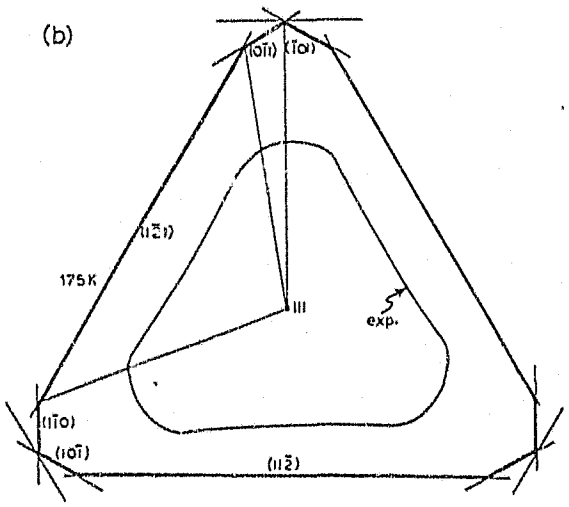


Fig. 6. The outlines of the experimentally observed bumps inscribed within the [111] yield loci. These yield loci have been constructed from the values of the critical resolved shear stresses for slip on planes of this zone obtained by Foxall *et al.* [3] (a) 298K (b) 175K.

scribed within the cylinder of maximum shear stress and therefore a/2 [111] dislocations created around the punch perimeter along arcs BCD, FGH and JKL of the upper surface (Figs. 2 and 7) must remain within the bulk of the crystal since climb at the temperature and strain rates used is unlikely. This is confirmed by the preferred chemical dissolution in these regions of the upper surface (Fig. 1b). A typical indentation of 10^{-2} cm would require a local edge dislocation content of 10^5.

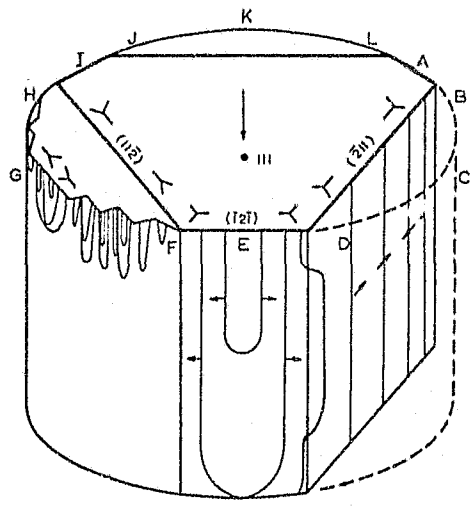


Fig. 7. A schematic representation of the deformation process described in the text. The core structure [1,2,20] of the dislocations is represented by the symbol ⋎ where the radial lines define movements which produce shear in the twinning sense.

However, for downward movement of material through the disc to produce a flat mound on the underside, shear must occur over the entire perimeter of the mound through the thickness of the disc. Since no shear is transmitted through the disc by the dislocations generated along the arcs BCD, FGH and JKL (Fig. 7), this must be achieved by the glide of screw dislocations from the corner regions LAB, DEF and HIJ along the chordal 'twinning' planes BD, HF and JL to produce the truncated triangular mound.

The dislocation content and movement are depicted in Fig. 7. The experimental evidence suggests that the dislocations which are generated mainly on twinning planes on the arcs BCD, FGH and JKL find cross slip around the glide cylinder, in response to the applied shear, a very difficult process. This results in the formation of dense arrays of stable screw dislocations dipoles and, therefore, severe work hardening. Conservation of volume requires that some material under the three segments (BCD, FGH and JKL) be transferred to the unloaded region of the upper surface of the sample. The bands of etch pits (Fig. 4) which propagate out on the respective {112} 'twinning' planes from the arcs indicate that the high shear stress, at the 'hard' regions on the perimeter of the punch, generates a/2 [111] dislocations of the sign appropriate to

the local upward movement of material at the free *upper* surface.

It is evident that the a/2 [111] screw dislocations generated on the 'anti-twinning' {112} planes and {110} planes in arcs LAB, DEF and HIJ of the glide cylinder (Figs. 2 and 7) find cross slip an easy process. Slip around the maximum shear surface proceeds until these dislocations are required to cross slip on to {112} 'twinning' planes. Once the dislocations have cross slipped on to these 'twinning' planes they find further cross slip difficult and move by planar glide across the three chordal planes of the cylinder in response to the applied shear. Although the driving stress on these planes is reduced with respect to the cylindrical surface [15,16], glide occurs along a softer and shorter path. Moreover, dislocations proceeding along these planes from adjacent corners of the triangle may mutually annihilate. The mechanism of deformation is confirmed by the etch pits of Fig. 5. Dislocations move in planar bands from the inner side of the deformation circle on traces of the {112} 'twinning' planes.

The dislocation processes described must occur simultaneously to permit the movement of the punch into the sample. The suggested mechanism is consistent with the improved definition of the triangular mound with increasing specimen thickness and with decreasing temperature. An increase in thickness gradually eliminates any possibility of material being 'punched through' in the 'hard' segments. A decrease in temperature makes cross slip even more difficult around the 'hard' arcs and, therefore, favours shear in the manner described.

A difference in the stability of dislocations to cross slip when moving on the various slip planes is suggested by the punching experiment. An explanation of this behaviour may be found in future extensions of the study of the effect of an applied shear stress on the screw dislocation core [20]. However, for the present, it should be noted that any interpretation of uniaxial deformation should take into account this varying stability to cross slip. For example, the orientation dependence of the slip plane observed by Foxall *et al.* [3] for tensile deformation of niobium crystals shows a large angular range for slip on the {112} 'twinning' planes which could be the consequence of the difficulty of cross slip off these planes. Dislocations which are originally gliding on {110} planes may cross slip on to the {112} 'twinning' planes in order to pass obstacles. The persistence of slip on these cross slip planes will account for the macroscopic observation.

The ability of dislocations on the various slip systems to cross slip will influence the deformation behaviour of b.c.c. metals by determining the number of jogs, of atomic dimensions or larger, created by the double cross slip mechanism. Electron microscopy studies and the recent direct observation of the initial movement of dislocations at yield in Fe - Si by high voltage electron microscopy [21] suggest that the mobility of screws is controlled by the motion of the jogs. Thus, the plastic anisotropy of the b.c.c. metals (discussed, for example, by Sherwood, Guiu, Kim and Pratt [22] will be determined indirectly by the orientation dependence of the probability of cross slip. The experiment described in this paper could, therefore, provide a convenient method of determining the relative stability to cross slip of dislocations moving on various slip planes and hence complement the uniaxial deformation studies.

ACKNOWLEDGEMENTS

The authors would like to thank Professor F.R.N. Nabarro for his invaluable discussions and Mrs. K. Peach for her assistance with the illustrations.

REFERENCES

1 J.W. Christian and V. Vítek, Rept. Progr. Phys., 33 (1970) 307.
2 J.W. Christian, Proc. 2nd Intern. Conf. on the Strength of Metals and Alloys, Asilomar: A.S.M., 1970, p. 31.
3 R.S. Foxall, M.S. Duesbery and P.B. Hirsch, Can. J. Phys., 45 (1967) 607.
4 T. Taoka, S. Takeuchi and E. Furubayashi, J. Phys. Soc. Japan, 19 (1964) 701.
5 B. Šesták and H. Zárubová, Phys. Status Solidi, 10 (1965) 239.
6 C.D. Statham, D. Vesely and J.W. Christian, Acta Met., 18 (1970) 1243.
7 B. Šesták and J. Blahovec, Phys. Status Solidi, 40 (1970) 599.
8 J.P. Hirth and J. Lothe, Phys. Status Solidi, 15 (1966) 487.
9 D.K. Bowen, J.W. Christian and G. Taylor, Can. J. Phys., 45 (1967) 903.

132

10 B. Šesták and S. Libovický, Conf. on the Relationship between the Structure and Mechanical Properties of Metals, Teddington, H.M.S.O., 1963, p. 158.
11 B. Šesták, N. Zárubová and V. Sládek, Can. J. Phys., 45 (1967) 1031.
12 A. Smakula and M.W. Klein, Phys. Rev., 84 (1951) 1013.
13 W.A. Rachinger and A.H. Cottrell, Acta Met., 4 (1956) 109.
14 E. Nembach, Phys. Status Solidi, 13 (1966) 543.
15 J. Boussinesq, Applications des Potentiels, Paris, 1885.
16 J.W. Harding and I.N. Sneddon, Proc. Cambridge Phil. Soc., 41 (1945) 16.
17 I.N. Sneddon, Proc. Cambridge Phil. Soc., 42 (1946) 29.
18 G.Y. Chin, Met. Trans., AIME, 3 (1972) 2216.
19 M.S. Duesbery, Phil. Mag., 19 (1969) 501.
20 M.S. Duesbery, V. Vítek and D.K. Bowen, Proc. Roy. Soc. (London) A 332 (1973) 85.
21 H. Saka and T. Imura, J. Phys. Soc. Japan, 32 (1972) 702.
22 P.J. Sherwood, F. Guiu, H.C. Kim and P.L. Pratt, Can. J. Phys., 45 (1967) 1075.

REFERENCES

Abrikosov, A.A. (1957) Soviet Phys., J.E.T.P., 5 : 1174

Alefeld, G. (1969) Phys. Stat. Sol., 32 : 67.

Alers, P.B. (1957) Phys. Rev., 105 : 104.

Alers, G.A. and Waldorf, D.L. (1962) I.B.M. J1. Res. Dev., 6 : 89.

Anderson, P.W. (1962) Phys. Rev. Lett., 9 : 309.

Anderson, P.W. and Kim, Y.B. (1964) Rev. Mod. Phys., 36 : 39.

Andres, K., Olsen, J.L., and Rohrer, H. (1962). I.B.M. J. Res. Develop., 6 : 84.

Andrew, F.R. (1948) Proc. Roy. Soc. (London), A 194 : 98.

Appleyard, J.R., Evetts, J.E., and Campbell, A.M., Sol. Stat. Comm., 14 : 567 (1974)

Armstrong, P.E., Dickinson, J.M. and Brown, H.L. (1966). Trans. Met. Soc. AMIE, 236 : 1404.

Aston, D.R., Dubeck, L.W. and Rothwarf, F. (1971) Phys. Rev. B., 3 : 2231.

Baird, D.C. and Wright, L.S. (1972) J. of Low Temp. Phys., 8 : 177.

Baird, D.C. (1964) Can. J. Phys., 42 : 1682.

Baramidze, G.A. and Saralidze, Z.K. (1970) Soviet Phys., J.E.T.P. Lett., 12 : 179.

Barker, J.R. (1950) British Journal Appl. Phys., 1 : 65.

Bean, C.P. (1962) Phys. Rev. Lett., 8 : 250.

Bean, C.P. (1964) Rev. Mod. Phys., 36 : 31.

Bean, C.P. and Livingston, J.D. (1964) Phys. Rev. Letters, 12 : 14.

Bean, C.P., de Blois, R.W. and Nesbitt, L.B. (1959) Journal Appl. Phys., 30 : 1976.

Bean, C.P. and Doyle, M.V. (1962) J. Appl. Phys., 33 : 3334.

Berman, R., Brock, J.C.F. and Huntley, D.J. (1965) Adv. in Cryogenic Eng., 10 : 233-238.

Bockris, J. O'M., Beck, W., Genshaw, M.A., Subramanyan, P.K. and Williams, F.S. (1971) Acta Metall., 19 : 1209.

Bowen, D.K., Christian, J.W. and Taylor, G. (1967). Can. J. Phys., 45 : 903.

Brailsford, F. (1966), Physical Principles of Magnetism., D. van Nostrand Company Limited, London.

Brown, W.F. (1962), Magnetostatic Principles in Ferromagnetism (North Holland Publishing Company, Amsterdam).

Buck, O., Thompson, D.O. and Wert, C.A. (1971) J. Phys. Chem. Solids, 32 : 2331.

Bullough, R. and Newman, R.C. (1962) Proc. Royal Soc., A266 : 98.

Campbell, A.M. (1969), J. Phys. C, 2 : 1492.

Campbell, A.M. and Evetts, J.E. (1972) Advances in Physics, 21 : 19 199-428.

Campbell, A.M., Evetts, J.E. and Dew-Hughes, D. (1968) Phil. Mag., 18 : 313.

Cantelli, R., Mazzolai, F.M. and Nuovo, M. (1969) Phys. Stat. Sol., 34 : 597.

Cape, J.A. and Zimmerman, J.M. (1967) Phys. Rev., 153 : 416.

Carslaw, H.S. and Jaeger, J.C. (1959) Conduction of heat in Solids, Oxford Univ. Press, (London II ed.).

Claiborne, L.T. (1963) J. Phys. Chem. Solids, 24 : 1363.

Clarke, J.M. and Mordike, B.L. (1966) Appl. Material Res. 5 : 181.

Coffey, H.T. (1967) Phys. Rev., 166 : 447.

Coote, R.I. (1970) Thesis, Cambridge.

Cottrell, A.H. (1948) Rep. Conf. Strength of Solids, Phys. Soc., Bristol, p. 30.

Cottrell, A.H. and Bilby, B.A. (1949) Proc. Phys. Soc., A62 : 49.

Cribier, D., Jacrot, B., Madhav Rao, L., and Farnoux, B. (1964) Physics Letters, 9 : 106.

Das Gupta, A. and Kramer, E.J. (1972) Materials Science Center, Report 1629.

de Gennes, P.G. (1966) Superconductivity of Metals and Alloys (W.A. Benjamin, Inc., New York).

de Gennes, P.G. (1965) Solid State Comm., 3 : 127.

De Sorbo, W. (1963) Phys. Rev., 132 : 107.

De Sorbo, W. and Healy, W.A. (1964) Cryogenics, 4 : 257.

Dew-Hughes, D. (1966) Mater. Sci. Eng., 1 : 2.

Dew-Hughes, D. (1972) Rep. Prog. Phys., 34 : 821.

Dew-Hughes, D. and Witcomb, M.J. (1972). Phil. Mag., 26 : 73.

Dollins, C. and Wert, C. (1969) Acta Metall., 17 : 711.

Eilenberger, G. (1964) Z. Physik., 180 : 32.

Eilenberger, G. (1967) Phys. Rev., 153 : 584.

Eilenberger, G. and Buttner, H. (1969) Z. Physik., 224 : 335.

Essmann, U. (1971) Physica., 55 : 83.

Essmann, U. and Träuble, H. (1967) Phys. Letters., 24 : 526.

Evetts, J.E., Campbell, A.M. and Dew Hughes, D. (1968), J. Phys. C., 1 : 715.

Faber, K. and Schultz, H. (1972) Scripta Met., 6 : 1065.

Fast, J.D. (1971) Interaction of Metals and Gases Vol. 2, Phillips Technical Library, Macmillan Press Limited.

Fetter, A.L. and Hohenberg, P.C. (1969) Superconductivity (Vol. 1) Edited by R.D. Parkes (Marcel Dekker Inc., New York).

Fetter, A.L. and Hohenberg, P.C. (1967) Phys. Rev., 159 : 330.

Fietz, W.A. and Webb, W.W. (1969) Phys. Rev., 178 : 657.

Fink, H.J. (1966) Phys. Rev. Lett. 16 : 447.

Cribier, D., Jacrot, B., Madhav Rao, L., and Farnoux, B. (1964) Physics Letters, 9 : 106.

Das Gupta, A. and Kramer, E.J. (1972) Materials Science Center, Report 1629.

de Gennes, P.G. (1966) Superconductivity of Metals and Alloys (W.A. Benjamin, Inc., New York).

de Gennes, P.G. (1965) Solid State Comm., 3 : 127.

De Sorbo, W. (1963) Phys. Rev., 132 : 107.

De Sorbo, W. and Healy, W.A. (1964) Cryogenics, 4 : 257.

Dew-Hughes, D. (1966) Mater. Sci. Eng., 1 : 2.

Dew-Hughes, D. (1972) Rep. Prog. Phys., 34 : 821.

Dew-Hughes, D. and Witcomb, M.J. (1972). Phil. Mag., 26 : 73.

Dollins, C. and Wert, C. (1969) Acta Metall., 17 : 711.

Eilenberger, G. (1964) Z. Physik., 180 : 32.

Eilenberger, G. (1967) Phys. Rev., 153 : 584.

Eilenberger, G. and Buttner, H. (1969) Z. Physik., 224 : 335.

Essmann, U. (1971) Physica., 55 : 83.

Essmann, U. and Träuble, H. (1967) Phys. Letters., 24 : 526.

Evetts, J.E., Campbell, A.M. and Dew Hughes, D. (1968), J. Phys. C., 1 : 715.

Faber, K. and Schultz, H. (1972) Scripta Met., 6 : 1065.

Fast, J.D. (1971) Interaction of Metals and Gases Vol. 2, Phillips Technical Library, Macmillan Press Limited.

Fetter, A.L. and Hohenberg, P.C. (1969) Superconductivity (Vol. 1) Edited by R.D. Parks (Marcel Dekker Inc., New York).

Fetter, A.L. and Hohenberg, P.C. (1967) Phys. Rev., 159 : 330.

Fietz, W.A. and Webb, W.W. (1969) Phys. Rev., 178 : 657.

Fink, H.J. (1966) Phys. Rev. Lett. 16 : 447.

Finnemore, D.K., Stromberg, T.F. and Swenson, C.A. (1966) Phys. Rev., 149 : 231.

Foner, S. (1963) Rev. Scient. Instrum., 40 : 369.

Fournet, A. and Mailfert, G. (1970) J. Phys. Paris 31 : 355.

Foxall, R.A., Duesberry, M.S. and Hirsh, P.B. (1967) Can. J. Phys., 45 : 607.

Freyhardt, H.C. (1969) Z. Metalkde, 60 : 409.

Freyhardt, H.C. (1971a) Phil. Mag., 23 : 345; (1971b) Ibid., 23 : 369.

Freyhardt, H. (1969) Z. Mettalkde., 60 : 409.

Freyhardt, H. and Haasen, P. (1967) Z. Metalkde, 12 : 856.

Friedel, J., de Gennes, P.G., and Matricon, J. (1963) Appl. Phys. Lett., 2 : 119.

Galaiko, V.P. (1968) J.E.T.P. Letters, 7 : 230.

Ginzburg, V.L. and Landau, L.D. (1950) Zh. Eksperim. i. Teor. Fiz., 20 : 1064.

Good. J.A. and Kramer, E.J. (1970) Phil. Mag., 22 : 329.

Goodman, B.B. (1961) Phys. Rev. Letters, 6 : 597.

Goodman, B.B. (1962) I.B.M. I. Res. Dev., 6 : 63.

Goodman, B.B. (1966) Reports on Prog. in Phys., 29 : 445.

Gorsky, W.S. (1935) Phys. Z. SU., 8 : 457.

Gorter, C.J. (1933) Arch. Mus. Teyler, 7 : 378.

Gorter, C.J. and Casimir, H.B.G. (1934), Physica, 1 : 306.

Gottlieb, M. and Jones, C.K. (1966) Phys. Letters, 30 : 150.

Ham, F.S. (1959) J. Appl. Phys., 30 : 915.

Hampshire, R.G. and Taylor, M.T. (1972) J. Phys. F, 2 : 89.

Hanada, R., Suganuma, T. and Kimura, H. (1972) Scripta Met., 6 : 483.

Harden, J.L. and Arp, V. (1963) Cryogenics, 3 : 105.

Hardie, D. and McIntyre, P. (1972) Metal Science Journal, 6 : 40.

Harper, S. (1951) Phys. Rev., 83 : 709.

Hazzeldine, P.M. and Hirsch, P.B. (1967) Phil. Mag., 15 : 121.

Higgins, R.J. and Yung Kwan Chang (1968) Rev. Sci. Instr., 39 : 522.

Hoffman, D.W. and Cohen, M. (1973) Acta. Met., 21 : 1215.

Horn, F.W. and Ziegler, W.T. (1947) J. Am. Chem. Soc., 69 : 2762.

Hudson, W.R. (1968) Rev. Sci. Instr. (U.S.A.), 89 : 253.

Jacobs, A.E. (1971) Phys. Rev. B., 4 : 3016 - 3027, 3029 - 3034.

Jaeger, J.C. (1956) Elasticity, Fracture and Flow, Methuen and Co. Limited, London.

Jones, K.A. and Rose, R.M. (1969) Trans. Met. Soc. AIME, 245 : 67.

Kammerer, U. (1969a) Z. Phys., 227 : 125; (1969b), Phys. Stat. Sol., 34 : 81.

Keesom, W.H. (1924) Rapp. 4e. Cong. Solvay : 288 - 298.

Kim, Y.B., Hempstead, C.F. and Strnad, A.R. (1962) Phys. Rev. Lett., 9 : 306.

Kistner, G., Rubin, R. and Sosnowska, I. (1971) Phys. Rev. Lett., 27 : 1576.

Kleiner, W.H., Roth, L.M. and Autler, S.H. (1964) Phys. Rev., 133 : A1226.

Krageloh, U. (1970) Phys. Stat. Sol., A2 : 559.

Kramer, L. (1966) Phys. Lett., 23 : 619.

Kramer, E.J. (1973) J. Appl. Phys., 44 : 1360.

Kramer, E.J. and Bauer, C.L. (1967) Phil. Mag., 15 : 1189.

Kronmüller, H. and Seeger, A. (1969) Phys. Stat. Sol., 34 : 781.

Kulik, I.O. (1966) J.E.T.P., Pisma Redaksiyn.3 : 398.

Kunzler, J.E. (1961) Rev. Mod. Phys., 33 : 501.

Kuper, C.G. (1968) An Introduction to the Theory of Superconductivity, Clarendon Press, Oxford.

Labusch, R. (1968) Phys. Rev., 170 : 470.

Labusch, R. (1969a) Phys. Stat. Sol., 32 : 439.

Labusch, R. (1969b) Crystal Lattice Defects, 1 : 1.

Labusch, R. (1973) private communication.

Landau, L.D. and Lipshitz, E.M. (1960) Electrodynamics of Continuous Media, Pergamon Press, N.Y.

Livingston, J.D. and Desorbo, W. (1969) Superconductivity Vol. 2, Edited by R.D. Parkes (Marcel Dekker, Inc., New York).

Lindenfeld, P. (1967) Rev. Sci. Instr., 32 : 9.

Livingston, J.D. and Schadler, H.W. (1964) Prog. Mater. Sci., 12 : 183.

London, F. (1961) Superfluids: Vol. 1. Dover Press, New York, pp 125-130.

London, H. (1963) Phys. Letters, 6 : 162.

London, F. and London, H. (1935) Proc. Roy. Soc., A149 : 71.

Low, F.J. (1961) Adv. Cryogenic. Eng., 7 : 514.

Lowell, J. (1970) J. Phys. C., 2 : 372.

Lowell, J. (1972) J. Phys. F. (Metal Physics), 2 : 547.

Maki, K. (1964) Physics, 1 : 21; (1964) Physics, 1 : 127.

Maki, K. (1965) Annals of Physics, 34 : 363.

Meissner, W. and Ochsenfeld, R. (1933) Naturwiss, 21 : 787.

Melville, P.H. (1971) J. Phys. C., 5 : 147-158.

Milne, I. and Gibbons, D.F. (1972) J. Appl. Phys., 5 : 1955.

Miyahara, K., Irie, F. and Yamafuji, K. (1969) J. Phys. Soc., Japan, 27 : 290.

Morel, P. (1959) J. Phys. Chem. Solids, 24 : 1363.

Muhlschlegel, B. (1959) Z. Physik., 155 : 313.

Nabarro, F.R.N. (1967) Theory of Crystal Dislocations, Clarendon Press, Oxford.

Nabarro, F.R.N. (1972) J. Less-Common Metals, 28 : 257.

Nabarro, F.R.N. and Quintanilha, A.T. (1970) Mat. Res. Bull., 5 : 699.

Narlikar, A.V. and Dew-Hughes, D. (1964) Phys. Stat. Sol., 6 : 383.

Narlikar, A.V. and Dew-Hughes, D. (1966) J. Material Sci., 1 : 317.

Nembach, E. (1966) Phys. Stat. Sol., 13 : 543.

Neumann, L. and Tewordt, L. (1966). Z. Physik, 189 : 55.

Neumann, L. and Tewordt, L. (1966), Z. Physik, 191 : 73.

Obst, B. (1969) Phys. Lett., 28A : 662.

Olafsson, R. and Allen, J.F. (1972) J. Phys. F., 2 : 123.

Park, J.G. (1969) Adv. Phys., 18 : 103.

Pearl, J. (1964) Appl. Phys. Letters, 5 : 65.

Pearl, J. (1965) Low Temperature Physics LT9, edt. by J.C. Daunt, D.O. Edwards, F.J. Milford and M. Jagub (Plennus Press Inc., N.Y., 1965) page 566.

Pippard, A.B. (1953) Proc. Roy. Soc., A216 : 547.

Pippard, A.B. (1969) Phil. Mag., 19 : 217.

Pippard, A.B. (1955) Phil. Mag., 46 : 1104.

Powers, R.W. and Doyle, M.V. (1959) J. Appl. Phys., 30 : 514.

Pryde, J.A. and Titcomb, C.G. (1969) Trans. Faraday Soc., 65 : 2758.

Pryde, J.A. and Tsong, I.S.T. (1971) Acta Met., 19 : 1333.

Quintanilha, A.T. (1972) Thesis (University of the Witwatersrand, S.A.)

Richards, D.B., Edwards, L.R., Cornforth, C.M. and Legvold (1970) Rev. Sci. Ins., 41 : 6.

Robinson, F.N.H. (1959) Journal of Sci. Instr., 36 : 481.

Rothwarf, F., Rao, C.T. and Dubeck, L.W. (1972) Sol. State. Comm., 11 : 23.

Rose, K.A. and Jones, R.M. (1969) Trans. AIME, 245 : 67.

Saint James, D. and de Gennes, P. (1963) Phys. Lett., 7 : 306.

Saint James, D., Sarma, G. and Thomas, E.J. (1969) Type II Superconductivity, Pergamon Press.

Sarver, C.E. and Blakemore, J.S. (1967) Cryogenics, 7 : 299.

Schoek, G. and Seeger, A. (1959) Acta Metalkde, 7, 469.

Seeger, A. (1970) Comments Sol. St. Phys., 3 : 97.

Seeger, A. and Kronmüller, H. (1968) Phys. Stat. Sol., 27 : 371.

Seraphim, D.P. (1960) Solid State Electronics, 1 : 368.

Seraphim, D.P. and Marcus, P.M. (1962) I.B.M. J1, Res. Dev., 6 : 94.

Serin, B. (1969) Superconductivity, Vol. 2 (Ed. R.D. Parks) Marcel Dekker Inc., N.Y. pp 925-976., pp 817-923.

Shoenberg, D. (1937) Proc. Cambridge Phil. Soc., 33 : 260.

Shoenberg, D. (1952) Superconductivity, Cambridge Univ. Press.

Shubnikov, L.V., Khotkevich, V.I., Shepilev, Yu. D., and Riabinin, Yu. N (1937), Zh. Eks. i Tior. Fiz., 7 : 221.

Silcox, J. and Rollins, R.W. (1963) Appl. Phys. Lett., 2 : 231.

Stern, R., Levy, M. Kagiwada, R. and Rudnick, I. (1962) Appl. Phys. Lett., 2 : 80.

Stoner, R.E. and Herbert, R.H. (1970) J. Appl. Phys., 41 : 3706.

* Taylor, G. and Christian, J.W. (1967a) Phil. Mag., 15 : 877.

Taylor, G. and Christian, J.W. (1967b) Phil. Mag., 15 : 893.

Tedmon, C.S., Rose, R.M. and Wulff, J. (1965) J. Appl. Phys., 36 : 829.

Terman, F.E. (1943) Radio Engineers Handbook, McGraw Hill, N.Y. p. 60.

Tewordt, L. (1964) Z. Physik, 189 : 55.

Timoshenko, S. and Goodier, J.N. (1951) Theory of Elasticity, 2nd Ed. (McGraw Hill) N.Y.

Toth, L.E. and Pratt, I.P. (1964) Appl. Phys. Lett., 4 : 75.

Vandersande, J. (1974) Ph.D. Thesis, University of the Witwatersrand, S.A.).

*Taylor, G. and Christian, J.W. (1966) D. Phil. Thesis, University of Oxford.

Van Landuyt, J., Gevers, R., and Amelinckx, S. (1966). Phys. Stat. Sol., 13 : 467.

Walter, R.J. and Chandler, W.T. (1965) Trans. TMS-AIME, 233 : 762.

Webb, W.W. (1963) Phys. Rev. Letters, 11 : 191.

Webb, W.W. (1971) J. Appl. Phys., 42 : 107.

Westlake, D.G. (1969) Trans TMS-AIME, 245 : 287.

Westlake, D.G. (1972) Scripta Met., 6 : 887.

Westlake, D.G. and Gray, W.R. (1966) Appl. Phys. Lett., 9 : 3.

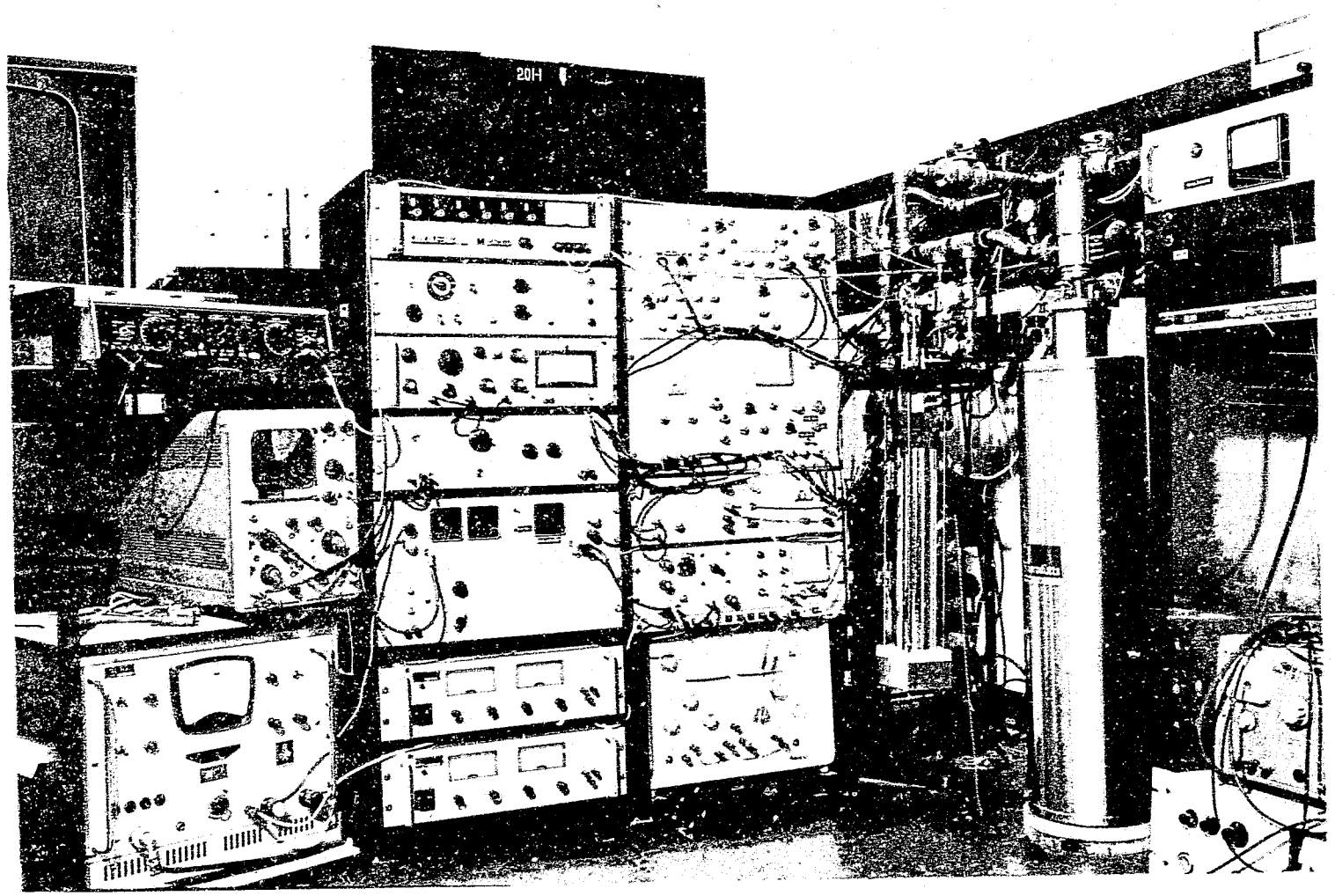
Wiseman, C.D. (1966) J. Appl. Phys., 37 : 3599.

White, G.K. (1962) Phil. Mag., 7 : 271.

White, G.K. (1959) Experimental Techniques in Low-Temperature Physics, Clarendon Press, Oxford.

Yamafuji, K. and Irie, F. (1967) Phys. Lett. A., 25 : 387.

Zoller, P. and Dillinger, J.R. (1969) Am. Journal of Physics, 37 : 519.



Author Doyle T B
Name of thesis Fluxon pinning and Geometrial effects in A type 11 superconductor 1975

PUBLISHER:
University of the Witwatersrand, Johannesburg
©2013

LEGAL NOTICES:

Copyright Notice: All materials on the University of the Witwatersrand, Johannesburg Library website are protected by South African copyright law and may not be distributed, transmitted, displayed, or otherwise published in any format, without the prior written permission of the copyright owner.

Disclaimer and Terms of Use: Provided that you maintain all copyright and other notices contained therein, you may download material (one machine readable copy and one print copy per page) for your personal and/or educational non-commercial use only.

The University of the Witwatersrand, Johannesburg, is not responsible for any errors or omissions and excludes any and all liability for any errors in or omissions from the information on the Library website.